High-frequency Ground Motion Scaling and Ground Shaking scenarios for earthquakes in Central Greece

By: Chantelle-Marie Dimech

Tutor: Dr. Sebastiano D'Amico

A thesis presented to the Department of Geosciences at the University of Malta in Fulfillment of the Requirements for the Degree of Doctor of Philosophy

2021

Abstract

Assessing seismic hazard is important to consider whilst studying the seismology of a region. For seismologists and structural engineers, earthquake ground motion prediction is a crucial aspect of their work. Latest national hazard maps facilitate the planning and design of earthquake resistant infrastructure. These maps are produced after a precise calibration of ground motion predictive relationships, which are calculated as a function of distance from the source, magnitude, and frequency for the region using various mathematical and data processing techniques such as regression analysis. The aim of this study is to provide a complete description of the characteristic of the ground-motion for the Corinth Gulf region, for which this has not been done so far. Waveforms from around 297 events were obtained from 65 three-component stations around central Greece, all part of the Hellenic Unified Seismic Network. For this region, we employed a general form for a predictive relationship including the source excitation term, an attenuation operator and an operator to account for the site effect. The functional form of the crustal attenuation term depends principally on the attenuation parameter and on the geometrical spreading. Excitation terms are modelled by using a Brune spectral model. Simulations are carried out using EXSIM and ground motion scenarios (in terms of peak ground acceleration and peak ground velocity as a function of magnitude and distance) are computed for the study area. Furthermore, it is envisaged that the results obtained can later be used for upgrading seismic hazard maps and for engineering designs as well as

implementing tools like ShakeMap®, as well as to be used for implementing evacuation plans and risk mitigation strategies.

Table of contents

Chapter **Page number**

List of Figures

Figure number **Page number**

List of tables

Table number **Page number**

Acronyms

PGA: Peak Ground Acceleration

PGV: Peak Ground Velocity

RVT: Random Vibration Theory

RMS: Root mean square

NEHRP: National Earthquake Hazard Reduction Program

HUSN: Hellenic Unified Seismic Network

SAC: Seismic Analysis Code

USGS: United States Geological Survey

Dedication

To the strong women

who enrich my life every day.

"The Lord is my shepherd; I shall not want.

He makes me lie down, in green pastures.

He leads me beside still waters.

He restores my soul."

Psalm 23:1-3

Acknowledgements

First of all, I would like to thank Dr. Sebastiano D' Amico for guiding me these past years, including during my undergrad dissertation. His constant patience, guidance and faith in me has been instrumental. I am proud to have worked with a brilliant seismologist such as he is. I would also like to thank Dr. Christos Evangelidis, Dr. Efthimios Sokos and Mr. George Bozionelos for providing me with the necessary data for the Corinth Gulf to conduct this study. It was an honour to have worked with Greek colleagues on such a project. A big thanks also goes to Profs. Robert B. Hermann for helping me with any issue regarding the programme used during this study. His prompt response helped me carry on with the flow on the project. Another thank you goes to my best friend Esther, who provided me with the necessary help and information to plot the maps using GIS software and for proofreading my thesis. To my boyfriend, Adrian, I also would like to show my heartfelt gratitude especially for all his patience, support and most of all for believing in me every step of the way. He made me see the light during the difficult moments. I would also like to thank him for proofreading my thesis and providing his opinion as well. Finally, to my family, I thank you with all my heart for everything that you have done for me and for putting up with me these past few months, which was not easy. They have believed in me ever since I was young and gave me the confidence I needed to carry on. I hope I have made them proud with what I have achieved.

Chapter 1: Introduction

1.1. Importance of ground motion prediction

Earthquakes have been some of the most powerful natural disasters since Earth's formation billions of years ago. A critical factor to how the Earth is shaped today, earthquakes have been classified as natural disasters due to the high risk of damage and human suffering brought about, which in turn requires a necessity for a country to appeal for international help. It is important to consider seismic hazard assessment whilst studying the seismology of a region due to its social benefits from hazard reduction. For seismologists and structural engineers, earthquake ground motion prediction is a crucial aspect of their work. It is applied to construct buildings which are more resilient to ground motion, as well as to design hazard maps which give an indication of future ground motion probabilistically. Earthquake prediction is described commonly as the most accurate forecasting of the time, size and place of an impending earthquake (Scholz, 2002). However, forecasting these 3 characteristics at the same time has proven to be quite difficult although creating simulations of the possible place and size of ground motion is more commonplace.

Recently, large and destructive earthquakes that have struck in heavily populated areas worldwide (Izmit, Turkey, 17th August 1999; Chi-Chi, Taiwan 20th September 1999; Sumatra, 26th December 2004; L'Aquila, Italy, April 6th, 2009) have intensely highlighted the issue of having a large area of the

buildings constructed within and nearby epicentral areas. For example, during the L'Aquila and Amatrice earthquakes (2009 and 2016, respectively) about 600 persons perished and over 100,000 were left homeless, making these the deadliest Italian earthquakes since the 1980, Irpinia earthquake. Other examples of recent deadly earthquakes are the 2010 and 2021 magnitude 7.0 and magnitude 7.2 Haiti earthquakes, the former leaving over 230,000 people dead and over 250,000 collapsed buildings (Bilham, 2010), whilst the latter destroyed 129,000 buildings and caused over 2000 fatalities (ECHO, 2021). Another recent earthquake is the Aegean Sea earthquake, another magnitude 7.0 event, that left over 200 people dead and over 15,000 people were left homeless, making it the deadliest earthquake in 2020 (Wei-Haas, 2020).

Although extremely costly, building structures which resist earthquakes and reconstructing old buildings should be on the agenda even for developed Western countries. This can be facilitated by using available national hazard maps for planning and design. These maps can be created after a precise calibration of ground motion predictive relationships for the area using numerous data processing and mathematical techniques such as regression analysis. Seismologists prioritize the updating of existing hazard maps as new data enables ground motion recomputation and reduces the related uncertainties. Ground motion can be quantitatively estimated by using the so-called predictive relationships (see Kramer, 1996), which enable the calculation of specific ground-motion parameters as a function of distance from the source, magnitude and frequency. It is important to note that these should be calibrated in the area under study. A significant number of strong motion data is usually regressed to obtain those attenuation relationships (Campbell

and Bozorgnia, 1994; Boore et al., 1993; Ambraseys et al., 1996, Ambraseys and Simpson, 1996; Sabetta and Pugliese, 1987, 1996).

In this study we propose to derive attenuation relationships as well as determine ad-hoc scenarios basing our computation on the evaluation of attenuation properties and source parameters calibrated in the study area, using only weak-motion data and background seismicity.

1.2. Aim and Research Question

The main aim of this study is to quantitatively describe the regional attenuation, site and source characteristics to eventually evaluate the amplitude of strong ground motion anticipated from future earthquakes in the study area. To do so, low magnitude earthquakes with weak motion can be used to create simulations for high magnitude, strong motion earthquakes which may occur in a seismically active region. In this study, the background seismicity is used to perform the analysis (details in Malagnini et al., 2000b, 2007). The reason why background seismicity was mostly used is the fact that there is insufficient strong motion data from the Corinth Gulf region to provide reliable ground motion parameters used for the purpose of this research. Furthermore, this methodology has been applied globally using background seismicity and weak motion data (see section 3.1.1). Background seismicity can be used to evaluate the attenuation properties of the crust as proposed by Chouet et al. (1978) and later proven by Raoof et al. (1999) and Malagnini et al. (2000b, 2007). Putting it simply, with this method, regionally calibrated attenuation relationships can be developed even where data from strong motion earthquake events is not available.

In particular, the PhD project will focus mainly on the Corinth Gulf in central Greece where these kinds of studies have not been carried out (Figure 1). Datasets consist of seismograms from a large number of recent earthquakes recorded in the last few years with magnitudes greater than 2.5. These will then be processed using regression analysis to obtain the required parameters, such as the source parameter, to produce propagation simulations for the region. Through the use of the attenuation and source parameters estimated in the study area, as well as known information regarding mapped faults, stochastic simulations will be performed (Motezidian and Atkinson, 2005; Assatourians and Atkinson, 2007; Boore, 2009) in order to predict the anticipated ground shaking term, for example, of Peak Ground Acceleration (PGA) and Peak Ground Velocity (PGV).

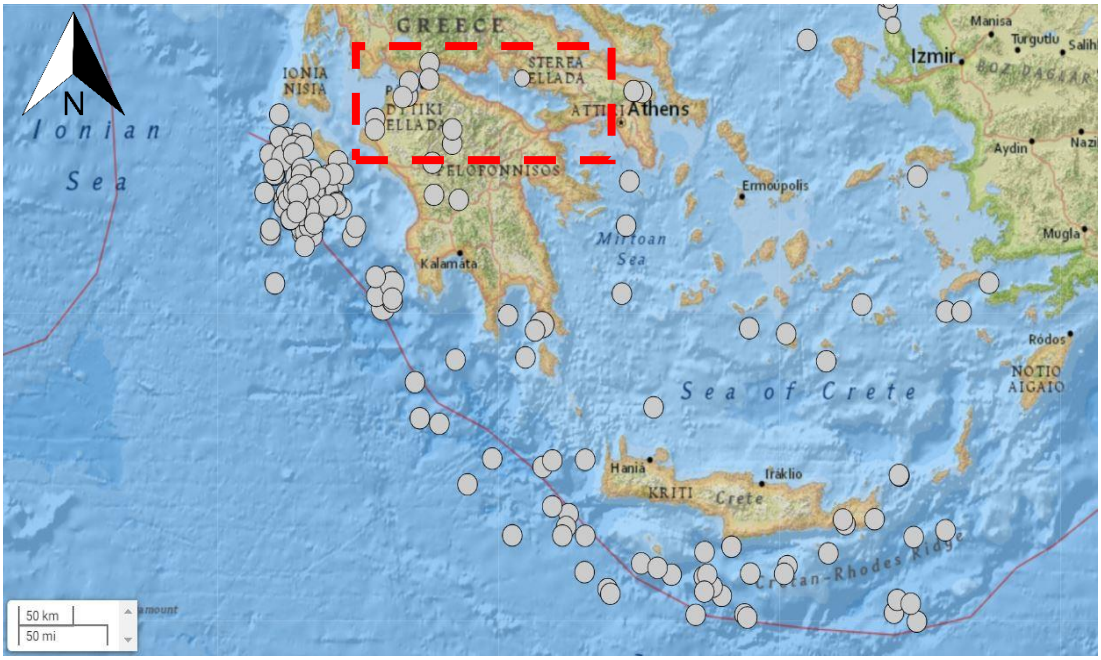

FIGURE 1: THE CORINTH GULF AREA (WITHIN THE RED BOX) WHICH IS THE FOCUS OF THIS STUDY. THE CIRCLES REPRESENT THE EARTHQUAKES WITH A MAGNITUDE 2.5 OR MORE WHICH HAVE OCCURRED FROM THE 1ST OF JANUARY 2018 TO 1ST OCTOBER 2018. COORDINATES USED: 39.385° N, 27.51 ° E; 34.289 ° N,19.775 ° E. SOURCE: USGS EARTHQUAKE CATALOGUE

Furthermore, the results obtained by the study can eventually be applied to upgrade the latest hazard map of central Mediterranean countries and for

engineering designs. Shake Map® (Wald et al., 2005) can also be applied for this study area by using the obtained results, since it uses this type of information to create a swift earthquake response. ShakeMap® is a tool that is used to depict the magnitude and spread of ground shaking after a destructive earthquake event, and offers useful information for the public, emergency response, civil protection and loss estimation.

The use of this methodology to create seismic hazard simulations has been applied previously in different seismically active regions globally. D'Amico et al. (2012) used regression analysis to obtain information regarding the earthquake source, site properties and wave propagation in the Taiwan region to be able to predict the earthquake ground motion by using data from strong motions which occurred in 1999 for comparisons. Malagnini et al. (2007) have also used a similar methodology applied for the San Francisco region and developed the weak motion based predictive model via predictive equations which use small magnitude events. Panzera et al. (2016) used strong-motion predictions in Siracusa to analyse the response of buildings and extent of damage by also studying the lithospheric properties of the region. Locally, D'Amico & Galea (2013) used the stochastic approach to obtain ground-motion simulations for the Maltese Islands using an extended source-model code to create present day simulations of similar earthquakes that affected the Maltese Islands in the past. The results of these studies, as well as other studies conducted globally, can be seen in more detail in section 3.1.1 and in Appendix A.

1.3. Brief outline of Methodology

The methodology on which this study is based to define the attenuation properties has been successfully applied globally: northwestern United States (Herrmann and Dutt, 1999; Jeon and Herrmann 2004), California (Raoof et al., 1999; Malagnini et al., 2007), eastern North America (Atkinson and Boore, 2006), central United States (Herrmann and Malagnini, 1996), Mexico (Ortega et al., 2003), Italy (Malagnini et al., 2000a,c: 2002; Morasca et al., 2006; Scognamiglio et al., 2005), Turkey (Akinci et al., 2001, 2006), Central Europe (Malagnini et al., 2000b, Bay et al., 2003), and India (Bodin et al., 2004). Some locations for which this methodology has been applied in the central Mediterranean are also indicated in Figure 2. However, this approach has never been applied in several areas of the Central Mediterranean such as Greece. Luckily, the recent distribution of a large number of seismic broadband stations permits us to obtain a decent data set for performing the required analysis and to obtain ground motion predictive relationships for deriving earthquake ground motion scenarios. Lack of seismic coverage and data is in fact one of the reasons why attenuation properties for Greece have not been derived yet. Determining the crustal attenuation will obtain the site, source and path parameters of seismic events as described using the methodology by Malagnini et al. (2007). These are then applied to obtain the peak ground acceleration and velocity. Attenuation relationships also consider the duration parameter as a function of hypocentral distance and frequency by using the random vibration theory (see section 3.2). This theory estimates the extrema of random time histories and time-domain parameters and obtains peak

motions regarding the peak acceleration, peak displacement, peak velocity, etc.

The attenuation and source parameters are then used for stochastic simulations (see Boore, 1983) which simulate strong motion events by using finite fault geometry. This has been used as an essential tool to predict ground motion near the epicenters of large earthquakes (Hartzell, 1978; Heaton and Hartzell, 1986; Somerville et al., 1991; Tumarkin and Archuleta, 1994; Zeng et al., 1994). Simulating several small earthquakes as subevents that are part of a larger fault-rupture event is one of the typical approaches to simulate ground motion for large earthquake. This is applied by dividing a large fault into a series of N sub-faults, and each one is assumed to be a small point source (Hartzell, 1978); the acceleration spectrum can be modelled for each point source, being proportional to the sub-fault seismic moment, corner frequency, distance from the observation point, attenuation parameters, stress drop, and near surface effects (commonly indicated by the term “kappa)”.

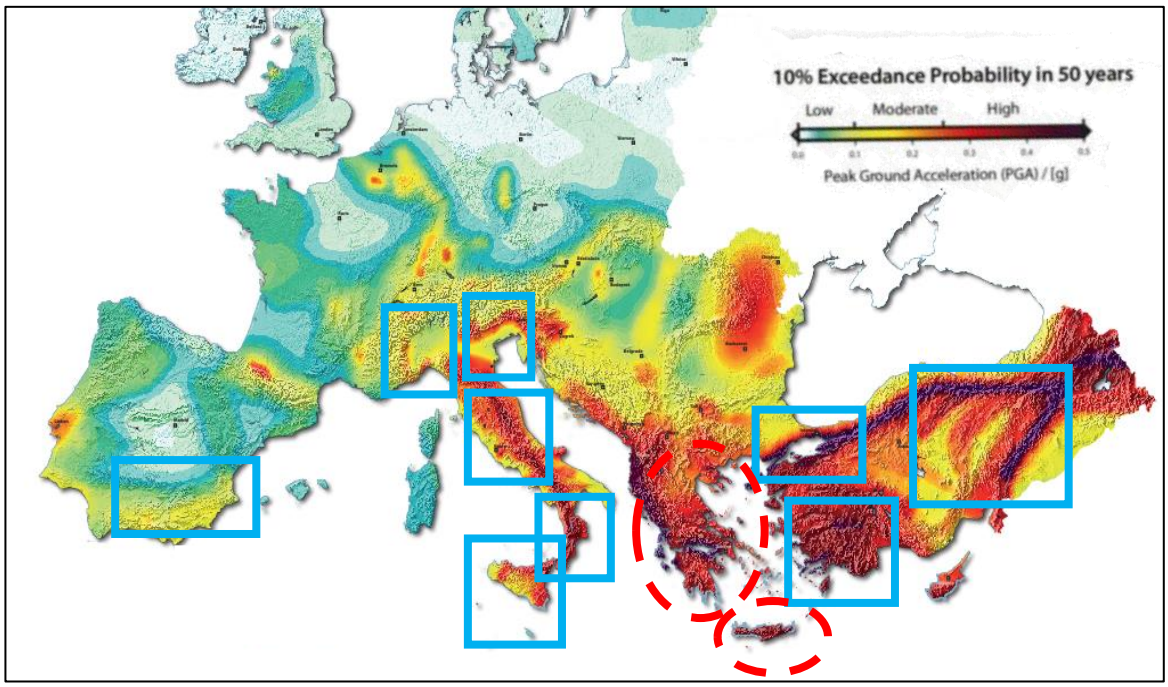

FIGURE 2: LOCATIONS (SOLID LINE IN BLUE) FOR WHICH THE METHODOLOGY HAS BEEN APPLIED IN THE NORTHERN MEDITERRANEAN AREA. DASHED LINE AREAS IN RED ARE THE LOCATIONS OF GREECE FOR WHICH SUCH A STUDY HAS NOT BEEN DONE YET. THE BACKGROUND MAP IS THE 2013 EUROPEAN SEISMIC HAZARD MAP. SOURCE: WIEMER ET AL., 2016

Chapter 2: Literature review

2.1. Introduction to the origin of seismology

The phenomena which have surrounded the occurrence of an earthquake have long been in the interest of the ancient Greeks. Since before the Classical period, which started around 500 B.C., the Greeks believed that earthquakes were caused by the god Poseidon when he was angered by striking his trident to the ground (Buxton, 2004). However, Greece was also the country from which great philosophers originated, and these were the pioneers of scientific thinking. Greek philosophers such as Anaximenis of Miletos (585-528 B.C.) and Aristotle (384-322 B.C.) presumed that earthquakes occurred due to an interaction with the earth's interior such as temperature changes (Anaximenis's theory) or air currents as concluded by Aristotle (Kouskouna and Makropoulos, 2004).

The importance of earthquakes to the ancient Greeks has recently been investigated in a study by Stewart and Piccardi (2017), in which they discussed how ancient Greeks built important buildings and cities such as Mycenae and Ephesus, in areas affected by seismic activity. These cities were built over underground fault lines to be used for groundwater and also to have exits for buildings. One of the most important sites in ancient Greek culture was the Oracle at Delphi in central Greece. According to ancient beliefs, the priestess Pythia used to inhale a vapour rising from a fissure and then received visions of prophecy sent by the god Apollo. De Boer and Hale (2000) discussed new findings which suggest that the site is located on a major WNW-ESE fault zone

with minor NNW-SSE fractures which intersect and provide pathways for rising groundwater. One spring is located below the temple of Apollo from which the prophecies were received. A bituminous limestone formation below the area led to the formation of hydrocarbon gases which were released due to seismic events. This release of gases that can induce narcotic effects, is what inspired the origin of prophecies in this location.

There is no doubt therefore that the ancient Greeks inspired scientists to investigate earthquakes and their occurrence. The complex Greek seismotectonics as well as that of the Mediterranean region in general is what helped inspire such beliefs and this shall be discussed in more detail in this chapter.

2.2. Tectonics of the Mediterranean region

The Mediterranean region is part of the westernmost area belonging to the Alpine-Himalayan orogenic belt. This belt has been formed due to the complex interaction between the Eurasian, African and Arabian plates (Vannucci et al., 2004). In the central Mediterranean, the tectonics is caused by the convergence of the African and Eurasian plate which have been in motion for around 100 million years and are presently converging at a rate of 5 $mmyr^{-1}$ to the north-east (Goes et al., 2004). The region is not so simple as different tectonics are present such as compressional, extensional, and strike-slip kinematics which all coexist in close association (Vannucci et al., 2004). However, subduction only occurs at the Calabrian Arc to the south of Italy, at the Hellenic Arc to the south-west of Greece, and at the Cyprian Arc of Cyprus, all of which can be described as back arc extensional basins (Pondrelli et al.,

1998). The figure below (figure 3) indicates the locations of these arcs as well as the locations and names of the main fault zones of the nearby region.

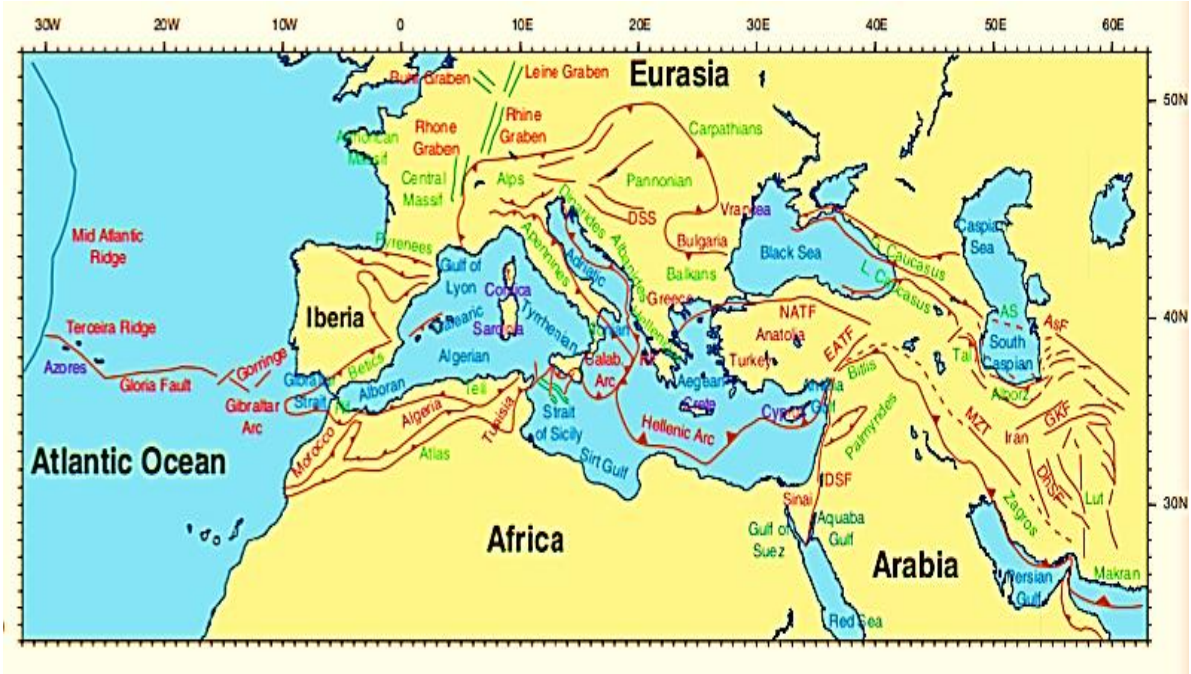

FIGURE 3: MAP OF MAJOR FAULTS IN THE MEDITERRANEAN REGION AND THE MIDDLE EAST. THE RED LINES INDICATE THE ALPINE OROGENY, THRUST AND STRIKE-SLIP FAULTS WHILE GREEN INDICATES EXTENSION. SOURCE: VANNUCCI ET AL., 2004

2.2.1. The Eastern Mediterranean

Although the main contributing plates for the Mediterranean region are the Eurasian, African and Arabian plates, other micro plates such as the Anatolian plate are also contributing to the area's tectonics, especially of the Eastern Mediterranean. Both the Arabian and the African plates are moving northwards, with the latter moving much slower than the former, whereas the Anatolian plate is pushing towards the west and the European plate is progressing towards the southeast (Nur and Cline, 2000; McKenzie, 1972; Doutsos et al., 1987). The Anatolian plate is also adjacent to another microplate, the Aegean microplate, on which Greece is located, and because of these plates, tectonics are much more complicated in the Aegean. Whilst

the Anatolian microplate is moving westwards, the Aegean microplate is moving towards the south-westerly direction and both contribute to the intense seismic activity of the Aegean (Dewey and Sengor, 1979). A triple junction in the northeast of the Mediterranean is formed by the African, Eurasian and Arabian plates and the motion of these plates are accommodated by the presence of the Cyprian Arc (an eastern arcuate structure), the East Anatolian Fault and the Dead Sea transform fault (Jackson and McKenzie, 1988a). The Arabian plate moves in a NNW direction at a rate of approximately 2.5cmyr^{-1} along the northern boundary, pushing Anatolia westwards but this does not affect the tectonics of Greece directly (Skarlatoudis et al., 2004). The Anatolian plate is moving westwards along the North-Anatolian Fault relative to Eurasia while travelling along the East-Anatolian Fault relative to Africa (McKenzie, 1978). Harsch and Kuepfer (1980) concluded that a subduction model for the Anatolian-African plate boundary is not suitable and that the relationship between extensional, strike-slip and compressional deformation indicates convergent strain with a broad diffuse zone in the Mediterranean. When compared to the convergence of Africa and Eurasia, the Anatolian plate is moving at a faster rate, extending from east to west as velocity increases westwards (Reilinger and McClusky, 2000).

On the other hand, the African and Eurasian lithosphere are converging together at a rate of less than 1cmyr^{-1} in the north-south direction at the southern edge of the Aegean region (the Aegean microplate), which in turn is moving in the south-west direction with respect to African plate at a rate of 4 to 4.5cmyr^{-1} (McClusky et al., 2000). This movement in the south-west direction is quite fast and as a result, the eastern Mediterranean lithosphere is

subducted beneath the Aegean with a Benioff zone of a depth approximately up to 160km deep (Skarlatoudis et al., 2004). With respect to Europe, Anatolia-Aegea is rotating counter-clockwise at a rate of 28mmyr^{-1} along the North Anatolian fault as indicated by the measurements taken in Greece and Turkey by Le Pichon et al. (1995). This shows that central Greece is an extension zone mainly concentrated within the Corinth Gulf to the east, and it in turn is located within the aforementioned rotation directed to the south and clockwise rotation of northern Greece. Figure 4 indicates the movements of the Arabian, African, Eurasian, Anatolian and Aegean plates relatively together, along with the zones of extension, subduction and collision.

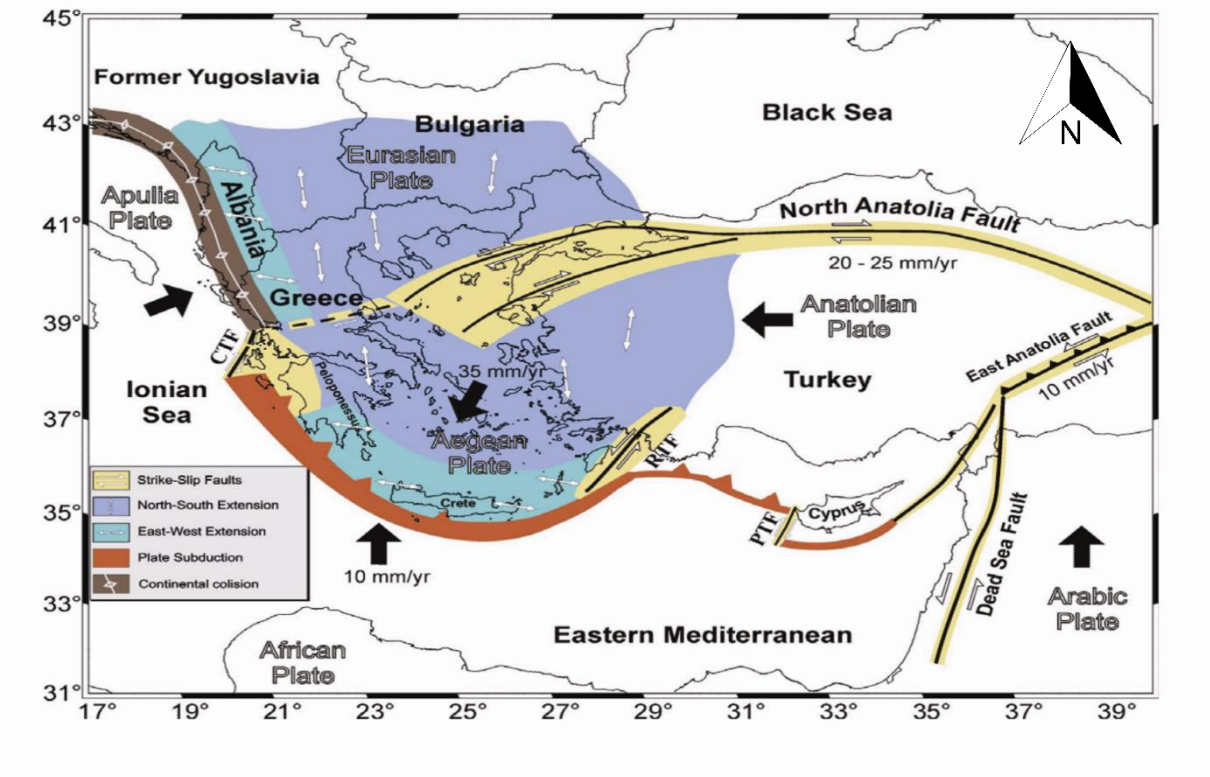

FIGURE 4: DIRECTION AND VELOCITY OF MOVEMENT OF THE PLATES IN THE EASTERN MEDITERRANEAN TOGETHER WITH THE TYPE OF FAULTING THAT OCCURS
SOURCE: MODIFIED VERSION FROM PAPAZACHOS & PAPAZACHOU 2003 BY MOUNTRAKIS ET AL., 2006

Within the Eastern Mediterranean area, subduction occurs at the Hellenic arc and the Cyprian Arc while continental-continental collision is observed between eastern Turkey and the Caucasus (Taymaz et al., 1991). The

continental crust of the Aegean region is extending due to the African plate to the north underneath western Turkey and the Aegean region whilst the motion of the Arabian plate northwards relative to Eurasia is causing crustal sharpening and thickening in eastern Turkey (Taymaz et al., 2004). Strong spatial stress field variations have resulted from the complicated geotectonic setting of the Eastern Mediterranean with 4 main zones which are:

1. The Hellenic Arc subduction zone and the Adriatic-western Balkan collision, which are zones of compression.
2. Strike-slip faulting at the North Anatolia-North Aegean trough and Cephalonia zone.
3. N-S extension at the back-arc Aegean area.
4. E-W extension which is parallel to the compression zone mentioned previously (Papazachos and Kiratzi, 1996; Skarlatoudis et al., 2004).

The Hellenic Arc is one of the three arcuate subduction zones which shaped the seismotectonic setting of the eastern Mediterranean. The other two zones are the Calabrian Arc (mentioned in the previous section) and the Cyprian Arc (Moores and Vine, 1971). The Hellenic and Cyprian Arcs shall be discussed in further detail through this chapter.

According to a study to calculate stress release for Greece by Margaris and Hatzidimitriou (2002), the Brune stress has been calculated to be 55±16 bars, the dynamic rms stress is 72±26 bars while the apparent stress is 17±10 bars indicating that thrust events are higher in values than normal and strike-slip faults. Along plate boundaries, seismicity is seen along Northern Africa, Sicily, the Tyrrhenian Basin, the Calabrian Arc, the Apennines and Alps, and into the Dinarides, Hellenides and the Hellenic Arc (DeJonge et al., 1994). Seismicity

within this region is marked by large clusters of seismic events at the Hellenides and around the Aegean, with the former having a change from collision to subduction in the distribution of seismicity indicated by the change in depths of events, with the Hellenic Arc having most events at depths greater than 50km due to its long and wide descending slab (Vannucci et al., 2004). Earthquake magnitudes of approximately 7.0 have been observed in the Aegean and Ionian Seas with strike-slip focal mechanisms. One such event occurred on the 8th of June 2008 when a strong earthquake rupturing the NW Peloponnese was the first strong modern earthquake to occur in the Greek mainland (Papadopoulos et al., 2010).

Cyprus is located on the southern part of the border line between the African and Eurasian plates, where collision has led to another arcuate zone of shortening known as the Cyprian Arc which extends from the Gulf of Antalia in the west to the Gulf of Iskenderum in the east (Kalogeras et al., 1999). More specifically, the plates involved are the Anatolian plate to the south of Eurasia and the Nubian and Sinai blocks of the African plate, an interaction which has been occurring since the Neogene (Harrison et al., 2014; McKenzie, 1970). Although the plate boundary is poorly defined, southwards of Cyprus, the segment is a northward dipping subduction zone with an arcuate trench running parallel to the southern and southwestern coastline of Cyprus (Kempler and Ben-Avraham, 1987; Payne et al., 1995). Structures in this part of Cyprus accommodate both convergence and left lateral strike-slip tectonics between these plates (Harrison et al., 2013).

According to Makris (1981), refraction seismic data indicates that the crust in the vicinity of Cyprus is oceanic and consistent with subduction of the oceanic

lithosphere belonging to the African plate. The oceanic crust is about 8km thick, overlain by a thick sedimentary layer of about 12km while Cyprus is 30km thick consisting of continental crust (Papazachos et al., 1999a; Khair et al., 1997). Makris et al. (1997) concluded that in western Cyprus, fault systems are activated by the oceanic lithosphere being subducted below Cyprus. Seismic activity in the Cyprian region is significantly lower than in Greece and Turkey with shallow earthquakes located along the Cyprus Arc and Dead Sea fault zone while earthquakes with intermediate depth occur in central Cyprus (Kythreoti et al., 2002; Cagnan and Tanircan, 2010). Several strong earthquakes have occurred in the past with 7 strong magnitude 6.0 events between 1901 and 1997 (ex: Paphos, 1953 with magnitude 6.5), even though most epicentres occurred in the sea where there is no sufficient coverage from stations (Papazachos et al., 1999). Kalogeras et al. (2009) and Algermissen and Rogers (2004) tried to identify suitable attenuation relationships for Cyprus. For shallow earthquakes, both studies concluded that the attenuation obtained by Campbell and Bozorgnia (1994) for the western United States earthquakes is the most suitable according to observed data. In a recent study by Cagnan and Tanircan (2010), data obtained for a return period of 475 years of rock conditions further confirm that the southern coastline experiences the highest seismic hazard using the peak ground acceleration values.

The Cyprian Arc, which has been mentioned previously in the discussion, is located to the south of Cyprus starting from Castelrizo Island near Turkey and ends where the African and Eurasian plates converge near the Turkey-Syria border (Kythreoti et al., 2002). To the west, the Cyprian Arc is linked to the Hellenic Arc whilst to the east, the Arc extends towards the Dead Sea and

East Anatolian faults (Wdowinski et al., 2006; Taymaz et al., 2004). Although the structure of the Cyprian Arc is complicated and it is not clear if it is a zone of thrusting or a plate boundary, the tectonic regime is generally considered to be a compressional zone between the African and Eurasian plates (Mart et al., 2002). The tectonics of the Cyprian Arc is also affected by the subduction of the Ionian microplate as evidence from extension, compression and strike-slip data suggest (Mart et al., 2002). Along the Arc, tectonics also change from subduction to the south, collision with the Eratosthenes seamount and transform deformation in the east (Papadimitriou et al., 2006).

In general, over the last century, the arc has experienced little seismicity which started to increase after the 1950s adding to more knowledge available of the area such as the magnitude 6.8 Paphos earthquake (1996) and the magnitude 6.2 Adana earthquakes (1998) (Aktar et al., 2000; Arvidsson et al., 1998). However, compared to the Hellenic Arc, the Cyprian Arc experiences low levels of seismicity. Both arcs differ from one another in various ways. Cyprus and Crete are both located on the same plate boundary and therefore have similar tectonic settings (Jackson et al., 1988b). However, extension differs for both regions. Extension in the Hellenic arc has been continuously active with rollback and extension behind the Hellenic trench resulting in extensional basins near the Corinth rift system and the Peloponnese gulf with a rate of extension around 20 to 60mmyr^{-1} (Jackson et al., 1988a). On the other hand, extension in the Cyprus arc, which began during the Miocene, is less extensive and produced smaller basin systems (Payne et al., 1995). Additionally, plate motion differs for both regions with normal relative motion on the west and subparallel motion in the east of the Cyprian Arc, while along the Hellenic Arc

relative motion changes from normal in the central part and becomes partly oblique towards the sides of the arc (Wdowinski et al., 2006). Volcanic activity is also non-existent near the Cyprian Arc whilst the Hellenic Arc has a well-developed volcanic arc system which is quite active (Payne et al., 1995). Another major difference is the way subduction is present at both arcs. At the Hellenic Arc, subduction occurs throughout its length with a rate of convergence at 100mmyr^{-1} whilst the Cyprian Arc experiences subduction, collision, and transcurrent motion with convergence rates calculated at 30mmyr^{-1} (Jackson et al., 1988b; Wdowinski et al., 2006). The higher convergence rate for the Hellenic Arc indicates higher seismicity levels occurring at depths up to 300km (Wdowinski et al., 2006).

2.3. General tectonic setting of Greece

Numerous studies on Greece have been conducted regarding different aspects of its seismotectonics such as the earthquake focal mechanisms in the Aegean (McKenzie, 1972; Ritsema, 1974; Drakopoulos and Delibasis, 1982; Papadoupolos et al., 1986; Melis et al., 1989), empirical predictive relations (Theodulidis and Papazachos, 1992; Margaris et al., 2002), computing the scaling parameter (Boatwright, 1980; Anderson, 1997; Margaris and Hatzidimitriou, 2002), simulation of ground motion and earthquake design (Makropoulos et al., 1990; Margaris, 1994), and peak ground acceleration (Makropoulos and Burton, 1985; Papaioannou, 1984; Skarlatoudis et al., 2003; Danciu and Tselentis, 2007). The knowledge gathered from these studies, as well as others, have helped to gain a better understanding of

Greece, its tectonics and seismic activity. Some of these studies shall be discussed in further detail in this chapter and Chapter 4.

Greece is located partly on the Aegean plate (the south) and partly on the Eurasian plate (the north) and starting from the south moving northwards, its main morphological features (Figure 5), which shall be discussed in more detail, include:

1. The Mediterranean Ridge which ranges from the Calabrian Rise to the Florence Rise near Cyprus. This feature, however, it is not actually a mid-oceanic ridge (Limanov, Woodside, Cita and Ivanov, 1996; Finetti, 1976).
2. The Hellenic trench, a system of deep troughs up to a depth of 5000m parallel to the front of the Mediterranean Ridge (Vannucci et al., 2004).
3. The Hellenic arc, consisting of an inner volcanic arc and an outer sedimentary arc (Maratos, 1972).
4. The Gulf of Corinth, an asymmetric half graben in the Aegean Sea and the focus of the study (Ambrasyeys, 1996)
5. The north Aegean Sea which is found north of the volcanic arc and is connected to the Marmara Sea and Black Sea by the Dardanelles and the Bosphorus respectively (Makropoulos and Burton, 1984).

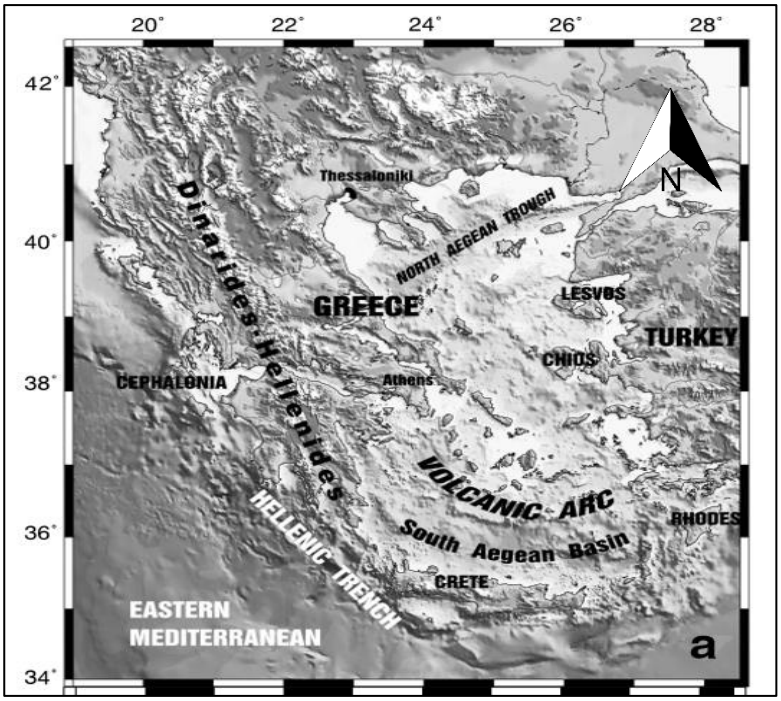

FIGURE 5: MAP SHOWING THE MAIN GEOMORPHOLOGICAL FEATURES OF GREECE
SOURCE: SKARLATOUDIS ET AL., 2003

The basic features of the Aegean are affected by the interaction between the Apulian-Eurasian continental lithospheres and has led to thrust faulting extending up to the island of Cephalonia while subduction of the African lithosphere underneath the Aegean occurs on the convex side of the Hellenic Arc. Both thrust zones are linked by strike-slip faulting at Cephalonia Island (Papazachos et al., 1991). The western coast of central Greeca and Ibania experiences thrust faulting whilst strike-slip faulting can be noted along the Sea of Marmara to the north Aegean Sea (Margaris et al., 2002). The Aegean area is dominated by extension in the entire inner area of the Aegean Sea and surroundings with the exception of north-western Anatolia and the northern Aegean (Margaris et al., 2002; Papazachos and Papaioannou, 1993).

Extension is also present in the Apennines and this extension, together with that of the Aegean, coexists with adjacent compression which dominates the

eastern coast of the Adriatic Sea up to the Hellenic trench, then trends in an almost east-west direction along the Hellenides mountain range (Vannucci et al., 2004; Margaris and Hatzidimitriou., 2002). The focal mechanisms for the Aegean are characterised bynormal faulting with changes at the outer thrust zone with the T-axis becoming parallel to the P-axis of the thrust zone's field of compression (Papazachos et al., 1991). Figure 6 in the following page shows the moment tensors for the Aegean province.

A study by Campbell (1981) showed that thrust faulting results in higher ground motion than normal or strike-slip faulting whilst Spudich et al. (1999) also suggested that earthquakes with normal faults events or strike-slip faults in a zone of extensional stress may have ground motions which are lower than other forms of shallow, crustal earthquakes. However, another recent study by Skarlatoudis et al., (2003) empirically demonstrated that the effects of thrust and strike-slip faulting in Greece are similar. With regards to subduction, two seismotectonic related regimes can be described. One is the trench ward compression regime around the Ionian Islands (of which Cephalonia is the largest) while the second regime is an extensional back-arc characterized by normal faults from 10-15km length which are located at central Greece, the Aegean Islands and the Peloponnese mountains (Koukouvelas et al., 1996; Roberts and Jackson, 1991).

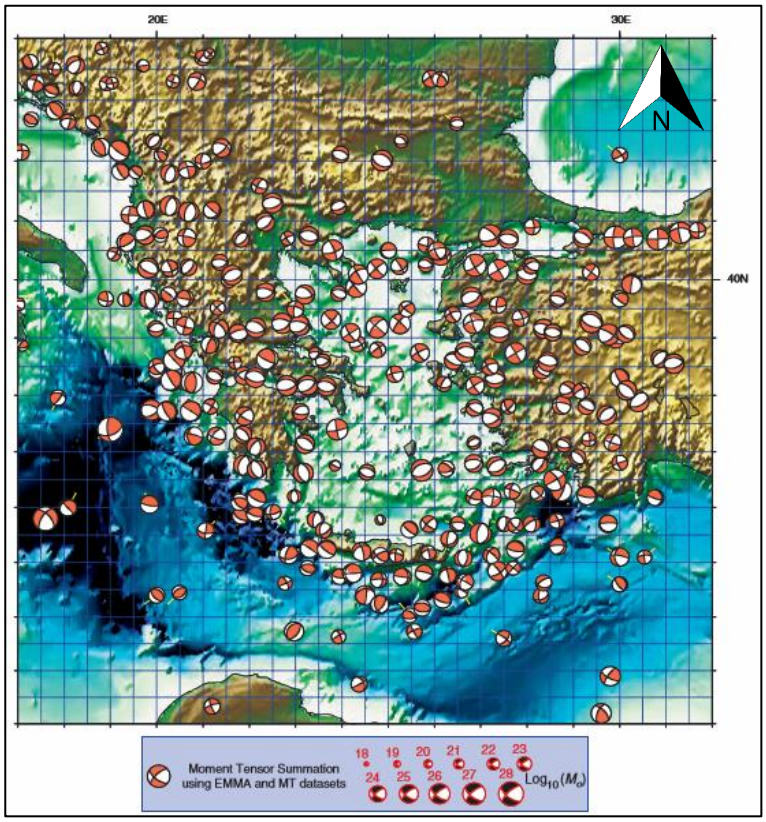

FIGURE 6: THE MOMENT TENSORS OF THE AEGEAN REGION FOR EARTHQUAKES WITH DEPTHS GREATER THAN 50KM
SOURCE: VANNUCCI ET AL., 2004

2.3.1. Northern and western Greece

Northern Greece is a region that forms part of a continental collision, compelled by the Hellenic subduction zone and Anatolia's westward extrusion, between north-western Greece and Albania (Mountrakis et al., 2006). Tectonic activity in north-western Greece has been shaped by compression at or near the Miocene epoch and again around the lower Pliocene and finally during the middle Pleistocene (Underhill, 1989). Subduction of the African plate beneath Eurasia started from the late Miocene onwards along the Hellenic arc from the Ionian Islands to Crete and eastwards to Rhodes to eventually create the Hellenic volcanic arc (McKenzie, 1978). The oceanic subduction then becomes continental convergence between Albania and north-western

Greece located around Zakynthos Island with reverse faulting on a grander scale around the rest of the Ionian Islands (Hatzfeld et al., 1995). Brittle deformation characterizes northern Greece with some data indicating that seismic activity here is concentrated along normal faults which either stand alone or are part of larger faults such as the 70km long Aliakmonas zone in Western Macedonia, and the Kavala–Xanthi–Komotini fault zone in Eastern Macedonia and Thrace as concluded by a study by Mountrakis et al. (2006). These faults are interlinked together forming major structures such as the NE-SW striking Aliakmonas and E-W striking Kavala– Xanthi–Komotini fault zone.

Western Greece, on the other hand, is part of the Ionian area which is the boundary flanked by the African and Eurasian plates, as well as the Aegean and Adriatic microplate, and it is where oceanic subduction present along the Hellenic Arc converts into continental collision between Greece and Apulia (Haslinger, 1998). The Ionian region, which consists of western Greece, north-western Peloponnesus and the Ionian Islands, experiences the strongest earthquakes which occur in the Aegean especially beneath the Ionian Islands according not only to data from the last century but even further back in historic time (Haslinger, 1998; Hatzfeld et al., 1995). One example of a recent strong earthquake in the Ionian Sea is that from 2018 when a magnitude 6.8 earthquake struck in October, an earthquake which was felt in Malta and a tsunami warning was even issued. Seismically, the central Ionian Islands experience activity influenced by the movement of the dextral Cephalonia transform fault. This fault is the only obvious, strike-slip fault zone in continental Greece and since seismic energy release is larger for strike-slip faults, seismic activity is higher near this fault (Hatzfeld et al. 1995). It joins the

continental collision of Apulia and continental Greece with the subduction along the Hellenic arc, and is comprised of the Lefkada segment, which trends NNE-SSW in the north and a NE-SW Cephalonia segment to the south (Haslinger, 1998; Le Pichon et al., 1995; Karastathis et al., 2015). This fault, together with the Ionian segment of the Hellenic Arc being subducted in a north-eastern direction underneath the island of Cephalonia results in very high seismicity around the island and a complex tectonic setting (Karastathis et al., 2015).

The areas where most recorded strike-slip and thrust earthquakes occur (western Greece and Ionian Islands) are characterised by relatively low Q values due to the thick layers of sediment at chosen recoding sites by Skarlatoudis et al. (2003) since surficial layers of soft sediments are affected strongly by the low-frequency part of seismic waves. Figure 7 depicts the location of the Ionian Channel, together with the islands of Cephalonia and Zakynthos in 3 zones of isopics (sedimentary rock with same facies).

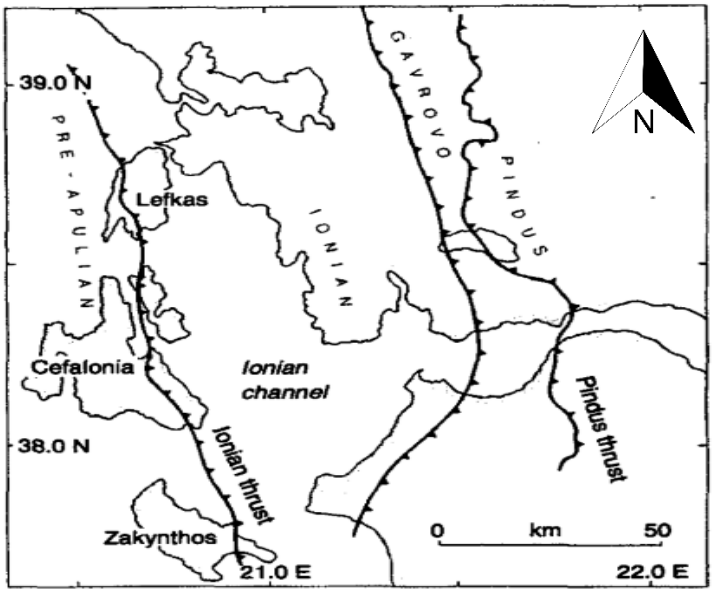

FIGURE 7: SETTING OF 3 ISOPICS AROUND IONIAN CHANNEL (GAVROVO-TRIPOLITZA, IONIAN AND PRE-APULIAN)
SOURCE: BROOKS ET AL., 1988

Between Albania and north-western Greece, the region of Epirus is the area where the transition from an extensional inner Aegean to a compressional outer Aegean takes place with main tectonic structures including thrust belts trending NNW which are cut by almost perpendicular strike-slip normal faults (Underhill et al., 1989). Hatzfeld et al. (1995), using microseismic data obtained from Epirus, and the Ionian Islands, concluded that for north-western Greece the seismicity is shallower than 40km with an eastward dip. This observation is attributed to the change in focal depth together with the effects of evaporate intrusion and deep seismic activity in the internal Ionian Sea which is a thrust fault. In this part of Greece, there is also the presence of the Hellenides Mountains, which are part of the Alpine orogeny, formed also from the collision of the African and Eurasian plates during Mesozoic and Cenozoic eras (Dinter, 1998). These mountains mark the southern part of the Albanides and Dinarides and are a typical fold and thrust belt (Hatzfeld et al., 1995). Alpine folding and over thrusting of the surface layers led to a dislocation at the eastern Mediterranean. This gave rise to large fault zones in the Hellenides running NNW-SSE and WSW-ENE where, along the latter, motion is right lateral and down thrown on the northern side, while on the former, motion is left lateral and downthrown on the southwest side (Galanopoulos, 1966). The Hellenides can be divided into several tectonostratigraphic zones such as the Internal and External Hellenides. The former has an NNW-SSE trending belt and lies to the east belonging to the Hellenic hinterland, which is also crystalline (Anders et al., 2005; Himmerkus et al., 2009). The External Hellenides belong to the western side and form part of the Hellenic foreland. These formed due to the collision between the Pelagonian microcontinent and

the Apulian continental margin after eastwards subduction of an intervening ocean (Xypolias and Koukouvelas, 2001). Figure 8 shows the kinematics involved between the external and internal Hellenides orogeny.

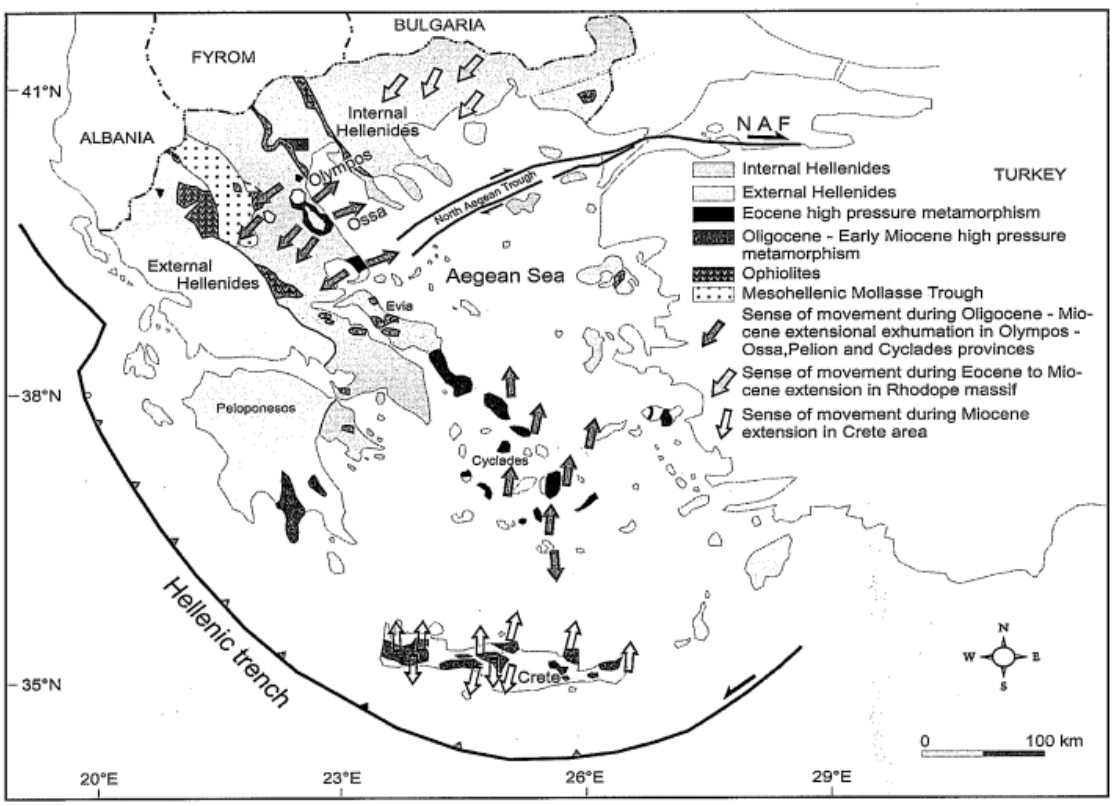

FIGURE 8: KINEMATICS AND STRUCTURE BELT OF THE HELLENIDES
SOURCE: KILIAS ET AL., 2002

2.3.2. Central Greece

This area of Greece shall be described in some detail as it is the focus for the research project given that the Corinth Gulf is located here. Before discussing the seismotectonics of this dynamic area, it is important to have an idea as to some strong magnitude earthquakes which have occurred in the past. Table 1 is a summary of some major events spanning from 1861 to 1995, together with the location, magnitude and damage that occurred. The information was compiled from various sources which include Papadopoulos, 2002; Papadopoulos et al. 2000; Lekidis et al. (1999); Albini et al. (2017); and the online catalogue of the United States Geological Survey.

TABLE 1: A SUMMARY OF RECENT STRONG MAGNITUDE EARTHQUAKES (M_w >6) FOR THE CORINTH GULF

Year	Location	Magnitude	Description
1861	Valimitika,	6.7	Occurred on 26th December. Valamitika was levelled while around 20 known people were killed. A large tsunami struck in nearby areas.
1888	Aigio; Galatidi	6.1	Occurred on 9th September. A destructive earthquake that left 1 person dead and over 20 injured. Submarine slides occurred causing damages.
1965	Galaxidhion	6.8	Occurred on 31st March. 6 people were killed and some damage to buildings occurred.
1965	Eratine	6.3	Occurred on 6th July. Around 575 buildings collapsed, and a person drowned by a local tsunami.
1981	Perachora,	6.7, 6.4 and 6.4	Three destructive earthquakes that struck on 24th and 25th February, and 4th March respectively. 22 people died, over 500 were injured and over 8,000 households destroyed
1995	Aigio	6.5	Occurred on 15th June. 26 people were killed, 60 more injured and around 1071 buildings severely damaged causing around $660 million of damage, making it the most recent deadly disaster of the Corinth Gulf area.

These events are just a few of some earthquakes that occurred within the Corinth Gulf, located at different faults. For instance, the 1992 event occurred at the Galaxidi fault between the Helike and Xilokastro normal faults. This event is thought to be an asperity due to the number of aftershocks that followed the main shock. This Magnitude 5.9 event trended E-W with a shallow dip of around 30^o (Hatzfeld et al., 1996). Another event, the 15th June 1995 earthquake, occurred along the Aigio fault trending E-W and produced amongst the highest PGA and PGV ever recorded for Greece (Lekidis, Karakostas, Dimitriu, Margaris, Kalogeras and Theodulis, 1998).

Central Greece together with the Aegean Sea is a rapidly deforming region dominated by the westward motion of the Anatolian plate and the south-westward motion of the southern Aegean, both motions with respect to Eurasia (McKenzie, 1978). The main feature of this area is that both the Aegean Sea and central Greece experience shallow seismic events and together with the presence of two aseismic blocks, there is no indication of subcrustal evidence that the Northern Anatolian Fault is linked to the seismic region of central Greece or that of the Corinth Gulf (Makropoulos et al., 1984). According to Le Pichon et al. (1995), central Greece is a transition zone between the clockwise rotation of northern Greece and the counter-clockwise rotation of Anatolia-Aegea in the southeast. The northern part of the Aegean Sea is characterized by intermediate depth shocks but are fewer in number than in the south, while thrust and normal faulting exist with low depth seismicity (Papazachos, 1976). Taymaz et al. (1991) used recent data and focal mechanisms to update the information given by McKenzie (1978) in their study. The main points concluded by the 1991 study indicates that in the western Aegean region, extension dominates the tectonics with normal faults striking NW to WNW while the eastern and central Aegean faulting is right-lateral strike-slip trending NE-ENE. Central mainland Greece is also part of an extensional back arc regime which also includes the Aegean Islands and the Peloponnese. The normal faults accommodating this extension run typically from 10 to 15km in length with slip rates of up to 1.5mmyr^{-1} (Roberts and Jackson, 1991). Figure 9 indicates the relative velocities across Greece in mm/year.

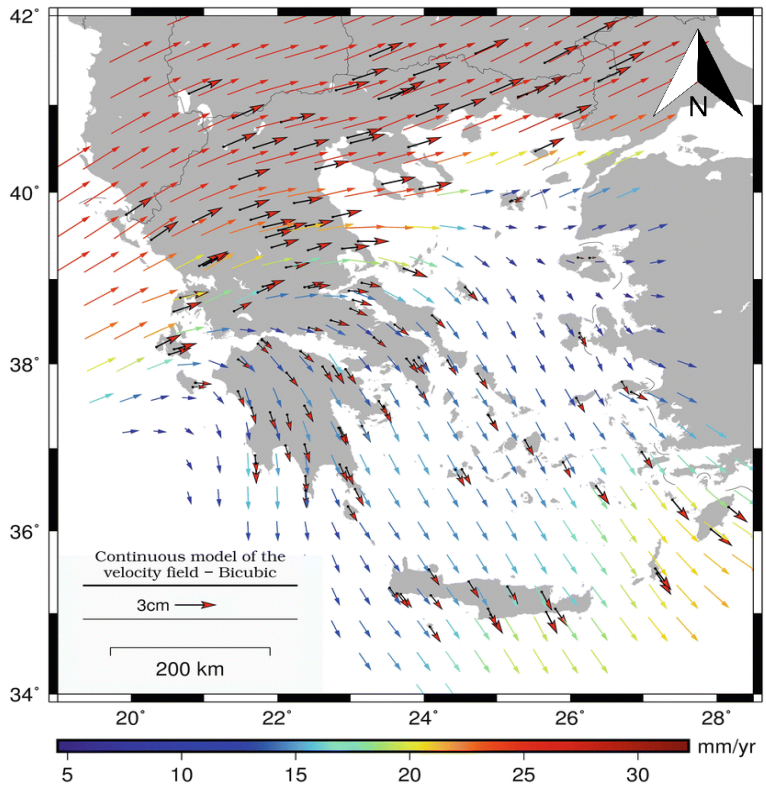

FIGURE 9: A GEODETIC VELOCITY FIELD FOR GREECE DERIVED FROM GPS DATA BETWEEN 2008 AND 2014 FROM 155 STATIONS.
SOURCE: BITHARIS ET AL., 2016

For the Corinth Gulf area, the coastal shape is described as being a 120^{o} north oriented structure, which is much wider and deeper on the eastern side near Corinth than the west. It is one of three grabens, one of which is the Gulf of Patras, located at the western end of these 3 grabens (Patras-Corinth-Saronicos) formed by crustal extension and trending WNW-ESE (Ferentinos et al., 1985; Melis et al., 1989). According to Brooks et al. (1988), the Patras area is at the junction of 2 structural trends with a system involving an N-S extension. These are the Gulf of Corinth graben, a WNW-ESE extension zone, while the second is the Rio graben with NE-SW faulting. According to the study by Melis et al. (1989), the Gulf of Patras and the Gulf of Corinth are linked by a narrow strait called the Rio-Antirio strait, which experiences high seismicity but generally events are shallow with a depth ranging from 2-25km while a seismicity gap is observed in the central-western part even though active

faulting affects the seabed. In the north-eastern area of the Gulf, a NE-SW section indicates high seismicity with events lying in a dipping zone that is poorly defined with focal depths increasing to the northeast up to about 25km. Figure 10 is a seismicity map indicating all the events that occurred within the western part of the Corinth Gulf between 2000 and 2015 nearby the Gulf of Patras and the Gulf of Corinth.

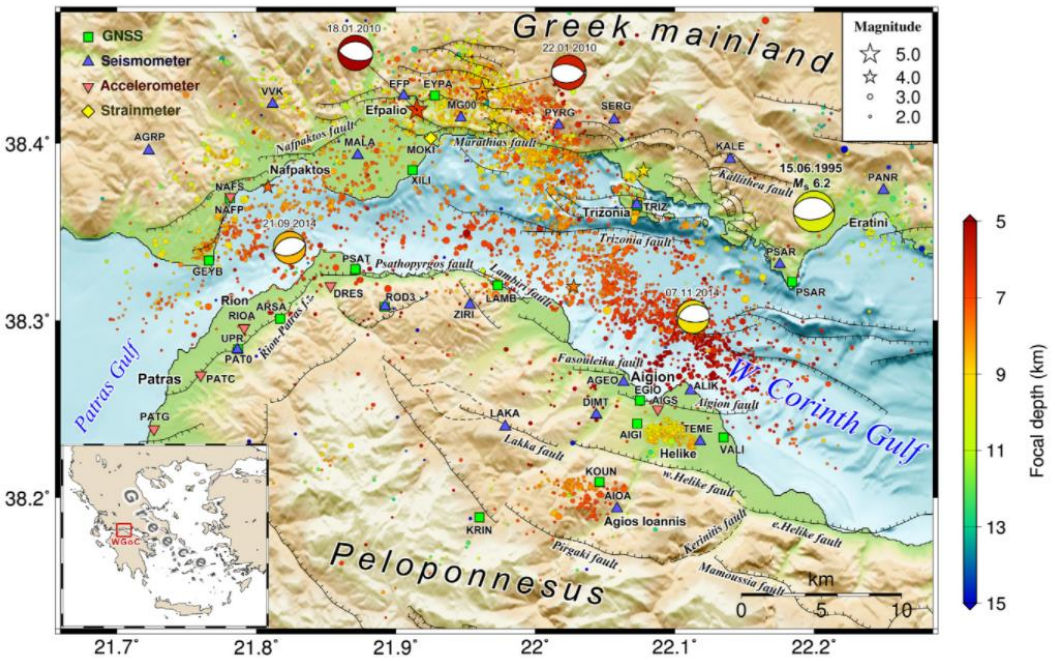

FIGURE 10: SEISMICITY MAP FOR THE WESTERN PART OF THE CORINTH GULF. EPICENTRES INDICATE RELOCATED SEISMICITY DURING 2000-2015 AS CIRCLES FOR M_W <4.5 AND AS STARS FOR $M_W \geq 4.5$. STARS ARE PROPORTIONAL TO MAGNITUDE. FOCAL MECHANISMS ARE FOR EVENTS WITH $M_W \geq 5.0$ INCLUDING THE 1995 EVENT.
SOURCE: KAVIRIS ET AL., 2021

The Gulf of Corinth Rift is an asymmetric half graben characterised by a crease in the north and border faults to the south, which is dominated by high rates of deformation, amongst the highest in the Mediterranean and is located at the westernmost propagating edge of the North Anatolian Fault (Ambraseys, 1996; Moretti et al., 2003; Armijo et al., 1996). There are major faults on the southern edge of the Gulf which are north-dipping with a dip of around 55º to

70º (Latorre et al.,2004). These fault in the south are the most active and can reach up to 20km long and are predominantly dip-slip (Gawthorpe et al., 2017) The current extension which affects the rift is due to the Aegean Sea extension which started in the Miocene leading to a topography which runs in an NNE-SSW direction and also includes the Corinth Gulf WNW-ENE axial zone of subsidence (Armijo et al., 1996); De Boer and Hale, 2000).

The rift itself disconnects the Peloponnese from continental Greece and is elongated to a length of 105km bounded by the previously mentioned E-W faults (Moretti et al., 2003). The aforementioned Delphi fault is an example of a fault in the Gulf of Corinth area, but the main faults are the Psathopyrgos, the Helike and the Xylokastro faults, with lengths up to 25km long and are all normal faults (Piccardi, 2000). These faults are marked in blue, yellow and black respectively in figure 11 which indicates other major and minor faults of the area.

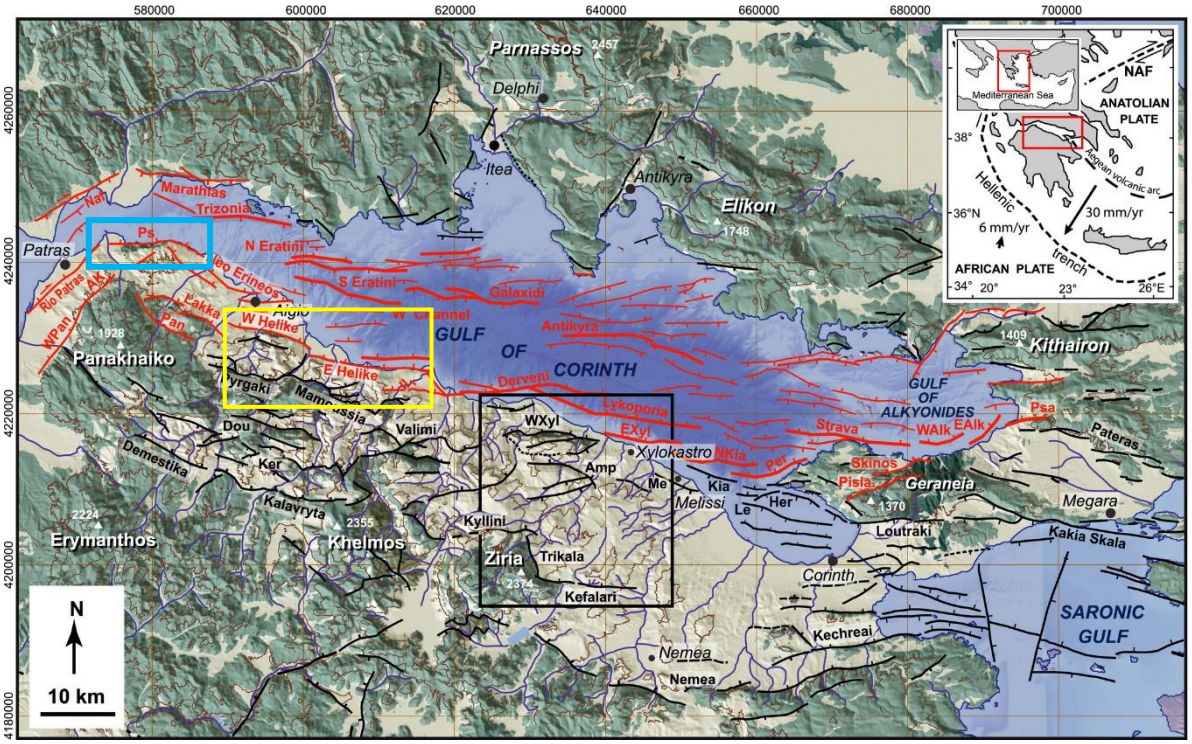

FIGURE 11: MAP SHOWING MINOR AND MAJOR FAULTS OF THE GULF OF CORINTH. THE INSET MAP IS SHOWING THE EXACT LOCATION OF THE CORINTH GULF IN CENTRAL GREECE.
SOURCE: GAWTHORPE ET AL., 2017

Focal mechanisms and seismicity indicate that the Gulf can be divided into the east Gulf and west Gulf. The western end is connected to the Gulf of Patras and experiences N-S extension of about 14 to 15mmyr^{-1} near the AIgion fault (Hatzfeld et al., 2000). On the other hand, the east Corinth is wider with deep basin water up to 860m with crustal thickness decreasing from west to east (Moretti et al., 2003). Extension in the east is slower than the west with extension reaching rates of 10mmyr^{-1} near the Xilokastro faults (Hatzeld et al., 2000; Briole et al., 2000). Rigo et al. (1996) concluded that in general the fault solutions indicate E-W trending normal faulting for the Gulf of Corinth with a nodal plane dipping 10-25^{o} due north between 8-11km deep. Rietbrock et al. (1996) further confirm that normal faulting is active at low angles. High seismicity is experienced in the region with large magnitude earthquakes sometimes exceeding magnitude 6 such as the events which occurred in 1981 (M=6.7, 6.4 and 6.4; see Table 1) near Corinth studied in detail by King et al. (1985). The study concluded that the east Corinth has different focal mechanisms and seismicity than the west with normal faulting dipping at 45^{o} angles which contrasts to the low angle seismicity found by Rigo et al. (1996) and the depth ranges vary between 4 and 13km. The study also concluded that antithetic faults (minor, secondary faults) are more active in the east than in the west. Although many theories have been concluded to try and reproduce the differences between the east and western Gulf such as the elastic model suggested by Armijo et al. (1996), Hatzfeld et al. (2000) have concluded that the rotating domino model by Jackson and McKenzie (1983) is the best fit since it is consistent with the topography and the transition between a more brittle eastern Corinth. The model explains that the faulting geometry in the

west can be caused due to the rotation around a horizontal axis of a normal rotation of the faults which are active and originally were dipped at 45^{o} like in the eastern Gulf. The rotation then occurred by 15^{o} along a horizontal axis to produce the 30^{o} dip of present day. Figure 13 explains this scenario and the differences between the east and western Gulf while figure 12 depicts a brittle body over a ductile material, and the extension of both materials causes finite shear strain to form between the layers and in the absence of gravity forms a structure as seen in (b) with the dotted lines in (c) indicating that the displacement between the ductile and brittle material is not relative. King et al. (1985) suggest that a connecting process is expected at shallower depths for the Corinth Gulf due to the fact that the brittle surface fails in shear at steep angles.

On the other hand, the elastic model proposed by Armijo et al. (1996) uses the assumption that the seismogenic crust is forming an elastic plate over a viscoelastic lower crust, with the modulus for the seismogenic crust behaving as if its elastic modulus has decreased by a factor of 1000. This model is quite accurate for the eastern Gulf since the dip in the western part is shallower.

The strait which connects the Gulf of Corinth with the Gulf of Patras, the Rio-Antirrio strait, is highly characterised by seismic activity which is described as having a low stress drop, source radius, and seismic slip according to Melis et al. (1995). They compare it with Patras which, on the contrary, has a higher stress drop, low source radius and medium seismic slip events, and to the Corinth Gulf which experiences the highest stress drop, seismic slip events ranging from medium to high and fairly low source radius events.

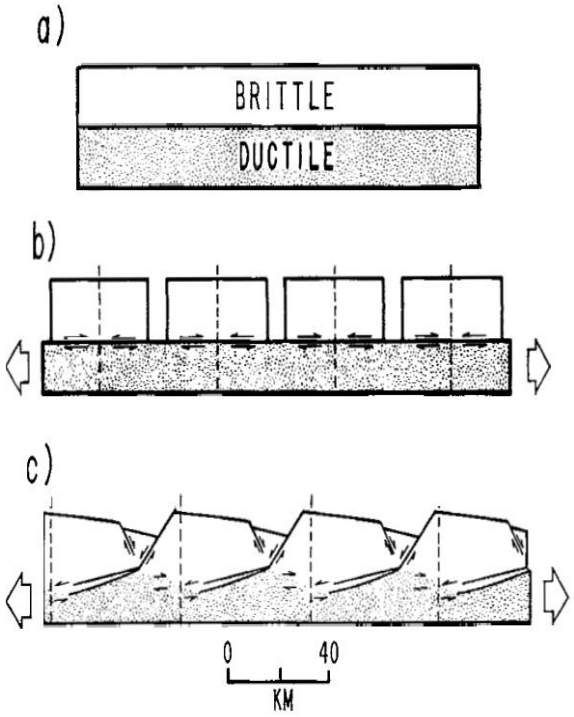

FIGURE 12: BRITTLE AND DUCTILE LAYERS LEADING TO LISTRIC NORMAL FAULTING
SOURCE: KING ET AL., 1985

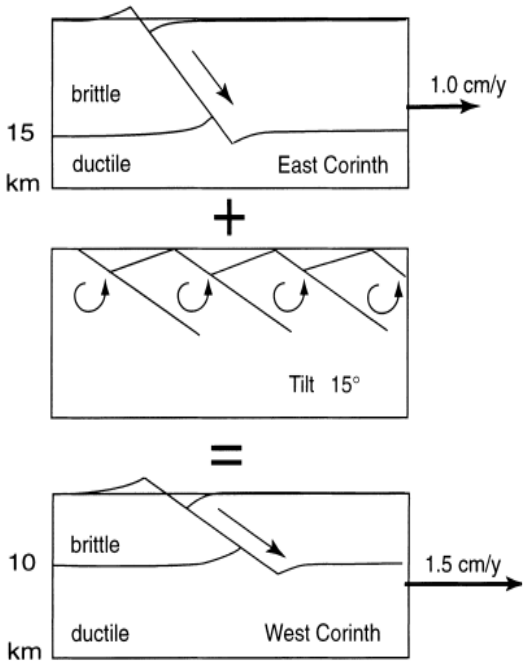

FIGURE 13: DIFFERENCES BETWEEN THE EASTERN AND WESTERN GULF
SOURCE: HATZFELD ET AL., 2000

Athens, which is also located in Central Greece, has long been considered as aseismic since it was built on highly rigid schist that is not vulnerable to earthquakes. However, since Athens is expanding its urban area, the expansion has entered seismic regions making Athens vulnerable to tremors (Makris et al., 2004). Papadopoulos and Arvanitides (1996) calculated that Athens' risk is amongst the highest in Greece and in fact this was confirmed a couple of years later when a magnitude 5.9 earthquake occurred in September 1999, which was one of the costliest natural disasters for Greece recently.

2.3.3. Southern Greece

For southern Greece, the major tectonics are influenced mostly by the presence of the Hellenic Arc and trench, which are part of the most important features both for this area of the eastern Mediterranean as well as the Mediterranean region. Considered as the highest seismically active region of

Europe, the Hellenic Arc is where the African and Eurasian plates collide and where the African lithosphere is undergoing subduction from the south-southwest beneath the Eurasian plate (Papadopoulos et al., 2009; Papazachos et al., 1997). More specifically, the eastern Mediterranean lithosphere is undergoing subduction beneath the Aegean microplate forming the Hellenic trench (Kokinou et al., 2008).

The African lithosphere is rotating counter clockwise along the trench relative to Eurasia with a rollback of the lithosphere which is being subducted (Papadopoulos et al., 2009). The mean dipping angle of the African plate is around 35^{o} (Makropoulos et al., 1984). The subduction zone is described by the shallow part of the Wadati-Benioff zone which is intersecting the outer part of a sedimentary arc. Figure 14 indicates the major features of this region such as the volcanic arc and Hellenic forearc, as well as the types of faults present.

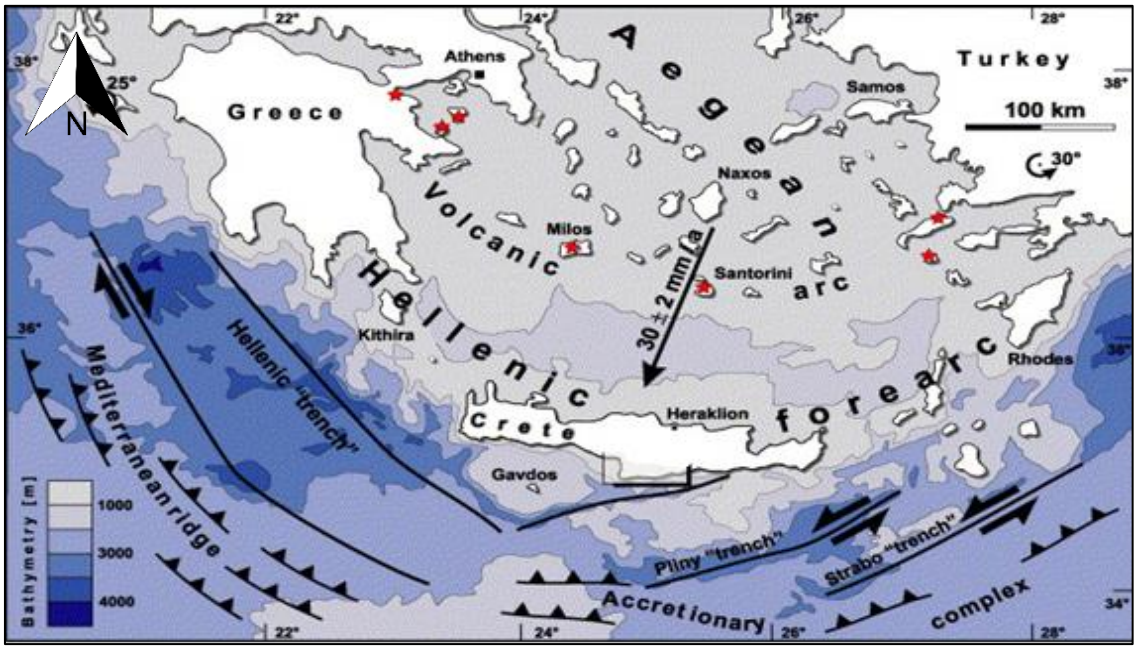

FIGURE 14: THE MAJOR FEATURES OF THE HELLENIC ARC REGION SHOWING STRIKE-SLIP FAULTING NEAR TRENCHES AND SUBDUCTION NEAR THE ACCRETIONARY PRISMS
SOURCE: PETEREK AND SCHWARZE, 2004

The northwest part of the Hellenic region includes the collision between the Apulian platform and the Hellenides, marking a continent-continent type boundary between the African and Aegean plates (Le Pichon and Angelier, 1979). The southern end of the Hellenic arc, which involves the islands of Crete and Rhodes, has been correlated with left-lateral strike-slip faulting since the Pliocene along the Strabo and Pliny trenches as depicted in the figure 16 (Kokinou et al., 2008). Between the north and south regions, deformation in the Aegean plate on the Peloponennos and Kythiara-Antikythiara strait led to an arc normal and arc parallel extension, together with strong compression that is perpendicular to the Hellenic trench (Papazachos and Kiratzi, 1996; Kokinou et al., 2008). The Hellenic subduction zone and the Aegean plate are characterized by thick continental crust as is the property of most areas near convergent boundaries (Karastathis et al., 2015). Compression along the Hellenic Arc has led to folding and to the formation of the Mediterranean Ridge, an accretionary prism which further contributed to crustal thickening (Yem et al., 2011). Makris (1978) had suggested that, compressional processes compelled the lithosphere to descend into the asthenosphere due to the presence of a hot mantle plume extending to the bottom of the lithosphere. This could also explain the thickening of crust along the Hellenic Arc which according to this study is an effect of crustal down-buckling at the compressional front. During the last 13 years, the squeezing of the Aegean plate between the African and Eurasian plates led to the high seismicity of the region with earthquakes capable of reaching magnitude 8.0 recorded since early historic times (Papadopoulos et al., 2009). In 2008, an earthquake storm occurred nearby the Hellenic Arc and trench (Papadopoulos et al., 2009). An

earthquake storm (or earthquake sequence) occurs when strain on a fault accumulates gradually over time with inactivity and is eventually released, sometimes even after hundreds of years, in the form of large earthquakes each one triggering the next (Ambraseys, 1971).

At the southernmost part of the Hellenic Arc, the island of Crete is located. Continental collision and the wedging of the mantle underneath the Aegean crust related to African slab retreat from Quaternary uplift, led to the formation of this island represents an emerging high in the Hellenic forearc (Caputo et al., 2010). The area is considered as having important tectonic deformation from the subduction of the African plate underneath the European plate (Delibasis et al., 1999). Tomography studies of the area around Crete indicate that seismicity is a result of the African lithospheric slab spreading to the zone of transition and into the lower mantle beneath Europe (Kokinou et al., 2008). Crete is characterized by dip-slip normal faults extending along 2 large systems almost oriented WNW-ESE and NNE-SSW, with the latter quite diffused over the island together with roughly N-S extension linked with ruptures along oblique and normal faults, while the former system is mainly found along the southern coast of central Greece indicating compression (Caputo et al., 2010). Le Pichon and Angelier (1976) and Jackson (1994) identified three successive fault group generations on Crete. The first group represent E-W trending faults, the second group has large to moderately sized N-S striking faults and cut across the first group while the last group consists of kilometre scale faults which are located on Crete. To the southwest of Crete lies the Mediterranean Ridge, an accretionary wedge formed from the accumulating sediments of the subducted African plate beneath the Aegean

microplate (Kokinou et al., 2008; Laj et al., 1982). The Ridge is made up of curved submerged relief which is approximately 1300km long and 150-300km wide (Chaumillon and Mascle, 1997). Sediments are up to 10km thick with gentle slopes of 1-2^{o} with small amplitude surficial deformations according to seismic refraction and seismic reflection experiments (Makris, 1976; Makris and Stobbe, 1984; Belderson et al., 1978). Between the ridge and Crete there are troughs trending E-NE (Kokinou et al., 2008).

In general, Crete is a region of intense seismic activity which occurs in a 100km wide belt following the Hellenic trench to southern Crete with seismic activity decreasing northwards until it becomes aseismic towards the Sea of Crete that is part of the Aegean extensional area (Delibasis et al., 1999). Studies indicate that low magnitude earthquakes occur near the coast and the onshore part of Crete and epicentres are oriented N-S to the west of Crete, while to the east, Crete is characterized by E-W trending epicentres (Kokinou et al., 2008; Delibasis et al., 1999; Hatzfeld et al., 1993). The depth of earthquake events also varies around Crete depending on the mechanism involved. With the African and Eurasian plates converging, intermediate depth earthquakes tend to occur whilst crustal extension in the Aegean is associated with shallow events (Taymaz et al., 1990). These shallow earthquakes with a depth less than 60km are characterized by focal mechanisms with extensional stress trending NE-SW and NW-SE (Delibasis et al., 1999; Armijo et al., 1992). Crustal events less than 25-30km in depth have been recorded to have magnitudes up to 7.0 according to historical data (Caputo et al., 2010).

Chapter 3: Methodology

3.1. Brief description of method

Mapping seismic hazards is one of the many goals of seismology and this study is based upon one method which involves using attenuation relationships to obtain site parameters, source characteristics and information regarding the propagation path, which will eventually lead to obtaining the peak ground acceleration and velocity (Papazachos and Papaioannou, 1993; Jeon and Hermann, 2004). These so-called ground motion parameters describe the severity and an earthquake's capability to damage together with the seismological, geological and topographic factors which affect them (Danciu and Tselentis, 2007). Seismic attenuation relationships are obtained by using a significant data set of small to moderate earthquakes and background seismicity with good coverage from seismic stations. These relationships consider the duration parameter as a function of distance and frequency by using the random vibration theory (Fatehi and Hermann, 2008; D'Amico et al., 2012).

The rms averaged Fourier spectral amplitudes and peak values of narrow bandpass-filtered ground velocity time histories are linearly regressed to obtain a regional predictive relationship parameterizing the propagation function, D (R, f), as a piecewise linear function to estimate geometrical spreading, the crustal attenuation and a function that describes the effective duration of the ground motion in the region (Ortega et al., 2003; Akinci et al., 2006). The excitation terms are then found using the excitation spectral model

which includes the stress parameter $\Delta\sigma$, of Brune's single-corner source model and a high-frequency attenuation term exp(−πκf) to eventually obtain an estimation of the pseudo spectral acceleration (Mancilla et al., 2008). The source stress parameter obtained could be inadequate to be used for larger events. However, such knowledge is important since source scaling aids in earthquake rupture simulations and therefore it is required to understand whether the source scaling is self-similar (earthquakes can be described by constant stress drop) or not (D'Amico et al., 2012).

3.1.1 Methodology applied on a global scale

This methodology has been applied to various regions worldwide on a global scale to use in seismic hazard mapping, amongst many other uses. Some studies where this has been applied include Utah and Yellowstone (Jeon and Hermann, 2004); the Pacific Northwest, Central and Northern California (Fatehi and Hermann, 2008); Southern California (Raoof et al., 1999); San Francisco (Malagnini et al., 2007); Mexico (Ortega et al., 2003); Spain (Mancilla et al., 2008); Switzerland (Bay et al., 2003); Germany (Malagnini, 1999); Western Anatolia (Akinci et al., 2013); Marmara region (Akinci et al., 2006); India (Bodin et al., 2004); Taiwan (D'Amico et al., 2012), South Korea and South-Eastern Canada (Jeon, 2004). The results of these studies have been summarized in Appendix A whilst the map in Figure 15 on the next page shows the approximate locations for these global studies together with their authors.

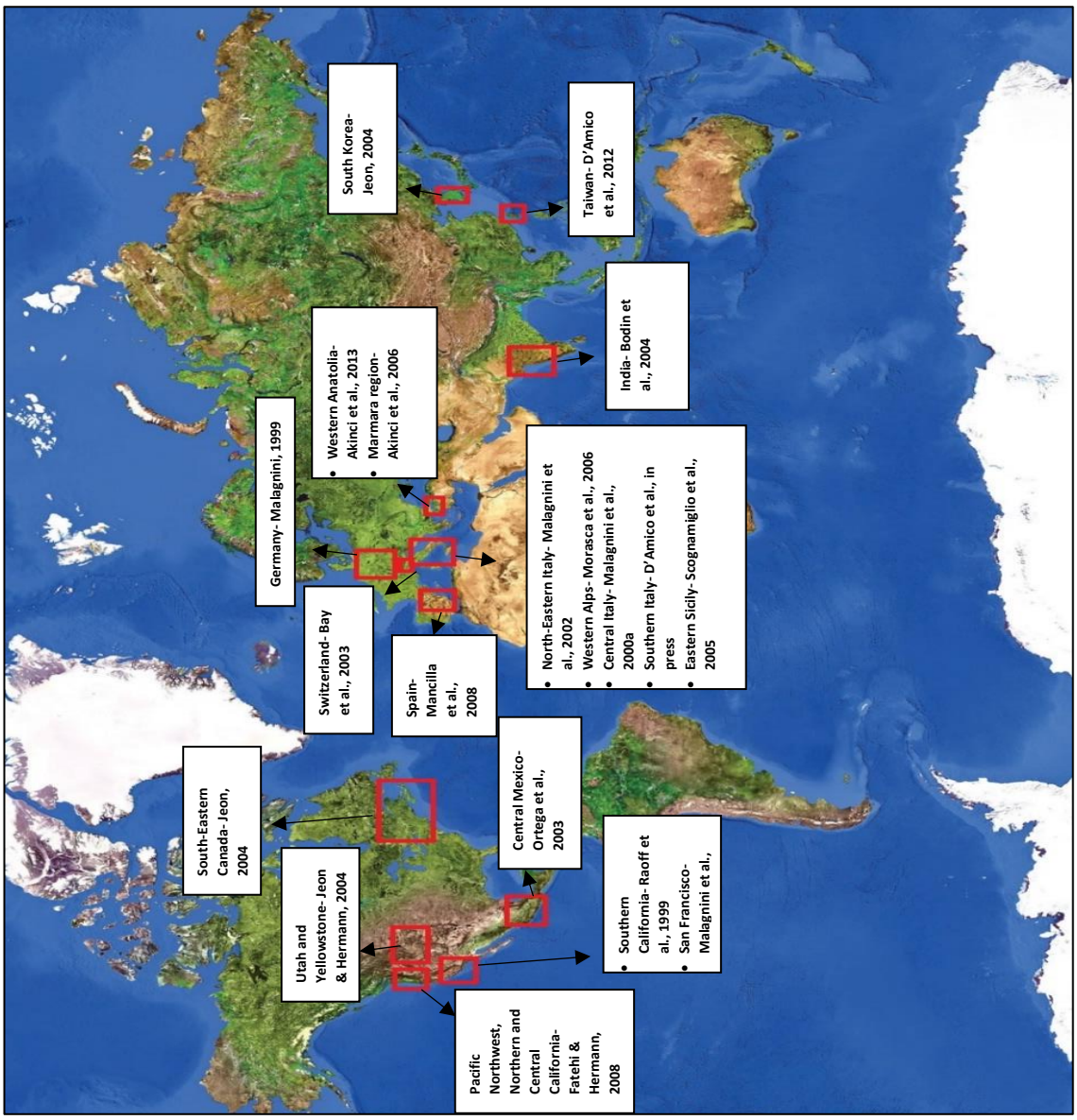

FIGURE 15: A MAP INDICATING THE GLOBAL LOCATIONS OF WHERE THIS STUDY HAS BEEN APPLIED TOGETHER WITH THE STUDIES' THEIR RESPECTIVE AUTHORS

The methodology has also been applied to different parts of Italy, as is with the case in California, because different attenuation parameters can be found for different areas within the same country since the material can change the attenuation properties of the propagating seismic waves hence resulting in various attenuation parameters which can be applied. Figure 16 shows how the attenuation changes throughout Italy, obtained from the studies which are also summarized in Appendix A.

The figure also gives an indication as to the geometrical spreading in relation to the attenuation of each region, superimposed in the seismic hazard map of Italy. These regions include eastern Sicily (Scognamiglio et al., 2005); Southern Italy (D'Amico et al., in press), Central Italy (Malagnini et al., 2000a); Western Alps (Morasca et al., 2006) and North-Eastern Italy (Malagnini et al., 2002).

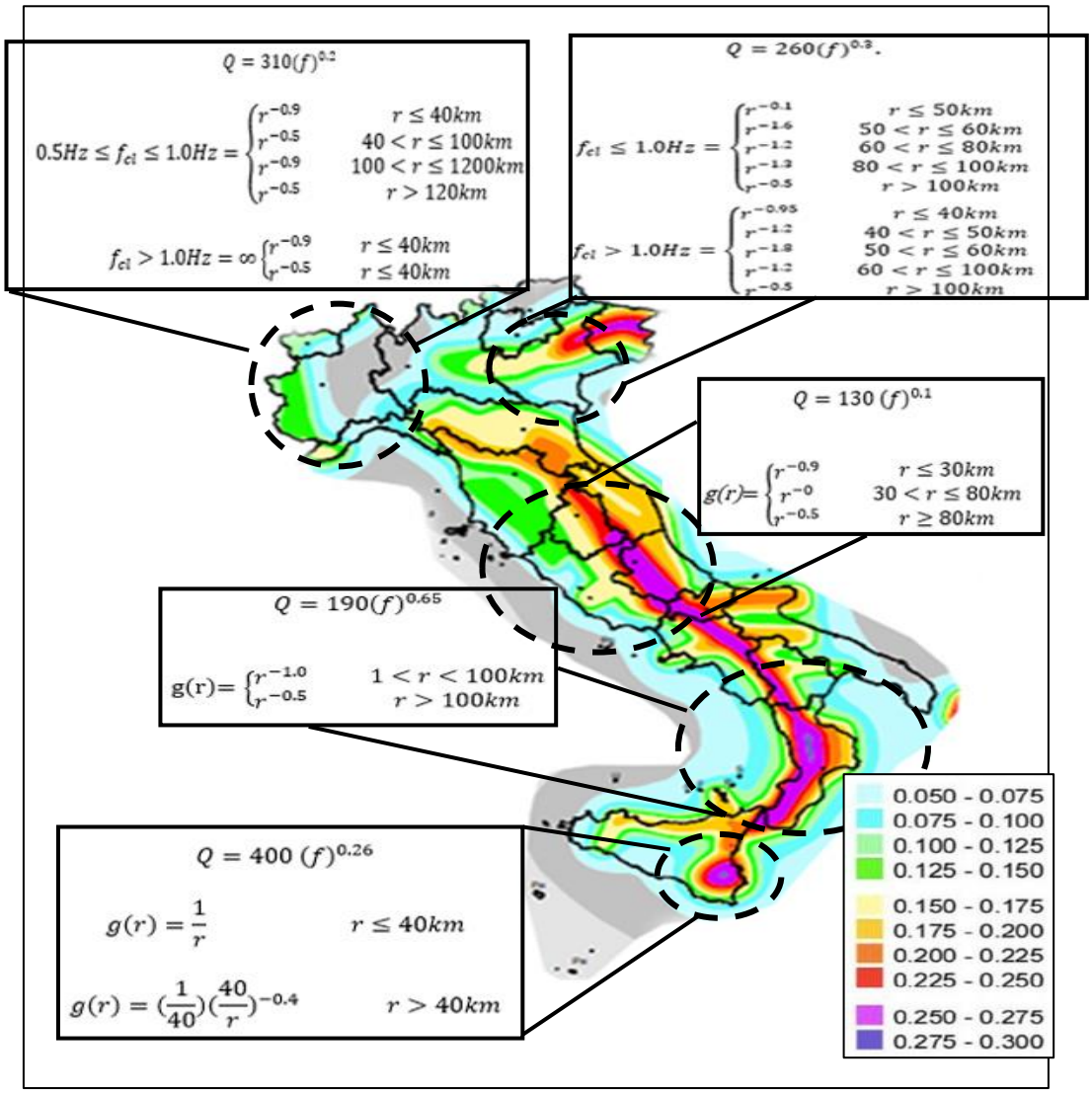

FIGURE 16: THE ATTENUATION PARAMETERS FOR THE ITALIAN REGION SUPERIMPOSED ON THE ITALIAN SEISMIC HAZARD MAP: WESTERN ALPS (MORASCA ET AL., 2006), EASTERN ALPS (MALAGNINI ET AL., 2002), CENTRAL ITALY (MALAGNINI ET AL., 2000A, SOUTHERN ITALY (D'AMICO ET AL., IN PRESS) AND EASTERN SICILY (SCOGNAMIGLIO ET AL., 2005).
SOURCE: D'AMICO ET AL., 2011

3.2. Random vibration theory

Random vibration theory (RVT) is a statistical tool used for seismic hazard analysis which estimates the extrema of random time histories and time-domain parameters that describe the ground motions given its spectrum and duration in time (Malagnini et al., 2000b; Malagnini et al., 2007). It is a quick way to obtain these peak motions regarding peak acceleration, peak displacement, peak velocity, etc.... (Boore, 2003). RVT is often used instead of time-series analysis because a single RVT analysis provides the mean site response without the need for a group of input-time histories (Kottke and Rathje, 2013). However, the methodology does tend to over predict site amplifications especially at lower frequencies (0.2-0.3Hz) (Rathje and Ozbey, 2006). It is necessary to quantify the effective duration of the seismogram as a function of frequency and hypocentral distance (Malagnini and Hermann, 2000c). In summary, the theory derived by Cartwright and Longuet-Higgins (1956) provides an estimation of the ratio of peak motion (a_{max}) to rms motion (a_{rms}) by using Parseval's theorem to obtain a_{rms} in terms of the squared acceleration spectrum:

$$\int_{-\infty}^{\infty}|a(t)|^2 dt = \frac{1}{2\pi}\int_{-\infty}^{\infty}|A(\omega)|^2 d\omega \qquad (1)$$

where a(t) is the acceleration time history and A(ω) is the Fourier amplitude spectrum given by:

$$A(\omega) = \Omega_0(2\pi f_0)^2 \qquad (2)$$

where Ω_0 is the spectral level at low frequencies and $f_0 = 1/T_d$, with T_d referring to the duration of the shear wave signal. Assuming that the motion

with most significance occurs in the shear wave arrival window and that spectral amplitudes are cut off at f=fmax (Hanks, 1979) by anelastic attenuation, then:

$$\int_0^{T_d}|a(t)|^2dt = \frac{2}{2\pi}\int_{2\pi f_0}^{2\pi f_{max}}|A(\omega)|^2d\omega \quad (3)$$

where t=0 which is equal to the shear wave arrival and Td is the duration of the shear wave signal. The rms acceleration is the given by:

$$a_{rms} = \left[\frac{1}{T_d}\int_0^{T_d}|a(t)|^2dt\right]^{1/2} \quad (4)$$

If f_0=1/Td, then the rms acceleration becomes:

$$a_{rms} = 2^{\frac{1}{2}}(2\pi)^2\Omega_0 f_0^3\left(\frac{f_{max}}{f0}\right)^2 \quad (5)$$

To predict the peak acceleration from the rms acceleration, Hanks and McGuire (1981) used the following equation:

$$\frac{a_{max}}{a_{rms}} = [2\ln(N)]^{1/2} \quad (6)$$

where N is the number of extrema in the time interval T. The extrema relate to all the places where the first derivative of the time series is equal to zero and for a broadband function, there is a possibility of having numerous local extrema (Boore, 2003). The above equation assumes that time series is stationary with uncorrelated peaks, which is not always true in accelerograms (Boore, 1983). If $\tilde{f}$ is the predominant frequency of the motion, then:

$$N = 2\tilde{f}T \quad (7)$$

The constant '2' indicates that two extremas are present in each cycle of motion. The appropriate frequency when N is the number of extrema is :

$$\widetilde{f} = \frac{1}{2\pi}(m_4/m_2)^{1/2} \quad (8)$$

where m_2 and m_4 are the second and fourth moments of the energy density spectrum. According to Cartwright and Longuet-Higgins (1956), equation 6 is an approximation for large values of N. They used the following integral expression for the ratio of peak to rms:

$$\overline{\eta_{max}} = \frac{1}{2^{1/2}}\int_0^\infty \left\{1 - \left[1 - (1-\varepsilon^2)^{1/2}e^{-0}\right]^N\right\}\theta^{-1/2}d\theta \quad (9)$$

Where ε is a measure of the r.m.s. width of the energy spectrum E. Boore (1983) expanded the integrand of the integral by the binomial series and integrated term by term to yield:

$$\frac{E(a_{max})}{a_{rms}} = \sqrt{\frac{\pi}{2}}\sum_{l=1}^{N}(-1)^{l+1}\frac{C_l^N}{\sqrt{l}}\xi^l \quad (10)$$

$E(a_{max})$ is the expected value of the largest extrema of acceleration and C_l^N are binomial coefficients ($\approx N!\,(N-l)!$). ξ is a measure of the bandwidth of the spectrum given by:

$$\xi = m_2/(m_0 m_4)^{1/2} \quad (11)$$

where m_0, is the zeroth moment of the energy density spectrum as ξ approaches unity with decreasing bandwidth. The kth moment is defined as:

$$m_k = \frac{1}{\pi}\int_0^\infty \omega^k\,|A(\omega)|^2\,d\omega \quad (12)$$

For large values of N, Cartwright and Longuet-Higgins (1956) derived the following asymptotic equation:

$$\frac{Ea_{max}}{a_{rms}} = [2\ \ln(N)]^{1/2} + \gamma/[2\ln(N)]^{1/2} \quad (13)$$

where γ is the Euler-Mascheroni constant equal to 0.57721…., while equation 6 is the first term of the above equation.

Another version for the ratio of peak to rms motion is given by Boore (2003) in this form:

$$\frac{a_{max}}{a_{rms}} = 2\int_0^{\infty}\{1 - [1 - \xi\exp(-z^2)]^{N_e}\}\ dz \quad (14)$$

where in this case, ξ is calculated by:

$$\xi = \frac{N_z}{N_e} \quad (15)$$

in which N_z and N_e are the number of zero crossings and extrema.

Boore (1983) provides another equation to calculate a_{rms} using the source duration T and Parseval's theorem to give:

$$a_{rms} = \left(\frac{m_0}{T}\right)^{1/2} \quad (16)$$

where T is given by:

$$T = f_c^{-1} \quad (17)$$

The relationship maximum amplitudes and rms amplitudes, which depends only on moments of the ground motion spectrum, needs to be considered when choosing the appropriate duration T (Boore, 1983). According to Boore (1983), random vibration theory is adequate for predicting ground motion, but

errors start to occur when N is small and when the successive peaks are strongly correlated. The former leads to results departing from time domain simulations whilst the latter is in violation of an assumption made in the theory.

3.3. Regression

3.3.1. General equation and constraints used

The first step involved is to correct each seismogram for instrument response and those having low signal to noise ratios are removed. The data is then converted to yield ground velocity in metres per second before picking the P and S arrival times. Each waveform is then band pass filtered about a corner frequency, f_c. This is carried out using an eight-pole high pass Butterworth filter which has a corner frequency at $f_c l/\sqrt{2}Hz$, followed by an eight-pole low-pass Butterworth filter that has a corner frequency at $\sqrt{2f_c Hz}$. For this study, the following frequencies were chosen: 0.25, 0.40, 0.60, 0.85, 1.25, 1.75, 2.50, 3.50, 5.00, 7.00, 9.00, 12.50, 17.50 and 20.00Hz. Once filtering is completed, parameters are then required to estimate peak values for amplitude of ground motion which depends on independent site, source and path effects. The method to estimate peak ground motion for acceleration uses RVT to obtain attenuation, source spectrum and duration time (D'Amico et al., 2012). Akinci et al. (2006) describe well the equations and terms used to obtain the peak ground motion. There are different ways to write the equation but two of the most widely used are:

$$AMP_{kij}(f) = \log amp_{kij}(f) = EXC_i(f) + D(r_{ij}, r_{ref}, f)z + SITE_j(f) \quad (18)$$

And:

$$A_{ij}(f, r_{ij}) = EXC_i(r_{ref}, f) + SITE_j(f) + D(r_{ij}, r_{ref}, f) \quad (19)$$

where in equation 19, $A_{ij}(f, r_{ij})$ is the peak amplitude of ground motion velocity as a logarithm at a site 'j' (site index) for an earthquake 'i' (source index) for each filtered seismogram logged at the hypocentral distance r_{ij}. For equation 18, $AMP_{kij}(f)$ is the logarithm of the observed ground motion spectrum on the kth waveform (the rms average in a frequency band centred at the sampling frequency logarithmically) in relation to the ith source and recorded at the jth site. For both equations, f and r represent the frequency and hypocentral distance respectively with r_{ref} referring to the reference distance. EXC_i is the source (or excitation) term, referred to an adequate reference distance away from the source. The excitation term is equal to the source when the reference distance is equal to zero. The $SITE_j$ represents the site term (corresponding to the site on average) and is an effect of the wave propagation nearby the site, and $D(r_{ij}, r_{ref}, f)$ is the crustal propagation term, exhibiting the combined effect of the anelastic attenuation Q(f) and of the geometrical spreading g(r), and generates the signal from the reference distance to the observation distance. By utilizing the above equation, the path, site and source terms are obtained by arranging the observations into a large matrix and inverting them. However, constraints are required for this regression to obtain a stable inversion in the system and to decrease the number of degrees of freedom:

1. $D(r_{ref}) = 0$, where r_{ref}=40km.
2. The summation of all site terms at a particular frequency is equal to zero:

$$\sum_{i=0}^{nsites} Site_i(f) = 0 \quad (20)$$

3. The roughness of the attenuation function is minimized:

$$roughness = \sum_{i=1}^{n} D_{i-1} - 2D_i + D_{i+1} \quad (21)$$

The first constraint describes the excitation term's project distance with the reference distance chosen so as inaccuracies in the depth of the source at the chosen distance would be negligible. This also implies that supercritical reflections from the Mohorovičić discontinuity ought not to appear at the distance range which is chosen to complicate motions. The common site effects of the source term are reflected by the second constraint showing that the summation of some, or all, of the site terms is a null value and this leads to the conclusion that when the absolute average is not zero, its value is compelled into all distinct source terms. The third constraint is used by Ortega et al. (2003) to reduce the roughness of the attenuation function. The following figure on page 55 is a summary of the procedure which is followed to obtain the required results. The equation in the figure ($u(t) = s(t) * g(t) * i(t)$) is another simplified form of the equation 18.

3.3.2. Duration

Once filtering and waveforms are picked, the duration is required for further analysis. Duration is a function of earthquake size together with the dispersion and scattering along source-receiver paths that the elastic waves experience. It is important to estimate the ground motion duration at specific sites correctly for structural purposes, since a considerable amount of damage may occur at low levels of peak ground motion with a large duration that decreases the strength of certain structures (Kramer, 1996). The ground motion duration is

dependent on the rupture process and duration, the fault size, and the dispersion or scattering that the elastic waves experience along the path between the seismic station and the source. Quantifying the duration is important in this methodology in order to evaluate the attenuation of the peak ground velocity. The RVT uses the rms value of the time series and the spectral instances of the duration's Fourier amplitude spectrum to calculate the time domain maximum for the random time history of the duration by applying the definition used by Raoof et al. (1999). The definition states that the duration relates to the time window comprising between 5% and 75% of the cumulative seismic energy subsequently after the S-wave arrival. The duration is presumed to be in the form of T_s + T(r), where T_s is the source duration and T(r) is the contribution of the wave propagation, which is distance-dependent, to total duration (Herrmann, 1985).

Duration at a regional scale is affected by the crustal structure. At low frequencies below 1.0Hz, duration increases with distance and may increase more rapidly past the site of the first strong supercritical reflections (Malagnini et al., 2007). Duration tends to increase as the earthquake magnitude, distance, and scattering effect increase as well. However, due to the superiority of a single S-arrival rather than a group of arrivals, the high-frequency duration increases at a slower rate with distance.

3.3.3. Attenuation

Attenuation is used to describe the decrease in the amplitude of seismic waves as the distance increases due to geometrical spreading, since the energy is released over a larger area when rupture occurs. With regards to geometrical spreading, since energy travels spherically from the source, the amplitude of

seismic waves will decay by 1/r, whereby r is the distance from the source. Attenuation can either be intrinsic, caused by internal friction or anelastic processes whilst the wave is propagating, or attenuation can be scattering whereby the amplitudes seismic waves are scattered due to small heterogeneities (Shearer, 2002). These heterogeneities divide the high frequency wavefield into arrivals known as coda waves. Fundamental tools for seismic hazard assessment are the attenuation relations based on the recorded peak ground motions expressed as mathematical functions which relate the observed ground motions to the earthquake source, site and path parameters (Skarlatoudis et al., 2003). More specifically, attenuation relationships express ground motion parameters such as velocity or acceleration (site effects and focal mechanisms can also be used) as a function of earthquake distance from the epicentre and magnitude (Reiter, 1991).

Referring to the equation in the beginning of this section (equation 18), the distance term D(r,f) is a piecewise function representing the distance dependence at a fixed frequency and contains both geometrical spreading and anelastic attenuation. It has the expression:

$$D(r,f) = \sum_{j=1}^{N_{nodes}} L_j(r) D_j(f) \tag{22}$$

where $L_j(r)$= linear interpolation function, and $D_j(f)$ are node values. D (r, r_{ref},f) is then modelled using the following form:

$$D\left(r, r_{ref}, f\right) = \log g(r) - \log g\left(r_{ref}\right) - \frac{\pi f\left(r - r_{ref}\right)\log e}{\beta Q(f)} \tag{23}$$

This form models the regression results at a set of sampling frequencies. Malagnini et al. (2007) expresses this equation in the following way:

$$D(r, r_{ref}, f) = \log_{10}\left[\frac{g(r)}{g(r_{ref})}\right] - \left[\frac{\pi f}{\beta Q_0 f^n}(r - r_{ref})\right]\log_{10} e \quad (24)$$

Another form of this functional form is given by Ortega et al. (2003) as:

$$D(R, f) = \log\left(\frac{\log(R)}{g(R_0)}\exp\left[-\frac{\pi f(R-R_0)}{\beta Q_0 f^n}\right]\right) \quad (25)$$

For every form of the equation, g(r) refers to the geometrical spreading, r is the hypocentral distance, β is the shear-wave velocity, R_0 indicates the reference distance while Q(f) is the frequency dependent attenuation function describing the inelastic absorption and loss for scattering and complexity of propagation due to fluctuations of the elastic properties of the medium (Margaris and Hatzidimitriou, 2002). It is expressed by:

$$Q(f) = Q_0\left(\frac{f}{f_{ref}}\right)^n \quad (26)$$

With the parameter η defining the dependence on frequency of Q(f). If f_{ref} is chosen as 1 Hz, the equation takes the following form:

$$Q = Q_0 * f^n \quad (27)$$

3.3.4. Excitation terms

Following the attenuation term, the excitation term is then obtained. This indicates the excitation of ground motion at a reference distance at the earth's surface. The term is applicable for the average site class and is dependent on the site characteristics. The following functional form is used:

$$exc(f, r_{ref}) = C(2\pi f)M_0 s(f) g(r_{ref}) exp\left[-\frac{\pi r_{ref}}{\beta Q(f)}\right] v(f) \quad (28)$$

in which the generic rock site amplification V(f), that is relative to the hard rock, is determined from the shallow shear wave velocity structure close to the site.

The term $g(r_{ref})exp\left[-\frac{\pi r_{ref}}{\beta Q(f)}\right]$ embodies propagation effect, as a result of crustal attenuation and geometrical spreading, at the reference distance. Finally, C and $s(f)$ and calculated using the following equations:

$$s(f) = \frac{1}{1+\left(\frac{f}{f_c}\right)^2} \tag{29}$$

$$C = \frac{RVF}{4\pi\rho\beta^3} \tag{30}$$

C is a constant which includes the average source radiation pattern R, the effect of the free surface F, V which signifies the separation of the total shear wave energy into horizontal components, the shear velocity and the average crustal density. Another form of the equation for the excitation terms is as follows:

$$10^{EXC_i(r,ref,f)} = s(f,M_w)g(r_{ref})exp\left[-\frac{\pi f r_{ref}}{Q(f)\beta}\right]\{V(f)\exp(-\pi f\kappa_0)\}avg \tag{31}$$

In which $s(f,M_w)$ is the source excitation as a function of moment magnitude. κ_0 , which indicates the high frequency decay parameter, defines the decrease of the high frequency motion at a site attributable to the local Q(z) structure. The excitation term is then modelled using Brune's ω^2 source model. The source excitation above is given by:

$$\frac{CM_0(2\pi f)^2}{1+\left(\frac{f}{f_c}\right)^2} \tag{32}$$

in which C is the scaling factor and M_0 is the sub-fault seismic moment which is proportional to the stress drop.

3.3.5. Brune source model and stress drop

Brune's ω^2 source model describes, in terms of moment magnitude and stress drop, the spectrum of shear radiation and has been applied to estimate stress drop from earthquake spectra. The stress drop represented by the symbol $\Delta\sigma$ has no proper definition but is required to define the spectral shapes and levels of the empirical excitation terms. The stress drop was introduced to measure the discrepancy between the stress before and after rupture at a point on a fault (Margaris and Hatzidimitriou, 2002). To determine the PGV and PGA, the stress drop is an important source parameter that controls high frequencies and is based on determining the corner frequency especially for small earthquakes (Abercrombie, 1995; Allman and Shearer, 2009). This is done using the Fourier spectrum on displacements and is usually the intersection between a flat low frequency level and the slope describing the fall of high frequencies in Brune's ω^2 model (Courboulex et al., 2016). It is important to use the right fault geometry to obtain the stress drop since an inappropriate geometry could lead to large errors (Madaraiga, 1977). However, since Brune's model is used, it is assumed that the faults are circular. For a circular fault of radius R, the stress drop is calculated using:

$$\Delta\sigma = \frac{7}{16}\frac{M_0}{R^3} \tag{33}$$

For a rectangular fault with length L and width w:

$$\Delta\sigma = \frac{2}{\pi}\frac{M_0}{w^2 L} \tag{34}$$

For a rectangular dip-slip fault:

$$\Delta\sigma = \frac{4(\lambda+\mu)}{\pi(\lambda+2\mu)}\frac{M_0}{w^2 L} = \frac{8}{3\pi}\frac{M_0}{w^2 L} \tag{35}$$

Where the last equation assumes λ= μ.

However, we will only be using equation 33 used for circular faults since Brune's source model assumes that faults are circular. The seismic moment is estimated using the following equation:

$$M_0 = 0.79M_L + 1.2 \quad (36)$$

The radius of the source R is found using:

$$r = k\frac{\beta}{f_c} \quad (37)$$

Where β as the shear wave velocity is equal to 3.5km/s and k is a constant equal to 0.37 and depends on assumptions of the rupture model and type of wave. This value used in this research is the same as the one used in Brune (1970) though different k values are described in a study by Dong and Papageogiou (2003). Fault dimensions for large earthquakes can be found by using the aftershock area whilst, for smaller earthquakes, these fault dimensions are much harder to measure and may lead to significant errors in stress drop if the fault length or radius is improperly measured (Lay and Wallace, 1995). Stress drop and rupture velocity are assumed to be dependent of each other. In fact, a study by Causse and Song (2015) confirmed the trade-off between the two parameters. It is also observed that for smaller earthquakes a constant stress drop scaling could be the case but for larger earthquakes it is non-linear perhaps, due to the fact that the length of rupture is greater than the seismogenic layer (Shaw, 2009; Hanks, 1977; Derras et al., 2017). There is one disadvantage of using the corner frequency to determine the stress drop. According to Cotton, Archuleta and Causse (2013), corner frequency measurements are quite difficult to measure and are subject to

uncertainties. This could lead to an overestimation in stress drop, causing the variability obtained from between event ground motion residuals to be smaller than the one obtained from ground motion prediction equations, and this would be too large to be used for seismic hazard analysis (Oth, Miyake and Bindi, 2017). Additionally, according to Atkinson and Silva (2007), Brune's source model can also overestimate results at larger distances away from the source.

The far-field spectrum can also be calculated from Brune's model. The corner frequency and low frequency spectral level are two independent parameters that characterise the far-field spectrum, which is radiated by an earthquake from a point source model. From these 2 spectral parameters, various source estimations such as seismic moment and stress drop can be found (Margaris and Hatzidimitriou., 2002). The far-field spectrum predicted by Brune's model is:

$$U(\omega) = \frac{\Delta\sigma\beta}{\mu}\frac{1}{\omega^2+b^2} \tag{38}$$

where β is the shear-wave propagation velocity, and b= $2.33\beta/\alpha$ with α representing the radius of the fault.

The Brune spectral model can estimate the ground motions of earthquakes using also the information regarding the ground motion duration, regional attenuation and absolute site terms as a function of distance from the source for a range of different magnitudes. The site response is termed as 'absolute' due to the fact that they take into account the response of what is not in the average regional path terms, such as the absolute response from the depth of a bedrock that is prevalent to all sites to the surface. The Brune spectral model

is used in conjunction with a stochastic model which, for the case of high frequencies (>0.5-1Hz) is the EXSIM (stochastic EXtended SIMulator) simulation programme using finite fault simulations. The stochastic approach is used to predict the expected ground motion parameters (PGA and PGV) as a function of magnitude and distance (D'Amico et al., 2012). PGA is an important parameter for seismic resistant design since the product of PGA and mass is equivalent to the inertial force loading the structures (Danciu and Tselentis, 2007). PGA is controlled by the high frequency part of ground motion and is used by many engineers with regards to infrastructure resistance. It has been observed that ground motions with a high PGA tend to be more destructive, unless they last for a short period of time, resulting in less damage to structures (Kramer, 1996). Some engineers, on the other hand, think that PGD (peak ground displacement) correlates more to damage than other measuresand is in fact used in the seismic code which considers the drift to damage evaluation. . However, in this study, only the PGA and PGV shall be studied.

To combine seismological models of predicted seismic amplitude spectrum randomly, a stochastic model uses the fact that for observed strong motions large parts on the seismogram appear random and incoherent (Hanks and McGuire, 1981). Estimates of peak motions or time domain simulations can determine the motion at a site using this method by applying the random vibration theory for a given amplitude spectrum (Boore, 2003). The latter method has been explained in detail previously in the above description. The former, which refers to the time domain, involves modelling ground motion as

bandlimited finite duration white Gaussian noise (Boore. 1983). The simulation starts with generating windowed time series of Gaussian noise with zero mean and then the duration of ground motion provides that noise is produced for a duration (Hanks and McGuire, 1981). The noise spectrum is then multiplied by the specified spectrum after which it is transformed into the time domain to give the final time series (Boore. 2003).

In the EXSIM programme, the finite fault is simulated as a plane partitioned into a number of sub-faults which are in turn modelled as stochastic point sources by applying Brune's source spectrum. The computation of the radiation at a point of observation can reproduce the motion from the extended rupture by summing up the contributions that each sub-faults provides with amplitude scaling and appropriate delays. The size of the finite fault, especially a large one, can impact the amplitude, frequency content, and ground motion duration. The finite fault method can identify the earthquake source mechanism by using the fault geometry that includes hypocentre location, fault depth, the dip and strike angles, and sub-fault size. The Joyner-Boore distance is used in EXSIM, which refers to the closest distance to the surface projection of an extended fault, as is simulated in EXSIM. Figure 17 is a simplified diagram indicating how this distance is measured.

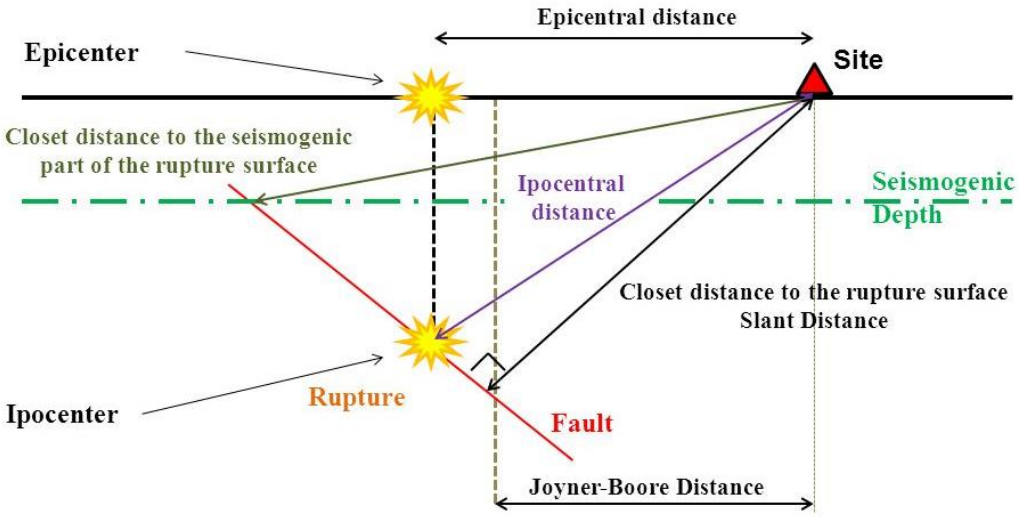

FIGURE 17: MEASUREMENT OF THE JOYNER-BOORE DISTANCE
SOURCE: FATEMEH JALAYER, 2014

Some papers use SMSIM (Stochastic Method SIMulator) instead of EXSIM, which is a point-source stochastic model and not a finite-fault model like EXSIM. These papers include, amongst others, the study by Morasca et al. (2006) for the Western Alps, Scognamiglio et al. (2005) for Eastern Sicily, Akinci et al. (2006) for the Marmara region in Turkey, and Malagnini et al. (2002) for North-eastern Italy. A detailed description of the method is described by Boore (2002) in a report. EXSIM and SMSIM differ in several ways producing different results such as the geometry and distance measures, definition and duration application and the approach to normalize the summations of the finite-source sub-source (Atkinson et al., 2009). However, Boore (2009) made some modifications in EXSIM in such a way that the results from both SMSIM and EXSIM can agree with each other for motions from a small earthquake at a large distance for both programs. These modifications include:

1. Time series are not truncated from each sub-fault

2. The inverse of the sub-fault corner frequency for the duration of motions from each sub-fault is used
3. The scaling of high frequencies is formulated on the integral of the squared Fourier acceleration spectrum
4. At frequencies near and less than the sub-fault corner frequencies, a filter function is used to boost spectral amplitudes.

Amongst some of the advantages of using EXSIM are that results are independent from sub-fault size, radiated energy is conserved, and in addition to these, during the rupture process only part of the fault is active at any time which simulates self-healing behaviour (Heaton, 1990; Atkinson and Boore, 2006).

3.3.6. Site terms

The type of rocks and soil present in an area have different responses to ground motion, such as the amplification of ground motion by soft soils (Kramer, 1996). Generally, for softer soils, the most significant amount of energy of seismic motion is concentrated at lower frequencies which control displacements, while for firmer soils or rock, the most significant energy is concentrated at higher frequencies which control accelerations (Theodulidis and Papazachos, 1992). The term V(f) quantifies the divergence from the mean seismic spectra for every station as a result of properties characterising the shallow geology of the site (Bay et al., 2000). As a by-product of linear regression, the site terms are obtained for each sample frequency (Malagnini et al., 2000b). The constraint in equation 20 is used to define an average bed-rock-site condition and represents what would be logged by the average network site at the reference hypocentral distance (Bay et al., 2003; Akinci et

al., 2013). Horizontal motion characteristics are found by analysing horizontal site terms or through observing the horizontal to vertical site term ratios (Malagnini et al., 2002). This H/V ratio is considered to be a stable site characteristic and is independent of earthquake magnitude, distance, source location and mechanism (Atkinson, 1993; Theodulidis et al., 1996). The ratio can change depending on the location of the site. For instance, for eastern North America, the ratio is given by Atkinson (1993) as:

$$\log H/V = 0.0519 + 0.117 \log f \tag{39}$$

To classify the site, a common method is to use the average shear wave velocity at the top 30m and is denoted as V_s^{30} (Vipin et al., 2009). The procedure to obtain this value is described by the National Earthquake Hazard Reduction Program (2003) using equations 3.3-1 to 3.5-4. For each site class, different shear wave velocity ranges are listed depending on the type of rock or soil. Table 2 lists the suggested velocities and corresponding site classification according to the NEHRP.

TABLE 2: NEHRP SITE CLASSIFICATION

Site Class	Rock or soil type	Velocity (V_{30})
A	Hard Rock	>1.5km/s
B	Rock	0.76m/s<V_{30}> 1.5km/s
C	Very dense soil and soft rock	0.36km/s<V_{30}>0.76km/s
D	Stiff soil	0.18km/s<V_{30}>0.36km/s

3.4. Error Analysis

Error measurements and uncertainties on parameters such as Q and stress drop, are not provided using the stochastic method. Instead, to resample the data and estimate errors, the bootstrap method can be used (Fatehi and Hermann, 2008). The bootstrap method uses data from a sample study known as 'sample population' and is then resampled (with replacement) to create a large number of data sets known as 'bootstrap samples' (Singh and Xie, 2008). Multiple estimates of the model will give estimates of the model variance and a histogram of these computed values is called the 'bootstrap distribution of the statistic' (Fatehi and Hermann, 2008). Since resampling is done with replacement, it is possible that an element of the original data set may be exhibited in the new data set more than once. The bootstrap estimate of standard deviation θ is:

$$\hat{\sigma}BOOT = \left[\frac{1}{L-1}\sum_{i=1}^{L}(\widehat{\theta_i^*} - \bar{\theta})^T(\widehat{\theta_i^*} - \bar{\theta})\right]^{1/2} \quad (40)$$

where $\widehat{\theta_i^*}$ is an estimator of the statistic θ calculated for the bootstrap resample i, and $\bar{\theta}=\sum_i^L \widehat{\theta_i^*/L}$ (Efron and Tibshirani, 1994). The programme which shall be used to obtain the required parameters, uses this bootstrap method to acquire error bounds for the parameters by having it embedded in its code. Figure 18 on the next page is a summary of the procedure that has been described in this chapter.

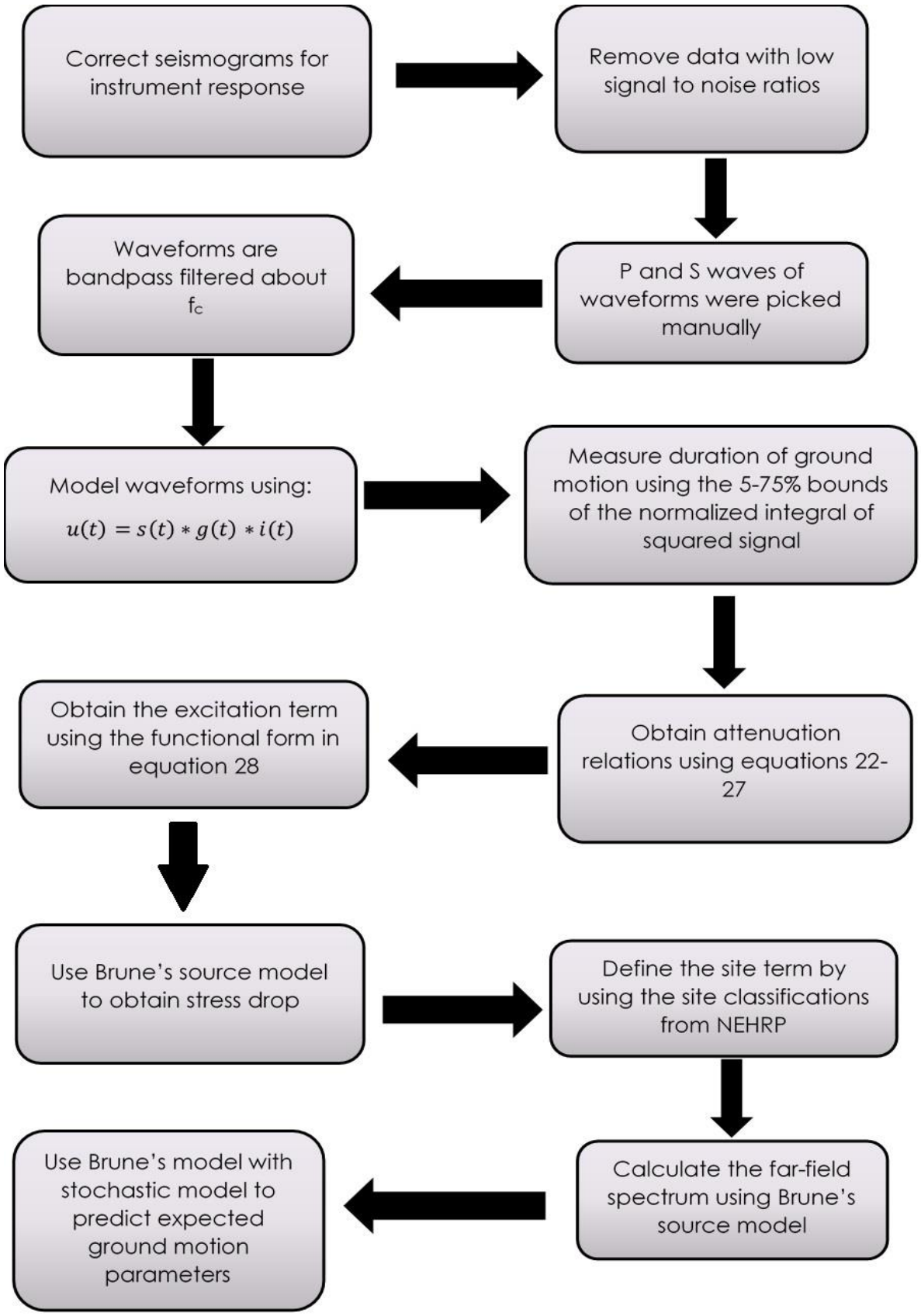

FIGURE 18: SUMMARY OF PROCEDURE INVOLVED

Chapter 4: Data set, Processing and Results

4.1. Data set

For the study, waveforms and earthquake catalogues were obtained from the data base belonging to the National Observatory of Athens. The stations from which the waveforms were recorded are part of the Hellenic Unified Seismic Network (HUSN), which consists of approximately 120 stations located around Greece.

297 events from 65 three-component stations around central Greece were analysed to obtain ground-motion parameters. Table 10 in Appendix B is a list of these events together with their locations and local magnitude. These events were small magnitude events ranging from magnitude 2.5 to 4.4. Another dataset with much more recent and larger events, ranging from magnitudes 4.7 to 6.7 was obtained to use further on during the research project to obtain a stress drop relationship with magnitude. This dataset is tabulated in table 11 (also in Appendix B). Additionally, in Appendix C, there are plots which indicate the number of recordings as a function of distance for each station.

Although large magnitude data is scarce, the data is sufficient to establish attenuation relationships and other ground motion parameters using small events. From the earthquake catalogue in Table 10, graphs showing the magnitude and depths of the earthquakes under study were obtained to gain

an initial view of the characteristics of the earthquake events. These are shown in figures 19 and 20 .

As can be observed from Figure 20, the depths are shallow with most of the events happening at depths between 16-20km. Depths rarely exceed 35km because the crustal thickness for central Greece is approximated at 31-35km deep (Makris and Stobbe, 1984). The events are localised around the Corinth Gulf but other events from the Ionian Sea in the west and the Aegean Sea in the east were also used to obtain a wider evaluation of the ground motion parameters of Central Greece. Figure 21 is a map showing the locations of the earthquake events that were used in this study whilst Figure 22 indicates the locations of the events together with their relative depth. It should be noted that for the Gulf of Corinth, the most frequent events occur between 10 to 20km deep. There are also a few shallow events for which its focal point originated at depths less than 10km. Only one event occurred at a depth between 20 to 30km deep. Events deeper than 30km occurred closer to the Ionian Sea.

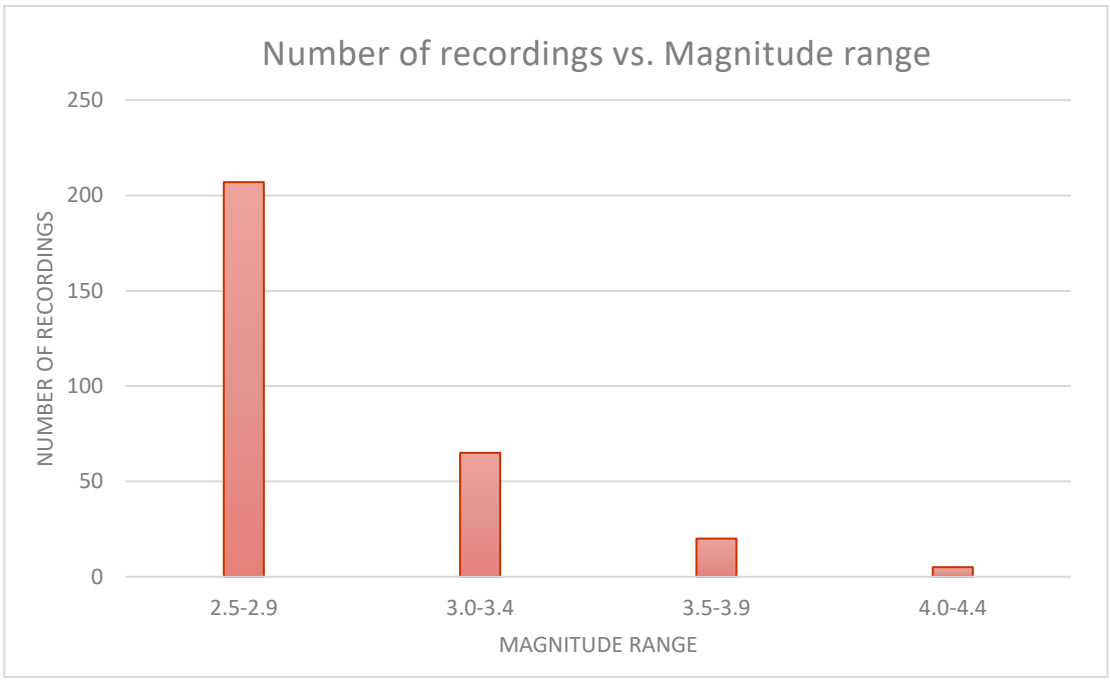

FIGURE 19: A GRAPH SHOWING THE MAGNITUDE DISTRIBUTION OF DATA

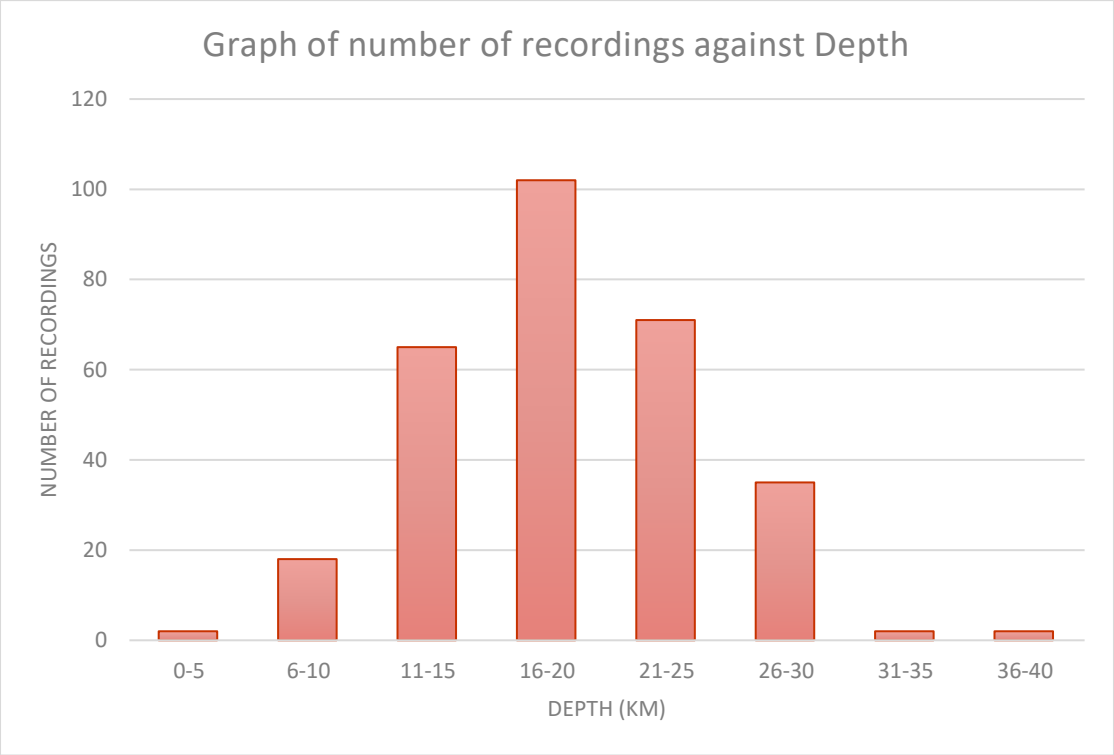

FIGURE 20: A GRAPH SHOWING THE DEPTH DISTRIBUTION OF DATA

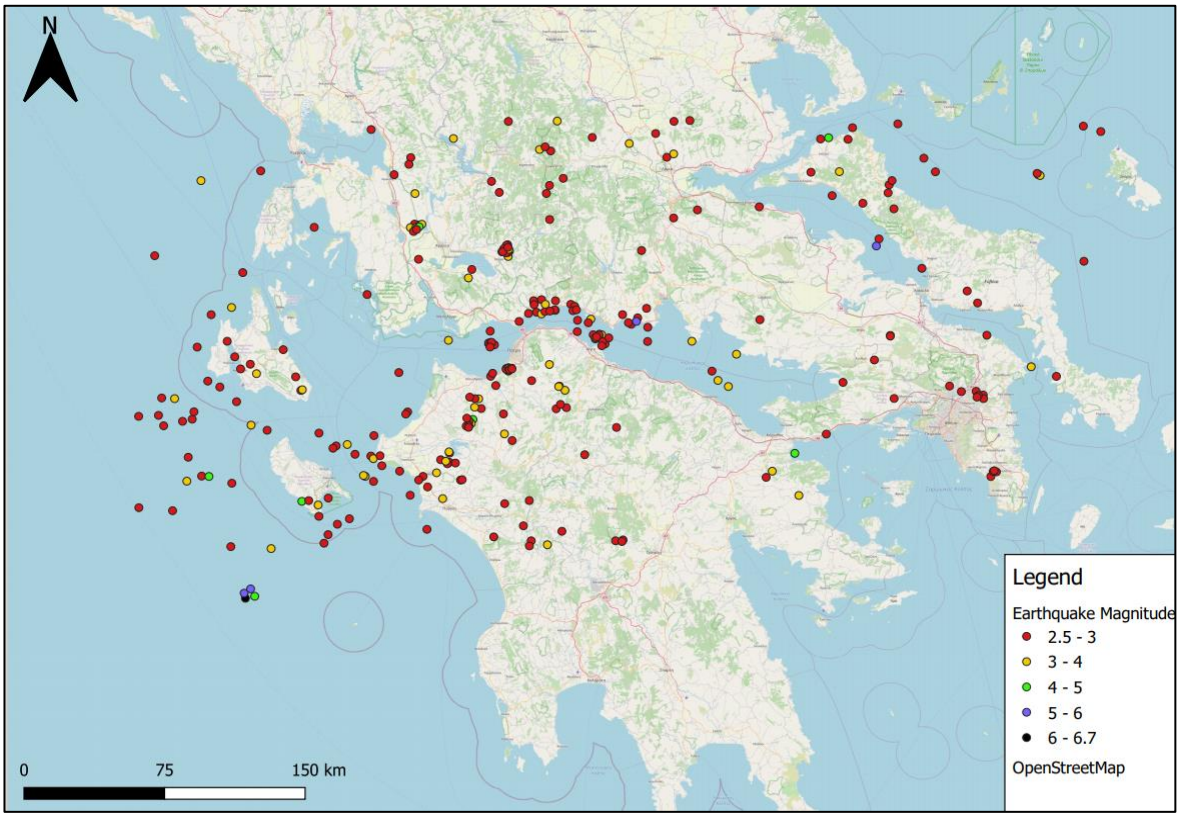

FIGURE 21: MAP INDICATING EARTHQUAKE LOCATIONS USED IN THIS STUDY FOR CENTRAL GREECE.

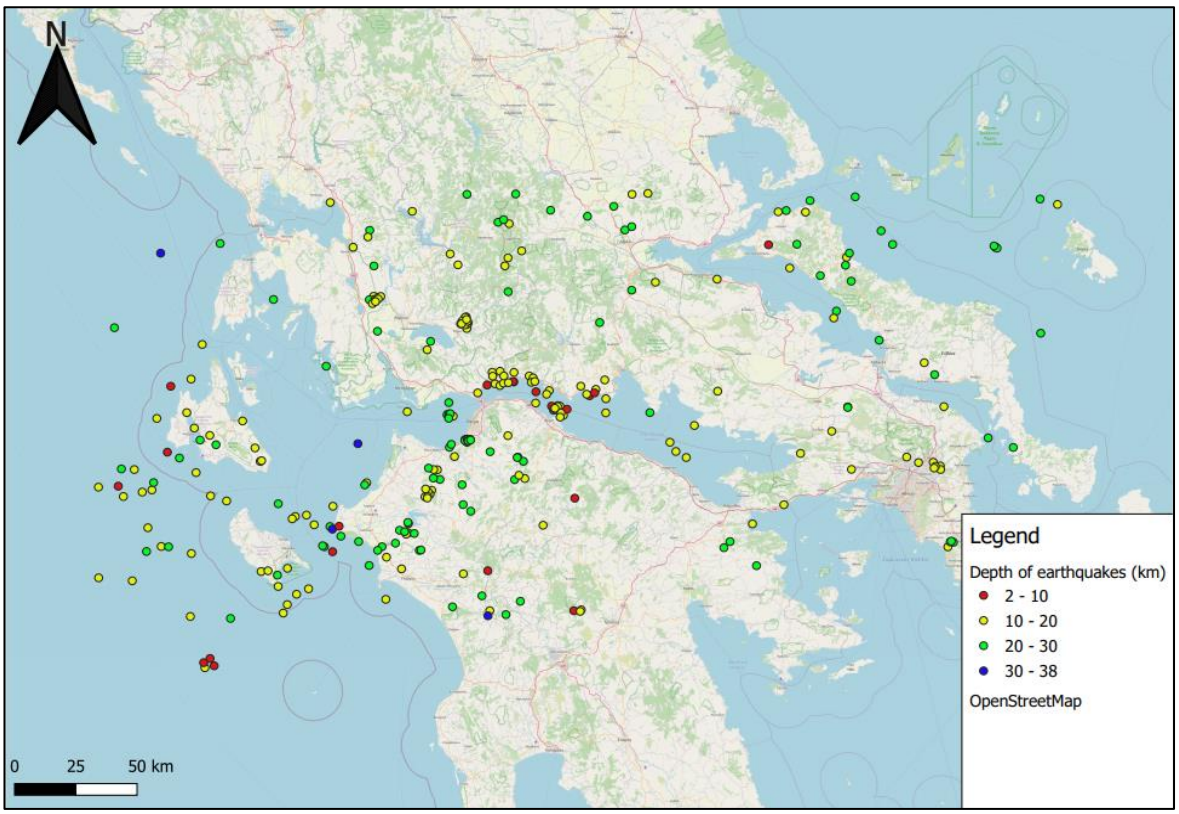

FIGURE 22: MAP SHOWING LOCATIONS OF EARTHQUAKES RELATIVE TO THE DEPTHS IN KM.

4.1.1 Stations used in study

85 stations forming part of the HUSN were used for the purpose of this study. The stations are 3D component telemetric, digital seismic stations with broadband and have recently been deployed in different parts of the Hellenic region in 2007. The stations helped to further seismic studies in this highly seismically active region to increase knowledge regarding the seismotectonics of the region as well as to provide an insight as to possible large magnitude earthquakes which might occur in the future, as is the purpose of this study.

Although all stations listed in Table 3 on the next page were used for the study, some stations in the map (Figure 23) on page 69 registered more background noise than others. One of the reasons could be the distance of the station from the recorded event. Another reason could also be the material of the site on

which the station is located, although most stations are located on rock sites. Such stations were used as a last resort when data from stations nearby the event was lacking. It is also important to note that all the stations are located on land. So far there are no stations installed at sea forming part of HUSN. This is one of the improvements that could be implemented to improve the recording of seismic events, especially those that occur offshore. If more data can be provided from different locations, especially at sea, then more accurate ground motion relationships can be established.

TABLE 3: LATITUDES AND LONGITUDES OF STATIONS USED FOR STUDY

Latitude	Longitude	Station Name	Latitude	Longitude	Name
36.718	22.9469	VLI	38.5933	21.9209	ANX
36.7622	22.3337	DYR	38.5986	21.1833	PDO
36.8245	21.7071	MES2	38.616	21.525	PVO
36.8955	21.742	PYL	38.6496	22.9989	LKR
37.1437	22.0424	MES1	38.7664	22.659	AXAR
37.1609	24.4853	SERI	38.7889	20.6578	LKD2
37.1787	21.9252	ITM	38.8791	23.209	SMIA
37.2309	22.0333	MES4	38.8831	24.5482	SKY
37.2488	21.6725	MES3	38.9166	21.8105	EVR
37.3703	22.3793	VLX	39.0211	22.336	AGG
37.383	23.1502	KRND	39.1654	23.8639	AOS
37.5063	23.2368	DID	39.3057	23.2219	NEO
37.5278	22.2708	TRIP	39.366	23.1918	XOR
37.5324	21.7089	AMT	39.4086	22.9396	FYTO
37.696	20.785	ZKS	39.5315	20.3299	IGT

37.8524	23.7942	VLY	39.5647	22.0144	THL
37.9363	22.3423	GUR	39.6562	20.8487	JAN
37.9738	23.7177	ATH	39.7127	19.7962	KEK
37.9879	22.9743	LOUT	39.9363	23.6768	PAIG
38.0228	22.9673	LTK	39.9549	21.3632	KPRO
38.0321	24.437	KARY	40.0724	18.4675	SCTE
38.0435	22.1504	KLV	40.1033	22.4892	LIT
38.0473	23.8638	PTL	40.1959	21.1384	PENT
38.0559	21.4648	RLS	40.3033	21.7821	KZN
38.0779	23.9331	DION	40.3325	23.9791	OUR
38.1102	20.7884	KFL	40.3733	23.4444	PLG
38.1768	20.5886	VLS	40.4147	21.0489	NEST
38.2401	21.9785	LAKA	40.7817	21.3836	FNA
38.4112	22.5271	DSF	40.9558	22.4029	GRG
38.4133	22.0566	SERG	41.162	22.898	KNT
38.4269	21.9058	EFP	40.8206	23.3556	SOH
38.4593	20.5623	FSK	37.5278	22.2708	TRIP

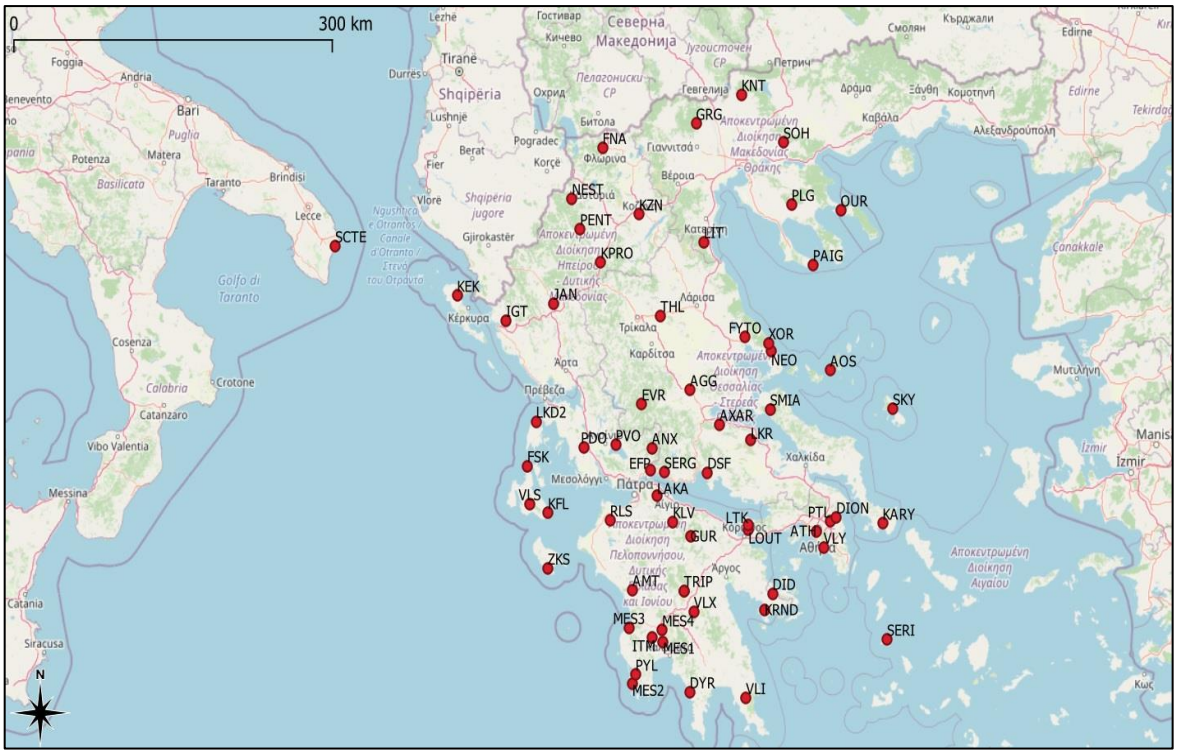

FIGURE 23: MAP SHOWING LOCATIONS OF STATIONS USED IN THE STUDY

As can be observed from the above map, stations such as PENT, VLI, SCTE, and KZN are further away from the Corinth Gulf. Most often, such stations provided waveforms as in Figure 24 for stations PENT, VLI, and NEST, that were influenced by a lot of background noise, and were also hindered by the distance from the event epicentre. Such waveforms, for which the P and S wave arrival time was difficult to establish, were not used but were kept as backup just in case there was insufficient data.

Stations close to the Corinth Gulf such as LAKA, AXAR, RLS and KLV provided good quality waveforms that were used to obtain the required ground motion parameters for the Corinth Gulf further on into the study. The picked P and S waves for such stations such as LAKA, RLS, and EFP are depicted in Figure 25. Once P and S waves are picked manually for stations that provided good waveforms, data processing to process high frequency ground motion could then proceed. This is the basis to obtain the necessary parameters

which will eventually be used to simulate strong motion earthquakes further on in the study for the Corinth Gulf.

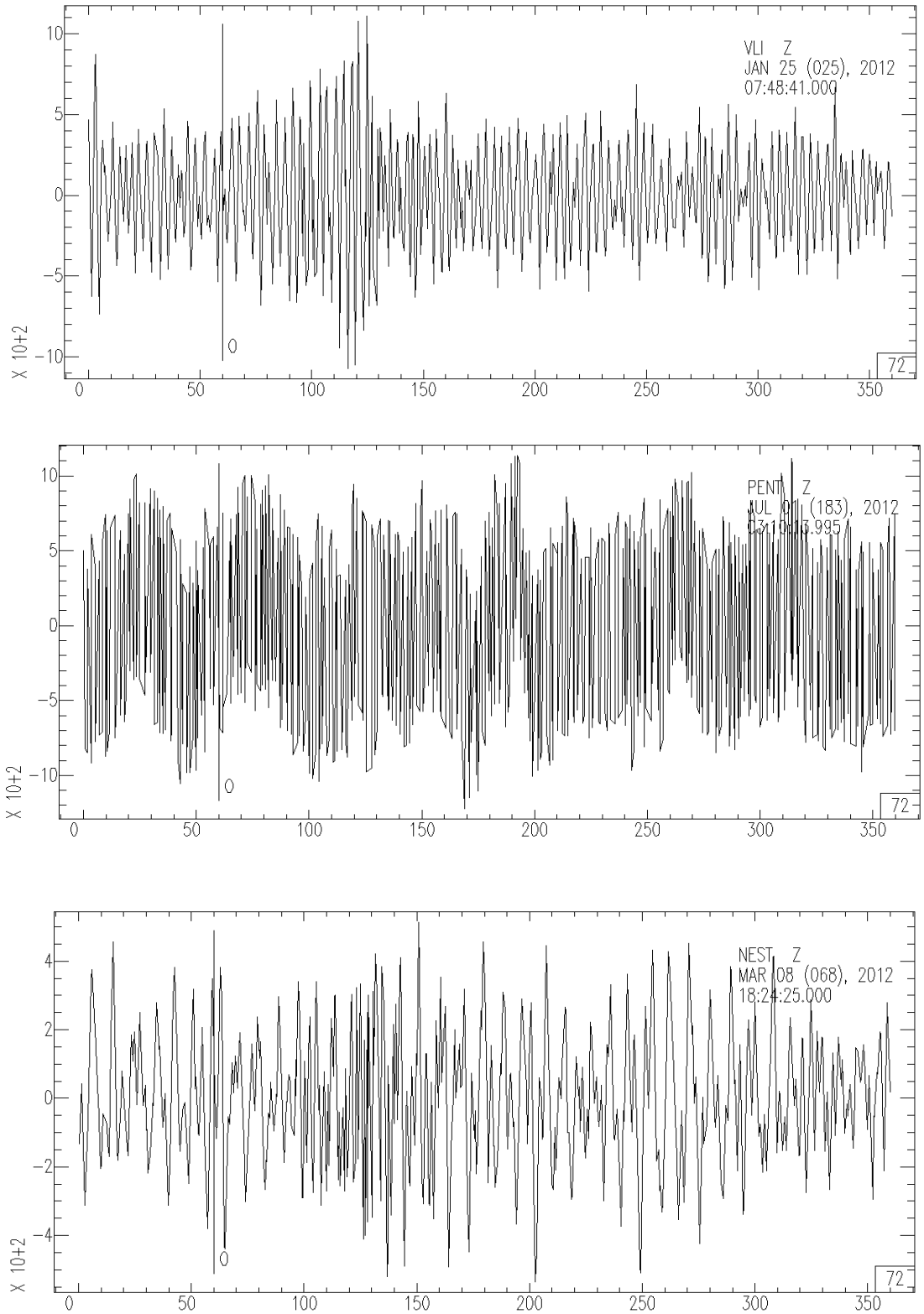

FIGURE 24: UNUSED WAVEFORMS WITH BACKGROUND NOISE FOR STATIONS PENT, VLI AND NEST

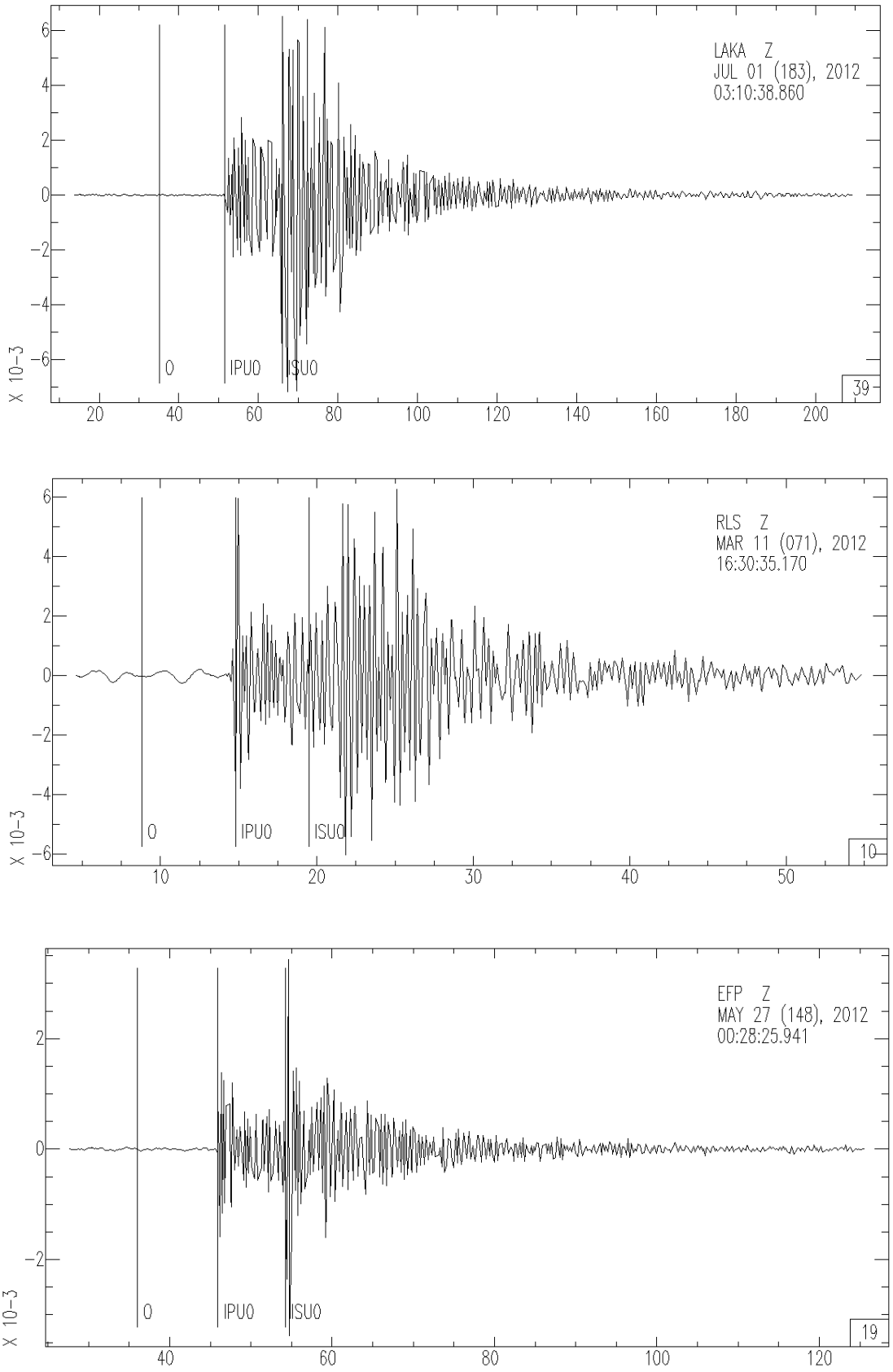

FIGURE 25: WAVEFORMS PICKED FOR P AND S WAVE ARRIVAL TIME FOR STATIONS LAKA, RLS AND EFP

Once P and S wave picking was complete, the necessary computer programmes were installed from the following link:

http://www.eas.slu.edu/eqc/eqc_cps/getzip.html

These programmes are used to process high frequency ground motion to define the propagation of high frequency S-waves. After installing and compiling the required programs, the directories were organised accordingly and using a script to install local projects, the maximum distance for regression (100km) and the maximum number of frequencies (mentioned in section 3.3.1) were entered. A background of basic knowledge on bash scripting was required to modify and create scripts accordingly for the procedure. Before starting the regressions, the sac headers were checked to see if all the information required was present. Figure 26 is a screenshot showing one example of a sac trace header for the station AMT.z. The meaning of the required information is listed within the SAC manual by Hermann (2013).

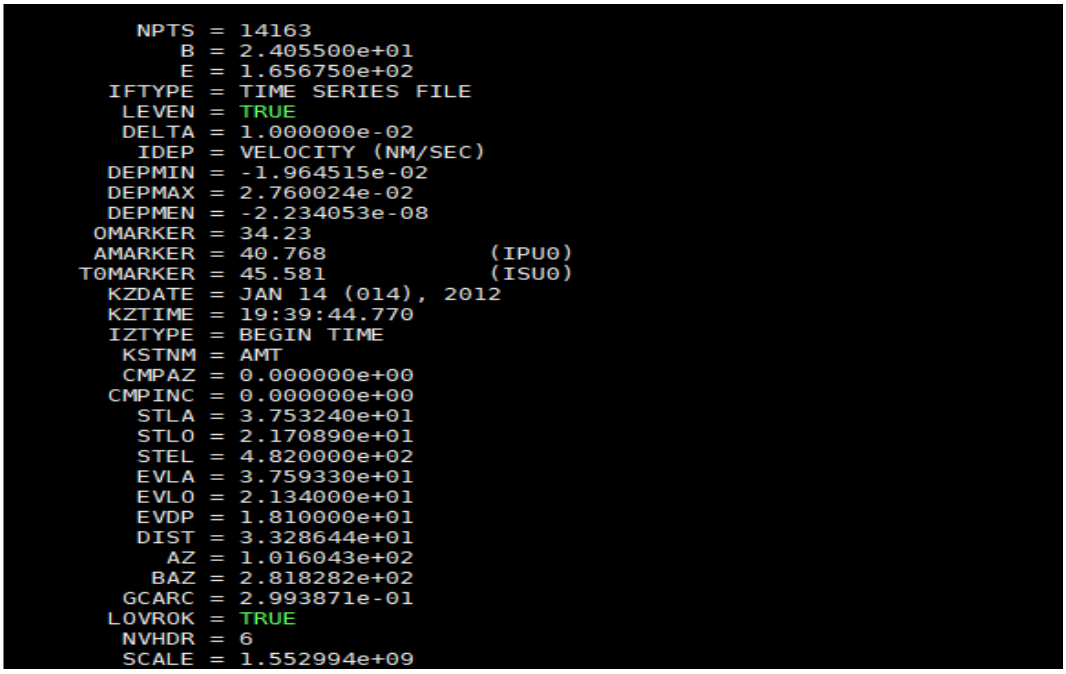

FIGURE 26: INFORMATION REQUIRED IN SAC TRACE HEADER SUCH AS EVENT LATITUDE AND LONGITUDE, THE TIME AND THE DATE OF THE EVENT.

One important description that was missing was the unique trace code to describe the ground motion components. This unique number is assigned to each of the 3 components belonging to every station used in the study. A total of 297 components were used for regressions. While allocating the unique trace code to the stations, the data was filtered through the use of Butterworth band pass filters at frequencies between 0.25 and 20Hz so as to remove instrument response. To do so, it is important to make sure that all poles and zeros of each event are acquired. Once this was done, data processing could then be carried out.

4.2. Data Processing

The next step was to create tables for each event which were then used for regressions. These were created using a script which initially defines the indices and unique frequencies for processing and then processes each of the components E, N and Z to create the required tables. Figure 27 is an example of one of these tables for the station DID for its E component.

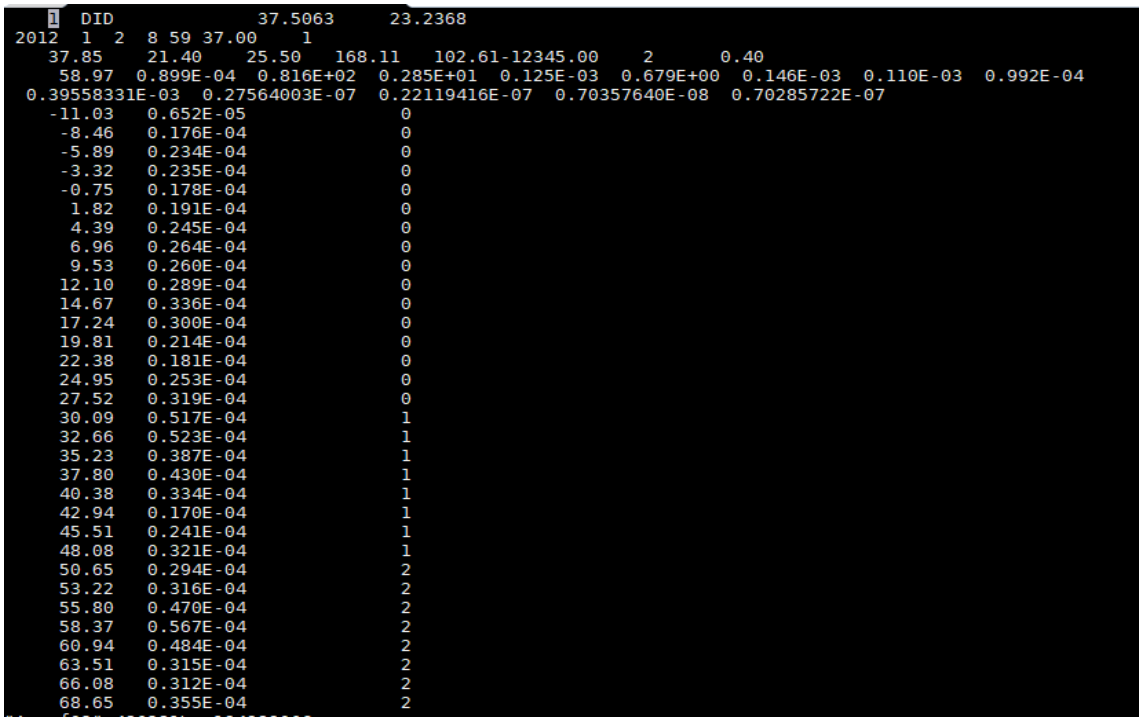

```
   1  DID             37.5063     23.2368
2012  1  2  8 59 37.00    1
   37.85    21.40    25.50   168.11   102.61-12345.00    2      0.40
    58.97  0.899E-04  0.816E+02  0.285E+01  0.125E-03  0.679E+00  0.146E-03  0.110E-03  0.992E-04
 0.39558331E-03  0.27564003E-07  0.22119416E-07  0.70357640E-08  0.70285722E-07
   -11.03   0.652E-05              0
    -8.46   0.176E-04              0
    -5.89   0.234E-04              0
    -3.32   0.235E-04              0
    -0.75   0.178E-04              0
     1.82   0.191E-04              0
     4.39   0.245E-04              0
     6.96   0.264E-04              0
     9.53   0.260E-04              0
    12.10   0.289E-04              0
    14.67   0.336E-04              0
    17.24   0.300E-04              0
    19.81   0.214E-04              0
    22.38   0.181E-04              0
    24.95   0.253E-04              0
    27.52   0.319E-04              0
    30.09   0.517E-04              1
    32.66   0.523E-04              1
    35.23   0.387E-04              1
    37.80   0.430E-04              1
    40.38   0.334E-04              1
    42.94   0.170E-04              1
    45.51   0.241E-04              1
    48.08   0.321E-04              1
    50.65   0.294E-04              2
    53.22   0.316E-04              2
    55.80   0.470E-04              2
    58.37   0.567E-04              2
    60.94   0.484E-04              2
    63.51   0.315E-04              2
    66.08   0.312E-04              2
    68.65   0.355E-04              2
```

FIGURE 27: THE INFORMATION DISPLAYED WITHIN THE TABLES CREATED SUCH INFORMATION ABOUT THE EVENT AND THE STATION RECORDING IT.

The first line gives the unique station code, the station character code, and its latitude and longitude. The second line indicates the year, month, day, hour, minute, second and a unique I.D to identify the event. The third line gives the event latitude and longitude, event depth, hypocentral distance from event to station, the azimuth, the event magnitude, the unique I.D for the filter frequency and the actual filter frequency. The fourth line specifies the following properties:

a. the time of peak amplitude
b. the peak filtered amplitude
c. duration of the peak motion
d. the velocity of the peak amplitude observation
e. the random vibration theory estimate of the peak amplitude
f. Frequency of zero crossings of peak signal
g. The 10% and 90% bounds on the estimated peak motion
h. Maximum amplitude of P arrival

The final line gives details on the Fourier velocity spectra of the signal within the duration window and the energy bounds, to estimate intrinsic and scattering attenuation. As for the columns, the first column gives information on the travel time of the window while the second column is the RMS amplitude. The final column is a code indicating whether the i envelope was before the P (primary wave) (0), between P and S (secondary wave) (1), between S and the stable code (2) and the stable code (3).

4.2.1. Regressions

Once all the required information and files are obtained, the next step is to regress the data to obtain the attenuation and the source term. A series of processing scripts are required to prepare the data accordingly for regression.

Initial processing produces duration estimates which are required to define the duration window from the signal. The distance dependent duration is found at each frequency and due to noise, an L2 algorithm is used to obtain the best fit. The derived distance relations are obtained and plotted graphically as shown in the figure 28. This plot is only used for diagnostic purposes.

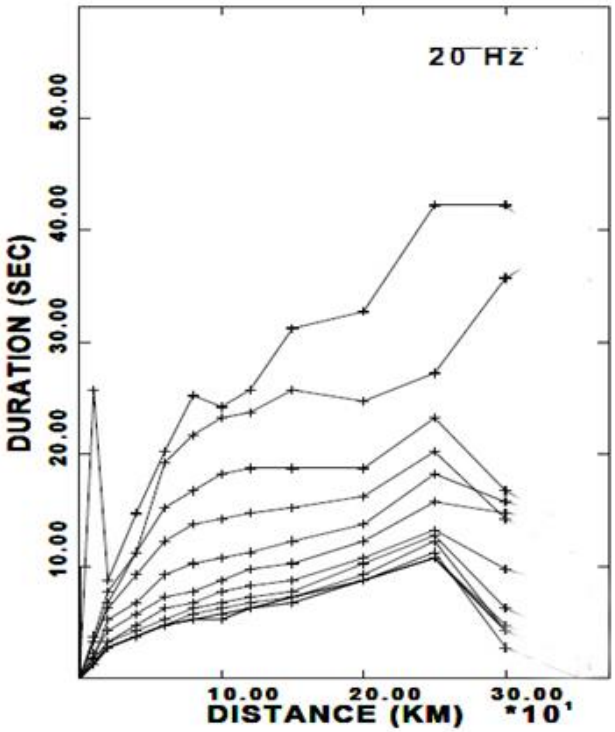

FIGURE 28: SUMMARY OF FREQUENCY DEPENDENT DURATION. EACH LINE INDICATES A DIFFERENT FREQUENCY WHICH ARE: 0.25, 0.40, 0.60, 0.85, 1.25, 1.75, 2.50, 3.50, 5.00, 7.00, 9.00, 12.50, 17.50 AND 20.00HZ.

As can be seen from Figure 28, the distance dependent duration starts to increase up to 250km. Then for some cases, the duration decreases slightly. The maximum frequency is 20Hz for this study. Figure 29 shows the durations for 0.25Hz, 0.85Hz, 7Hz and 20Hz. The circles are individual duration estimates for the seismic events. A quick glance at the plots indicates that for

frequencies below 0.85Hz, there is more scattering of the data while for 20Hz, data is more clustered. The durations, which are represented by the lines, increase up to a hypocentral distance of 300km, which is the maximum distance used in the data. This is similar as to what is depicted in Figure 28 above, which shows all the durations on one plot for each frequency used. The durations are also generally decreasing with increasing frequency range. The duration T(r) for these lines was plotted using the median values through the use of an L1 norm.

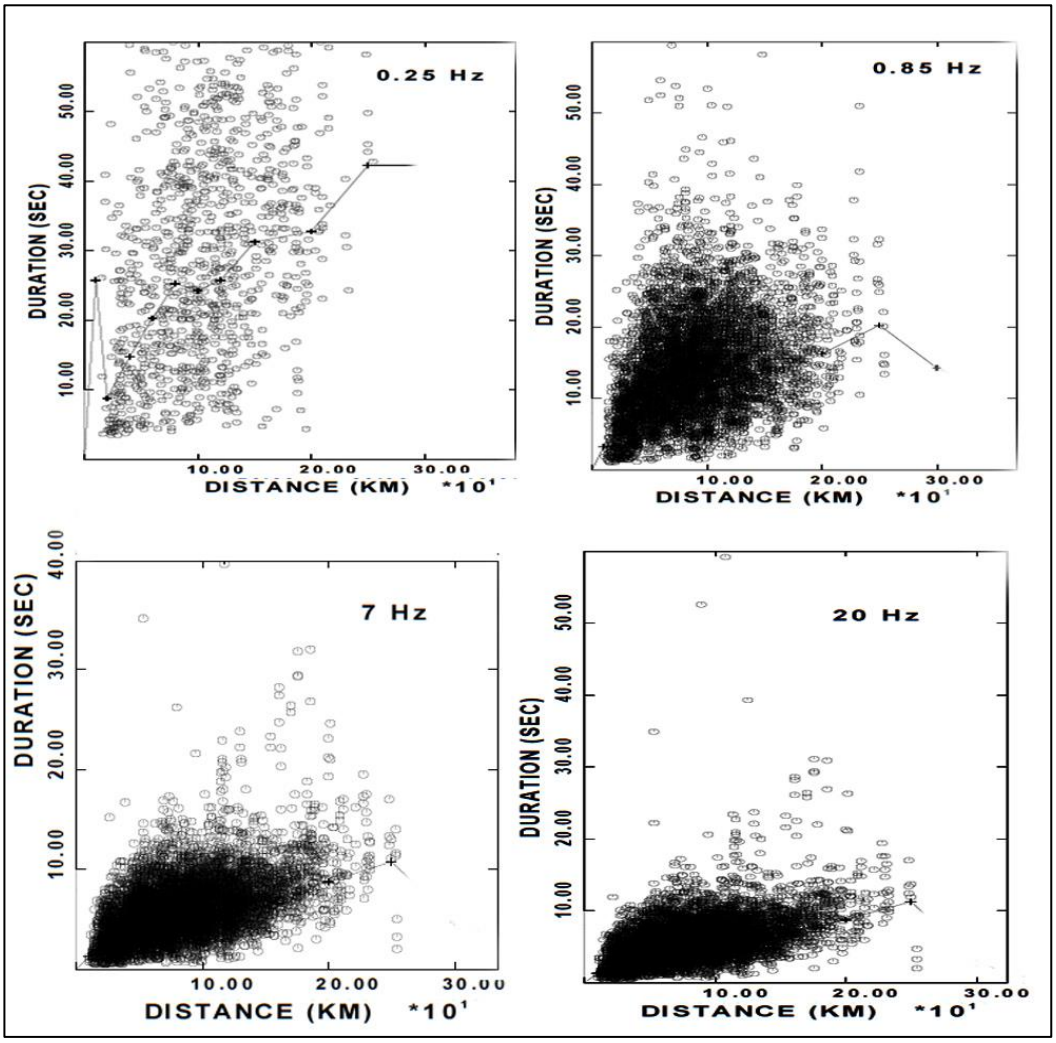

FIGURE 29: DURATIONS AT 0.25HZ, 0.85HZ, 7HZ AND 20HZ. THE CIRCLES INDICATE DURATION ESTIMATES FOR EACH INDIVIDUAL EVENT WHILE THE LINES REPRESENT THE DURATION MEASURED USING A MEDIAN VALUE METHOD.

The duration is subsequently defined in a series of plots created at each frequency. Figure 30 is an example of one such plot at the frequency of

1.25Hz. The numbers above each plot such as in the first one: 4592=1336+3172+84 show that there were 4592 observations of which 3172 fell within the 5-95% bounds, 1336 which were below and 84 which were above. A good data set requires more than 80% of the data to fall within the 5% to 95% bounds, as is the case with the data set used for this study.

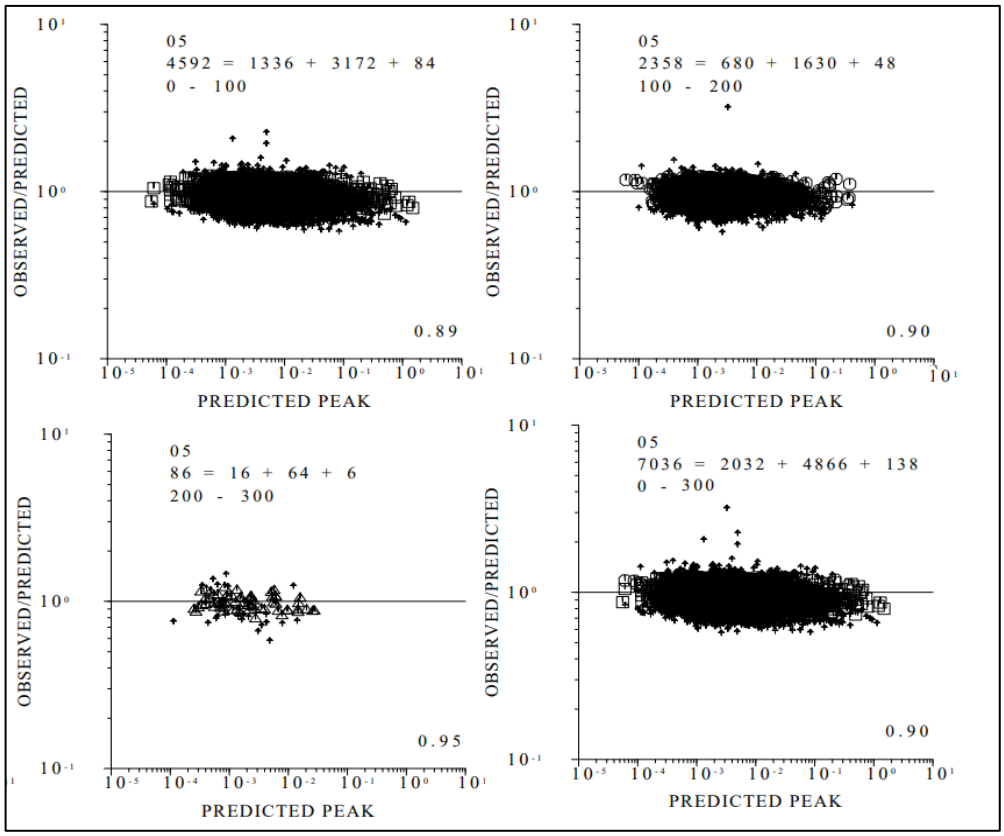

FIGURE 30: THE TEST FOR THE RANDOM VIBRATION THEORY. EACH PANEL REPRESENTS A DISTANCE RANGE FROM 0 UP TO 300KM, WHILST THE FOURTH PANEL (BOTTOM RIGHT) IS A COMPILATION OF ALL DISTANCES. THE HORIZONTAL AXIS GIVES THE ACTUAL AMPLITUDE, WITH SCATTER EXPECTED AT LOWER AMPLITUDE SIGNALS. THE NUMBERS ON EACH PLOT SUCH AS 4592=1336+3172+84, INDICATE THAT THERE WAS A TOTAL OF 4592 OBSERVATIONS, OF WHICH 3172 FELL INTO THE 5-95% BOUNDS ON THE PREDICTION, 1336 WERE BELOW AND 84 WERE ABOVE. A GOOD DATA SET REQUIRES AROUND 80% OF THE DATA TO FALL WITHIN THE 5-95% BOUNDS (OBSERVATION VS. PREDICTION), AS IS IN THE CASE FOR THE DATA SET FOR THE CORINTH GULF.

The next step was to obtain the regression results for the propagation term D(r). In Figure 31, which compares frequencies of 0.4Hz (left) and 12.50Hz (right), the top panels show the D(r,f) term using the coda normalization technique. This provides an independent estimate of D(r,f) not influenced from instrument response or unknown site and source effects. The amplitude of the

peak motion is divided by the coda level and accounts for instrument gain, source excitation and site amplification effects (Aki, 1980). The red line indicating the coda represents the attenuation functional computed by linear interpretation between each nodal point. The middle panels make a comparison between the regression in distance (in blue) and the coda (in red). The results are not completely linear for 0.4Hz but are in good agreement for 12.50Hz, except for distances larger than 100km where they deviate slightly. The bottom panels then show the final residuals as a function of distance. After obtaining these results, the 3-component propagation term D(r) is attained from the regression of the Fourier velocity data at the frequencies chosen. This is the observed attenuation from the data provided as shown in Figure 32.

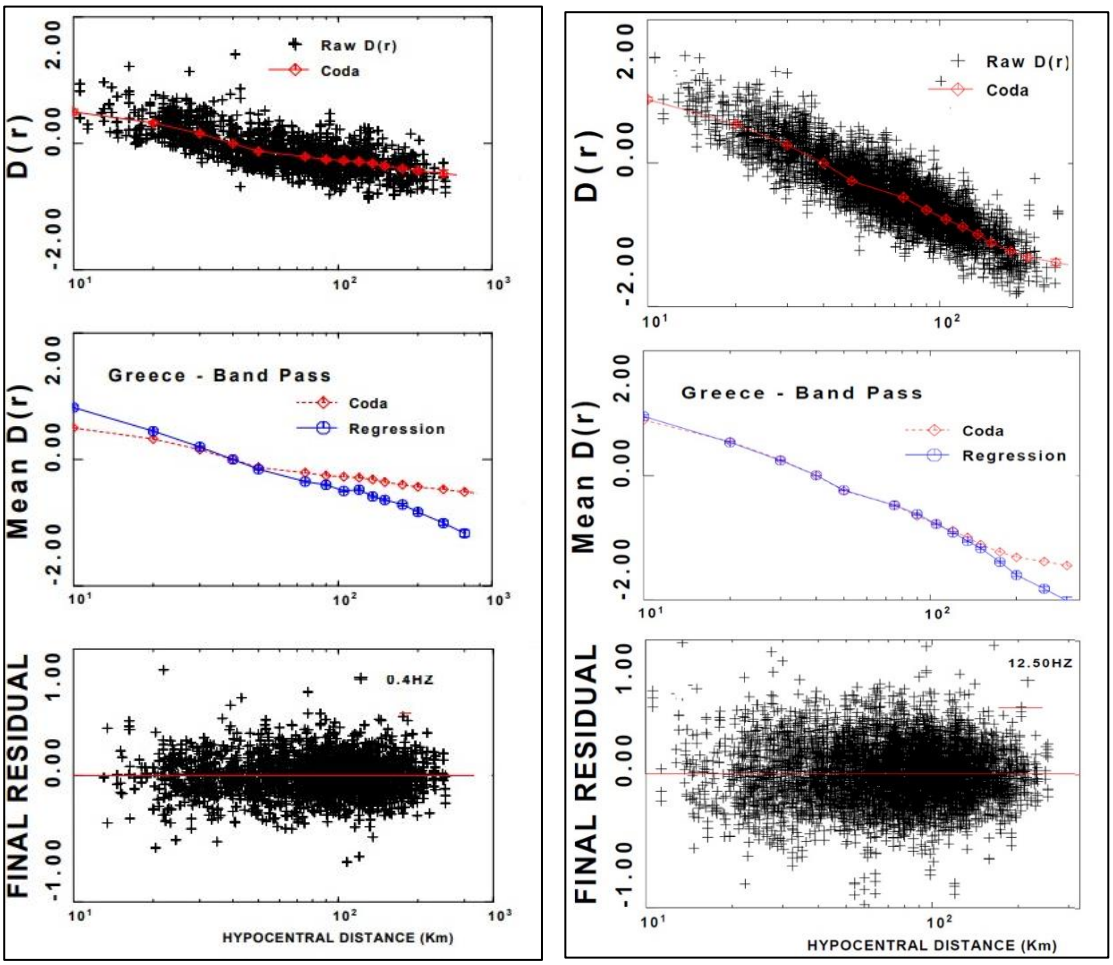

FIGURE 31: REGRESSION RESULTS FOR FOURIER VELOCITY DATA AT 0.4HZ (LEFT) AND 12.50HZ (RIGHT). THE TOP PANELS SHOW THE D(R,F) TERM USING CODA NORMALIZATION. THE MIDDLE PANELS SHOW THE COMPARISON BETWEEN REGRESSION IN DISTANCE (BLUE) AND CODA (RED). THE BOTTOM PANELS INDICATE THE FINAL RESIDUALS AS A FUNCTION OF DISTANCE.

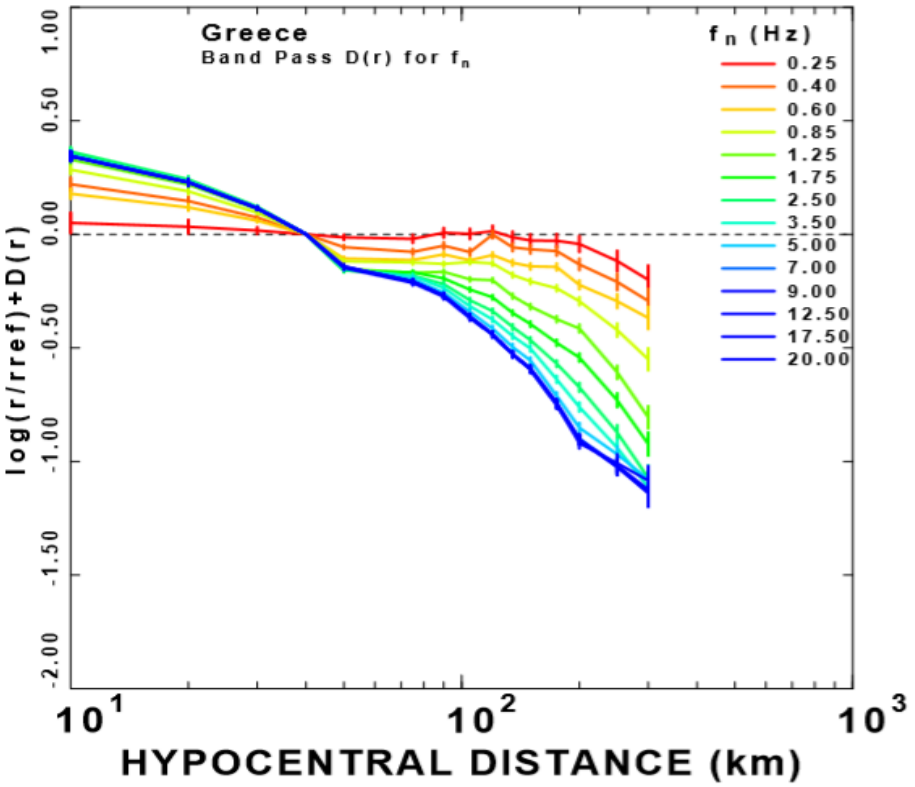

FIGURE 32: THE EMPIRICAL REGIONAL ATTENUATION FUNCTIONAL D(R,F) FOR 3 COMPONENT FOURIER VELOCITY SPECTRAS (COLOURED LINES) AS OBTAINED FROM THE REGRESSION OF DATA FOR FREQUENCIES 0.25, 0.40, 0.60, 0.85, 1.25, 1.75, 2.50, 3.50, 5.00, 7.00, 9.00, 12.50, 17.50 AND 20.00HZ

4.3. Results

4.3.1. Modelling Propagation and source parameters

For modelling the resulting propagation terms, forward modelling was used to estimate the g(r), Q(f) and the κ_{eff}. The below functions and values were obtained through trial and error by comparing the observed and predicted models together for the attenuation and geometrical spreading. κ_{eff} was suggested to be 0.030 sec with the following attenuation terms:

$$Q(f) = 160\left(\frac{f}{f_{ref}}\right)^{0.50}$$

The geometrical spreading was estimated to be a five-segment function as below:

$$g(r) = \begin{cases} r^{-1.2} & r < 30km \\ r^{-0.9} & 30 < r < 50km \\ r^{-1.0} & 50 < r < 80km \\ r^{-0.5} & 80 < r < 100km \\ r^{-0.7} & r > 100km \end{cases}$$

The figure below plotted regional attenuation functional showing the theoretical estimates in black lines.

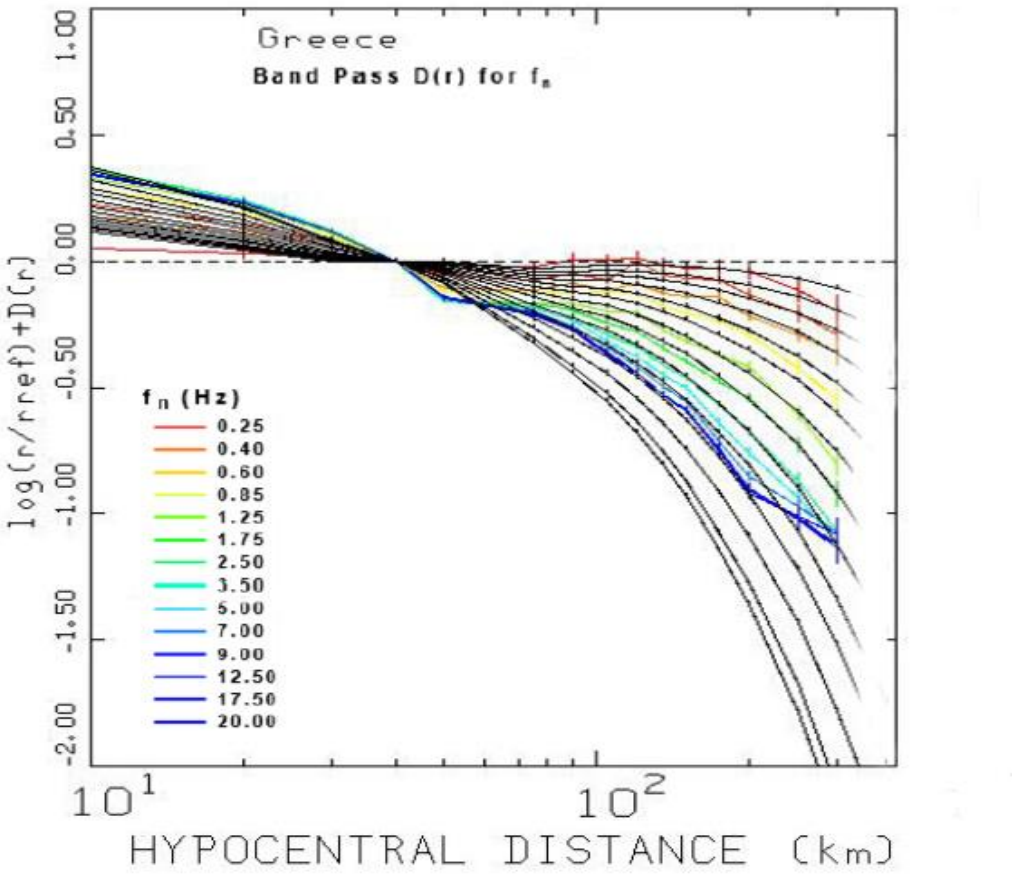

FIGURE 33: THE REGIONAL ATTENUATION FUNCTIONAL FROM THE REGRESSIONS OBTAINED FOR THE GULF OF CORINTH AT THE SAMPLING FREQUENCIES 0.25, 0.40, 0.60, 0.85, 1.25, 1.75, 2.50, 3.50, 5.00, 7.00, 9.00, 12.50, 17.50 AND 20.00HZ. THE BLACK LINES ARE THE THEORETICAL ESTIMATES OF THE REGIONAL ATTENUATION OBTAINED FROM THE EMPIRICAL D(R,F) FUNCTION ,THAT IS NORMALIZED TO ZERO AT THE CHOSEN REFERENCE HYPOCENTRAL DISTANCE OF 40 KM. THE DASHED LINE INDICATES AN ATTENUATION ∝ 1/R

It should be noted that for the empirical curve for the frequency of 20Hz, the curve seems to be departing from the predicted trend at approximately 210km. The attenuation value of 160 also indicates a high attenuation in the Corinth Gulf and this parameter has to be considered in the seismic hazard evaluation which is affected mostly by local seismicity. The results also suggest spherical spreading loss up to 80km and cylindrical spreading loss above 80km. The predicted and observed excitation terms are then plotted for the moment magnitudes ranging between 2.5 and 4.5 using Brune's spectral model together with the regional attenuation and site term for the Corinth Gulf. Further details on the excitation and the stress drop can be found in section 4.3.2. using the regional attenuation terms, the site term, and Brune's spectral model as explained in the previous chapter. The excitation of the peak filtered velocity represents the average expected level of ground motion at a reference distance of 40 km. To compute these, the density value used is $2.8 g/cm^3$ whilst the shear wave velocity is $3.7 km/sec$. Kappa, or $\boldsymbol{\kappa_{eff}}$, is a high frequency filter which is defined through the attenuation term and controls the high frequency content of the spectrum for small magnitude earthquakes. It is important to calibrate the stress drop and kappa values. This is because a trade-off exists between the two and the values chosen can affect simulations later on (D'Amico et al., 2018). For all the events in the study, the excitation terms for magnitudes between Mw = 2.5 and 4.5 are compared to estimates found by applying the RVT. Theoretical source terms are represented by the red curves for different magnitudes whilst the green curves represent the observed data. The stress drop was calibrated to be about 200bars for a rock site with the generic rock site amplification factor V(f) of 1 (site class A). Table 4 shows the

spectral source parameters applied for modelling the source term in the Corinth Gulf. Kappa was obtained through trial and error and the value of 0.030sec is typical of generic rock sites which usually have values between 0.02 and 0.05secs (Van Houtte, Drouet and Cotton, 2011). For each station used in the study, the frequency dependent coda site term was produced from the regression results using the 3-components. In Figure 34, the coda site term for station VLX can be observed.

TABLE 4: SPECTRAL PARAMETERS FOR CORINTH GULF TO OBTAIN EXCITATION TERMS

Parameter	Numerical Value
ρ	$2.8 g/cm^3$
β	$3.7 km/sec$
$\Delta\sigma$	$200 bars$
κ_{eff}	$0.030 sec$
fc	$4.9\text{x}106\beta(\frac{\Delta\sigma}{M0})^{1/3} Hz$

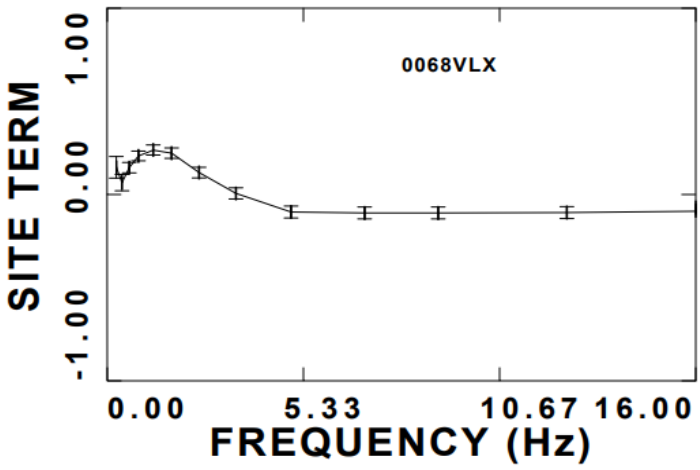

FIGURE 34: THE FREQUENCY DEPENDENT CODA SITE TERM FOR 3-COMPONENTS FOR STATION VLX

The stress drop that describes the excitation term through this procedure might be inadequate to describe larger events. Therefore, it is necessary to include the possibility of whether earthquake source scaling is self-similar (same stress drop for all magnitudes) or not. In the case that it is not self-similar, the stress parameter is quantified as a function of magnitude. This shall be done in the next procedure.

4.3.2. Calibrating and computing stress drop manually

The stress drop is an essential and crucial parameter to take into account in order to properly characterise the source of a given earthquake. It is also important for performing simulations and to understand the energy released during an event. Indeed, the stress drop parameter relates to regional earthquakes and how it can vary with magnitude. This parameter (computed as a function of magnitude) is required to obtain reliable simulations for large magnitude events for the Corinth Gulf and has a valid and robust set of results to be coupled and/or compared with the ground motion prediction equations derived in the broader area. The stress parameter is important to obtain as it controls the amplitude of high frequency radiation. Once the moment magnitude is calculated for each event, the corner frequency is then required by computing the Fourier amplitude spectra in displacement. For this procedure, 16 events were used ranging from a magnitude of 3.0 up to a magnitude of 5.3, an event which occurred on the 30th of March 2019 nearby the Corinth Gulf. The events recorded at each station were analysed to produce Fourier amplitude spectra using the set of programmes gsac.

Though this procedure, graphs similar to those in Figures 35 and 36 were produced for each seismogram. From those, a manual estimate of the corner

frequency could be obtained as shown in the figures. Figure 35 is for a small event of magnitude 3.9 whilst Figure 36 indicates a larger but moderate event with magnitude 5.3. The difference between the two is quite clear but as expected, events larger than a magnitude of 5 usually have a corner frequency that is less than 1Hz (Allman and Shearer, 2009). Once the corner frequency is obtained, the radius of the event is calculated using equation 37 whilst the stress drop is calculated using equation 33 in bars. Since the stations were grouped for every event, a final average could then be obtained for each of them.

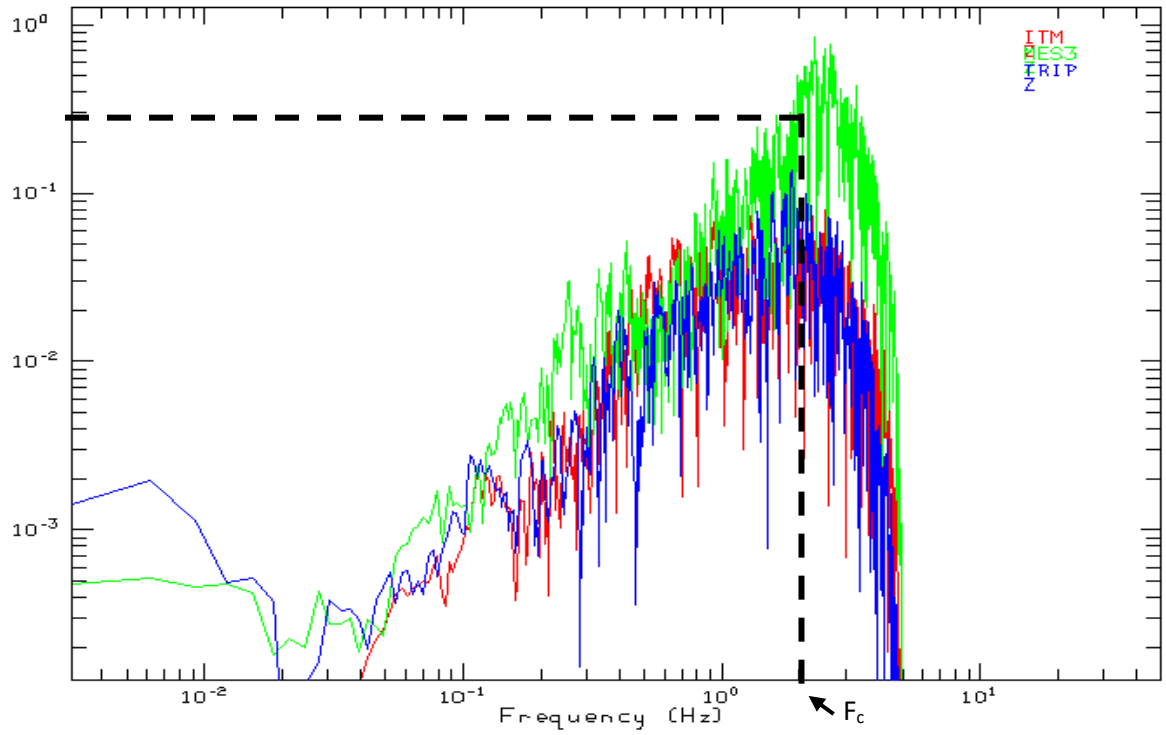

FIGURE 35: THE FOURIER AMPLITUDE SPECTRA IN DISPLACEMENT FOR THE EVENT OF MAGNITUDE 3.9. THE INTERSECTION BETWEEN THE FLAT AND THE FALL OF THE SLOPE IS THE ESTIMATION OF THE CORNER FREQUENCY, WHICH IN THIS CASE IS ESTIMATED TO BE 2.0HZ.

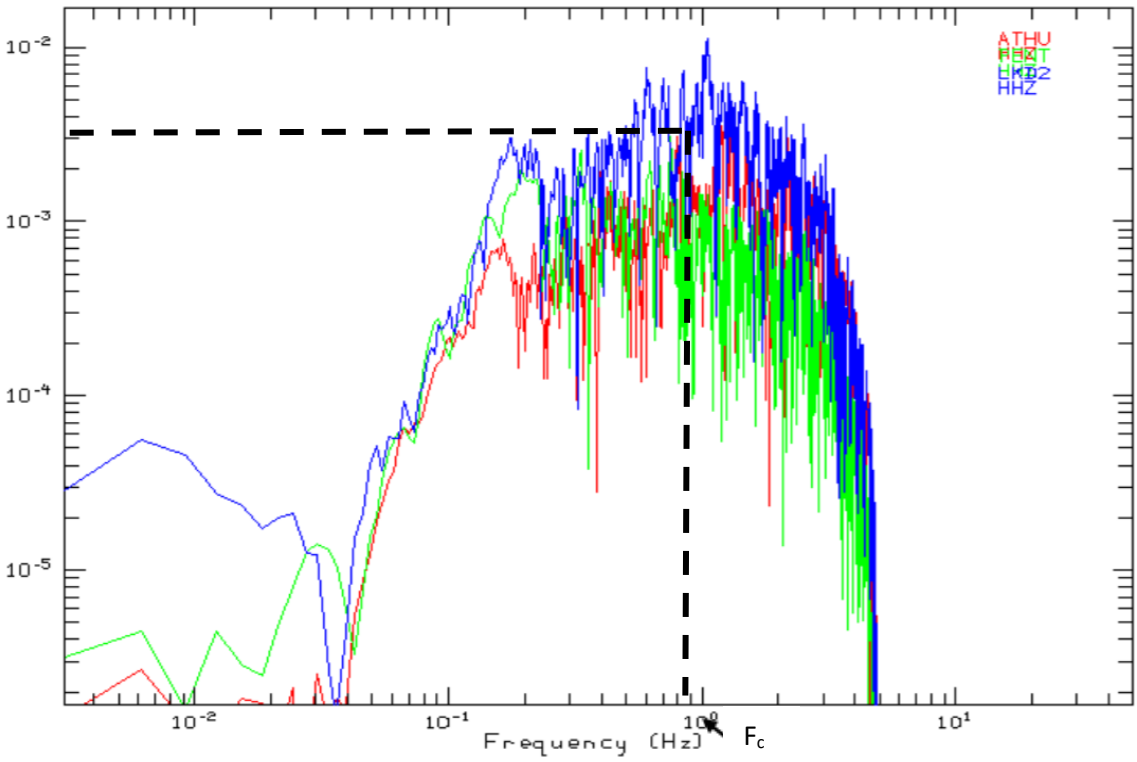

FIGURE 36: THE FOURIER AMPLITUDE SPECTRA IN DISPLACEMENT FOR THE EVENT OF MAGNITUDE 5.3. AS EXPECTED THE VALUE FOR THE CORNER FREQUENCY IS LESS THAN 1HZ. FOR THIS EVENT, IT IS APPROXIMATELY BETWEEN 0.8-1HZ.

The obtained stress drops are then plotted as a linear graph to obtain a function of stress drop against magnitude resulting in the plot below.

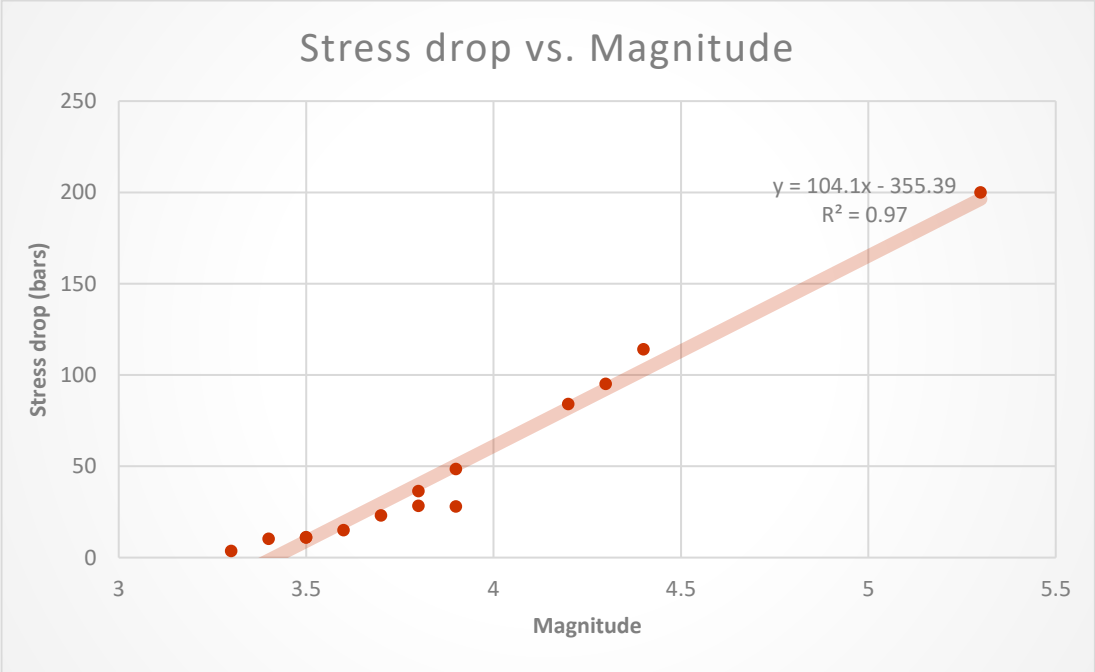

FIGURE 37: A GRAPH SHOWING THE FUNCTION OF STRESS DROP AGAINST MAGNITUDE

The obtained equation $y = 104.1x - 355.39$ is a predictive equation to estimate relationship between stress drop as a function of magnitude. The value of R^2, also known as the coefficient of determination, also indicates this goodness of fit. A value of 0.97 indicates that it would predict 97% of the data fit in the regression model. Whilst this method is quick and requires few programming to obtain stress drop, one disadvantage is that the exact corner frequency value could vary depending on the reading and peaking performed by the operator. A slight change in frequency makes a large difference in the stress. As Cotton et al. (2013) state, measuring corner frequency is difficult and leads to an overestimation of the stress drop. Using the simulations obtained from EXSIM in the following procedure, these values will be verified with the simulated stress drop to obtain a much better linear relationship of stress and magnitude.

4.3.3. Evaluating PGA and PGV through simulation procedures: the EXSIM programme

In Boore's (2003) paper on stochastic modelling, the stochastic method is described as a method that is used to obtain simulated ground motions by distributing the earthquake motion over a duration that is associated with the distance from the source and the earthquake magnitude, as well as considering the relevant source parameters. The EXSIM is mostly used to simulate high-frequency ground motions with frequencies greater than 0.1Hz (D'Amico et al., 2012; 2018), which is ideal for the research being done for this thesis. Being stochastic, the distribution can be described as having a random probability distribution or a pattern which can be statistically evaluated by not necessarily precisely calculated, and high frequency events have been

observed to exhibit this stochastic behaviour due to earth's heterogeneity (Assatourians, 2008). As described previously in section 3.3.5, the commonest approach to the stochastic method is to subdivide a large fault into smaller faults with each one being treated as a point source. Summing up the contributions of all the sub sources, which are treated as stochastic point sources, will obtain the ground motion at the observation point (Schneider, Silva and Stark, 1993; Hartzell, 1978). The stochastic approach is characterized by various advantages such as providing a simplified representation of the source, path and site effects in context of random noise, and is quick and easy to apply. Despite that it may provide the solutions to difficult problems sooner than the deterministic approach, it does not provide a detailed representation (Aki, 1989; Assatourians, 2008).

Both SMSIM (previous version) and EXSIM have been used for previous studies based on the stochastic approach (see section 3.3.5.), with the former being used for point source and the latter used for finite-faulting (Hartzell, 1978). Atkinson et al. (2009) highlights the 3 main differences between the two programmes related to the source geometry, the definition and application of duration, and how the finite-source and sub-source summations are normalized. In SMSIM, the geometry is a point, with the distance from the source being the hypocentral distance, whilst for EXSIM the geometry is a plane and the distance from observation point depends on the location of the sub-source. At larger distances, the measures for both programmes will be similar. With regards to duration, in SMSIM it is the source duration based on the corner frequency, but using EXSIM with the presence of sub-sources, the duration is the time required for rupture along the length of the fault, including

the ruptures of sub-sources, and the arrival time is delayed when arriving at the observation point. Lastly, one important difference is in the stress drop parameter which comes directly from Brune's model in SMSIM for a given stress parameter. In EXSIM, things get more complicated and the stress drop can be different for each sub-source, therefore a summation of all sub-sources is required based on an algorithm which normalizes high-frequency spectra. Boore (2009) did some modifications to EXSIM so that both programmes can give similar results as explained in section 3.3.5.

In EXSIM, Brune's ω^2 model is used to describe the source effect while an empirical attenuation and duration model describe path effects together with the use of the dynamic corner frequency, a concept introduced by Motazedian (2002) whilst using this concept to adapt the previous programme FINSIM (Motazedian, 2002). Here the corner frequency becomes a parameter that controls the spectral shape whilst being a function of time (Motazedian and Atkinson, 2005). The different simulations produced by EXSIM and FINSIM can be observed in Figure 38. With the dynamic corner frequency, the frequency content of the simulated time series for each of the sub faults is controlled by the rupture history and it is noted that as rupture area grows, the corner frequency becomes lower (Yalcinkaya et al., 2012). The introduction of the dynamic corner frequency in EXSIM provided various advantages over its previous antecedent FINSIM. The methodology could be applied to a broader magnitude range whilst conserving moment and radiated energy of each sub-fault, independently of the sub-fault size. It also helped in developing ground motion relations in countries with insufficient data to be used for other existing models (Motazedian and Atkinson, 2005).

Being a stochastic model, EXSIM assumes that the rupture propagation from sub-fault to sub-fault mimics the overall directivity effect and assigns a uniform stress parameter to all sub-sources. A directivity effect occurs when the rupture duration time changes as a function of receiver location (Shearer, 2009). This results in the ground motion in the rupture propagation direction to be more dangerous in other areas away from the earthquake source. This latter problem was addressed by Assatourians and Atkinson (2007) by modifying the code in EXSIM to include variable stress parameters to include areas of high stress or asperities. This was done by multiplying the radiated source spectrum with the portion of low frequency of the spectrum whilst multiplying the other portion of the high frequency by a constant that is proportional to the stress parameter for each sub-fault raised to the power of $\frac{2}{3}$, according to Brune's source model.

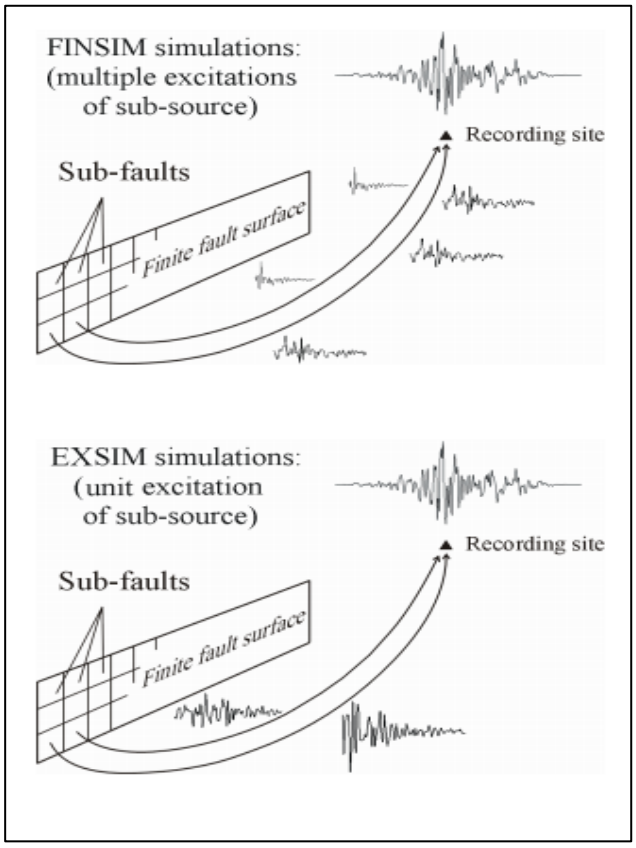

FIGURE 38: FINSIM (TOP) AND EXSIM (BOTTOM) SIMULATIONS BY SUB-DIVIDING A FAULT INTO SUB-SOURCES AND SUMMING THEM IN THE TIME DOMAIN.
SOURCE: ASSATOURIANS, 2008

Using Motazedian and Atkinson's (2005) methodology that is established upon the dynamic corner frequency approach, the corner frequency for the first sub-fault is as follows:

$$f_{011} = 4.9E + 6\beta \left(\frac{\Delta\sigma}{M_{011}}\right)^{1/3} \quad (41)$$

where M_{011} is the seismic moment of the first sub-fault, $\Delta\sigma$ is the stress drop (calculated in bars), β represents the shear-wave velocity (in km/sec) and E is the total radiated energy at high frequencies for the whole fault. The corner frequency for the ith sub-source (f_{ci}) can also be expressed as a function of the cumulative number of sub-sources:

$$f_{ci} = 4.9\ x\ 10^{6}\beta \left(\frac{N \times \Delta\sigma}{N_R \times M_0}\right)^{1/3} \quad (42)$$

where N is the total number of sub-sources and N_R is the total number of active sub-sources when the ith sub-souce is activated. To calculate the entire seismic signal at the area under study, the normalization factor H_{ij} is required to conserve high frequency amplitudes. Following an error that was indicated by Atkinson et al. (2009), the equation based on the velocity spectrum is as follows:

$$H_{ij} = \left(\frac{N \sum\{f/[1+\left(\frac{f}{f_0}\right)^2]\}^2}{\sum\{f/[1+\left(\frac{f}{f_{0ij}}\right)^2]\}^2}\right)^{1/2} \quad (43)$$

Where f_0 is the corner frequency of the whole event and f_{0i} being the corner frequency of the ith sub-source. The delayed sub-source contributions, which are properly normalized, are summated in the time domain as:

$$Acc_{tot}(t) = \sum_{i=1}^{N} H_i \times Acc(t - \Delta t_i - T_i) \quad (44)$$

where $Acc_{tot}(t)$ is the total seismic signal at the site, H_i is the normalization factor, $Acc\ (t)$is the signal of the i[th] sub-source activation, Δt_i is the delay time of the subsource while $T_i$is the fraction of rise time.

The source spectrum, propagation term and site amplification terms are the products which are used to calculate the Fourier acceleration spectrum of the ground from a source moment M_o at the distance r:

$$A(f, f, M) = S(f, M)\ \cdot G(r, f) \cdot Site\ (f) \quad (45)$$

For the source parameter, the fault is modelled with dimensions in kilometres, an azimuth and a dip as a rectangular plane, while the high frequency energy from the source depends on the stress parameter (Atkinson and Assatourians, 2014). For the propagation of the ground motion, EXSIM uses a multi-segment geometrical spreading function for which the number of segments, distance ranges of the segments (kilometres) and the exponents of R must be inputted. The anelastic attenuation is also inputted and has the form of:

$$Q(f) = \max\ (Q_{min}, Q_0 f_{\eta}) \quad (46)$$

For this equation, Q_{min}, Q_0 and η are specified by the user. Finally, the site response is modelled using 2 frequency dependent functions. One is the crustal and site amplification function which occurs due to the regional velocity gradient and amplification caused by the near-surface materials at the site (Boore and Joyner, 1997). The second function is a high cut filter function that can model the effects of kappa on fmax (Hanks, 1982). It is the final model

that uses all these 3 parameters which can be applied for seismic hazard mapping to improve engineering designs as well as to implement ShakeMap®.

EXSIM was used for this research project to obtain simulated PGA and PGV using inputted parameters obtained for site, path, and source effects. This approach aims to show that it is possible to obtain good and reliable values of PGA and PGV which can be used for planning and hazard/risk studies. In this study, the site class A is used for hard rock sites whilst the constraint in equation 20 applies this into the programme used. Values for selected events of different magnitudes ranging from 3.3 to 5.3 for the Corinth Gulf were simulated and compared with real data. The PGA and PGV of observed events are required to compare with the simulations. For PGV, this is done by using sac and reading the events individually. The sac header DEPMAX as in Figure 39 (marked in red box) in the following page is an indication for the value that represents PGV. The values for DEPMAX are converted to cm/sec to compare with the output simulations from EXSIM. Once the PGV from observed events is obtained, the PGA is acquired by differentiating the sac file.

As with PGV, DEPMAX indicates the value for PGA once converted to cm/sec^2 as in Figure 40 for AXAR.z. This process is repeated for selected stations that had waveforms with the least background noise, and for stations closest to the selected events. The events selected were also chosen to be of different magnitudes which include magnitude 3.3, 3.6, 3.8, 4.2, 4.3 and 5.3. EXSIM is then used to obtain simulated PGV and PGA. It is important to input the parameters obtained for propagation, site and source parameters in section 4.3.1 which include the geometrical spreading (g(r)), the frequency dependent attenuation function Q(f) and the high frequency decay parameter κ_{eff}.

Table 5 lists some of the parameters used for the processing in EXSIM. The fault strike and dip, and stress parameter are event dependent and were changed accordingly. The table shows the parameters used for the Magnitude 5.3 event. The file used for processing is chosen to be that used for Site A classification that was applied for rock sites. The stress drop used initially is the one obtained manually for each of the selected events as in section 4.3.2. Varying the stress parameter, repeated EXSIM simulations are produced until the simulated PGA and PGV are similar to the observed values.

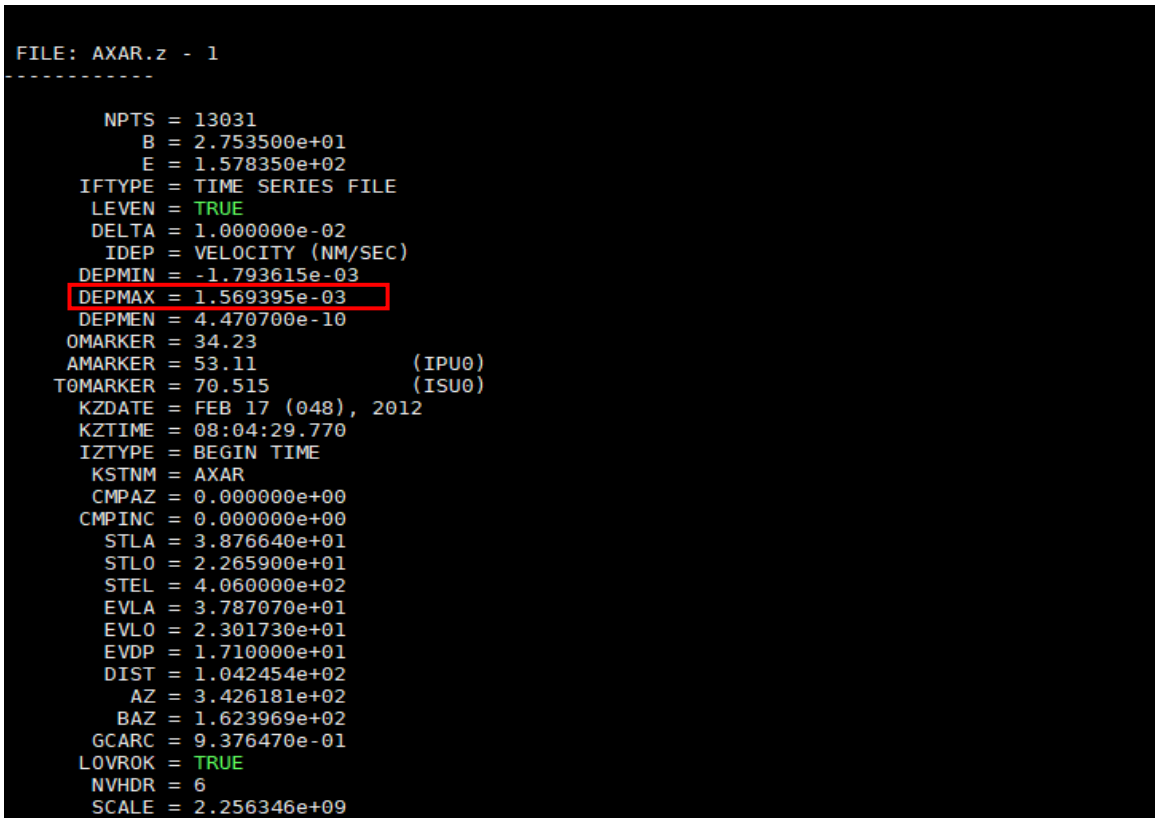

FIGURE 39: DEPMAX SAC HEADER USED TO OBTAIN VALUE FOR OBSERVED PGV

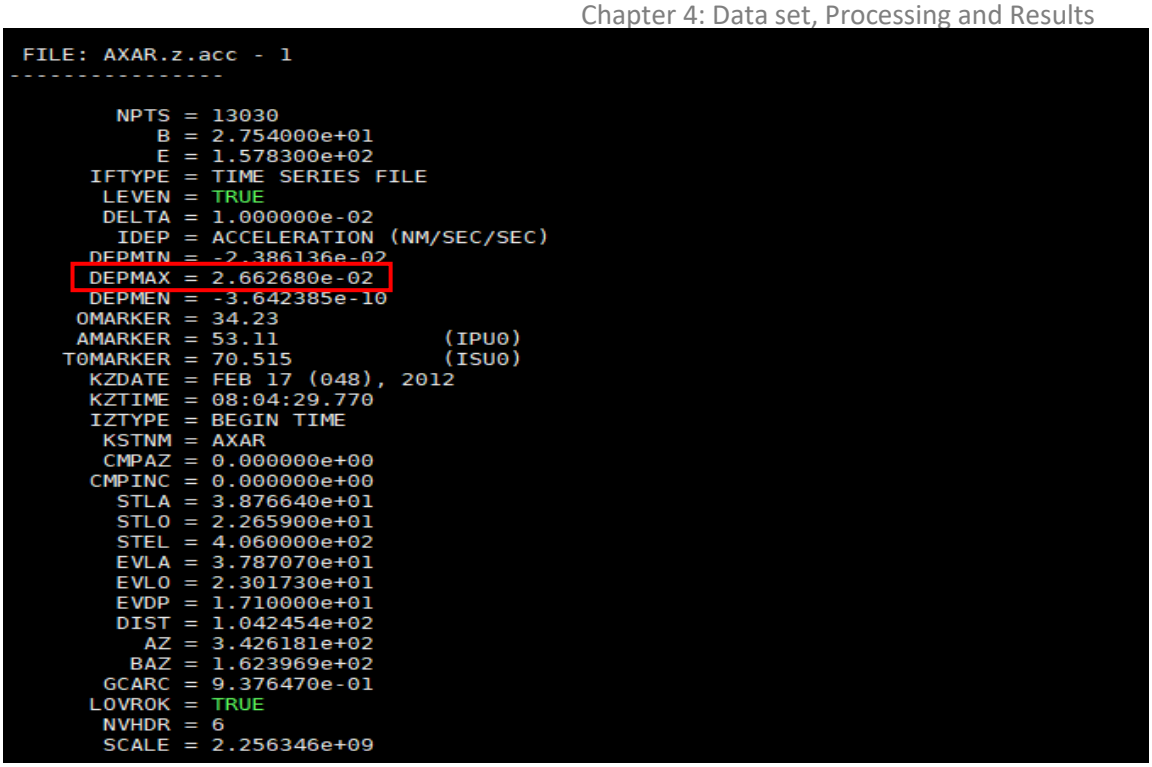

FIGURE 40: DEPMAX SAC HEADER USED TO OBTAIN VALUE FOR OBSERVED PGA

The impact of the stress parameter on the PGA values changes with the frequency and magnitude due to the effect of the corner frequency on the source spectrum (Atkinson and Boore, 2006). Together with the stress drop, the latitude and longitude of the event are required together with its depth, strike and dip angles. The density and shear wave velocity as obtained in section 4.3.1 are also inputted. Finally, the co-ordinates of the stations that will be used for processing are inputted lastly together with the number of stations used. These coordinates are the same as the coordinates for which there was observed data available.

TABLE 5: THE PARAMETER VALUES IN EXSIM TO OBTAIN SIMULATIONS FOR THE MAGNITUDE 5.3 EVENT

PARAMETER	PARAMETER VALUE
SHEAR WAVE VELOCITY	3.7km/sec
DENSITY	2.8g/cm^3
STRESS PARAMETER	180bars
KAPPA	0.030
GEOMETRICAL SPREADING	$g(r) = \begin{cases} r^{-1.2} & r < 30km \\ r^{-0.9} & 30 < r < 50km \\ r^{-1.0} & 50 < r < 80km \\ r^{-0.5} & 80 < r < 100km \\ r^{-0.7} & r > 100km \end{cases}$
QUALITY FACTOR	160
FAULT STRIKE AND DIP	95° and 68°
AMPLIFICATION FACTOR	Generic rock site
ɳ	0.50

EXSIM then simulates PGV and PGA according to the inputted parameters and these values are outputted in a file that produces the output as in Figure 41, which is showing an earthquake event that has a magnitude of 4.2. Viewing this file obtains the output below, which lists the station coordinates as well as the simulated PGV as psa-1.00 and simulated PGA as psa99.00 marked within the red boxes in the below figure. For this event, 10 stations with the least noise and as close to the event as possible were selected for processing.

isite	sitecoord(1)	sitecoord(2)	isitecoordflag	site_lat_degrees	site_lon_degrees	d_jb	d_cd2f	freq	psa-1.00	freq	psa99.00
1	38.766	22.659	1	38.766	22.659	104.30	105.69	-1.000E+00	5.195E-02	.900E+01	1.495E+00
2	37.974	23.718	1	37.974	23.718	61.82	64.14	-1.000E+00	1.505E-01	.900E+01	6.412E+00
3	37.506	23.237	1	37.506	23.237	42.95	46.81	-1.000E+00	2.711E-01	.900E+01	1.199E+01
4	38.078	23.933	1	38.078	23.933	83.02	84.76	-1.000E+00	8.729E-02	.900E+01	3.330E+00
5	37.952	21.711	1	37.952	21.711	114.55	116.05	-1.000E+00	4.121E-02	.900E+01	1.116E+00
6	38.411	22.527	1	38.411	22.527	73.89	75.84	-1.000E+00	1.197E-01	.900E+01	4.238E+00
7	38.047	23.864	1	38.047	23.864	76.22	78.12	-1.000E+00	1.084E-01	.900E+01	4.091E+00
8	36.718	22.947	1	36.718	22.947	126.07	127.44	-1.000E+00	3.064E-02	.900E+01	8.316E-01
9	37.852	23.794	1	37.852	23.794	67.39	69.53	-1.000E+00	1.328E-01	.900E+01	5.423E+00
10	37.370	22.379	1	37.370	22.379	77.34	79.55	-1.000E+00	1.280E-01	.900E+01	4.772E+00

FIGURE 41: THE OUTPUT SIMULATED PGV AND PGA USING EXSIM

This procedure was repeated until the simulated PGV and PGA wre similar to the values observed, obtained using SAC, by modifying the stress drop that was obtained manually for each event. The results were then tabulated and a graph of PGA (cm/sec^2) against station distance (km) was produced for each event to observe the relationship between the two values, as well as to indicate which stress drop value for the simulated event is the most similar to the values observed. Figures 42-47 show this PGA and station distance relationship for magnitudes ranging from 3.3 to 5.3 for earthquakes that are located within or nearby the Corinth Gulf. The PGA is plotted according to each different stress drop value in bars used in the simulations, to obtain a stress drop that is approximately equivalent to that of the observed data.

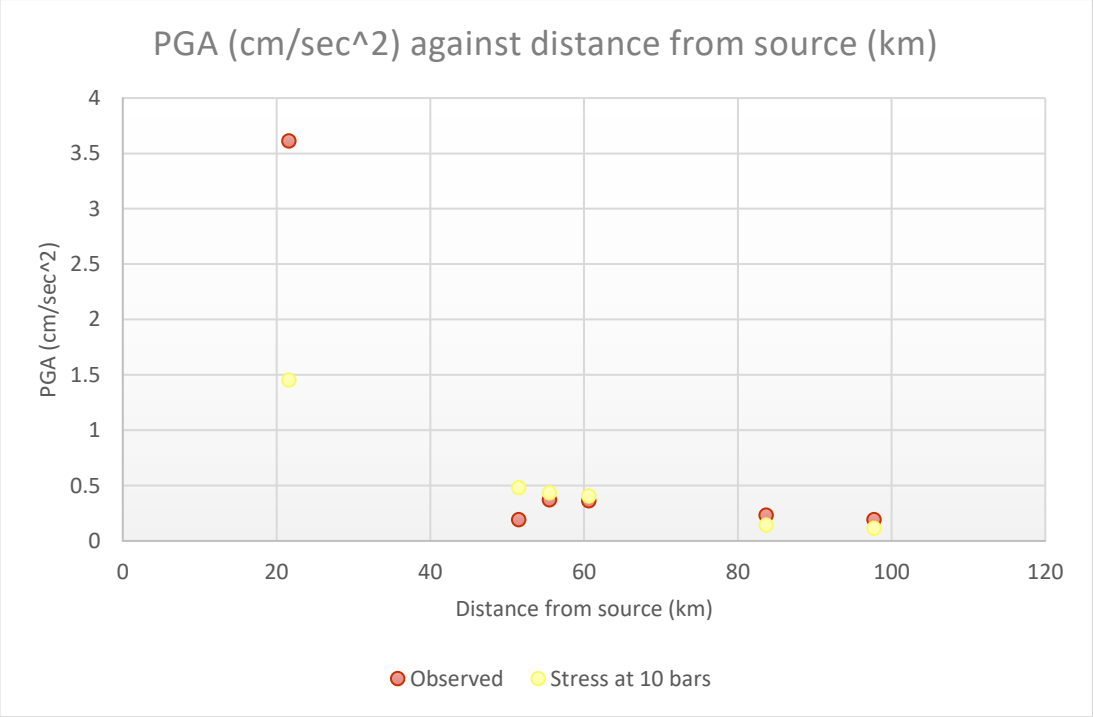

FIGURE 42: THE OUTPUT SIMULATED AND OBSERVED PGA PLOTTED AGAINST STATION DISTANCE IN KM FOR MAGNITUDE 3.3 EARTHQUAKE.

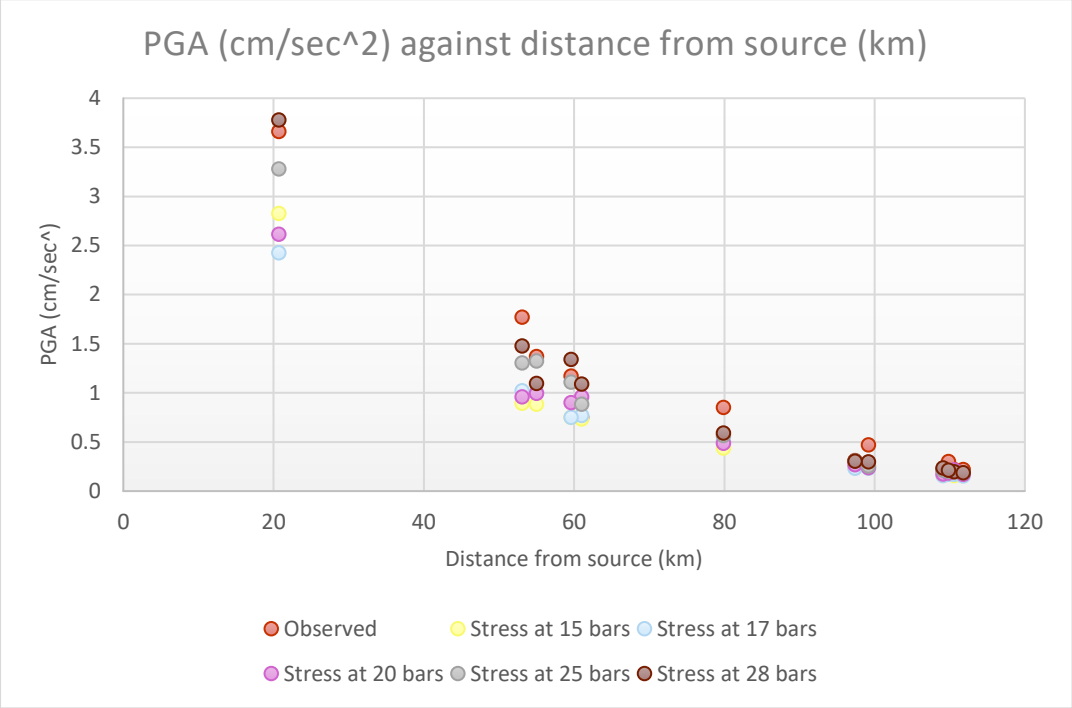

FIGURE 43: THE OUTPUT SIMULATED AND OBSERVED PGA PLOTTED AGAINST STATION DISTANCE IN KM FOR MAGNITUDE 3.6 EARTHQUAKE.

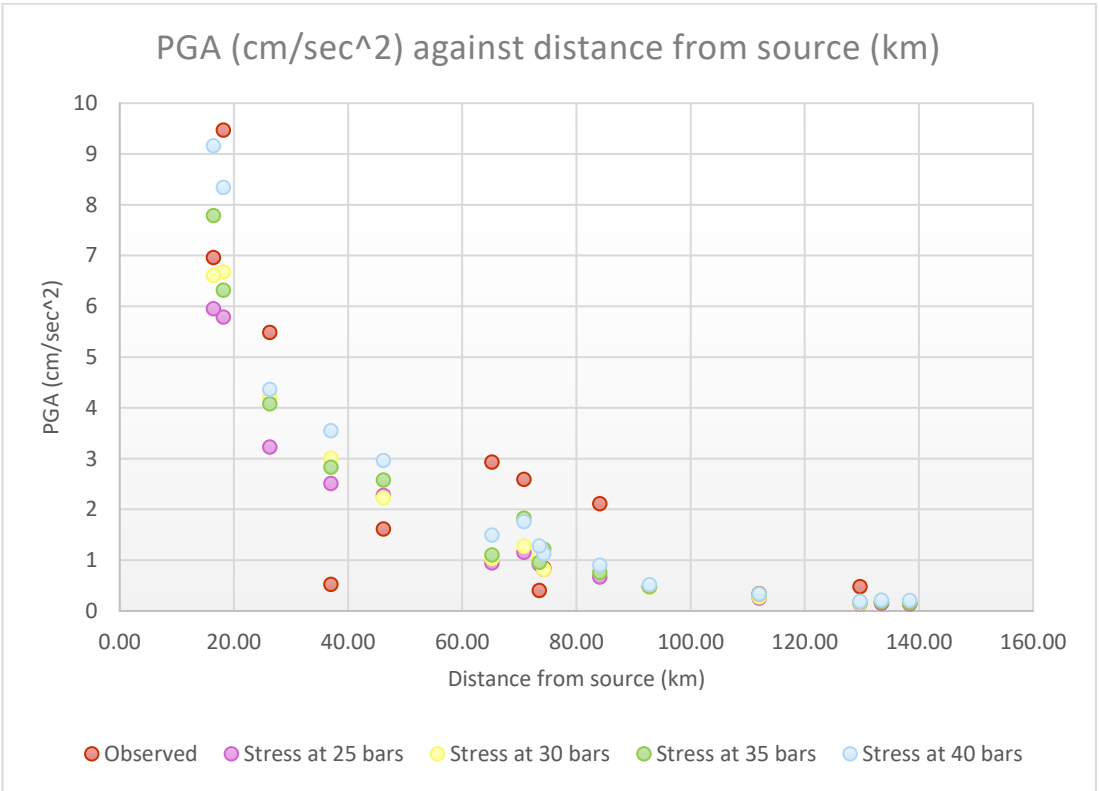

FIGURE 44: THE OUTPUT SIMULATED AND OBSERVED PGA PLOTTED AGAINST STATION DISTANCE IN KM FOR MAGNITUDE 3.8 EARTHQUAKE.

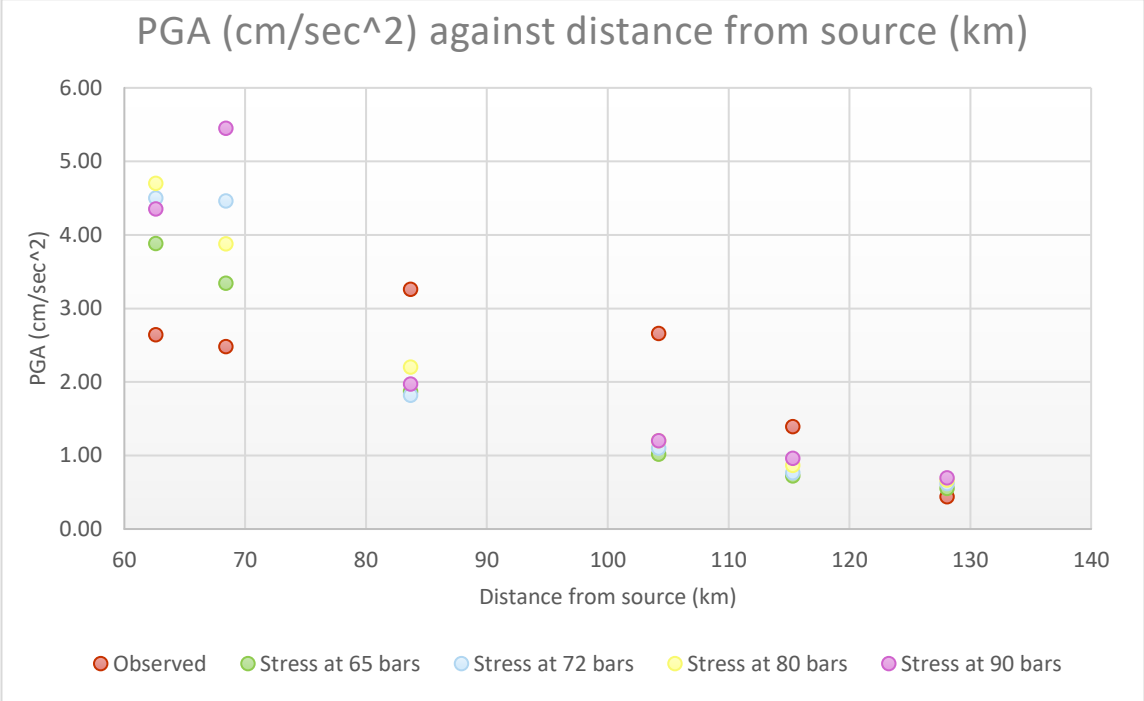

FIGURE 45: THE OUTPUT SIMULATED AND OBSERVED PGA PLOTTED AGAINST STATION DISTANCE IN KM FOR MAGNITUDE 4.2 EARTHQUAKE.

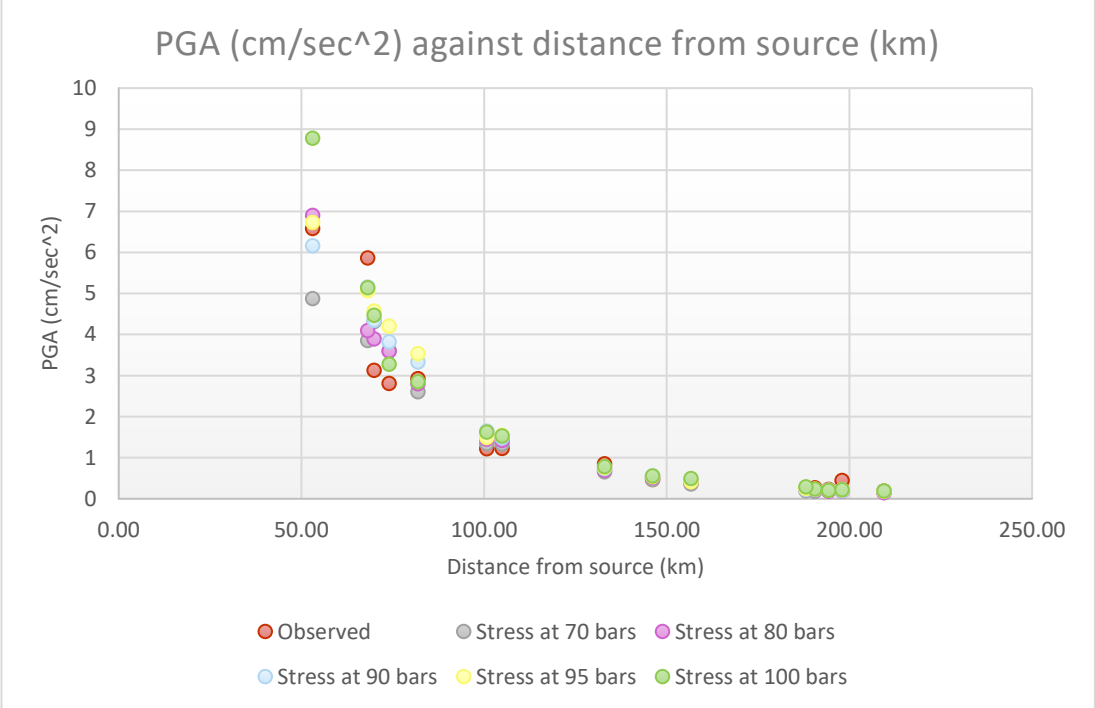

FIGURE 46: THE OUTPUT SIMULATED AND OBSERVED PGA PLOTTED AGAINST STATION DISTANCE IN KM FOR MAGNITUDE 4.3 EARTHQUAKE.

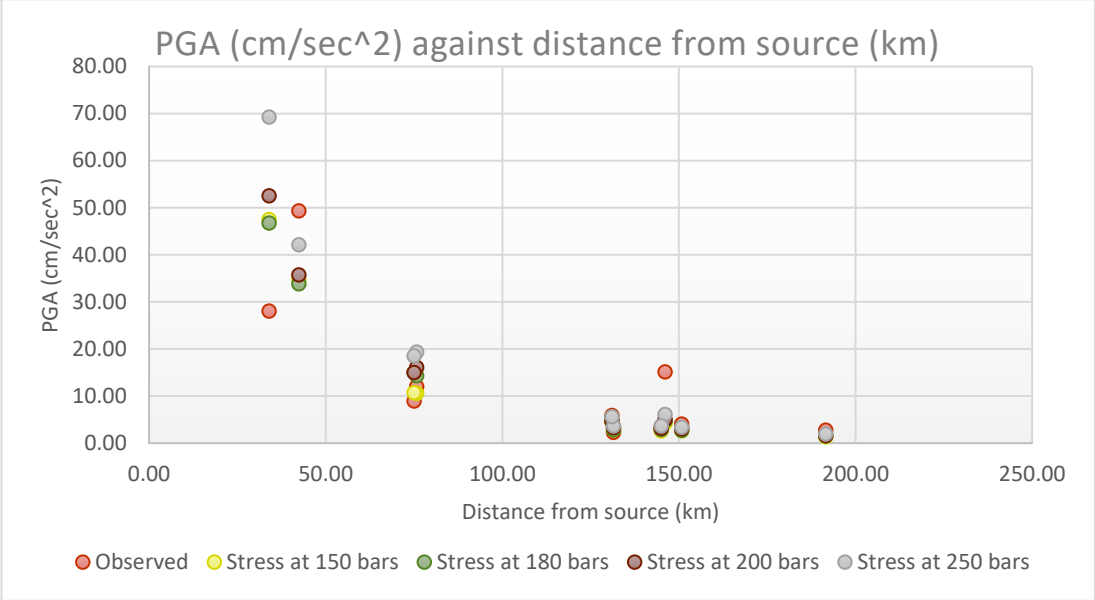

FIGURE 47: THE OUTPUT SIMULATED AND OBSERVED PGA PLOTTED AGAINST STATION DISTANCE IN KM FOR MAGNITUDE 5.3 EARTHQUAKE.

As expected from these graphs, the value of PGA decreases as the distance from the source increases since the earthquake energy is dissipated at larger distances. For some stations PGA was higher/ lower than the simulated ones. This could be a result of station errors. However, this is why an average value was obtained and the stress drop used was then compared with the one obtained using the corner frequency These figures were plotted in order to check if the relationship obtained in Figure 37 is valid to use in the simulations later on. This was done by only changing the stress drop value and keeping the other parameters constant. The stress drop that better fitted the data was the one used for each magnitude, superimposed on the plot, as obtained in Figure 35 from the stress drop estimated using the Fourier amplitude spectra (observed data). As the results between the stress drop from observed data and the simulated stress drop using EXSIM match, the linear plot for the observed data has been further validated to use for stress drop estimates for the Corinth Gulf. Table 6 lists these obtained simulated values for stress whilst

figure 48 is the resulting plot for these simulated values compared with the observed data.

TABLE 6: THE OBTAINED SIMULATED VALUES FOR STRESS DROP IN BARS TOGETHER WITH THEIR RESPECTIVE MAGNITUDES

Magnitude	Stress (bars)
3.3	10
3.6	28
3.8	30
4.2	80
4.3	90
5.3	180

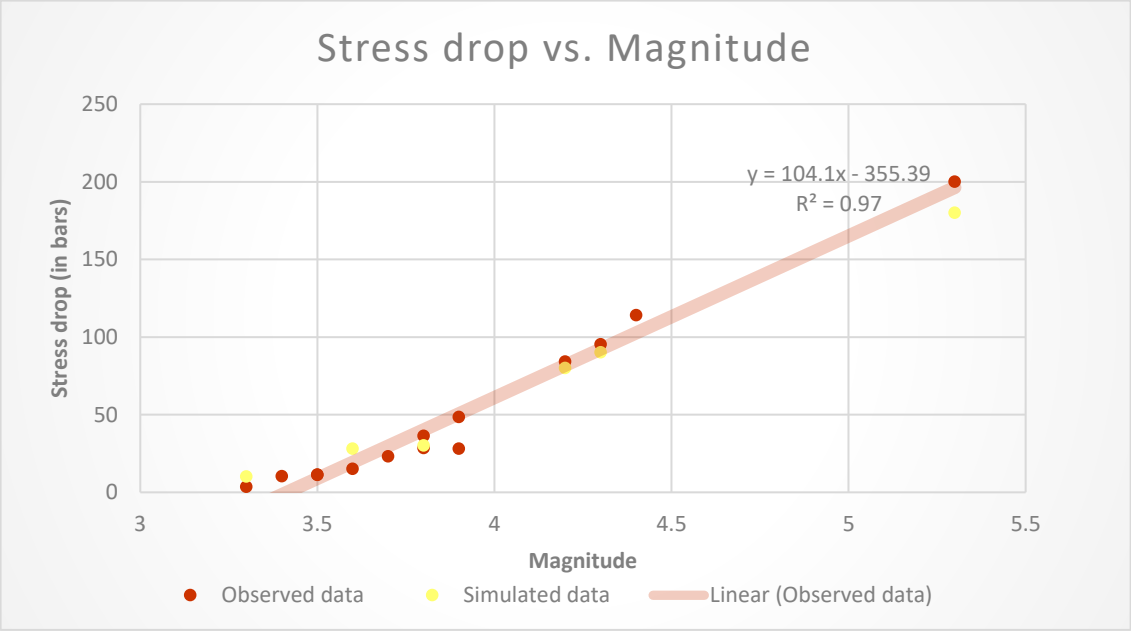

FIGURE 48: A GRAPH SHOWING THE FUNCTION OF STRESS DROP AGAINST MAGNITUDE FOR THE OBSERVED (MANUALLY ESTIMATED) AND SIMULATED (ESTIMATED USING EXSIM) DATA

Figures 49 and 50 plot all the PGA and PGV values for both observed and simulated values, respectively, against the distance from the source (km) for each of the magnitudes used for the simulations in a log-log scale. The PGV

also is an important parameter, especially since it is not as sensitive to higher frequency components and is therefore more likely than PGA to describe ground motion accurately at intermediate frequencies (Kramer, 1996). As expected, the PGA and PGV values increase as the magnitude of the event increases. These values also increase as stress drop increases and as the corner frequency decreases. PGA and PGV are also expected to increase should the soil class change such as site class D as seismic waves may scatter more. Plotting all the observed and simulated values together is important to check how close the values compare to each other. In fact, both figures indicate the closeness of the simulated values compared to the observed PGA and PGV.

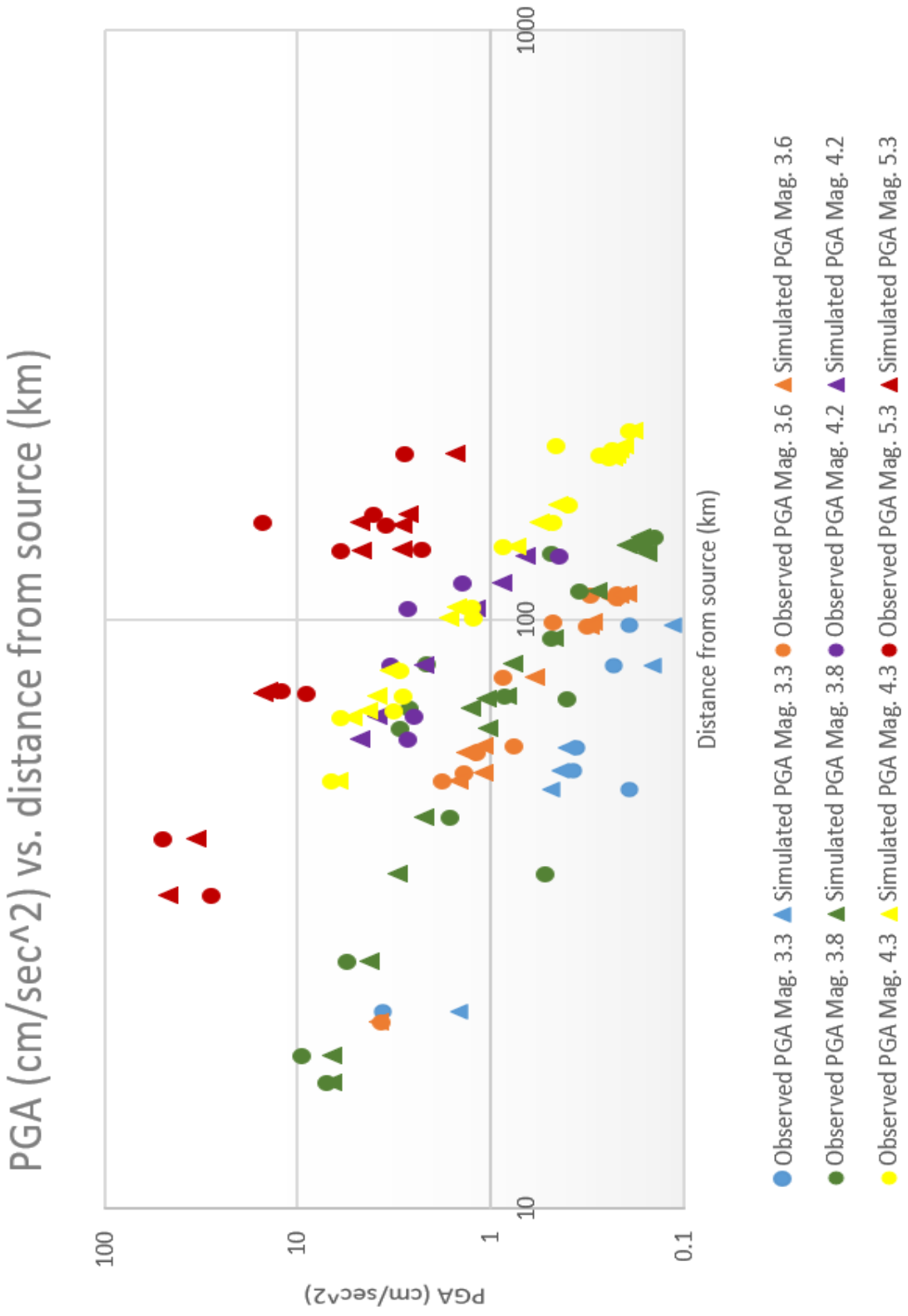

FIGURE 49: A GRAPH PLOTTING ALL THE SIMULATED PGA VALUES, WITH THE OBSERVED PGA FOR DIFFERENT MAGNITUDE VALUES RANGING FROM 3.3 TO 5.3, PLOTTED AGAINST THE STATION DISTANCE.

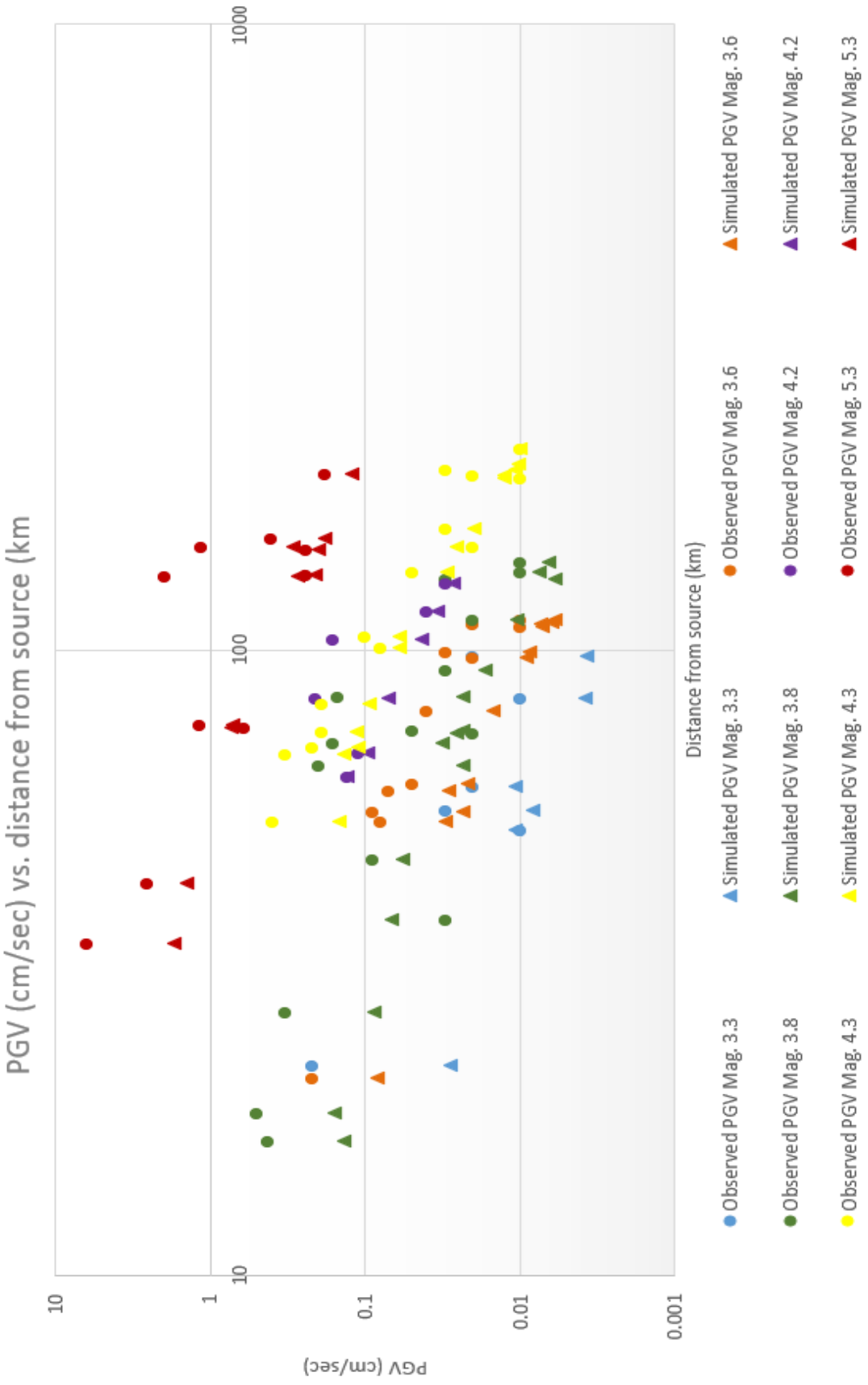

FIGURE 50: A GRAPH PLOTTING ALL THE SIMULATED PGV VALUES, WITH THE OBSERVED PGV FOR DIFFERENT MAGNITUDE VALUES RANGING FROM 3.3 TO 5.3, PLOTTED AGAINST THE STATION DISTANCE.

4.4 Simulations of large magnitude events using EXSIM

Using the information obtained with regards to the geometrical spreading, site term, excitation term and stress drop, it is then possible to obtain simulations of moderate to large magnitude events for the Corinth Gulf. The methodology was conducted based on past large events that occurred within or nearby the Corinth Gulf. This was done for events with normal faulting mechanisms as these occur more frequently within this area. The source location of the simulated earthquake is shown in Figure 51, together with the locations of hypothetical stations that were chosen to cover the whole of the Corinth Gulf and nearby areas. The location of the event was estimated nearby the Kakia-Skala fault on the eastern part of the Gulf. The stations were placed at 10km intervals on the latitude and 5km on the longitude. Simulations were conducted for events with magnitudes between 5.0 and 7.2. For magnitudes 5.0 to 5.9, the simulation was based on the magnitude 5.3 event that occurred on the 30th of March 2019. This event was a normal event, and the orientation of this fault was used for the simulation. Other parameters have been tabulated in Table 7. The stress drop was calculated by using the linear equation of the stress drop-magnitude relationship obtained as in Figure 48:

$$\Delta\sigma = 104.1M_w - 355.39 \quad (47)$$

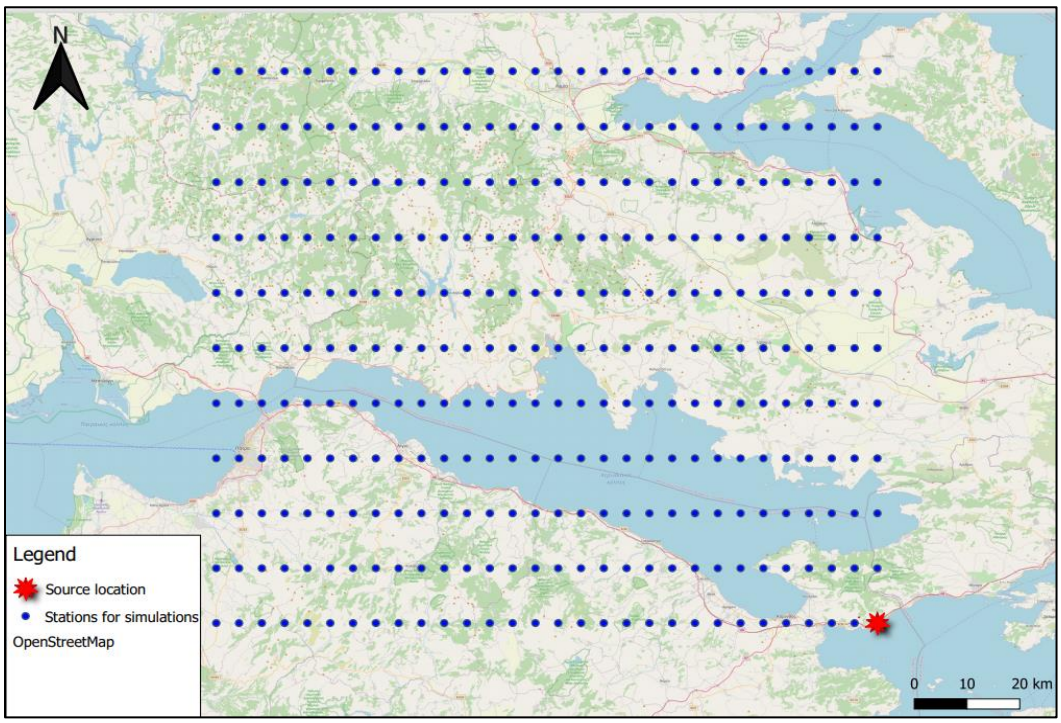

FIGURE 51: THE LOCATION FOR THE SIMULATED EVENT TOGETHER WITH LOCATIONS OF STATIONS USED FOR THE KAKIA-SKALA FAULT SIMULATIONS.

For each event between magnitude 5.0 and 5.9, only the stress drop was modified using equation 47. This is assuming that the earthquakes are not self-similar, therefore the stress parameter is quantified as a function of magnitude. The depth was chosen as 15km for all simulations as most earthquakes that occur within the Corinth Gulf frequently occur at depths between 10 to 20km. Using the PGA values obtained for the magnitude 5.0 event, a heatmap (see Figure 52) was produced to observe the spread and concentration of PGA according to the parameters used in the simulation. The legend indicates the values of the PGA in cm/sec^2 with the highest value being $104.6cm/sec^2$ and the lowest value being $1.47cm/sec^2$.

TABLE 7: THE PARAMETERS USED TO SIMULATE THE MAGNITUDE 5.0 EVENT.

PARAMETER	PARAMETER VALUE
LATITUDE AND LONGITUDE OF SOURCE	37.9265°; 23.9278 °
SHEAR WAVE VELOCITY	3.7km/sec
DENSITY	2.8g/cm^3
STRESS PARAMETER	165.11bars
KAPPA	0.030
GEOMETRICAL SPREADING	$g(r) = \begin{cases} r^{-1.2} & r < 30km \\ r^{-0.9} & 30 < r < 50km \\ r^{-1.0} & 50 < r < 80km \\ r^{-0.5} & 80 < r < 100km \\ r^{-0.7} & r > 100km \end{cases}$
QUALITY FACTOR	160
FAULT STRIKE AND DIP	95° and 68°
DEPTH	15.00km
AMPLIFICATION FACTOR	Generic rock site
η	0.50

For events with magnitudes between 6.0 and 6.9, the simulated event was based on the magnitude 6.4 event which occurred on the 25th of February 1981. The parameters used for these simulated events are similar to the ones above. Only the strike, dip and stress drop were modified accordingly. The strike and dip angles were modified to 264° and 34° respectively whilst the stress drop was modified as a function of magnitude. For Magnitude 6.0, the stress drop was calculated to be equal to 269.21 bars. The heatmap in figure 53 indicates the highest PGA value as being 367.6cm/sec^2 whilst the lowest value is 7.54cm/sec^2.

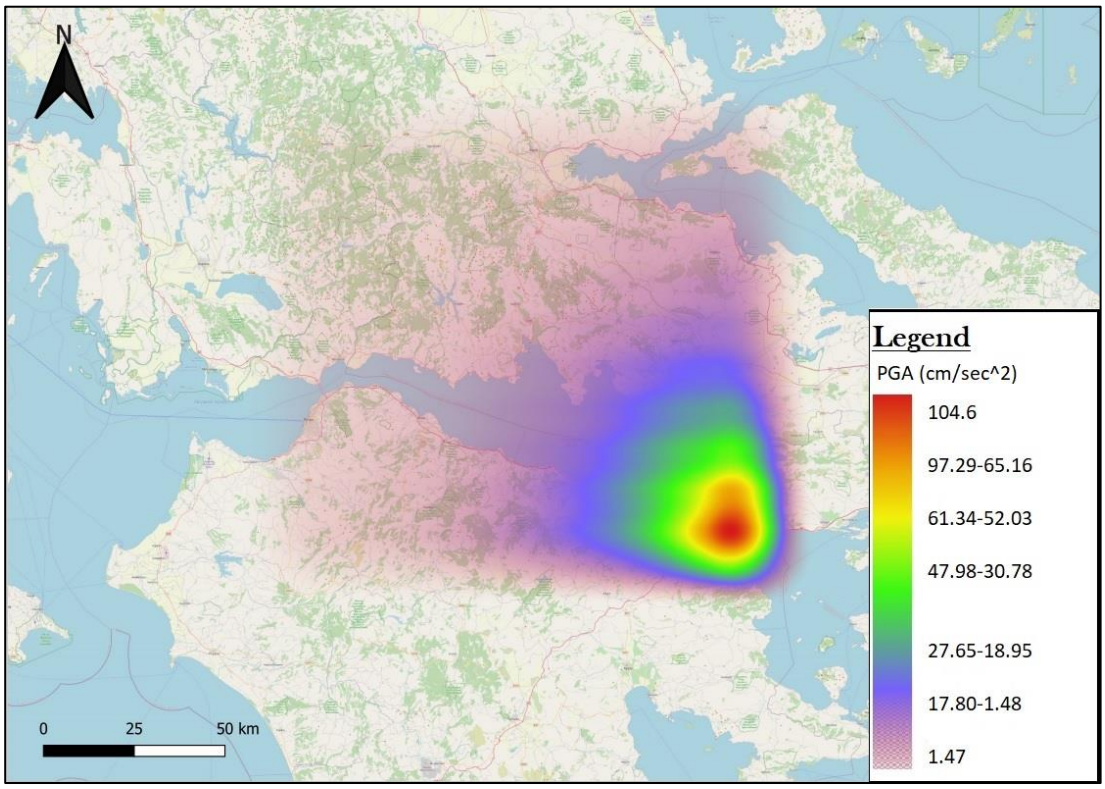

FIGURE 52: A HEATMAP SHOWING THE CONCENTRATION OF PGA VALUES FOR THE SIMULATED MAGNITUDE 5.0 EVENT IN CM/SEC^2

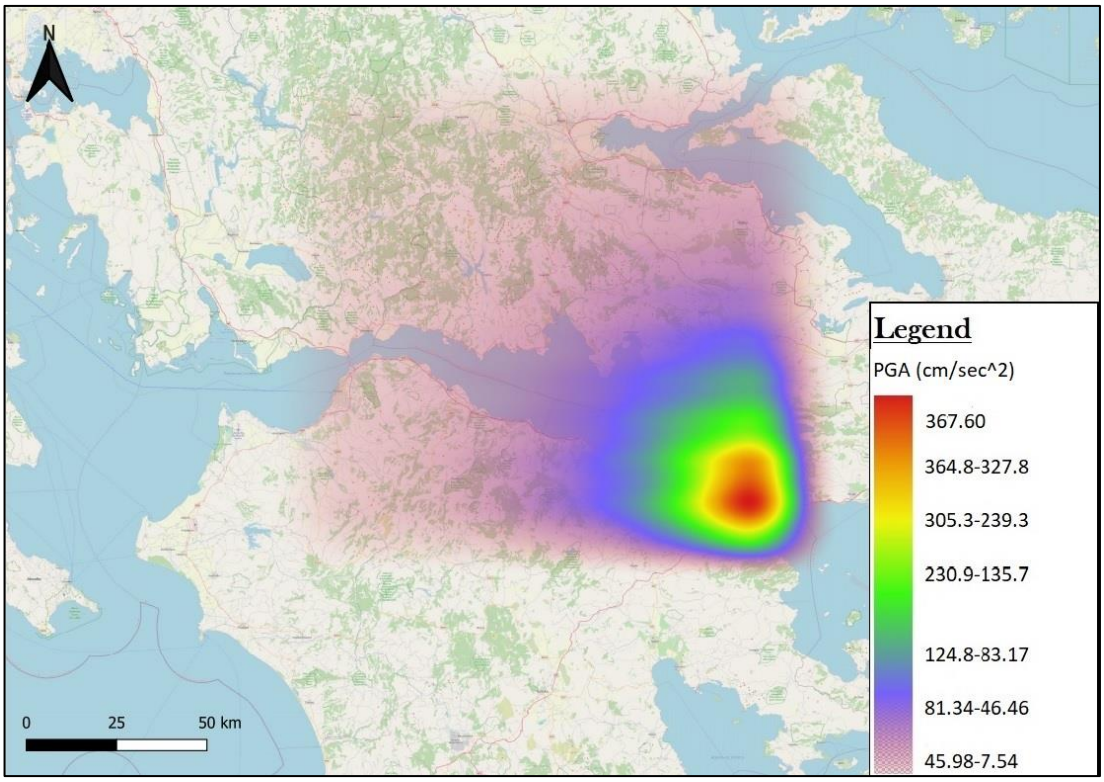

FIGURE 53: A HEATMAP SHOWING THE CONCENTRATION OF PGA VALUES FOR THE SIMULATED MAGNITUDE 6.0 EVENT IN CM/SEC^2

Events with magnitudes between 7.0 and 7.2, have so far not been recorded for the Corinth Gulf. The largest known earthquakes both were magnitude 6.7 events (refer to Table 1). The event that occurred on the 24th of February 1981, part of a cluster of 3 strong magnitude events, was used to base this simulation upon. This event was also characterized by a normal fault mechanism and the strike, dip and stress drop were changed accordingly whilst keeping the other parameters unchanged. The stress drop for a Magnitude 7.0 event was estimated to be 373.31 bars whilst the strike and dip angles are 285^{o} and 3.7^{o} for this event.

The heatmap in Figure 54, which shows a greater distribution of a stronger PGA value, indicates the highest PGA value as being 729.1cm/sec^2 whilst the lowest value is 27.35cm/sec^2. In engineering terms, the PGA close to the epicentre would be extremely high and may cause damage to infrastructure should the duration be long enough to cause damage. This further adds to the importance of having such information readily available to produce a hazard map for this region to improve planning of infrastructure and disaster response in the event of such strong magnitude earthquakes. In terms of PGV, the highest value for a magnitude 5.0 event has a value of 3.27cm/sec whilst the lowest has a value of 0.10cm/sec. For a magnitude 6.0 event, the highest value is 18.37cm/sec and the lowest value 0.74cm/sec, whilst for the magnitude 7.0 event the highest PGV obtained is 55.80cm/sec and the lowest as 4.29cm/sec.

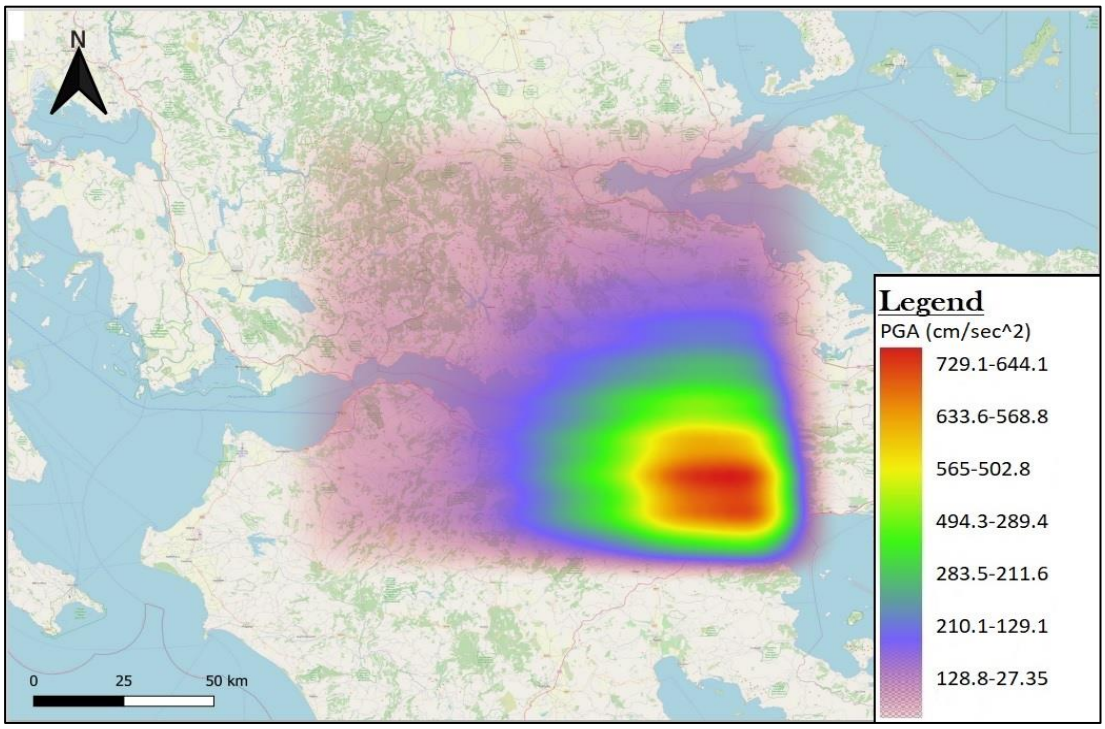

FIGURE 54: A HEATMAP SHOWING THE CONCENTRATION OF PGA VALUES FOR THE SIMULATED MAGNITUDE 7.0 EVENT IN CM/SEC^2

Events with strike-slip focal mechanisms rarely occur within the Gulf of Corinth. However, one event which was similar to a strike-slip event but had a normal fault mechanism is the Magnitude 5.9 event that occurred on the 18th of November 1992 at a depth of 14.5km. This event has been described as an asperity that occurred between two normal faults mentioned earlier in the discussion: the Helike and Xilokastro faults. This event is also known as the 1992 Galaxidi fault earthquake. The parameters used to simulate a Magnitude 5.0 event are tabulated in Table 8. For other magnitudes up until magnitude 7.2, the parameters except for the stress drop, remained unchanged. Equation 47 was used to calculate the different stress drop for each simulation. The source location was also modified and placed in the centre of the Corinth Gulf, contrary to the event used for simulating the normal fault mechanisms. Therefore, the hypothetical stations were located at circular intervals of 5km each away from the source and separated by 20 degrees. These station locations, together with the source location can be observed in Figure 55. The maximum distance from the source to the furthest station is 80km, since it

covers most of the Corinth Gulf similarly to the locations of the stations used in the simulations for the Kakia-Skala simulation.

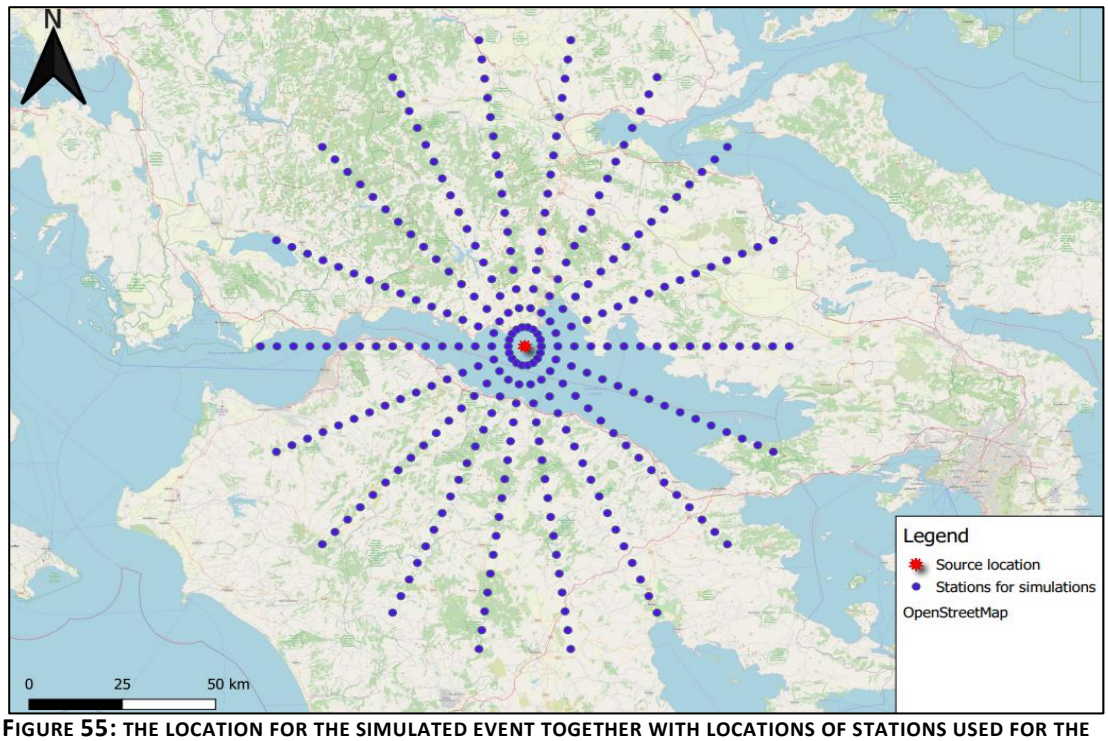

FIGURE 55: THE LOCATION FOR THE SIMULATED EVENT TOGETHER WITH LOCATIONS OF STATIONS USED FOR THE GALAXIDI FAULT SIMULATION.

TABLE 8: THE PARAMETERS USED TO SIMULATE THE MAGNITUDE 5.0 EVENT FOR THE GALAXIDI FAULT SIMULATION.

PARAMETER	PARAMETER VALUE
LATITUDE AND LONGITUDE OF SOURCE	38.307°; 22.452°
SHEAR WAVE VELOCITY	3.7km/sec
DENSITY	2.8g/cm^3
STRESS PARAMETER	165.11bars
KAPPA	0.030
GEOMETRICAL SPREADING	$g(r) = \begin{cases} r^{-1.2} & r < 30km \\ r^{-0.9} & 30 < r < 50km \\ r^{-1.0} & 50 < r < 80km \\ r^{-0.5} & 80 < r < 100km \\ r^{-0.7} & r > 100km \end{cases}$
QUALITY FACTOR	160
FAULT STRIKE AND DIP	302° and 79°

DEPTH	14.5km
AMPLIFICATION FACTOR	Generic rock site
η	0.50

Heat maps were also produced to identify areas with the highest PGA values. However, the maps only provide a simple overview as to the general spread of the PGA in intervals over the area of study. These heatmaps have been placed in Appendix D. For magnitude 5, the highest PGA value was estimated to be 132.2 cm/sec^2 whilst the lowest value is 6.65 cm/sec^2. These values are slightly higher than those obtained for normal fault mechanism simulations for the Kakia-Skala event, which may be a result of more energy being released at this asperity. For PGV, the highest value is 5.08cm/sec whilst the lowest is 0.37cm/sec. Similarly, for the simulated magnitude 6 event, the values are also higher than the 1981 event. The highest PGA and PGV values were 370.70cm/sec^2 and 19.38cm/sec respectively, whilst the lowest were 24.18cm/sec^2 and 1.69cm/sec. For the simulated event with a magnitude 7, the overall values are slightly lower than those simulated for the magnitude 7 event with a normal fault mechanism. The lowest PGA value is 52.43cm/sec^2 and the highest value is 655.50cm/sec^2. With regards to the PGV, the highest value is 49.71cm/sec and the lowest is 6.53cm/sec.

It is important to note the directivity effect in both of the simulations. The effect, which was predominantly stronger with the Galaxidi fault simulation, is a characteristic of the near-field domain, an area commonly tens of kilometres away from the epicentre but usually not more than 50km away. Directivity can either be forward, when rupture rises towards the site, or backwards in which

the rupture is in the opposite direction (see Figure 56). With forward directivity, this can have a significant increase in earthquake ground motion towards the site especially when taking into consideration the rupture front propagation and the velocity of the rupture front when the site is close to the fault but not to the epicentre, and when the slip direction is aligned with the site (Grimaz and Malisan, 2014). According to a study by Rathje, Faraj, Russell and Bray (2004), at distances less than 20km, directivity increases the low frequency part of ground motion. This was observed also in this study where forward directivity was noticed with the strongest PGA occurring between 5 to 15km for the simulations.The same distances also are observed with the PGV values. The directivity effect was more predominant as the magnitude increased. The importance of directivity needs to be taken into consideration when designing infrastructure in areas affected by this directivity due to the strong damage potential of near field characteristics such as this.

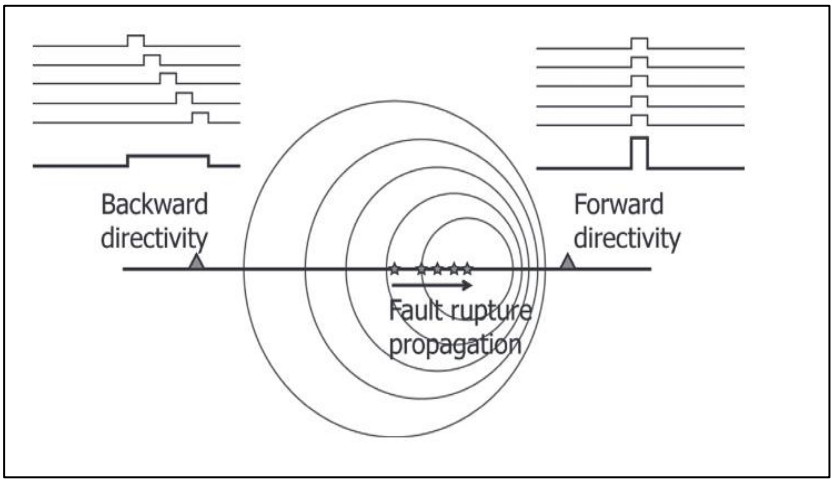

FIGURE 56: THE EFFECTS OF FORWARD AND BACKWARD DIRECTIVITY
SOURCE: GRIMAZ AND MALISAN (2014)

The main objective of this study was to obtain the physical ground motion parameters for the Corinth Gulf that characterise seismic events which have

occurred and will occur in the future. To validate that the estimated values obtained in this study can be used to describe the ground-motion scaling for the Corinth Gulf, the results from the simulations can be plotted together with the information that describe real seismic events which have occurred in the past. Additionally, this can also be done by plotting the linear equations obtained by Skarlatoudis et al. (2003) and Margaris et al. (2002), which are two studies that attempted to obtain ground motion predictive relations for Greece using a different methodology from the one used in this study. It is also worth noting another recent study by Boore at al. (2020) whereby a ground motion predictive model was derived for Greece using strong-motion data by computing residuals obtained from a global model and performing mixed effects analysis. This paper differs from the previously mentioned two studies, with which this study shall be compared with as they both use an optimization procedure to obtain results. This procedure was used to obtain the necessary predictive relationships based on the least square method using a singular value decomposition procedure. Regression analysis as a two-part process was applied to determine the required coefficients. Both studies used earthquakes from all over Greece with magnitudes greater than magnitude 4.5. differing from this study which specifically uses earthquakes from within or nearby the Corinth Gulf with magnitudes less than 4.4. The resulting equations from the study by Skarlatoudis et al. (2003) that were used to compare with the simulations of this study and the real events are as follows:

$$logPGA = 0.86 + 0.45M - 1.27log(R^2 + h^2)^{\frac{1}{2}} + 0.10F + 0.06S \pm 0.286 \quad (48)$$

$$logPGV = -1.47 + 0.52M - 0.93log(R^2 + h^2)^{\frac{1}{2}} + 0.07F + 0.11S \pm 0.305 \quad (49)$$

where the numerical terms are scaling coefficients obtained through regression, M is the moment magnitude, R indicates the epicentral distance and h is the depth of the earthquake focus in km. F and S are terms referring to the faulting mechanism of the earthquake and S is the site term. To compare with the results of this study, R was changed accordingly to the distances used in the study and h was 15km. F and S were taken as 0 since F=0 is for normal faults and S= 0 is used for rock sites. Similarly, the relations obtained by Margaris et al. (2002) are as follows:

$$lnPGA = 3.52 + 0.70M - 1.14log(R^2 + h^2)^{\frac{1}{2}} + 0.12S \pm 0.70 \quad (50)$$

$$lnPGV = -2.08 + 1.13M - 1.11log(R^2 + h^2)^{\frac{1}{2}} + -0.29S \pm 0.80 \quad (51)$$

Together with these studies, available data for strong motion events that occurred in the past was obtained through the USGS online catalogue which listed station data using the moment magnitude observed, showing the PGA and PGV observed at each site. Table 9 lists the information that characterise these strong motion events. For the magnitude 6.7 event, only two stations were available, since this occurred in 1981, when station coverage was lacking in Greece.

TABLE 9: THE CHARACTERISTICS OF THE EARTHQUAKES USED TO COMPARE WITH THIS STUDY AND PREVIOUS STUDIES.

Date	Magnitude	Fault Mechanism	Depth (km)	Location
30th March 2019	5.3Mw	Normal	10	Galaxidhion
17th February 2021	5.5Mw	Normal	5.3	Kamarai
18th November 1992	5.9Mw	Normal	14.5	Galaxidhion
15th June 1995	6.5Mw	Normal	14.2	Galaxidhion
24th February 1981	6.7Ms	Normal	33	Domvraina

The coming figures (Figures 57 to 62) show same of the graphical results when comparing the real events together with the results of this study and the relationships obtained in the studies by Skarlatoudis et al. (2003) and Margaris et al. (2002). These figures demonstrate that the model produced by this study through region-specific attenuation and source parameters for the Corinth Gulf has a good fit with the observed real events at distances less than 50km away from the source. On the other hand, the relationships obtained by both studies tend to underestimate the PGA and PGV values. However, the studies provide a better fit with real events at distances greater than 50km whilst the model from this study is slightly over estimated. The linear relationship obtained by Margaris et al. (2002) has a better fit with the model obtained through this study.

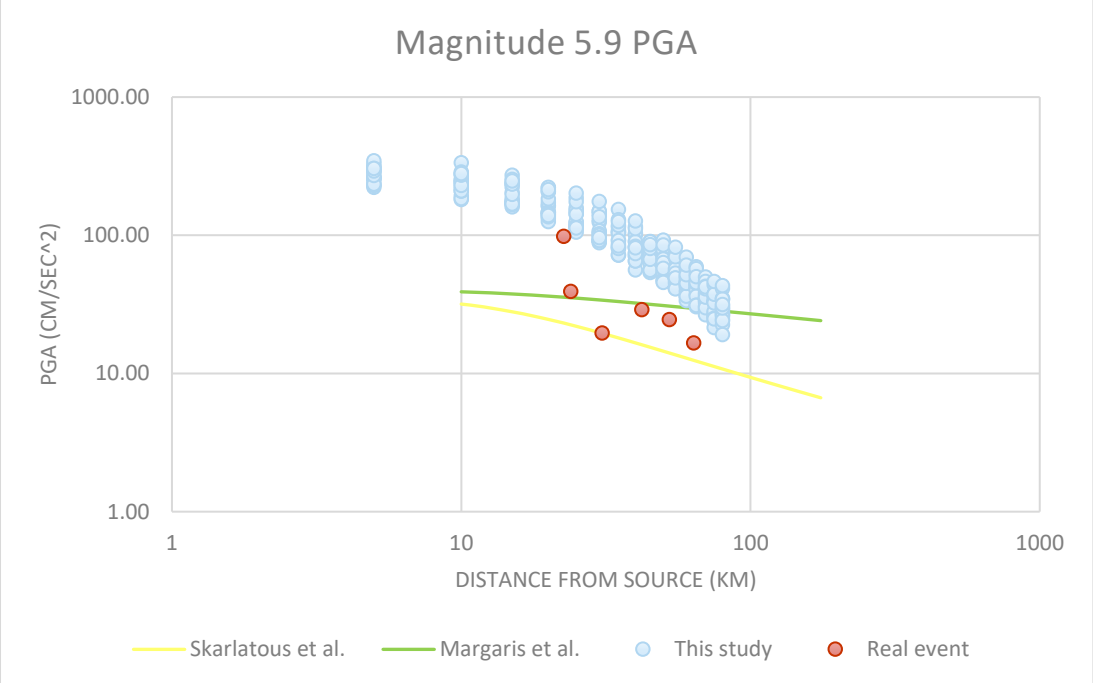

FIGURE 57: COMPARING PGA RESULTS OBTAINED THROUGH THE GROUND MOTION PARAMETERS DERIVED IN THIS STUDY TOGETHER WITH THE OBSERVED PGA VALUES OF A REAL EVENT AND LINEAR RELATIONS OBTAINED THROUGH PREVIOUS STUDIES FOR A MAGNITUDE 5.9 EARTHQUAKE IN A LOG-LOG SCALE.

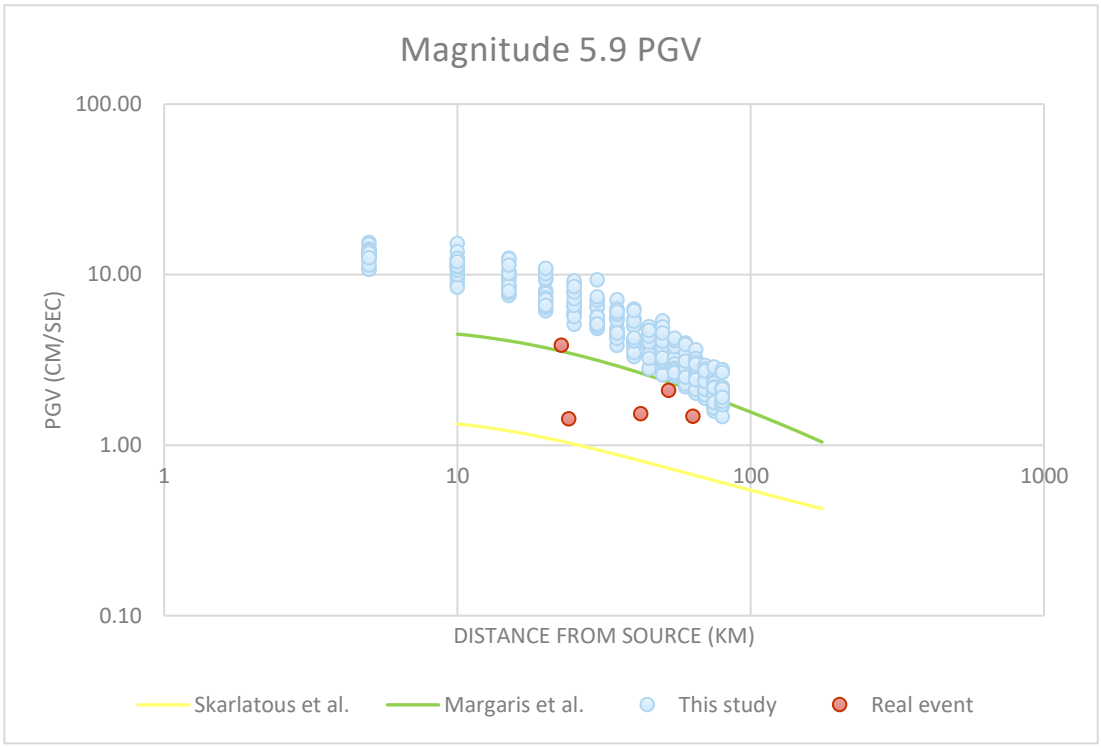

FIGURE 58: COMPARING PGV RESULTS OBTAINED THROUGH THE GROUND MOTION PARAMETERS DERIVED IN THIS STUDY TOGETHER WITH THE OBSERVED PGV VALUES OF A REAL EVENT AND LINEAR RELATIONS OBTAINED THROUGH PREVIOUS STUDIES FOR A MAGNITUDE 5.9 EARTHQUAKE IN A LOG-LOG SCALE.

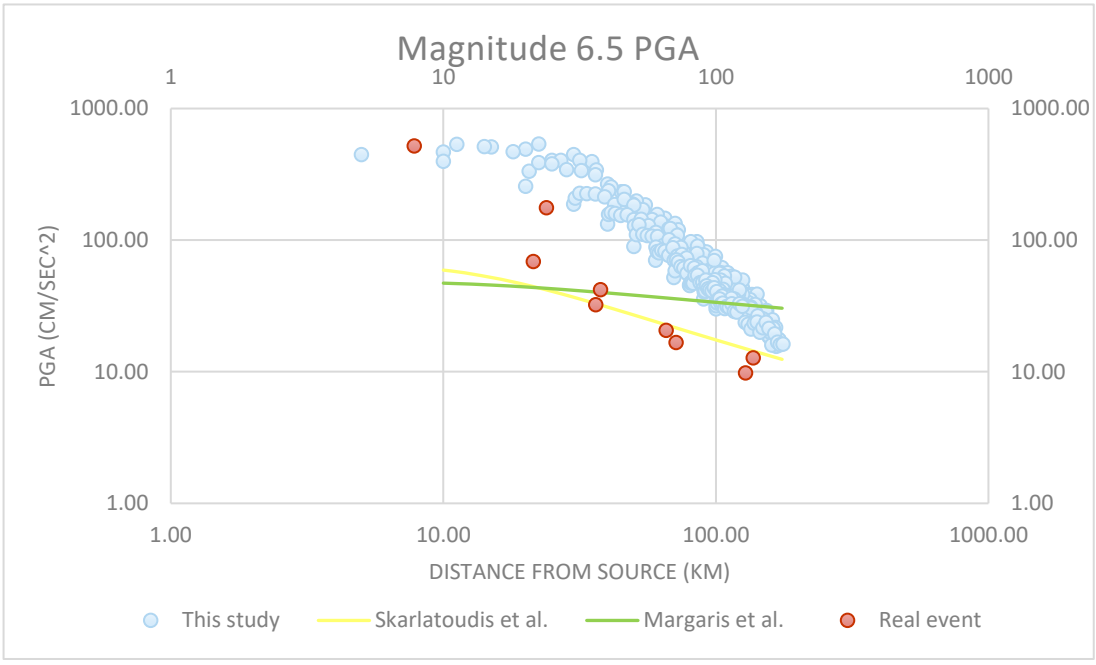

FIGURE 59: COMPARING PGA RESULTS OBTAINED THROUGH THE GROUND MOTION PARAMETERS DERIVED IN THIS STUDY TOGETHER WITH THE OBSERVED PGA VALUES OF A REAL EVENT AND LINEAR RELATIONS OBTAINED THROUGH PREVIOUS STUDIES FOR A MAGNITUDE 6.5 EARTHQUAKE IN A LOG-LOG SCALE.

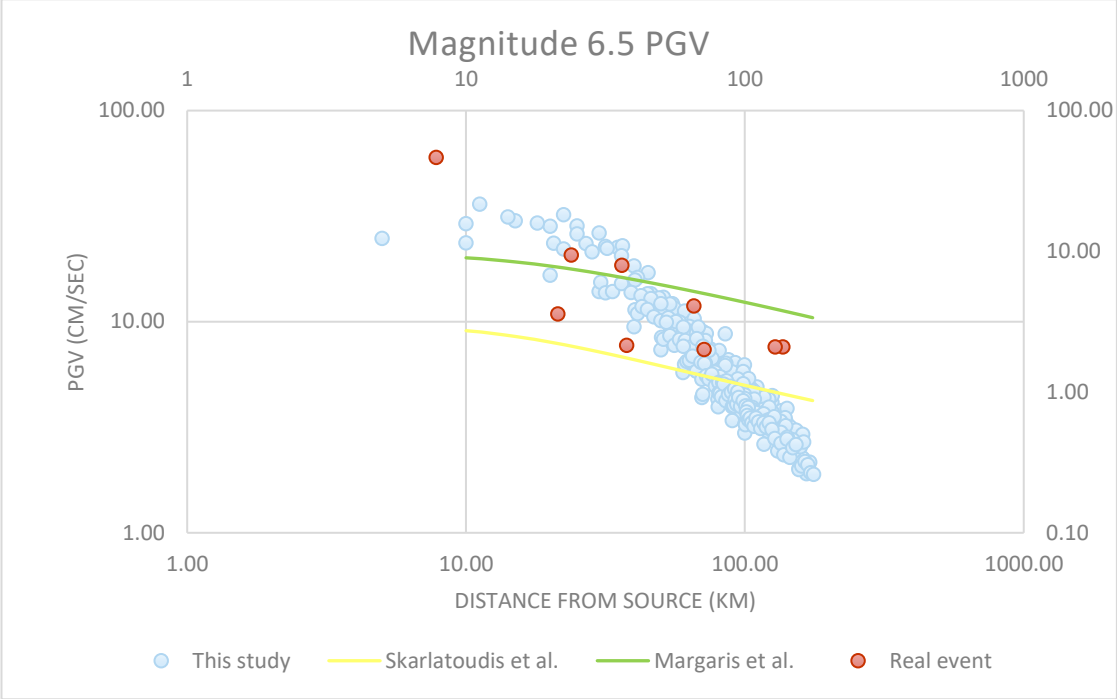

FIGURE 60: COMPARING PGV RESULTS OBTAINED THROUGH THE GROUND MOTION PARAMETERS DERIVED IN THIS STUDY TOGETHER WITH THE OBSERVED PGV VALUES OF A REAL EVENT AND LINEAR RELATIONS OBTAINED THROUGH PREVIOUS STUDIES FOR A MAGNITUDE 6.5 EARTHQUAKE IN A LOG-LOG SCALE.

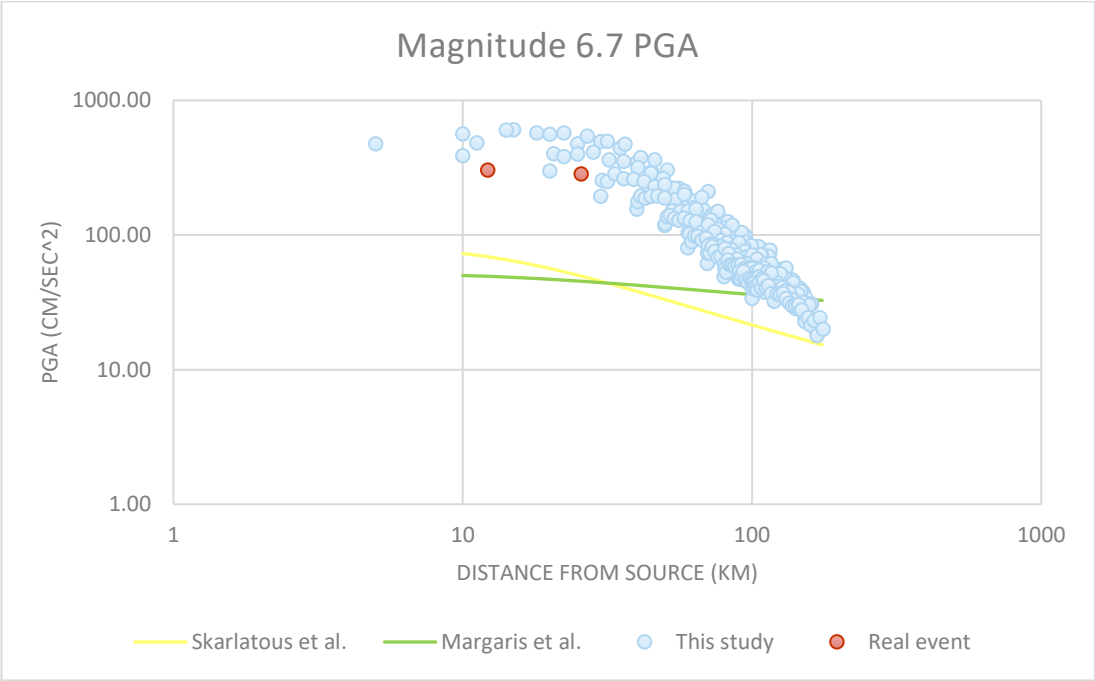

FIGURE 61: COMPARING PGA RESULTS OBTAINED THROUGH THE GROUND MOTION PARAMETERS DERIVED IN THIS STUDY TOGETHER WITH THE OBSERVED PGA VALUES OF A REAL EVENT AND LINEAR RELATIONS OBTAINED THROUGH PREVIOUS STUDIES FOR A MAGNITUDE 6.7 EARTHQUAKE IN A LOG-LOG SCALE.

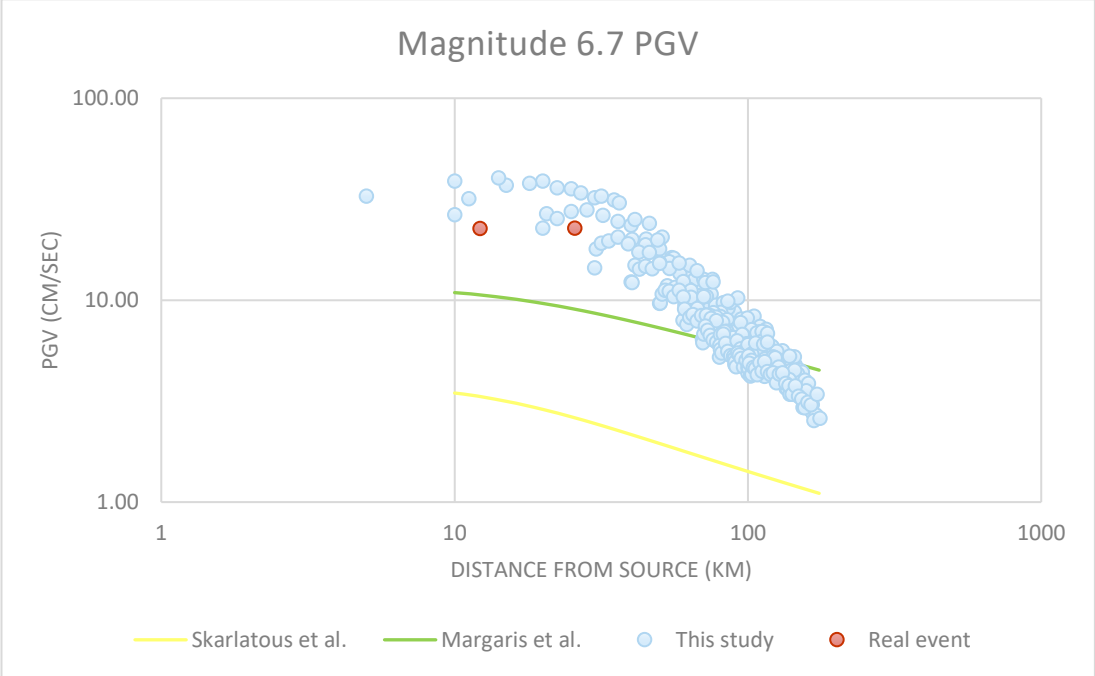

FIGURE 62: COMPARING PGV RESULTS OBTAINED THROUGH THE GROUND MOTION PARAMETERS DERIVED IN THIS STUDY TOGETHER WITH THE OBSERVED PGV VALUES OF A REAL EVENT AND LINEAR RELATIONS OBTAINED THROUGH PREVIOUS STUDIES FOR A MAGNITUDE 6.7 EARTHQUAKE IN A LOG-LOG SCALE.

To further demonstrate the fit with the real events compared with the simulated data for both the simulated events, one with a normal fault mechanism and the other with a strike-slip fault mechanism, figures 63 and 64 compile all the data from the simulated events with the real events. The majority of the values for the real events fall within the same values obtained through the simulations. Even though only weak-motion data was used, the study shows that it is possible to estimate ground motion parameters, even for areas for which data from strong-motion earthquakes is not available. The figures further validate that the ground motion parameters obtained to describe the attenuation, site and source parameters for the Corinth in this study can be used to determine the ground-motion amplitudes, such as PGA and PGV, for possible future earthquakes in the Corinth Gulf.

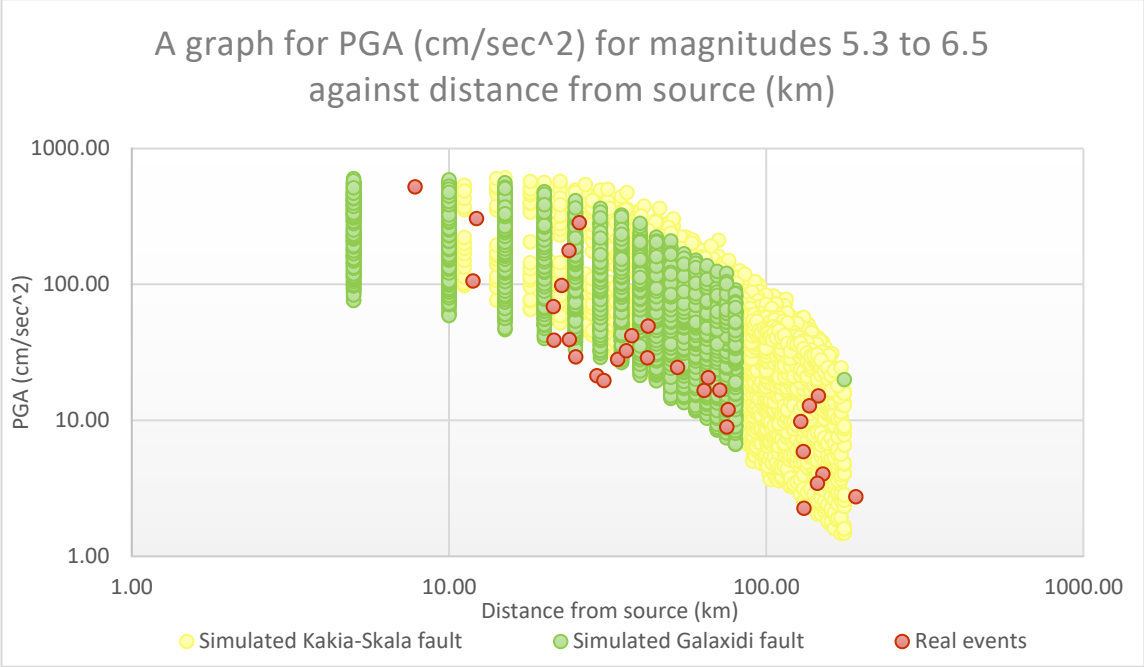

FIGURE 63: COMPARING PGA RESULTS OBTAINED THROUGH THE GROUND MOTION PARAMETERS DERIVED IN THIS STUDY TOGETHER WITH THE OBSERVED PGA VALUES OF REAL EVENTS FOR EARTHQUAKES WITH MAGNITUDES BETWEEN 5.3 TO 6.7 IN A LOG-LOG SCALE.

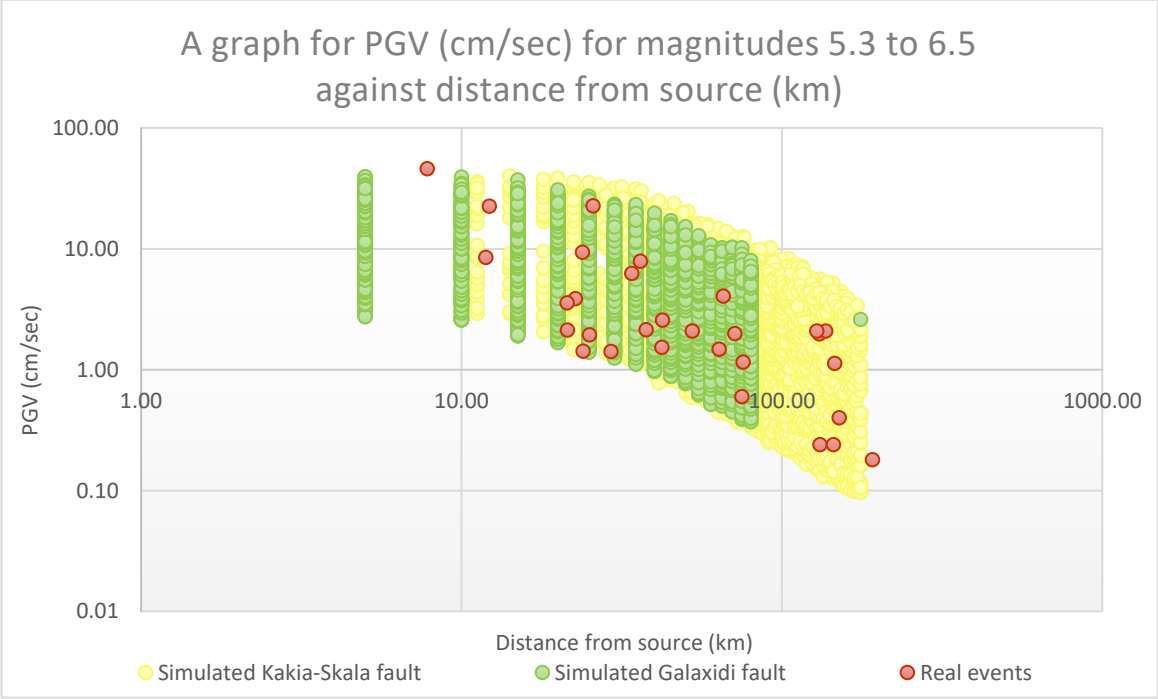

FIGURE 64: COMPARING PGV RESULTS OBTAINED THROUGH THE GROUND MOTION PARAMETERS DERIVED IN THIS STUDY TOGETHER WITH THE OBSERVED PGV VALUES OF REAL EVENTS FOR EARTHQUAKES WITH MAGNITUDES BETWEEN 5.3 TO 6.7 IN A LOG-LOG SCALE.

5. Conclusion

The goal of this study was to obtain the ground motion parameters that include the source, path and site parameters that characterise earthquake propagation within the Corinth Gulf. These were obtained through the use of ground motion predictive equations, derived through regressions, by which the site parameters, source characteristics and information regarding the propagation eventually led to obtaining the peak ground acceleration and velocity. Such a study using this methodology had not yet been conducted for this region, especially through the use of data from within or nearby this region. The ground motion scaling in the region of the Corinth Gulf was investigated by using 297 seismic events with low to moderate magnitudes ranging from 2.5 to 4.4, obtained through the Hellenic Seismic Unified Network in Greece. These events were used to obtain the ground motion parameters which include the attenuation, geometrical spreading, excitation terms and site term that characterize the Corinth Gulf. Once the data was checked for instrument response, the p and s wave arrival times were picked manually. To remove instrument response, Butterworth bandpass filters were used in the frequency range between 0.25Hz and 20Hz. The data was then regressed to obtain the durations and the empirical regional attenuation functional for the observed data for the Corinth Gulf. With regards to the duration, it was observed that signals with lower frequencies have longer durations, and that as distance increases, the duration increases as well. There was also more scattering exhibited for the duration at low frequencies less than 0.85Hz. Overall, it can

be concluded that durations decrease generally with increasing frequency and data becomes less scattered.

Forward modelling was then applied to obtain a proposed crustal attenuation parameter Q (f) for the Corinth Gulf. The following parameter was obtained:

$$Q(f) = 160\left(\frac{f}{f_{ref}}\right)^{0.50}$$

The value of Q_0 is 160 whilst the value η is 0.50. Locations with similar values of Q_0 are Utah, Southern California, Mexico, Marmara and western Anatolia whose values for Q_0 are 160, and 180 respectively. These values indicate that the regions are all affected mostly by local seismicity and there is high attenuation, meaning crustal propagation is less efficient in the Corinth Gulf, which is a characteristic of an unstable region. Compared to other regions worldwide, the attenuation value is lower than the regions of Yellowstone and Utah, and higher than other regions such as Northern and Central California, Switzerland, Germany, India, Canada, North-western and North-eastern Italy and Eastern Sicily. The geometrical spreading estimated for the Corinth Gulf, normalized to zero at the chosen reference hypocentral distance of 40 km, is as follows:

$$g(r) = \begin{cases} r^{-1.2} & r < 30km \\ r^{-0.9} & 30 < r < 50km \\ r^{-1.0} & 50 < r < 80km \\ r^{-0.5} & 80 < r < 100km \\ r^{-0.7} & r > 100km \end{cases}$$

These values suggest spherical spreading loss up to 80km and cylindrical spreading loss above 80km. The above also indicates that the Fourier amplitudes are decaying fast at distances less than 30km with a geometrical

spreading coefficient of g(r) = $r^{-1.2}$. The high-frequency parameter $\boldsymbol{\kappa_{eff}}$ was estimated to be:

$$\boldsymbol{\kappa_{eff}} = 0.030 secs$$

This value was used to fit the excitation terms for this study. The density value used is $2.8 g/cm^3$ whilst the shear wave velocity is $3.7 km/sec$. A stress drop parameter of $\Delta\sigma = 200 bars$ was used to estimate the theoretical excitation spectra. The source term used was the generic rock site amplification factor V(f) of 1.

For ground motion prediction, it is necessary to use a programme that models the stochastic method. This is required to check whether weak motion data is capable of producing simulations for strong motion events. For this study, EXSIM was used to obtain simulated PGA and PGV using inputted parameters obtained for site, path and source effects that were found earlier in the study. For this, values for selected events of different magnitudes ranging from 3.3 to 5.3 for the Corinth Gulf where used. A linear relationship between the stress drop and magnitude of events for the Corinth Gulf was initially obtained through both manually obtaining the corner frequency and through trial and error using EXSIM by comparing the observed PGA with simulated PGA. This is assuming that earthquakes are not self-similar and that the stress drop varies as a function of magnitude. The source mechanisms of the earthquakes were also defined for each simulation. The fault geometry, dip and strike were based on real events that occurred in the past within or nearby the Corinth Gulf region. This information together with the linear relationships for the stress drop as well as the obtained site, source and path parameters were all inputted

to simulate two earthquake events, both with normal focal mechanisms, in different locations within or nearby the Corinth Gulf for magnitudes ranging from magnitude 5 to 7.2 at the Kakia-Skala and Galaxidi faults respectively. Stations were placed at different distances to simulate scenarios for the PGA and PGV in the Corinth Gulf. To demonstrate whether the values obtained through simulations were valid or not, the results of this study were compared with the empirical predictive relations obtained by from previous studies, which both used an optimization procedure. These were applied by using similar parameters of depth and radius. It was found that the results of this study are slightly higher in value than both the studies. However, this study is closer to the equation obtained by Margaris et al. Five real events of different magnitudes of 5.3, 5.5, 5.9, 6.5 and 6.7 were also plotted, superimposed on the simulated data and the relationships obtained from the studies. It resulted that, on average, for the near field domain at distances less than 50km, the values were closer to this study whereas at the far field domain, the values of real events were closer to the other previous studies. The results from the simulation were more accurate for larger magnitudes greater than a magnitude of 6 whilst there was overestimation observed for smaller magnitudes. One reason for this is a result of the applied methodology (manually estimating stress drop and Brune's source model) which tends to overestimate results. The underestimation of the results by previous studies for distances close to the source indicates the importance of this study to predict expected ground motions for the Corinth gulf region.

Since the previous studies use data from all over Greece, it is essential to consider that Greece can have different regional attenuation characteristics,

such as Italy and California, and therefore using combined data to obtain predictive relations can lead to less reliable results. However, to predict the PGA and PGV at the source of the event, this study, which uses data only from within or around the Corinth Gulf, provides more reliable results whilst the other studies are slightly underestimated. The new model proposed by this study can be used to predict ground motions closer to the fault, and thus the results can be utilized to compile a new seismic hazard map for the Corinth Gulf to provide better information regarding possible PGA and PGV used in infrastructural planning and emergency protocols. These findings are similar to the case of Italy, also characterised by complex tectonics and surficial seismicity. Thus local attenuation functions can be estimated through Brune's spectral model implemented in EXSIM. One major drawback of the study is the lack of strong motion data together with lack of seismic station coverage at sea, since all the stations are located on land. In addition to the previous recommendation, it is also recommended to increase the network coverage of the Corinth Gulf so as more data could be obtained and therefore better ground motion prediction equations could be evaluated in the future. This recommendation could also be applied in various areas in Greece that are vulnerable to strong motion events such as the Ionian channel and the Hellenic Forearc. It is highly recommended that studies to obtain regional attenuation properties for these two seismically active zones, as well as other zones in Greece, are conducted to provide better ground motion parameters and further understand the propagation of seismic waves in these areas. This in turn will contribute towards a wholesome study on earthquake characteristics and attenuation characteristics for Greece.

References

Abercrombie, R. (1995). Earthquake source scaling relationships from -1 to 5 M_L using seismograms recorded at 2.5 km depth. *Journal of Geophysical Research, 100*, p. 24,015 – 24,036.

Aki, K. (1980). Scattering and attenuation of shear waves in the lithosphere. *Journal of Geophysical Research, 85*, pp 6496-6504.

Aki, K. (1989). *Deterministic and stochastic approaches in seismogram analysis*. In: Litehiser, J.J. (ed.) Observatory seismology: An anniversary symposium on the occasion of the centennial of the University of California at Berkeley seismographic stations, University of California Press, Berkeley, CA, United States (USA), p. 257-265.

Akinci, A., Malagnini, L., Pino, N.A., Scognamiglio, L., Hermann, R.B., & Eyidogan, H. (2001). High-frequency ground motion in the Erzincan region. Turkey: inferences from small earthquakes. *Bulletin of the Seismological Society of America, 91,* p. 1446–1455. DOI: 10.1785/0120010125

Akinci, A., Mueller, C., Malagnini, L., & Lombardi, A.M. (2004). Seismic hazard estimate in the Alps and Apennines (Italy) using smoothed historical seismicity and regionalized predictive ground-motion relationship. *Bulletin of Theoretical and Applied Geophysics, 45*(4), pp285-304).

Akinci, A., Malagnini, L., Hermann, R.B., Gok, & Sorensen, M.B. (2006). Ground motion scaling in the Marmara region, Turkey. *Geophysical Journal International, 166*, pp 635-651. DOI: 10.1111/j.1365-246X.2006.02971.x

Akinci, A., D'Amico, S., Malagnini, L., & Mercuri, A. (2013). Scaling earthquake ground motions in Western Anatolia, Turkey. *Physics and Chemistry of the Earth, 63,* pp 124-135. http://doi.org/10.106/j.pce.2013.04.013.

Aktar, M., Ergin, M., Ozalaybey, S., Tapirdamaz, C., Yoruk, A., & Bicmen, F. (2000). A lower-crustal event in the northeastern Mediterranean: the 1998 Adana Earthquake (Mw =6.2) and its aftershocks. *Geophysical Research Letters*, 27, p.2361–2364. *https://doi.org/10.1029/2000GL011412*

Albini, P., Rovida, A., Scotti, O., & Lyon-Caen, H. (2017). Large Eighteenth–Nineteenth Century Earthquakes in Western Gulf of Corinth with Reappraised Size and Location. *Bulletin of the Seismological Society of America, 107*(4), p 1663-1687. DOI: 10.1785/0120160181ff.

Algermissen, T. & Rogers, A. (2004). *A Cyprus earthquake hazard assessment: maps of probabilistic peak ground acceleration and uniform hazard pseudoabsolute acceleration spectral response.* UNOPS Seismic Hazard and Risk Assessment of the Greater Nicosia area report.

Allman, B.P., & Shearer, P.M. (2009). Global variations of stress drop for moderate to large earthquakes. *Journal of Geophysical research, 114,* B01310, p. 1-22. DOI:10.1029/2008JB005821

Ambraseys, N.N. (1971). Some characteristic features of the Anatolian fault zone. *Tectonophysics, 9*, p 143-165. DOI: 10.1016/0040-1951(70)90014-4

Ambraseys, N. (1996). Material for the investigation of the seismicity of central Greece. In: Stiros, S., & Jones, R.E. (eds), *Archaeoseismology.* Exeter: UK, Fitch Laboratory Occasional Paper, 7, p 23-26.

Ambraseys, N. N., & Simpson, K. A. (1996). Prediction of vertical response spectra in Europe. *Earthquake Engineering Structural Dynamics, 25*, p. 401–412.

Ambraseys, N. N., Simpson, K.A., & Bommer, J.J. (1996). Prediction of horizontal response spectra in Europe. *Earthquake Engineering Structural Dynamics, 25*, p. 371–400. https://doi.org/10.1002/(SICI)1096-9845(199604)25:4<401::AID-EQE551>3.0.CO;2-B.

Anderson, J. G. (1997). Seismic energy and stress-drop parameters for a composite model. *Bulletin of the Seismological Society of America, 87,* p. 85–96.

Anders, B., Reischmann, T., Poller, U., & Kostopoulos, D. (2005). Age and origin of granitic rocks of the eastern Vardar Zone, Greece: new constraints on the evolution of the Internal Hellenides. *Journal of the Geological Society, London, 162*, p. 857-870. https://doi.org/10.1144/0016-764904-077

Armijo, R., Lyon-Caen, H., & Papanastassiou, D. (1992). East–west extension and holocene normal faults scraps in the Hellenic arc. *Geology, 20*, p. 491–494.

Armijo, R., Meyer, B., King, G.C.P., Rigo, A., & Papanastassiou, D. (1996). Quaternary evolution of the Corinth Rift and its implications for the Late Cenozoic evolution of the Aegean. *Geophysical Journal International, 126*, p.11–53. https://doi.org/10.1111/j.1365-246X.1996.tb05264.x

Arvidsson, R., Ben-Avraham, Z., Eckstrom, G., & Wdowinski, S. (1998). Plate tectonic framework for the October 9, 1996 Cyprus earthquake. *Geophysical Research Letters, 25*, p. 2241–2244. DOI: 10.1029/98GL01547

Assatourians, K., & Atkinson, G. (2007). Modeling Variable-Stress Distribution with the Stochastic Finite-Fault Technique. *Bulletin of the Seismological Society of America, 97*, p. 1935-1949. DOI: 10.1785/0120060203

Assatourians, K. (2008). *Stress parameter distribution on an earthquake fault based on a stochastic modeling approach*. PhD theses, Carleton University, Ottawa, Canada.

Atkinson, G. (1993). Notes on ground motion parameters for eastern North America: Duration and H/V ratio. *Bulletin of the Seismological Society of America, 83*, p. 587-596.

Atkinson, G.M., Assatourians, K. Boore, D.M., Campbell, K., & Motazedian, D. (2009). A Guide to Differences between Stochastic Point-Source and Stochastic Finite-Fault Simulations. *Bulletin of the Seismological Society of America, 99* (6), p. 3192-3201. DOI: 10.1785/0120090058

Atkinson, G.M., & Assatourians, K. (2014). Implementation and Validation of EXSIM (A Stochastic Finite-fault ground motion simulation algorithm) and the SCEC Broadband platform. *Seismological Research Letters, 86*(1), p. 48-60.

Bay, F., Fah, D., Malagnini, L., & Giardini, D. (2003). Spectral shear-wave ground motion scaling for Switzerland. *Bulletin of the Seismological Society of America, 93,* p. 414–429. https://doi.org/10.1785/0120010232

Belderson, R.H., Kenyon, N.H., & Stride, A.H. (1978). Local submarine salt-karst formation on the Hellenic Outer Ridge, eastern Mediterranean. *Geology, 6*(7), p. 16-720.

Bilham, R. (2010). Lessons from the Haiti Earthquake. *Nature, 463* (18), p 878-879.

Bitharis, S., Fotiou, A., Pikridas, C., & Rossikopoulos, D. (2016). A new crustal velocity field of Greece based on seven years (2008-2014) continuously operating GPS station data. In: Freymueller J.T., & Sánchez L. (eds) International Symposium on Earth and Environmental Sciences for Future Generations. International Association of Geodesy Symposia, vol 147. Springer, Cham. https://doi.org/10.1007/1345_2016_230

Blumetti, A., Dramis, F., & Michetti, A. (1993). Fault-generated mountain fronts in the central Apennines (central Italy): Geomorphological features and seismotectonic implications. *Earth surface Processes and Landforms, 18,* p. 203-223. DOI: 10.1002/esp.3290180304

Boatwright, J. (1980). A spectral theory for circular seismic sources: simple estimates of dimension, dynamic stress drop and radiated seismic energy. *Bulletin of the Seismological Society of America*, *70*, p. 1–27.

Bodin, P., Malagnini, L., & Akinci, A. (2004). Ground motion scaling in the Kachchh basin, India, deduced from aftershocks of the 2001 M_w7.6 Bhuj earthquake, *Bulletin of the Seismological Society of America, 94*, p. 1658–1669.

Boore, D.M. (1983) Stochastic simulation of high-frequency ground motions based on seismological models of the radiated spectra. *Bulletin of the Seismological Society of America, 73*, p. 1865-1894.

Boore, D. M., Joyner, W. B., & Fumal, T.E. (1993). Estimation of response spectra and peak acceleration from western North America earthquakes: an interim report. *U.S. Geological Survey Open-File Report,* 93-509, 72 pp. DOI: 10.3133/ofr94127

Boore, D. M., & Joyner, W.B. (1997). Site amplifications for generic rock sites. *Bulletin of the Seismological Society of America, 87*, p. 327-341. DOI: 10.1.1.503.4738

Boore, D.D. (2002). *SMSIM — Fortran Programs for Simulating Ground Motions from Earthquakes: Version 2.0 — A Revision of OFR 96–80–A*. U.S. Geological Survey: U.S.A.

Boore, D.M. (2003). Simulation of Ground motion using the stochastic model. *Pure Applied Geophysics, 160*, p. 635-676. DOI: 10.1007/PL00012553.

Boore D. M. (2009). Comparing stochastic point- and finite-source ground-motion simulations: SMSIM and EXSIM, *Bulletin of the Seismological Society of America*, in press. DOI: 10.1785/0120090056.

Boore, D.M., Stewart, J.P., Skarlatoudis, A.A., Seyhan, E., Margaris, B., Theodoulis, N., Scordilis, E., Kalogeras, I., Klimis, N., & Melis, N.S. (2020). A Ground Motion Prediction Model for Shallow Crustal Earthquakes in Greece. *Bulletin of the Seismological Society of America, 111, p. 857-874.* DOI: https://doi.org/10.1785/0120200270.

Briole, P., Rigo, A., Lyon-Caen, H., Ruegg, J.C., Papazissi, K., Mitsakaki, C., Balodimou, A., Veis, G., Hatzfeld, D., & Deschamps, A. (2000). Active deformation of the Corinth rift, Greece: Results from repeated Global Positioning System surveys between 1990 and 1995. *Journal of Geophysical Research, 105* (B11), p 25,605 -25,625. DOI: 10.1029/2000JB900148.

Brooks, M., Clews, J.E., Melis, N.S., & Underhill, J.R. (1988). Structural development of Neogene basins in western Greece. *Basin Research, 1,* p 129-138. DOI: 10.1111/j.1365-2117.1988.tb00010.x

Building Seismic Safety Council. (2003). *NEHRP recommended provisions for seismic regulations for new buildings and other structures, part 1: Provisions*, *Report no. FEMA 450.* Building Seismic safety Council: Washington D.C., USA.

Buxton, R.G.A. (2004). *Complete World of Greek Mythology.* Thames and Hudson Ltd: London.

Cagnan, Z., & Tanircan, G.B., (2010). Seismic hazard assessment for Cyprus. *Journal of Seismology, 14*, p 225-246. DOI: 10.1007/s10950-009-9163-1.

Campbell, K.W. (1981). Near source attenuation of peak horizontal acceleration. *Bulletin of the Sociological Society of America, 74,* p 1441-1450.

Campbell, K. W., & Bozorgnia, Y. (1994). Near-source attenuation of peak horizontal acceleration from worldwide accelerograms recorded from 1957 to 1993. In: *Proc. Fifth U.S. National Conference on Earthquake Engineering, EERI, Berkeley, California, Vol. 1*, p. 283–292. DOI: 10.1785/0120040147

Caputo, R., Catalano, S., Monaco, S., Romagnoli, G., Tortorici, G., & Tortorici, L. (2010). Active faulting on the island of Crete (Greece). *Geophysical Journal International, 183*, p 111,126. DOI:10.1111/j.1365-246X.2010.04749.x

Carminati, E., Lustrino, M., Cuffaro, M., & Doglioni, C. (2010). Tectonics, magmatism and geodynamics of Italy: What we know and what we imagine. *Journal of the Virtual Explorer, 36*(9).

Carulli G. B., Nicolich, R., Rebez, A., & Slejko, D. (1990). Seismotectonic of the Northwest External Dinarides, *Tectonophysics, 79*, pp 11–25. DOI: 10.1016/0040-1951(90)90353-A

Cartwright, D.E., & Longuet-Higgins, M.S. (1956). The statistical distribution of the maxima of a random function. *Proceedings of the Royal Society of London, 237*, p. 212-232.

Catalano, S., De Guidi, G., Romagnoli, G., Torrisi, S., Tortorici, G. & Tortorici, L. (2007). The migration of plate boundaries in SE Sicily: Influence on the large- scale kinematic model of the African promontory in southern Italy. *Tectonophysics, 449*, p. 41-62. DOI: 10.1016/j.tecto.2007.12.003.

Catalano, S., De Guidi, G., Lanzafame, G., Monaco, C. & Tortorici, L. (2009). Late quaternary deformation on the island of Pantelleria: New constraints for the recent tectonic evolution of the Sicily Channel Rift (southern Italy). *Journal of Geodynamics, 48*, p. 75-82. DOI: 10.1016/j.jog.2009.06.005.

Cattaneo, M., Augliera, P., & Spallarossa, D. (1999). Anomalously deep earthquakes in North-western Italy. *Journal of Seismology, 3* (4), pp 431-425.

Causse, M., & Song. S.G. (2015). Are stress drop and rupture velocity of earthquakes independent? Insight from observed ground motion variability. *Geophysical Research Letters, 42,* p.1-7. DOI: 10.1002/2015GL064793

Chalouan, A., Michard, A., Feinberg, H., Montigny, R., & Saddiqi, O. (2001). The Rif mountain building (Morocco): a new tectonic scenario. *Bulletin de la Societe Geologique de France, 172*, p. 603-616. DOI: 10.2113/172.5.603.

Chaumillon, E., & Mascle, J. (1997). From foreland to forearc domains: New multichannel seismic reflection survey of the Mediterranean ridge accretionary complex (Eastern Mediterranean). *Marine Geology, 183,* p. 237-259. DOI: 10.1016/S0025-3227(97)00002-9.

Chouet, B., Aki, K., & Tsujiura, M. (1978). Regional variation of the scaling law of earthquake source spectra. *Bulletin of the Seismological Society of America*, *68*, 49–79.

Civile, D., Lodolo, E., Caffau, M., Baradello, L. & Ben-Avraham, Z. (2015). Anatomy of a submerged archipelago in the Sicilian Channel (central Mediterranean Sea). *Geological Magazine, First view*, p. 1-19. DOI: 10.1017/S0016756815000485.

Cotton, F., Archuleta, R., & Causse, M. (2013). What is sigma of the stress drop?. *Seismological Research Letters, 84* (1), p. 42-48. DOI: https://doi.org/10.1785/0220120087

Courboulex, F., Vallee, M., Causse, M., & Chounet, A. (2016). Stress drop variability of shallow earthquakes extracted from a global database of source time functions. *Seismological Research Letters, 87* (4), p. 912-918. DOI: https://doi.org/10.1785/0220150283

D'Amico, S., Akinci, A., Malagnini, L., & Galea., P. (2011). Prediction of High-Frequency Ground Motion Parameters Based on Weak Motion Data. In D'Amico S. (editor) *Earthquake Research and Analysis - New Frontiers in Seismology*, pages 69–86. InTech.

D'Amico, S., Akinci, A., & Malagnini, L. (2012). Predictions of high-frequency ground-motion in Taiwan based on weak motion data. *Geophysical Journal International, 189* (1), p. 611-628. DOI: 10.1111/j.1365-246X.2012.05367.x

D'Amico, S., & Galea, P. (2013). Earthquake ground-motion simulations for the Maltese Archipelago. *Journal of the Malta Chamber of Sciences, 1* (1). DOI: http://dx.medra.org/10.7423/XJENZA.2013.1.01.

D'Amico, S., Akinci, A., & Pischiutta, M (2018). High frequency ground-motion parameters from weak-motion data in the Sicily Channel and surrounding regions. Geophysical Journal International, 214, p. 148-163. DOI: 10.1093/gji/ggy107.

Danciu, L., & Tselentis, G.A. (2007). Engineering Ground-Motion Parameters Attenuation Relationships for Greece. *Bulletin of the Seismological Society of America, 97* (1B), p. 162-183. DOI: 10.1785/0120040087.

De Boer, J.Z., & Hale, J.R. (2000). The Geological origins of the Oracle at Delphi, Greece. In: McGuire, W.G, Griffiths, D.R., Hancock, P.L., & Stewart, I.S. (eds) *The Archaeology of Geological Catastrophes.* Geological Society, London, Special Publications, 171, p. 399-412.

DeJonge, M.R., Wortel, M.J.R., & Spakman, W. (1994). Regional scale tectonic evolution and the seismic velocity structure of the lithosphere and upper mantle; the Mediterranean region. *Journal of Geophysical Research, 99*, p 12091-12108.

Delacou, B., Sue, C., Champagnac, J.D., & Burkhard, M. (2004). Present day geodynamics in the bend of the Western and Central Alps, as constrained by earthquake analysis. *Geophysical Journal International, 158,* pp 753-774. DOI: 10.1111/j.1365-246X.2004.02320.x

Delibasis, N., Ziazia, M., Voulgaris, N., Papadopoulos, T., Stavrakakis, G., Papanastassiou, D., & Drakatos, G. (1999). Microseismic activity and seismotectonics of Heraklion Area (central Crete Island Greece). *Tectonophysics, 308*, p 237-248. DOI: 10.1016/S0040-1951(99)00076-1.

Dercourt, J., Zonenshain, L.P. & Ricou, L.E. (1986). Geological evolution of the Tethys belt from the Atlantic to the Pamirs since the Lias. *Tectonophysics, 123,* pp 241-315.

Derras, B., Cotton, F., Drouet, S., & Bard, P.Y. (2017). *Magnitude dependence of stress drop: What does the observed magnitude scaling of ground motions tell us?* Sixteenth World Conference on Earthquake Engineering, Jan 2017, Santiago, Chile, p. 4505.

Dewey, J.R., & Sengor, A.M.C. (1979). Aegean and surrounding regions: complex multiplate and continuum tectonics in a convergent zone. *Geological Society of America Bulletin, 90*, p. 84-92.

Dinter, D.A. (1998). Late Cenozoic extension of the Alpine collisional orogeny, north-eastern Greece: Origin of the north Aegean basin. *Geological Society of America Bulletin, 110*, p.1208-1226. https://doi.org/10.1130/0016-7606(1998)110<1208:LCEOTA>2.3.CO;2

Doglioni, C., Gueguen, E., Sabat, F., & Fernandez, M. (1997). The Western Mediterranean extensional basins and the Alpine orogen. *Terra Nova, 9*, p. 109-112.

Dong, G., & Papageorgiou, A. (2003). On a new class of kinematic models: Symmetrical and asymmetrical circular and elliptical cracks. *Physics of the Earth and Planetary Interiors, 137* (1), p. 129-151. DOI: 10.1016/S0031-9201(03)00012-8

Doutsos, T., Kontopoulos, N., & Poulimenos. G. (1988). The Corinth-Patras rift as the initial stage of continental fragmentation behind an active island arc (Greece). *Basin Research, 1*, p. 177-190.

Drakopoulos, J. & Delibasis, N.D. (1982). The focal mechanism of earthquakes in the major area of Greece for the period 1947-1981. *Seismology Lab. University of Athens, No. 2.*

Durand, B., Jolivet, L., Horvath, F. & Séranne, M. (eds.) (1999). *The Mediterranean Basins: Tertiary Extension within the Alpine Orogen*. Geological Society London: Special Publications, 156, 570 pp.

European Commission's Directorate-General for European Civil Protection and Humanitarian Aid Operations (ECHO) (2021). *Haiti - Earthquake, update (DG ECHO, GDACS, Copernicus EMS, Haiti Civil Protection) (ECHO Daily Flash of 20 August 2021).* Retrieved online on 24th August 2021 from:

https://reliefweb.int/report/haiti/haiti-earthquake-update-dg-echo-gdacs-copernicus-ems-haiti-civil-protection-echo-daily

Efron, B., & Tibshirani, R.J. (1994). *An introduction to the bootstrap*. Springer Science + Business Media: Dordrecht.

Fatehi, A., & Hermann, R.B. (2008). High-frequency ground motion scaling in the Pacific Northwest and in Northern and Central California. *Bulletin of the Seismological Society of America, 98* (2), pp 709-721. DOI: 10.1785/0120070051.

Ferentinos, G., Brooks, M. & Doutsos, T. (1985). Quaternary tectonics in the Gulf of Patras, western Greece, *Journal of Structural Geology, 7*, p. 713-717. https://doi.org/10.1016/0191-8141(85)90146-4.

Finetti, I. (1976). Mediterranean Ridge: a young submerged chain associated with the Hellenic Arc. *Bolletino di Geofisica Teorica e Applicata, 19*, p. 31-65.

Frizon de Lamotte, D., Saint Bezar, B., Bracéne, R. & Mercier, E. (2000). The two main steps of the Atlas building and geodynamics of the western Mediterranean. *Tectonics, 19*, p. 740- 761.

Galanopoulos, A.G. (1966). The seismotectonic regime of Greece. Annals of *Geophysics, 20* (1), p 109-119. https://doi.org/10.4401/ag-4987.

Gasparini, C., Iannacone, G., Scandone, P., & Scarpa, R. (1982). Seismotectonics of the Calabrian Arc*. Tectonophysics, 84*, p. 267-286. https://doi.org/10.1016/0040-1951(82)90163-9.

Gawthorpe, R.L., Leeder, M. R., Kranis, H., Skourtsos, E., Andrews, J. E., Henstra, G. A., Mack, G. H., Muravchik, M., Turner, J. A., & Stamatakis, M. (2018). Tectono-sedimentary evolution of the Plio-Pleistocene Corinth Rift, Greece. *Basin Research, 30*, p 448-479. doi: 10.1111/bre.12260

Geiss, E. (1987). A new compilation of crustal thickness data for the Mediteranean area. *Annales Geophysicae, 5B*, p. 623-630.

Grimaz, S., & Malisan, P. (2014). Near field domain effects and their consideration in the international and Italian seismic codes. Bollettino di Geofisica Teorica ed Applicata, 55(4), p. 717-738. DOI: 10.4430/bgta0130.

Goes, S., Giardini, D., Jenney, S., Hollenstein, C., Kahle, H.G. & Geiger, A. (2004). A recent tectonic reorganization in the south-central Mediterranean. *Earth and Planetary science letters, 226*, p. 335-345.

Hanks, T.C. (1977). Earthquake stress drops, ambient tectonic stresses, and the stresses that drive plates. *Pure Applied Geophysics, 115*, p. 441-458.

Hanks, T.C. (1979). *b* values and ω−γ seismic source models: Implications for tectonic stress variations along active crustal fault zones and the estimation of high-frequency strong ground motion. *Journal of Geophysical Research, 84* (B5), p. 2235-2242.

Hanks, T.C., & McGuire, R.K. (1981). The character of high frequency groun-motion. *Bulletin of the Seismological Society of America, 71*, p. 2071-2095.

Hanks, T. C. (1982). f max. *Bulletin of the Seismological Society of America, 72,* p. 1867-1879.

Harrison, R.W., Tsiolakis, E., Stone, B.D., Lord, A., McGeehin, J.P., Maha, S.A., & Chirico, P. (2013). Late Pleistocene and Holocene uplift history of Cyprus: implications for active tectonics along the southern margin of the Anatolian microplate. In: Robertson, A.H.F., Parlak, O., & Unlugenc, U.C. (eds) *Geological Development of Anatolia and the Easternmost Mediterranean Region. Geological Society, London, Special Puclications, 372,* p 561-584. DOI: 10.1144/SP372.3.

Harsch, W., & Kuepfer, T. (1980). Seismotectonic implications of relative motions between the African, Arabian and Turkish plates. *Proceedings to the Seventh World Conference on Earthquake Engineering,* September 8–13, 1980, Istanbul, pp. 253–260.

Haslinger, F. (1998). *Velocity structure, seismicity and seismotectonics of northwestern Greece between the Gulf of Arta and Zakynthos*. PhD Thesis: Swiss Federal Institute of Technology Zurich.

Hatzfeld, D., Besnard, M., Makropoulos, K., & Hatzidimitriou, P. (1993). Microearthquake seismicity and fault-plane solutions in the southern Aegean and its geodynamic implications. *Geophysical Journal International, 115*, p 799-818.

Hatzfeld, D.., Kassaras, L., Panagiotopoulos, D., Amorese, D., Makropoulos, K., Karakaisis, G., & Coutand, O. (1995). Microseismicity and strain pattern in north-western Greece. *Tectonics, 14*, p 773-785. DOI: 10.1029/95TC00839.

Hatzfeld, D., Kementzetzidou, D., Karakostas, V., Ziazia, M., Nothard, S., Diagourtas, D., Deschamps, A., Karakaisis, G., Papadimitriou, P., Scordilis, M., Smith, R., Voulgaris, N., Kiratzi, S., Makropoulos, K., Bouin, M.P., & Bernard, P. (1996). The Galaxidi Earthquake of 18 November 1992: A Possible Asperity within the Normal Fault System of the Gulf of Corinth (Greece). *Bulletin of the Seismological Society of America,86* (6), p 1987-1991.

Hatzfeld, D., Karakostas, V., Ziazia, M., Kassaras, I., Papadimitriou, E., Makropoulos, K., Voulgaris, N., & Papaioannou, C. (2000). Microseismicity and faulting geometry in the Gulf of Corinth (Greece). *Geophysical Journal International, 141*, p. 438-456.

Hartzell, S. (1978). Earthquake aftershocks as Green's functions. G*eophysical Research Letters, 5,* p. 1–14. https://doi.org/10.1029/GL005i001p00001.

Heaton, T., & Hartzell, S. (1986). Source characteristics of hypothetical subduction earthquakes in the Northwestern United States. *Bulletin of the Seismological Society of America, 76*, p. 675–708.

Heaton, T. (1990). Evidence for and implications of self-healing pulses of slip in earthquake rupture. *Physics of the Earth and Planetary Interiors, 64*, p. 1-20. DOI: 10.1016/0031-9201(90)90002-F.

Herrmann, R. B. (2013) Computer programs in seismology: An evolving tool for instruction and research. *Seismological research Letters, 84,* p. 1081-1088. DOI:10.1785/0220110096

Himmerkus, F., Reischmann, T., & Kostopoulos, T. (2009). Triassic rift-related meta-granites in the Internal Hellenides, Greece. *Geology magazine, 146*(2), p. 252-265.

Jackson, J.A., & McKenzie, D.P. (1983). The geometrical evolution of normal fault systems. *Journal of structural Geology, 5,* p. 471–482.

Jackson, J.A., & McKenzie, D. (1988a). Rates of active deformation in the Aegean Sea and surrounding areas. *Basin research, 1*, p 121-128.

Jackson, J., & McKenzie, D.P. (1988b). The relationships between plate motions and seismic moment tensors and the rates of active deformation in the Mediterranean and Middle East. *Geophysical Journal of the Royal Astronomical Society, 93,* p 45-73. DOI:10.1111/j.1365-246X.1988.tb01387.x

Jackson, J. (1994). Active tectonics of the Aegean region. *Annual Reviews of Earth and Planetary Science, 22*, p. 239-271. DOI: 10.1146/annurev.ea.22.050194.001323

Jeon Y.S., & Herrmann, R.B. (2004). High-frequency ground-motion scaling in Utah and Yellowstone. *Bulletin of the Seismological Society of America*, *94,* p. 1644-1657. DOI: 10.1785/012003225

Jeon, Y.S. (2004). High frequency earthquake ground motion scaling in southeastern Canada and Korea. *Dissertation Abstracts International, 65-11,* pp 5602- 5786.

Kalogeras, I., Stavrakakis, G., & Solomi, K, (1999). The October 9, 1996 earthquake in Cyprus: seismological, macroseismic and strong motion data. *Annals of Geophysics, 42* (1), p 85-97. DOI: 10.4401/ag-3702

Karastathis, V.K., Mouzakiotis, E., Ganas, A., & Papadopoulos, G.A. (2015). High precision relocation of seismic sequences above a dipping Moho: the case of the January-February 2014 seismic sequence on Cephalonia Island (Greece). *Solid Earth, 6*, p. 173-184. DOI:10.5194/se-6-173-2015

Kaviris, G., Elias, P., Kapetanidis, V., Serpetsidaki, A., Karakonstantis, A., Plicka, V., De Barros, L., Sokos, E., Kassaras, I., Sakkas, V., et al. (2021). The Western Gulf of Corinth (Greece) 2020–2021 Seismic Crisis and Cascading Events: First Results from the Corinth Rift Laboratory Network, *The Seismic Record.* 1, 85–95. DOI: 10.1785/0320210021.

Kempler, D., & Abvraham, B. (1987). The tectonic evolution of the Cyprian Arc. *Annales Tectonicae, 1*, p. 58-71.

Khair, K., & Tsokas, G.N. (1997). *The Levantine (eastern Mediterranean) crust by multiple source Werner deconvolution estimates of Bouguer gravity anomalies.* IASPEI 29th General Assembly, Thessaloniki, 18–28 August 1997 (abstracts volume).

Kilias, A.A., Tranos, M.D., Orozco, M., Alonso-Chaves, F.M., & Soto, J.I. (2002). Extensional Collapse of the Hellenides: A Review. *Revista Sociedad Geologica de Espana, 15*(3-4), p. 129-139.

King, G.C.P., Ouyang, Z.X., Papadimitriou, P., Deshamps, A., Gagnepain, J., Houseman, G., Jackson, J.A., Soufleris, C., & Virieux, J. (1985). The evolution of the Gulf of Corinth (Greece): an aftershock study of the 1981 earthquakes. *Geophysical Journal of the Royal Astronomical Society, 80,* p. 677-693. https://doi.org/10.1111/j.1365-246X.1985.tb05118.x

Kokinou, E., Moisidi, M., Tsanaki, I., Tsakalaki, E., Tsiskaki, E., Sarris, A., & Vallianatos, F. (2008). A seismotectonic study for the Heraklion basin in Crete (southern Hellenic Arc, Greece). *International Journal of Geology, 2* (1), p 9-15.

Kottke, A.R., & Rathje, E.M. (2013). Comparison of time-series and Random-Vibration Theory site response methods. *Bulletin of the Seismological Society of America, 103*(3), p. 2111-2127. DOI: 10.1785/0120120254

Koukouvelas, I., Mpresiakas, A., Sokos, E., & Doutsos, E. (1996). The tectonic setting and earthquake ground hazards of the 1993 Pyrgos earthquake, Peloponnese, Greece. *Journal of the Geological Society, 153*, p. 3949. doi:10.1144/gsjgs.153.1.0039

Kramer, S.L. (1996). *Geotechnical Earthquake Engineering*. Prentice Hall, Upper Saddle River, NJ.

Kythreoti, S., & Pilakoutas, K. (2002). *Earthquake Risk Assessment Case Study: Cyprus*. Unpublished PhD thesis, University of Sheffield.

Laj, C., Jamet, M., Sorel, D., & Valente, J.P. (1982). First paleomagnetic results from Mio-Pliocene series of the Hellenic sedimentary arc. *Tectonophysics, 86,* p. 45-68.

Latorre, D., Virieux, J., Monfret, T., Monteiller, V., Vanorio, T., & Got, J..L. A new seismic tomography of Aigion area (Gulf of Corinth, Greece) from the 1991 data set. *Geophysical Journal International, 159* (3), pp.1013-1031. DOI: 10.1111/j.1365-246X.2004.02412.xff.ffhal-00109358.

Lay, T., & Wallace, T.C. (1995). *Modern Global Seismology*. California:

Academic Press.

Lekidis, V.A., Karakostas, C.Z., Dimitriu, P.P., Margaris, B.N., Kalogeras, L., & Theodulidis, N. (1999). The Aigio (Greece) seismic sequence of June 1995: Seismological, strong motion data and effects of the earthquakes on structures. *Journal of Earthquake Engineering, 3(*3), p 349-380. DOI: 10.1080/13632469909350351

Lentini, F., Carbone, S. & Guarnieri, P. (2006). Collisional and postcollisional tectonics of the Apennic-Maghrebian oregen (southern Italy). In: Y. Diley & S, Paulides (eds.). *Postcollisional tectonics and magmatism in the Mediterranean region and Asia: Geological Society of America Special Paper 409***,** p. 57-81.

Le Pichon, X., & Angelier, J. (1979). The Hellenic Arc and trench system: a key to the neotectonic evolution of the Eastern Mediterranean area, *Tectonophysics, 60*, p 1-42. DOI: 10.1016/0040-1951(79)90131-8

Le Pichon, X.,Chamot-Rooke, N., & Lallemant, S. (1995). Geodetic determination of the of the kinematics of central Greece with respect to Europe: Implications for eastern Mediterranean tectonics. *Journal of Geophysical Research, 100* (B7), p. 12,675-12,690. DOI: 10.1029/95JB00317

Limanov, A.F., Woodside, J.M., Cita, M.B., & Ivanov, M.K. (1996). The Mediterranean Ridge and related mud diapirism: a background. *Marine Geology, 132*(1-4), p. 7-19.

Madaraiga, R. (1977). Implications of stress-drop models of earthquakes for the Inversion of stress drop from seismic observations. *Pure and Applied Geophysics, 115*, p. 301-316.

Makris, J. (1978). The crust and upper mantle of the Aegean region from deep seismic surroundings. *Tectonophysics, 46*, p 269-284.

Makris, J. (1981). Deep structure of the Eastern Mediterranean deduced from refraction seismic data. Eo*s Transactions American Geophysical Union, 62* (17), p 1-42.

Makris, J., & Stobbe, C. (1984). Physical properties and state of the crust and upper mantle of the eastern Mediterranean sea deduced from geophysical data. *Marine Geology, 55,* p. 347-363. DOI: 10.1016/0025-3227(84)90076-8

Makris, J., Stacker, J., & Gaye, M. (1997). *The normal seismicity of the Paphos area, Cyprus.* Report of the University of Hamburg, Institute of Geophysics.

Makris, J., Papoulia, J., & Drakatos, G. (2004). Tectonic Deformation and Microseismicty of the Saronikos Gulf, Greece. *Bulletin of the Seismological Society of America, 94* (3), p. 920-929. DOI: 10.1785/0120020209

Makropoulos, K.C., & Burton, P.W. (1984). Greek tectonics and seismicity. *Tectonophysics, 106*, p 275-304. https://doi.org/10.1016/0040-1951(84)90181-1

Makropoulos, K.C., & Burton, P.W. (1985). Seismic hazard in Greece. II. Ground acceleration. *Tectonophysics, 117*, p. 259–94.

Makropoulos, K., Voulgaris, N., & Likiardopoulos, A. (1990). A multi-methodological approach to seismic hazard assessment: An application for Athens (Greece). *Proceedings of the XXII Gen. Ass. ESC. Barcelona.* p. 585–591.

Malagnini, L. (1999). Ground motion scaling in Italy and Germany. *Dissertation Abstracts International, 60-08*, pp 3816-3987.

Malagnini, L.,. Hermann, R.B., & Di Bona, M. (2000a). Ground-motion scaling in the Apennines (Italy). *Bulletin of the Seismological Society of America*, *90*, p. 1062–1081. DOI: 10.1785/0119990152

Malagnini, L., Herrmann, R.B., & Koch, K. (2000b). Regional ground motion in scaling in Central Europe. *Bulletin of the Seismological Society of America*, *90*, p. 1052– 1061.

Malagnini, L., & Herrmann, R.B. (2000c). Ground motion scaling in the region of the 1997 Umbria-Marche earthquake (Italy), *Bulletin of the Seismological Society of America*, *90*, p.1041–1051. https://doi.org/10.1785/0119990150

Malagnini, L., Akinci, A., Hermann, R.B., Pino, N.A., & Scognamiglio, L. (2002). Characteristics of the ground motion in Northeastern Italy, *Bulletin of the Seismological Society of America*, *92*, p. 2186–2204. DOI: 10.1785/0120010219

Malagnini, L., Mayeda, K., Uhrhammer, R., Akinci, A., & Herrmann, R. (2007). A regional ground motion excitation/attenuation model for the San Francisco region. *Bulletin of the Seismological Society of America, 97*. https://doi.org/10.1785/0120060101

Malagnini, L., Akinci, A., Mayeda, K., Munafo, I., Hermann, R., & Mercuri, A. (2011). Characterization of earthquake-induced ground motion from the L'Aquila seismic sequence of 2009, Italy. *Geophysical Journal International, 184*, pp 325-337. doi: 10.1111/j.1365-246X.2010.04837.x

Mancilla, F., Hermann, R.B., Morales, J., & Stitch, D. (2008). Vertical ground motion in Southern Spain. *Bulletin of the Seismological Society of America, 98* (2), pp 733-745. DOI: 10.1785/0120070091

Maratos, G. (1972). *Geology of Greece*. University of Athens: Athens.

Margaris, V.N. (1994). *Azimuthal dependence of the seismic waves and its influence on the seismic hazard assessment in the area of Greece*. PhD Thesis: Thessaloniki University.

Margaris, B.N., & Hatzidimitriou, P.M. (2002). Source Spectral scaling and stress release estimates using strong-motion records in Greece. *Bulletin of the Seismological Society of America, 92*(3), p 1040-1059. DOI:10.1785/0120010126

Margaris, B. N.,. Papazachos, C. B, Papaioanou, C.A, Theodoulidis, N., Kalogeras, I., & Skarlatoudis, A.A (2002). Ground motion attenuation relations for shallow earthquakes in Greece. In: *Proceedings of the 12th European Conference on Earthquake Engineering, 9-13, September, London*.

McClusky, S., Balassanian,S., Barka, A., Demir, C., Ergintav, S., Georgiev, I., Gurkan, O., Hamburger, M., Hurst, K., Kahle, H., Kastens, K., Kekelidze, G., King, R., Kotzev, V., Lenk, O., Mahmoud, S., Mishin, A., Nadariya, M., Ouzounis, A., Paradissis, D., Peter, Y., Prilepin, M., Reilinger, R., Santli, I., Seeger, H., Tealed, A., Toksoz, M.N., & Veis, G. (2000). Global Positioning System constraints on plate kinematics and dynamics in the eastern Mediterranean and Caucasus. *Journal of Geophysical Research, 105,* p. 5695-5719. DOI: 10.1029/1996JB900351

McKenzie, D. P. (1970). Plate tectonics of the Mediterranean region. *Nature, 220,* p. 239–343.

McKenzie, D. P. (1972). Active tectonics of the Mediterranean region. *Royal Astronomical Society Geophysical Journal, 30*, p. 109-182. https://doi.org/10.1111/j.1365-246X.1972.tb02351.x

McKenzie, D.P. (1978). Active tectonics of the Alpine-Himalayan belt: the Aegean Sea and the surrounding regions. *Geophysical Journal of the Royal Astronomical Society, 55*, p 217-254.

Meletti, C., Patacca, E., & Scandone, P. (2000). Construction of a seismotectonic model: The case of Italy. *Pure Applied Geophysics, 157*, p. 11-35. DOI: 10.1007/PL00001089

Melis, N.S., Brooks, M. & Pearce, R.G., 1989. A microearthquake study in the Gulf of Patras region, western Greece, and its seismotectonic interpretation, *Geophysical Journal of the Royal Astronomical Society, 98,* p. 515-524. DOI:10.1111/j.1365-246X.1989.tb02286.x

Melis, N.S., Burton, P.W., & Brooks, M. (1995). Coseismic crustal deformation from microseismicty in the Patras area, western Greece. *Geophysical Journal International, 122*, p. 815-836. DOI:10.1111/j.1365-46X.1995.tb06840.x

Moores, E.M., & Vine, F.J. (1971). The Troodos massif, Cyprus, and other ophiolites as oceanic crust: evaluation and implications*. Philosophical Transactions of the Royal Society London, series A 268*, p. 443-466.

Morasca P., Malagnini, L., Akinci A., Spallarossa, D., & Herrmann, R.B. (2006). Ground motion scaling in the western Alps. *Journal of Seismology, 10,* p. 315-333. DOI 10.1007/s10950-006-9019-x

Moretti, I., Sakellariou, D., Lykousis, V., & Micarelli, L. (2003). The Gulf of Corinth: an active half graben? *Journal of Geodynamics, 36,* p. 323-340.

Motazedian, D. (2002). *Development of earthquake ground motion relations for Puerto Rico,* Ph.D. Thesis, Carleton University, Ottawa, Ontario, Canada.

Motazedian, D., & Atkinson, G.M. (2005). Stochastic Finite-Fault Modeling Based on a Dynamic Corner Frequency. *Bulletin of the Seismological Society of America, 95* (3), p 995-1010. DOI: 10.1785/0120030207

Mountrakis, D., Tranos, M., Papazachos, C., Thomaidou, E., Karagianni, E., & Vamvakaris, D. (2006). Neotectonic and seismological data concerning major active faults, and the stress regimes of Northern Greece. In: Robertson, A.H.F., & Mountrakis, D. (eds.) Tectonic Development of the Eastern Mediterranean Region. *Geological Society, London, Special Publications, 260*, p 649-670.

Nur, A., & Cline, E.H. (2000). Poseidon's Horses: Plate tectonics and Earthquake storms in the Late bronze Age Aegean and Eastern Mediterranean. *Journal of Archaeological Science, 27*, p 43-63. DOI:10.1006/jasc.1999.0431

Ortega, R., Herrmann, R. B. & Quintanar, L. (2003). Earthquake ground-motion scaling in Central Mexico between 0.7 and 7 Hz. *Bulletin of the Seismological Society of America*, *93*, p. 397–413. DOI: 10.1785/0120010279

Oth, A., Miyake, H., & Bindi, D. (2017). On the relation of earthquake stress drop and ground motion variability. *Journal of Geophysical Research: Solid Earth, 122,* p. 5474-5492. DOI:10.1002/2017JB014026.

Panzera, F., D'Amico, S., Lombardo, G., & Longo, E. (2016). Evaluation of building fundamental periods and effects of local geology on ground motion parameters in the Siracusa area, Italy. *Journal of Seismology, 20* (3), p. 1001-1019. DOI 10.1007/s10950-016-9577-5

Papadimitriou, E.E,. & Karakostas, V.G. (2006). Earthquake generation in Cyprus revealed by the evolving stress field. *Tectonophysics, 432*, p 61-72. DOI: 10.1016/j.tecto.2006.03.014

Papadopoulos, G.A., & Arvanitides, A. (1996). Earthquake risk assessment in Greece. In: Schenk, V. (ed.) *Earthquake hazard and risk*, Kluwer: The Netherlands, p. 221-229. DOI: 10.1007/978-94-009-0243-5_15

Papadopoulos, G.A. (2000). *Historical earthquakes and tsunamis in the Corinth Rift, Central Greece.* National Observatory of Athens, Institute of Geodynamics, Publication number 12, p 128.

Papadopoulos, G.A. (2002). Tsunami Hazard in the eastern Mediterranean: Strong earthquakes and tsnuamis in the Corinth Gulf, Greece. *Natural Hazards,* 29 (93), p 437-464. DOI: 10.1023/A:1024703531623

Papadopoulos, G.A., Karastathis, V., Charalampakis, M., & Fokaefs, A. (2009). A storm of strong earthquakes in Greece during 2008. *EOS Transcations American Geophysical Union, 90*(46), p 425-440.

Papadopoulos, G.A., Karastathis, V., Kontoes, C., Charalampakis, M., Fokaefs, A., & Papoutsis, I. (2010). Crustal deformation associated with east Mediterranean strike-slip earthquakes: The 8 June 2008 Movri (NW Peloponnese), Greece, earthquake M (6.4). *Tectonophysics, 492*, p 201-212. DOI: 10.1016/j.tecto.2010.06.012

Papaioannou, C.A. (1984). *Attenuation of seismic intensities and seismic hazard in the area of Greece*. PhD Thesis: Thessaloniki University.

Papanastassiou, D. (1999). Seismic Hazard Assessment in the area of MystrasSparta, South Peloponnesus, Greece, based on local seismotectonic, seismic, geologic information and on different models of rupture propagation. *Natural Hazards, 18*, p 237-251. DOI: 10.1023/A:1026464415095

Papazachos, B.C. (1976). Evidence of crustal shortening in the Northern Aegean region. *Bulletin of Applied Theoretical and Applied Geophysics, 13*, p. 66-71.

Papazachos, B.C. (1990). Seismicity of the Aegean and surrounding area, *Tectonophysics, 178*, p. 287-308.

Papazachos, B.C., Kiratzi, A.A., & Papadimitriou, E.E. (1991). Regional focal mechanisms for earthquakes in the Aegean area. *Pure and Applied Geophysics, 136*, p. 405-420. DOI: 10.1007/BF00878578

Papazachos, B.C., & Papaioannou, C.A. (1993). Regionalization of Seismic Hazard in Greece based on seismic sources. *Natural Hazards, 8*, p 1-18. DOI: 10.1007/BF00596232

Papazachos, C.B., & Kiratzi, A.A. (1996). A detailed study of the active crustal deformation in the Aegean and surrounding area. *Tectonophysics, 253,* p 129-153.

Papazachos, B. & Papazachou, C. (1997). *The Earthquakes of Greece*. Ziti Publications: Thessaloniki.

Papazachos, B.C., & Papaioannou, Ch.A. (1999). Lithospheric boundaries and plate motions in the Cyprus area. *Tectonophysics, 308*, p 193-204. DOI:10.1016/S0040-1951(99)00075-X

Patacca, E., & Scandone, P. (2007). Geology of the Southern Apennines*. Italian Journal of Geosciences, 7,* p. 75-119.

Payne, A.S., & Robertson, A.H.F. (1995). Neogene supra-subduction zone extension in the Polis graben system, west Cyprus. *Journal of the Geological Society, London, 152*, p 613-628. https://doi.org/10.1144/gsjgs.152.4.0613

Peterek, A., & Schwarze, J. (2004). Architecture and Late Pliocene to recent evolution of outer-arc basins of the Hellenic subduction zone (south-central Crete, Greece). *Journal of Geodynamics, 38*(1), p. 19-55.

Piccardi, L. (2000). Active faulting at Delphi, Greece: Seismotectonic remarks and a hypothesis for the geologic environment of a myth. *Geology, 28*(7), p 651-654. DOI: 10.1130/0091-7613

Platt, J.P., van den Eeckhout, B., Jansen, E., Konert, G., Simon, O.J., & Weijermars, R. (1983). The structure and tectonic *evolution of the Aguilon fold-nappe, Sierra Alhamilla, Betic Cordilleras, SE Spain. Journal of structural Geology, 5,* p. 519-538.

Platt, J.P., & Vissers, R.L.M. (1989). Extensional collapse of thickened continental lithosphere: A working hypothesis for the Alboran Sea and Gibraltar Arc. *Geology, 17,* p. 540-543.

Pondrelli, A., Morelli, A., & Boschi, E. (1998). Distribuzione della seismicita e area seismogenetiche nel Mediterraneo e in Europa*. ING Publication, 549*, p. 1-13.

Presti, D., Billi, A., Orecchio, B., Totaro, C., Faccenna, C. & Neri, G. (2013). Earthquake focal mechanisms, seismogenic stress, and seismotectonics of the Calabrian Arc, Italy. *Tectonophysics, 602*, p. 153-175. https://doi.org/10.1016/j.tecto.2013.01.030

Raoof, M., Hermann R. B., & Malagnini, L. (1999). Attenuation and excitation of three-component ground motion in southern California. *Bulletin of the Seismological Society of America*, *89*, p. 888–902.

Rathje, E.M., Faraj, F., Russell, S., & Bray, J.D.(2004). Empirical *relationships for frequency content parameters of earthquake ground motions. Earthquake spectra, 20* (1), p. 119-144.

Rathje, E.M., & Ozbey, M.C. (2006). Site-specific validation of random vibration theory-based seismic site response analysis. *Journal of Geotechnical and Geoenvironmental Engineering, 132(7*), p. 911-922.

Reilinger, R., & McClusky, S.C. (2000). GPS constraints on present-day plate motions and deformation in the eastern Mediterranean/ Caucasus region. *EOS Transactions American Geophysical Union, 81*(48).

Reitbrock, A., Tiberi, C., Scherbaum, F., & Lyon-Caen, H. (1996). Seismic slip on a low angle normal fault in the Gulf of Corinth: Evidence from high resolution cluster analysis of microearthquakes. *Geophysical Research Letters, 23* (14), p. 1817-1820. https://doi.org/10.1029/96GL01257

Reiter, l. (1991). *Earthquake Hazard Analysis: Issues and Insights*. Columbia University Press: USA.

Rigo, A., Lyon-Caen, H., Armijo, R., Deschamps, A., Hatzfeld, D., Makropoulos, K., Papadimitriou, P., & Kassaras, I. (1996). A microseismic study in the western part of the Gulf of Corinth (Greece): implications for large scale normal faulting mechanisms. *Geophysical Journal International, 126*, p. 663-688.

Ritsema, A.R. (1974). The earthquake mechanism of the Balkan region. *Netherlands Meteorological Institute. Sci. Rep, 74* (4), p. 1-36.

Roberts. S. & Jackson, J. A. (1991). Active normal faulting in central Greece: an overview. In: Roberts, A. M., Yielding, G., & Freeman, B. (eds). The Geometry of Normal Faults. *Geological Society London: Special Publications, 56*, p. 125-142.

Rosenbaum, G., Lister, G. S. & Duboz, C. (2002). Reconstruction of the tectonic evolution of the western Mediterranean since the Oligocene. In: Rosenbaum, G. and Lister, G. S. (eds) (2002). Reconstruction of the evolution of the Alpine-Himalayan Orogen. *Journal of the Virtual Explorer, 8,* p. 107 - 130.

Sabetta, F., & Pugliese, A. (1987). Attenuation of peak horizontal acceleration and velocity from Italian strong-motion records. *Bulletin of the Seismological Society of America*, *77*, p. 1491–1511.

Sabetta, F., & Pugliese, A. (1996). Estimation of response spectra and simulation of nonstationary earthquake ground motion. *Bulletin of the Seismological Society of America*, *86*, p. 337–352.

Scandella, L., Lai, C.G., Spallarossa, D., & Corigliano, M. (2011). Ground shaking scenarios at the town of Vicoforte, Italy. *Soil dynamics and earthquake engineering, 31,* pp 757-772.

Scarfi, L., Langer, H., & Gresta, S. (2003). High-precision relative locations of two micro-earthquake clusters in southeastern Sicily, Italy. *Bulletin of the Seismological Society of America, 93*(4), p. 1479-1497 https://doi.org/10.1785/0120020146

Scholz, C. (2002). *The mechanics of earthquakes and faulting*. (2nd ed.). Cambridge U.P.

Schneider, J. F., Silva, W. J., & Stark. C. (1993). Ground motion model for the 1989 M 6.9 Loma Prieta earthquake including effects of source, path, and site. *Earthquake Spectra, 9,* p. 251-287.

Scognamiglio, L., Malagnini, L., & Akinci, A., (2005). Ground motion scaling in eastern Sicily, Italy. *Bulletin of the Seismological Society of America*, *95*, p. 568-578. DOI: 10.1785/0120030124

Shaw, B.E. (2009). Constant stress drop from small to great earthquakes in magnitude-area scaling. Bulletin of the Seismological Society of America, 98, p. 871. DOI: 10.1785/0120080006.

Skarlatoudis, A.A., Papazachos, C.B., Margaris, B.N., Theodulidis, N., Papaiannou, C., Kalogeras, I., Scordilis, E.M., & Karakostas, V. (2003). Empirical Peak Ground-motion predictive relations for shallow earthquakes in Greece. *Bulletin of the Seismological Society of America, 93*(6), p 2591-2603. DOI: 10.1785/0120070176

Skarlatoudis, A.A., Margaris, B.N., & Papazachos, C.B. (2004). *Recent advances in Greece on strong motion networking and data processing.* The consortium of organizations for strong-motion observation systems (COSMOS) invited Workshop, California.

Singh, K., & Xie, M. (2008). *Bootstrap: A Statistical Method*. Unpublished manuscript, Rutgers University: USA. Retrieved online from:

http://stat.rutgers.edu/home/mxie/RCPapers/bootstrap.pdf

Spudich, P., Joyner, W.B., Lindh, A.G., Boore, D.M., Margaris, B.M., & Fletcher, J.B. (1999). SEA99: a revised ground motion prediction relation for use in extensional tectonic regimes. *Bulletin of the Seismological Society of America, 89* (5), p 1156-1170.

Somerville, P., Sen, M. & Cohee, B. (1991). Simulations of strong ground motions recorded during the 1985 Michoacan, Mexico and Valparaiso, Chile, earthquakes. *Bulletin of the Seismological Society of America, 81,* p. 1–27.

Stewart, I.S., & Piccardi, L. (2017). Seismic faults and sacred sanctuaries in Aegean antiquity. *Proceedings of the Geologists Association, 128* (5-6), p. 711-721.

Taymaz, T., Jackson, J.A., & Westway, R. (1990). Earthquake mechanisms in the Hellenic Trench near Crete. *Geophysical Journal International*, 102, p. 695–732. https://doi.org/10.1111/j.1365-246X.1990.tb04590.x

Taymaz, T., Jackson, J., & McKenzie, D. (1991). Active tectonics of the north and central Aegean Sea. *Geophysical Journal International, 106,* p 433490. https://doi.org/10.1111/j.1365-246X.1991.tb03906.x

Taymaz, T., Tan, O., & Yolsal, S. (2004). Active tectonics of Turkey and surroundings and seismic risk in the Marmara Sea region. In: Fujii, N., Kasahara, J., Higashihara, H., & Ogawa, K (eds.). *The Proceedings of "1st International workshop on active monitoring in the solid Earth Geophysics, extended abstract book*, p 110-115. Task group for active monitoring: Japan.

Theodulidis, N.P., & Papazachos, B.C. (1992). Dependence of strong-ground motion on magnitude-distance, site geology and macroseismic intensity for shallow earthquakes in Greece: I, peak horizontal acceleration, velocity and displacement. *Soil Dynamics and Earthquake Engineering, 11,* p 387-402. DOI:10.1016/0267-7261(94)90024-8

Theodulidis, N.P., Bard, P., Archuleta, R., & Bouchon, M. (1996). Horizontal-to vertical spectral ratio and geological conditions: the case of garner valley downhole array in southern California. *Bulletin of the Seismological Society of America, 86*, p. 306-319.

Tortorici, L., Monaco, C., Tansi, C., & Cocina, O. (1994). Recent and active tectonics in the Calabrian Arc (southern Italy). *Tectonophysics, 243*, p. 37-55.

Tselentis, G., & Danciu, L. (2008). Empirical relationships between Modified Mercalli Intensity and engineering Ground-motion Parameters in Greece. *Bulletin of the Seismological Society of America, 98*(4), p. 1863-1875. DOI: 10.1785/0120070172

Tumarkin, A., & Archuleta, R. (1994). Empirical ground motion prediction. *Ann. Geofis. 37*, p. 1691–1720

Underhill, J. R. (1989). Late Cenozoic deformation of the Hellenide foreland, western Greece. *Geological Society of America Bulletin, 101*, p. 613-634.

Vai, G.B. (2001). Structure and stratigraphy: an overview: Anatomy of an Orogen. In: Martini, P. & Vai, G.B. (eds), *Anatomy of an Orogen: the Apennines and Adjacent Mediterranean Basin.* Kluwer Academy Publisher, pp. 1532.

Valensise G. &Pantosti D. (2001). Database of potential sources for earthquakes larger than M5.5 in Italy. *Annali di Geofisica*, *44*, page 180.

Van Bemmelen, R.W. (1969). Origin of the western Mediterranean Sea. *Netherlands Journal of Geosciences, 26*, p. 13-52.

Vannucci, G., Pondrelli, S., Argnani, A., Morelli, A., Gasperini, P., & Boschi, E. (2004). An atlas of Mediterranean seismicity. *Annals of Geophysics, 47*(1), p. 247-306. https://doi.org/10.4401/ag-3276

Vidal, N.J., Marron, A., & Klaeschen, D. (2000). The structure of the Africa-Anatolia plate boundary in the Eastern Mediterranean. *Tectonics, 19*, p 723739.

Vipin, K.S., Anbazhagan, P., & Sitharam, T.G. (2009). Estimation of peak ground acceleration and spectral acceleration for South India with local site effects: probabilistic approach. *Natural Hazards Earth Systems Science, 9*, p. 865-878. https://doi.org/10.5194/nhess-9-865-2009

Wald, D.J., Quitoriano, V., Heaton, T., Kanamori, H., Scrivner, W.C., & Worder, B.C. (1999). *Shakemap Manual: Technical manual, users guide and software guide*. USGS Publication: USA. Retrieved online from:

https://pubs.usgs.gov/tm/2005/12A01/pdf/508TM12-A1.pdf

Wald D., Worden B., Quitoriano V., & Pankow K.L., (2005). Shake Map manual: technical manual, user's guide, and software guide. *U.S. Geological Survey Techiniques and Methods, book 12, section A,* 132 pp.

Wei-Haas, M.(2020). *Greece and Turkey earthquake driven by wild tectonics of the Aegean Sea.* Retrieved online from:

https://www.nationalgeographic.com/science/2020/10/greece-and-turkey-earthquake-driven-by-wild-tectonics-of-aegean-sea/

Wdowinski, S., Ben-Avraham, Z., Arvidsson, R., & Ekstrom, G. (2006). Seismotectonics of the Cyprian Arc. *Geophysical Journal International, 164*, p 176-181. DOI: 10.1111/j.1365-246X.2005.02737.x

Xypolias, P., & Koukouvelas, I.K. (2001). Kinematic vorticity and strain rate patterns associated with ductile extrusion in the Chelmos Shear zone (External Hellenides, Greece). *Tectonophysics, 338*, p. 59-77.

Yalcinkaya, E., Pinar, A., Uskuloglu, O., Tekebas, S., & Firat, B. (2012). Selecting the most suitable rupture model for the stochastic simulation of the 1999 Izmit earthquake and prediction of peak ground motions. *Soil Dynamics and Earthquake Engineering,* 42, p 1-16. DOI: 10.1016/j.soildyn.2012.05.018

Yem, L. M., Camera, L., Mascle, J., & Ribodetti, A. (2011). Seismic stratigraphy and deformational styles of the offshore Cyrenaica (Libya) and bordering Mediterranean Ridge. *Geophysical Journal International, 185*, p. 65–77. DOI: 10.1111/j.1365-246X.2011.04928.x

Zeng, Y., Anderson, J., & Yu, G. (1994). A composite source model for computing realistic synthetic strong ground motions. *Geophysical Research Letters, 21,* p. 725–728.

Appendix A

Global studies related to ground motion scaling

Utah

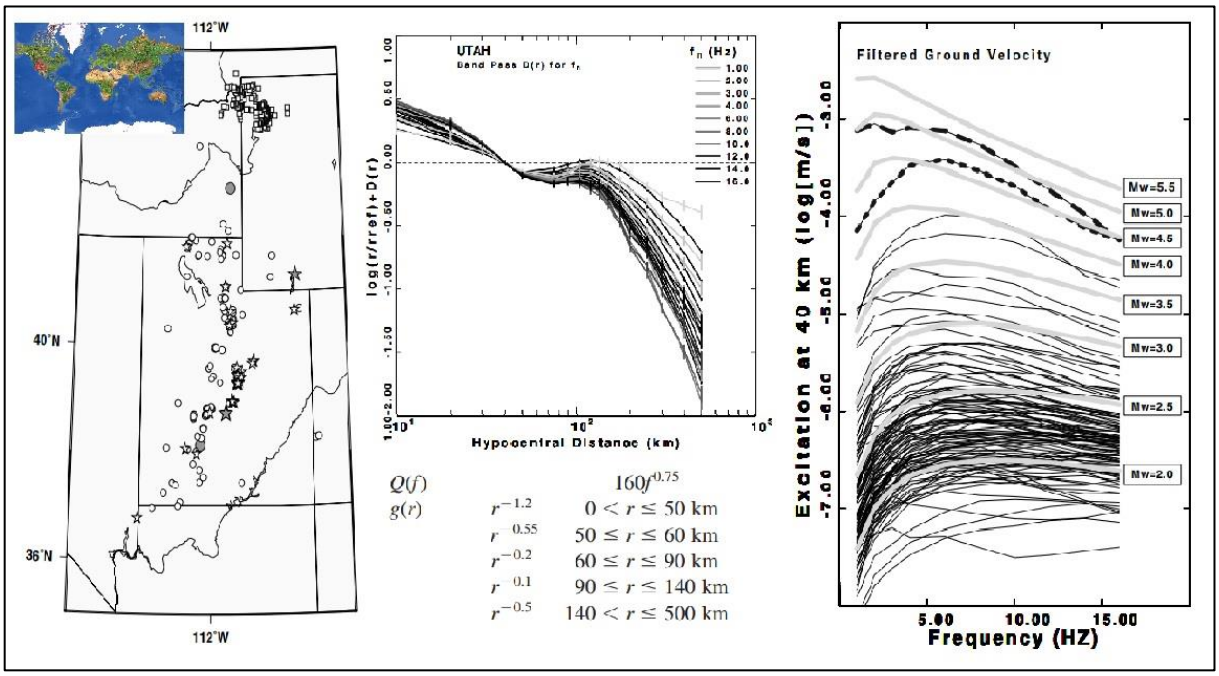

Yellowstone

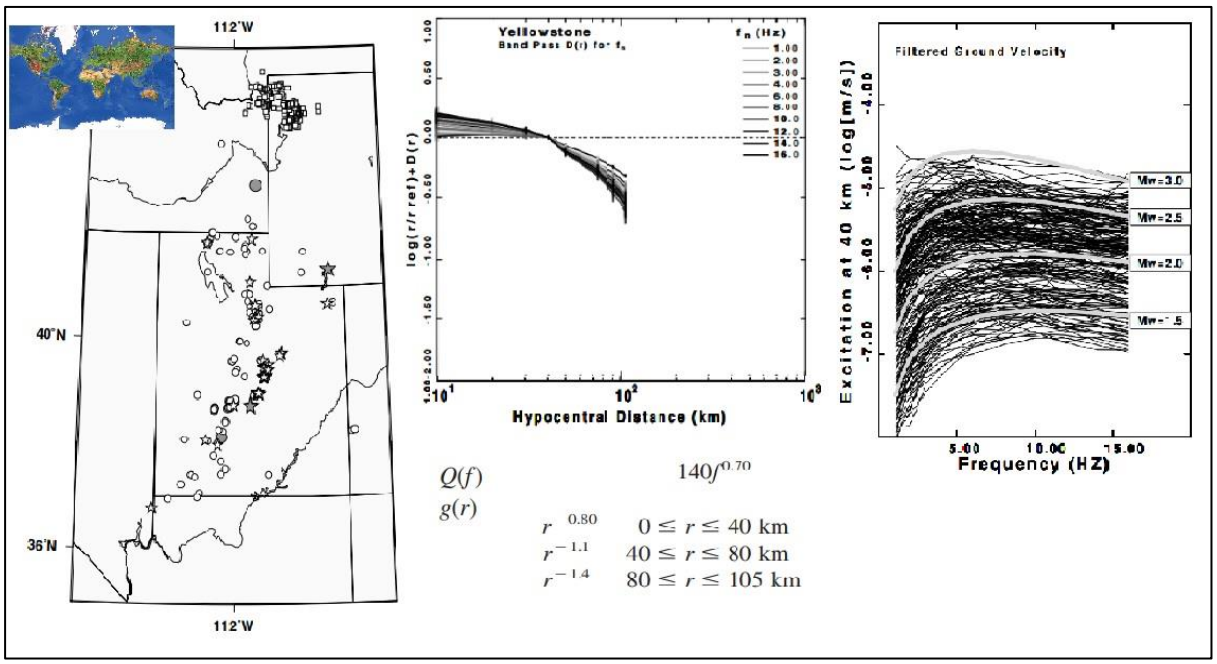

Pacific Northwest

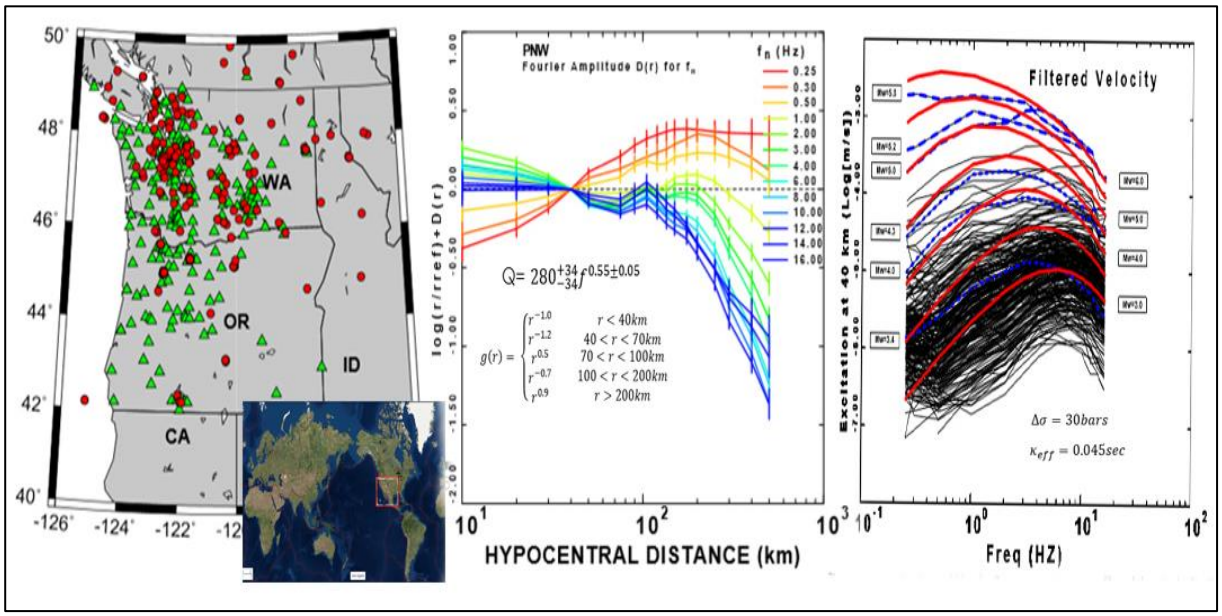

Northern California

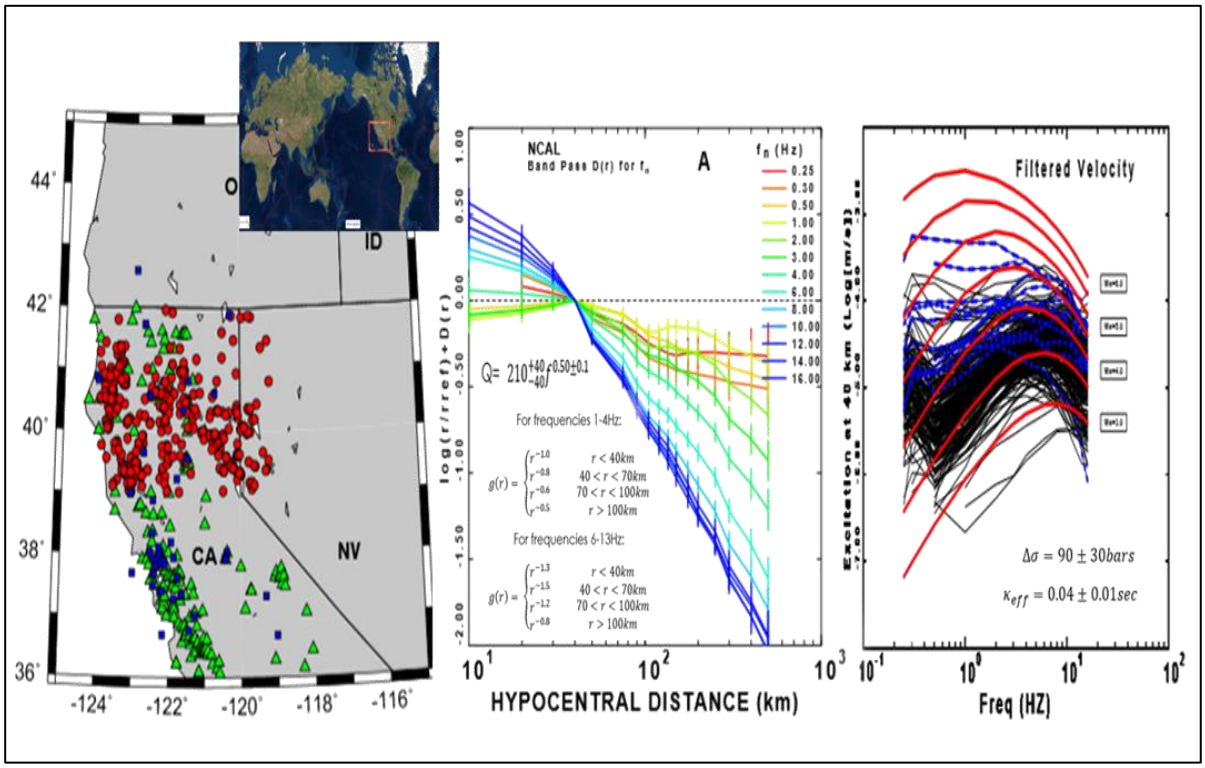

Central California

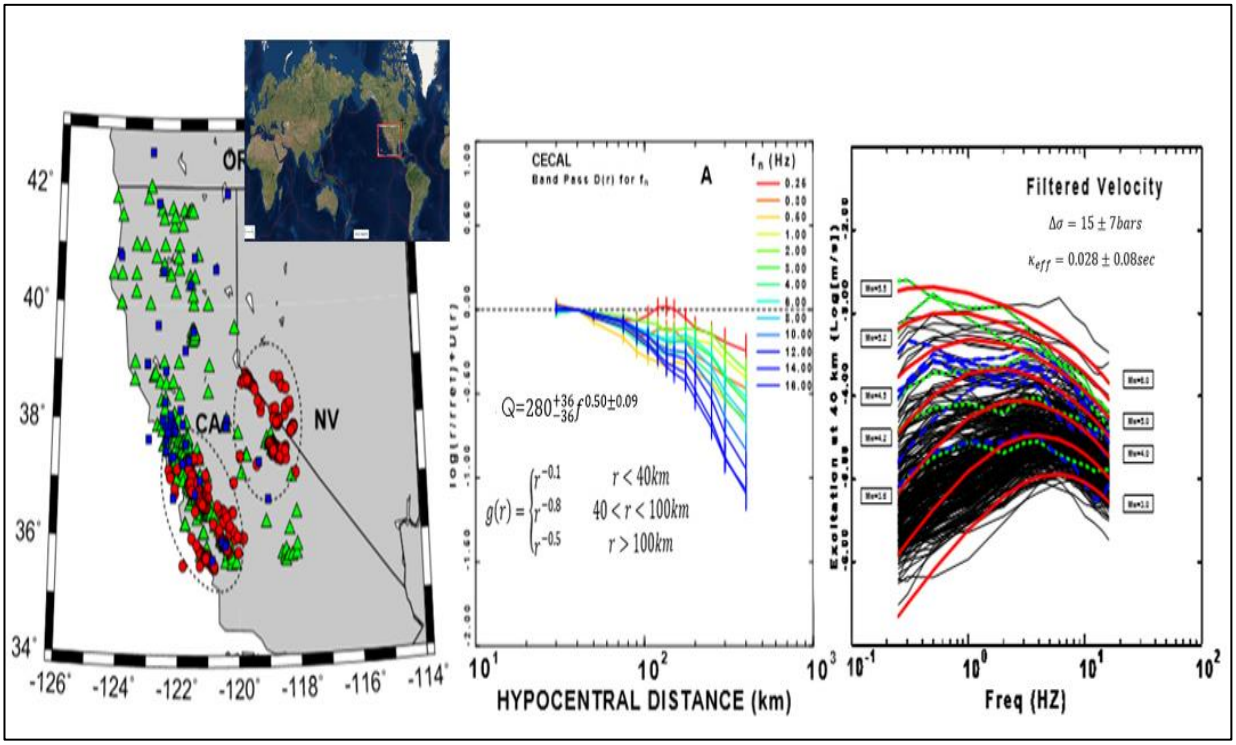

Southern California

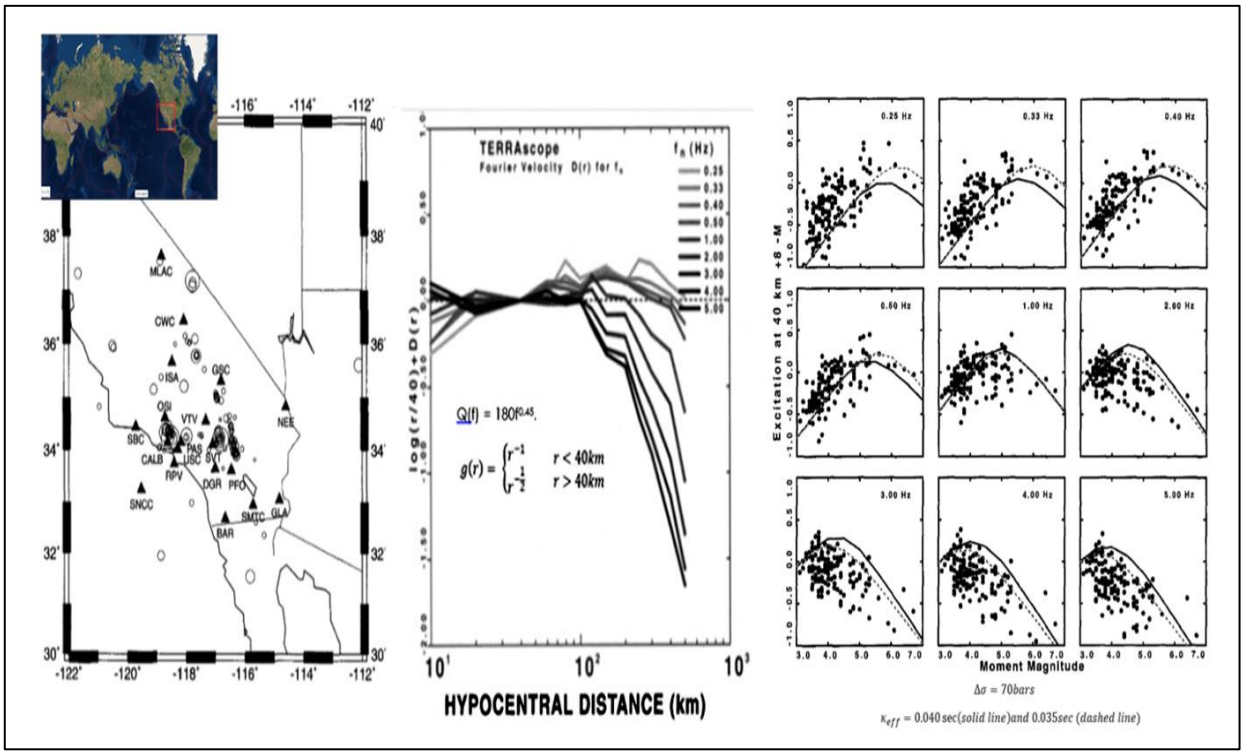

San Francisco

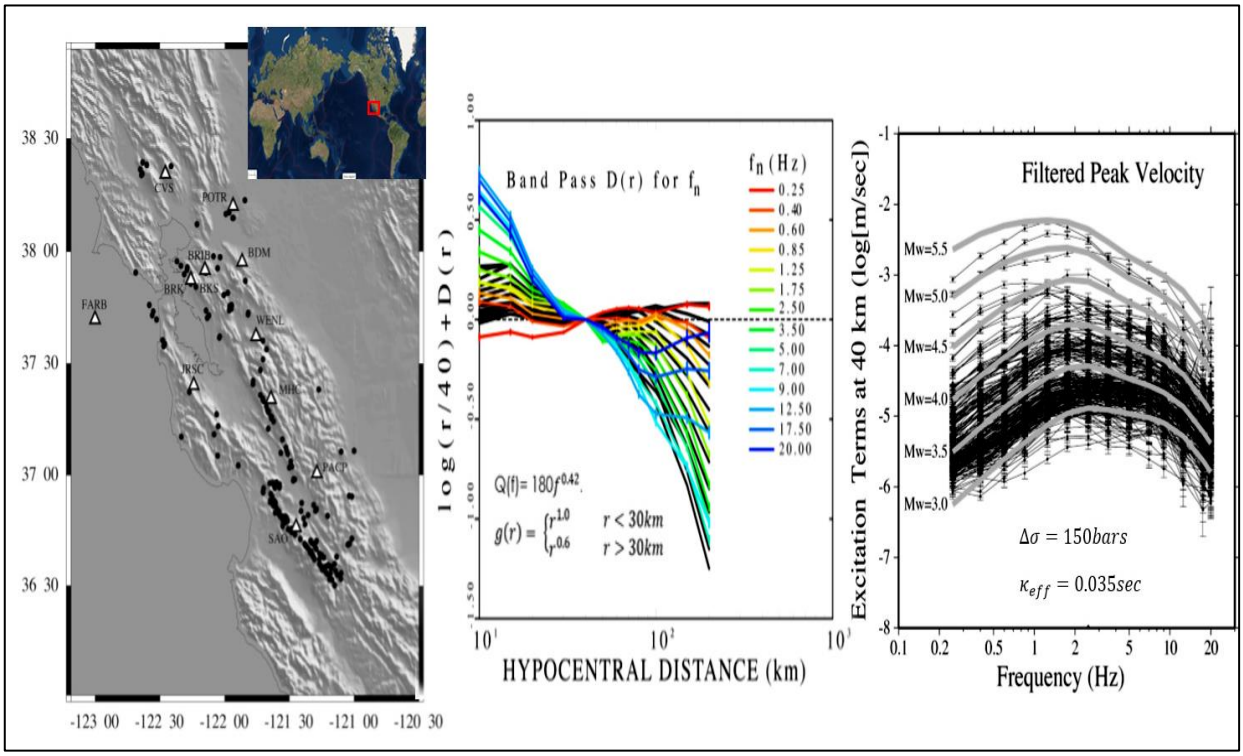

Mexico

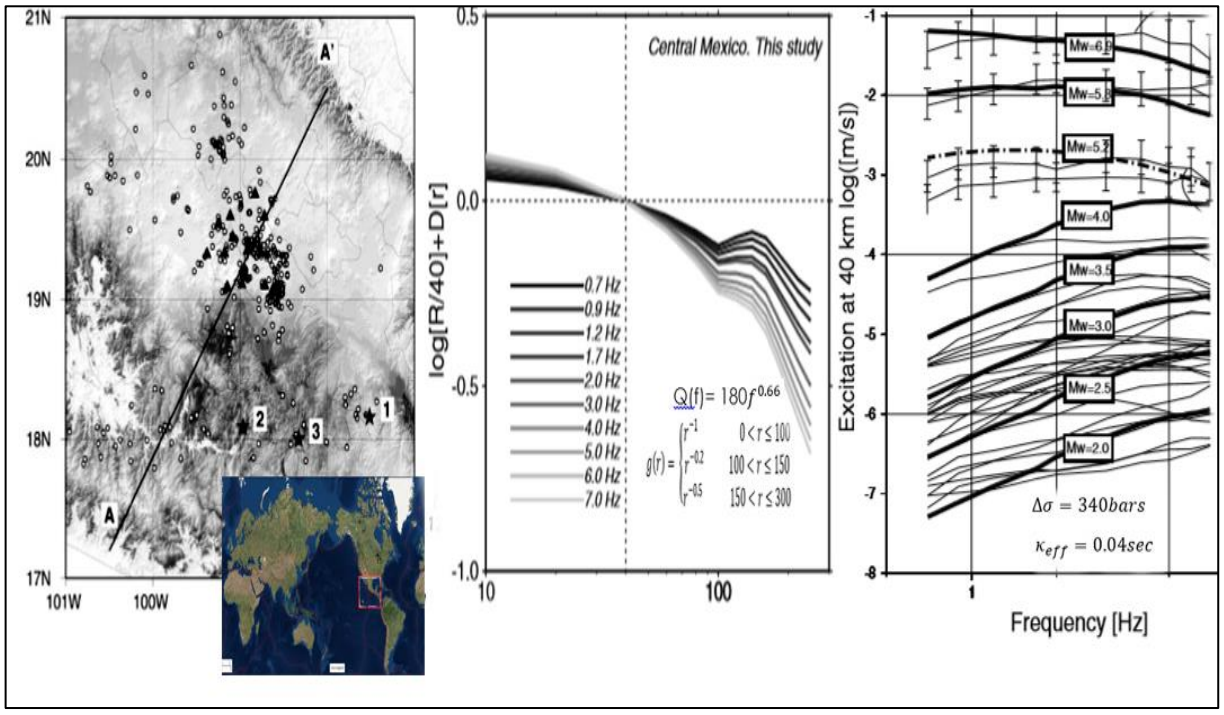

Spain

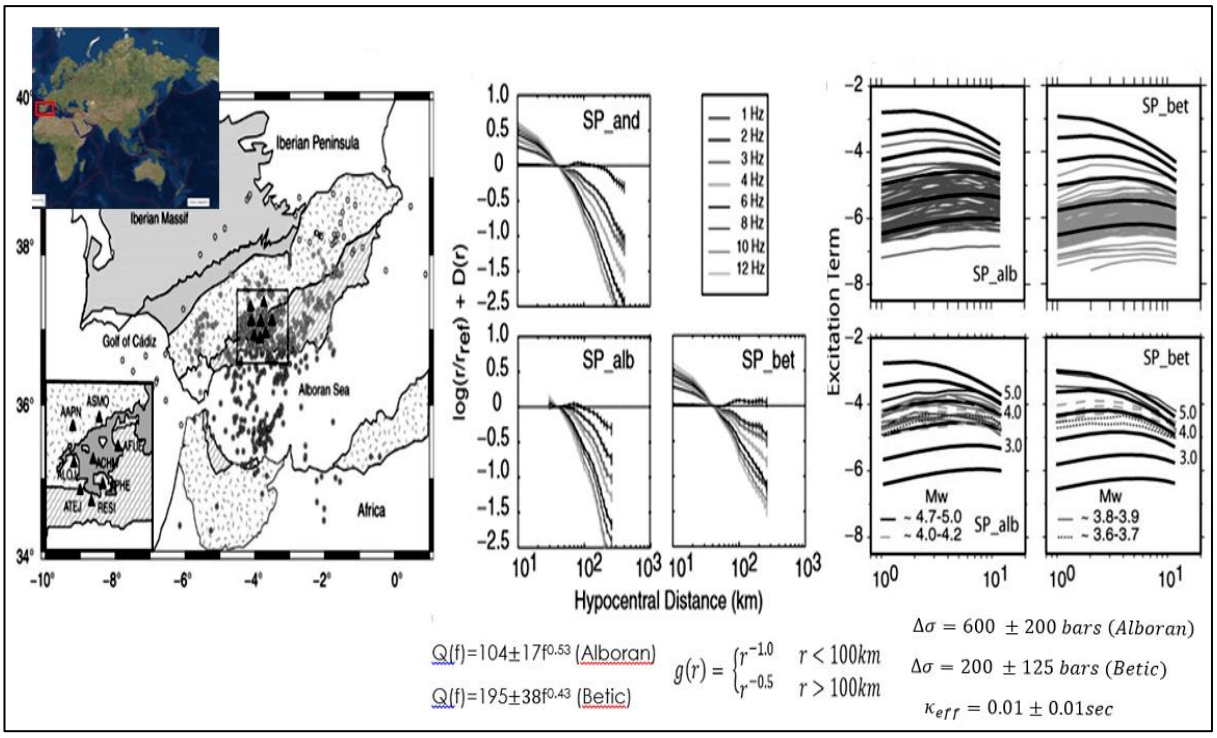

Germany

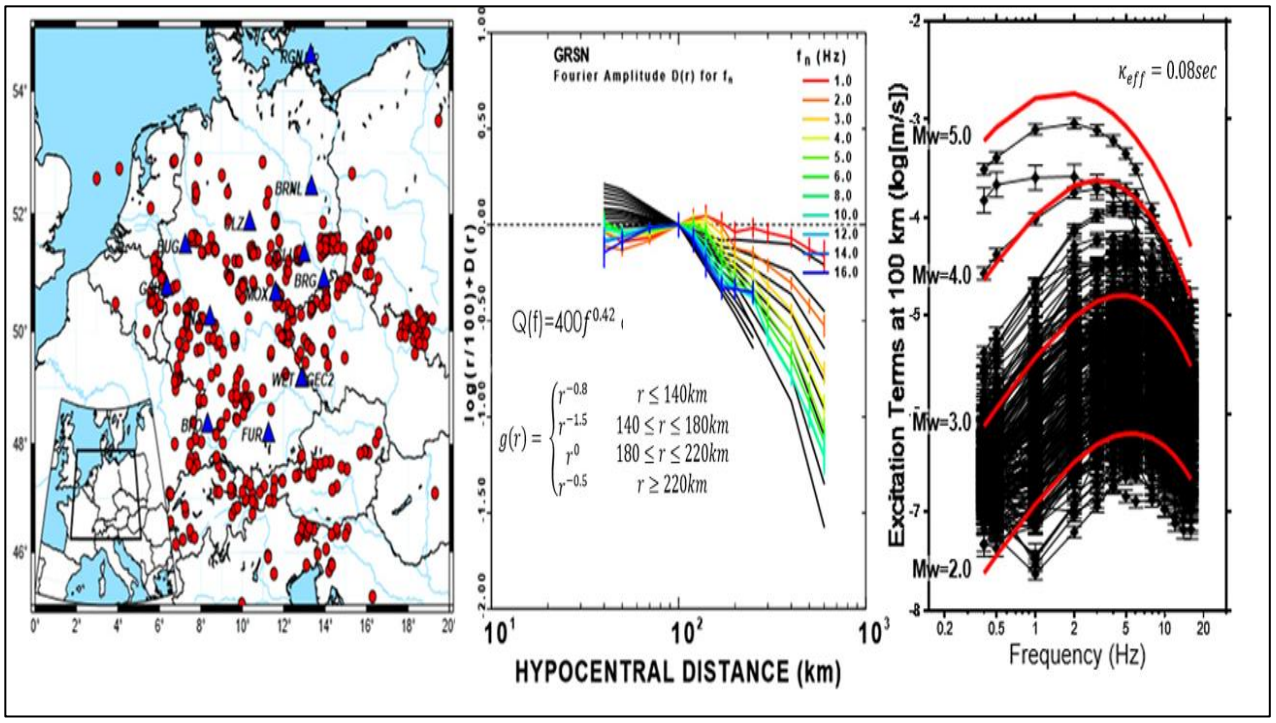

Switzerland

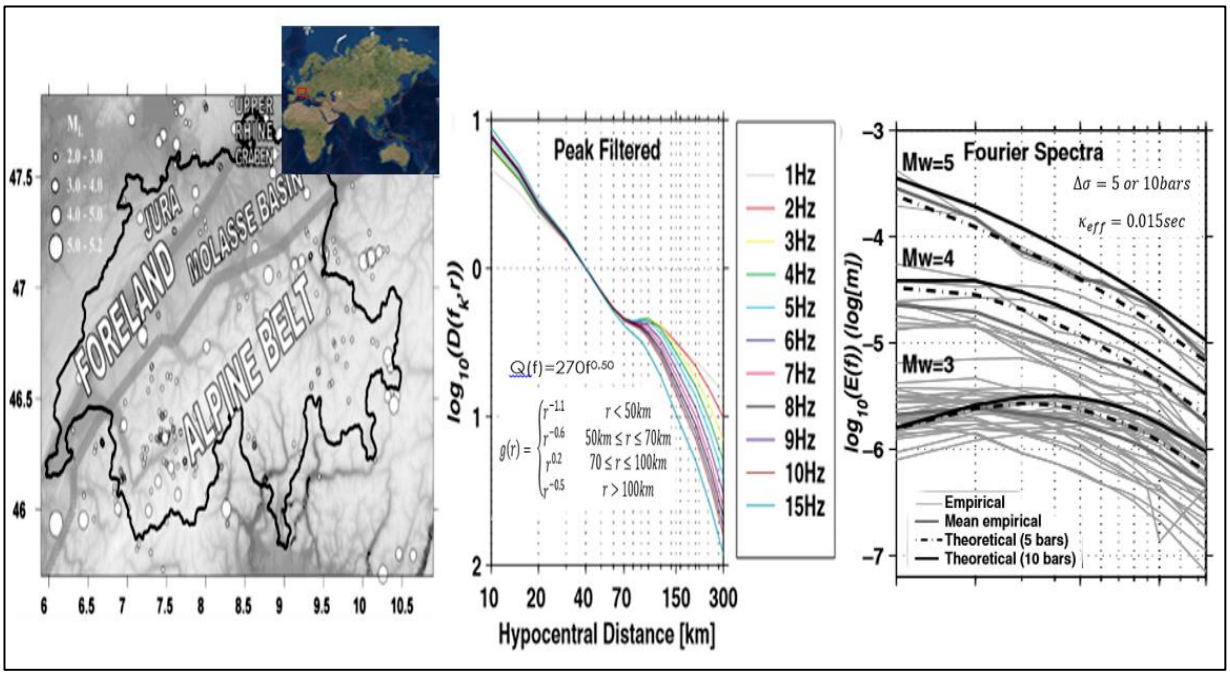

North-eastern Italy

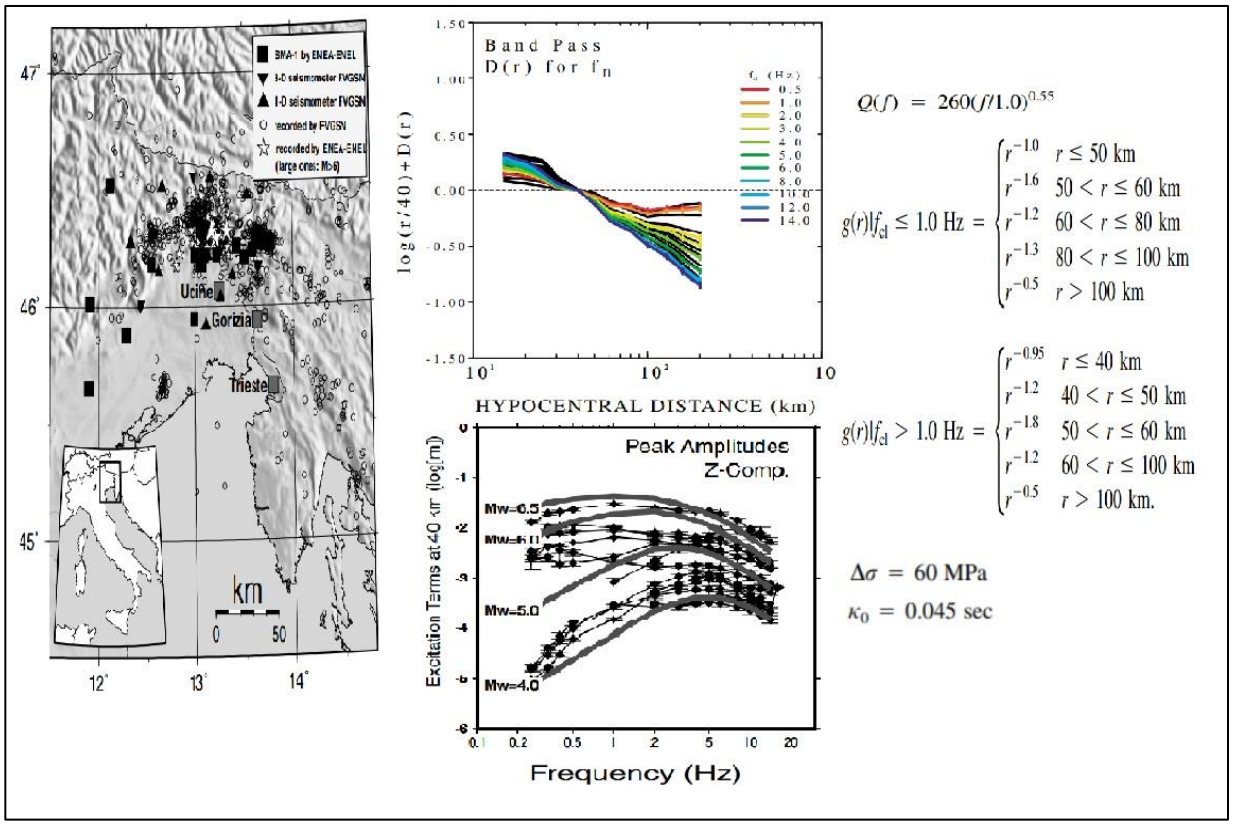

Western Alps

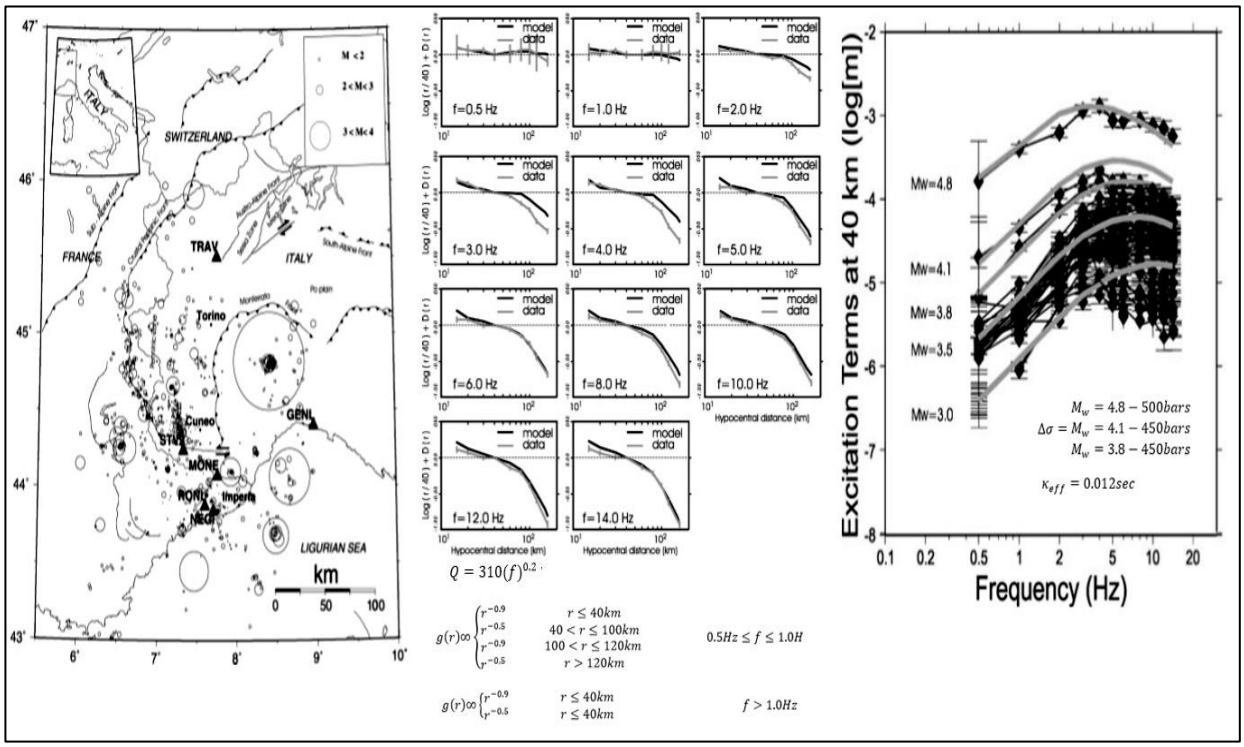

Central Italy

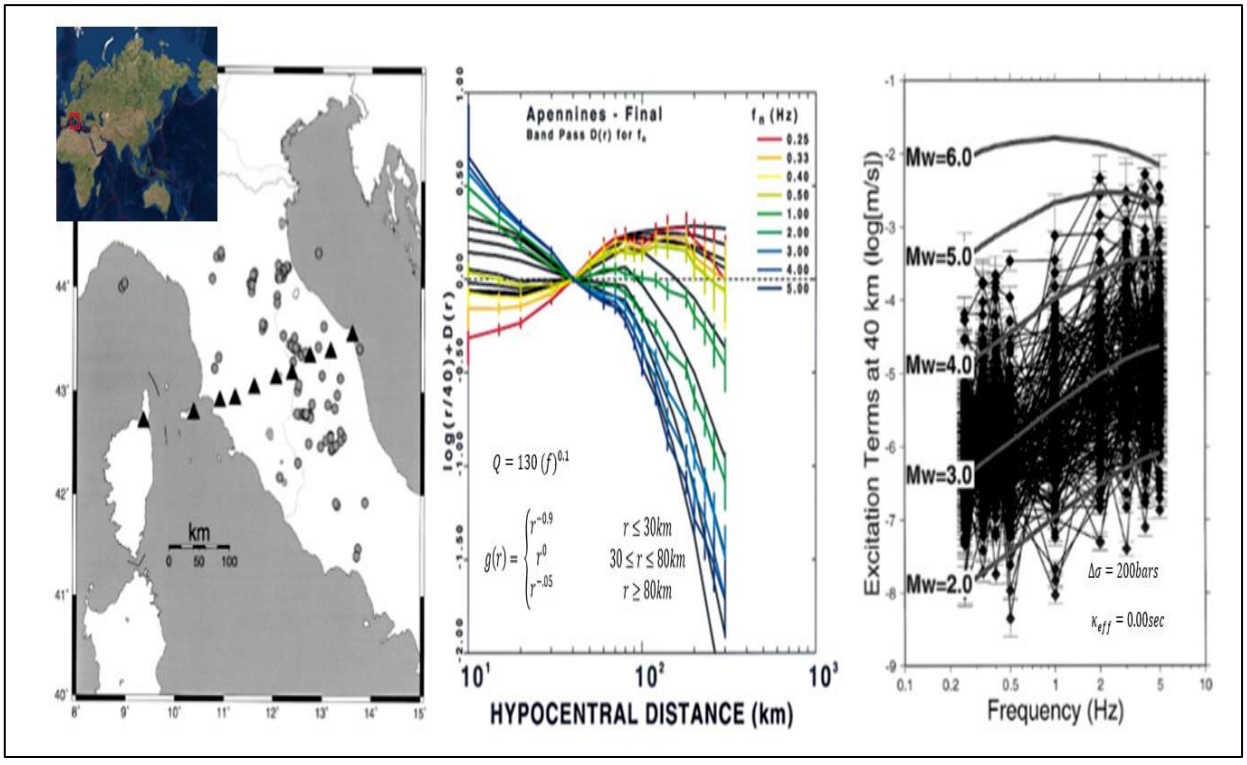

Eastern Sicily

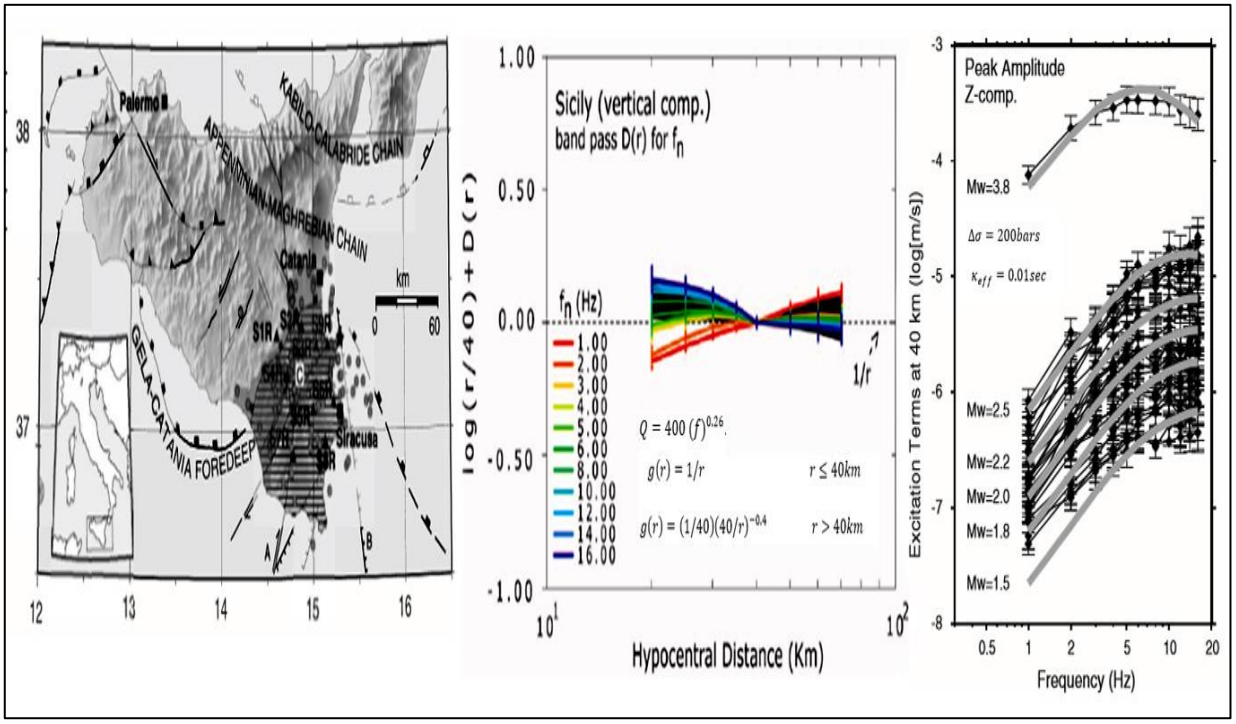

Marmara Region

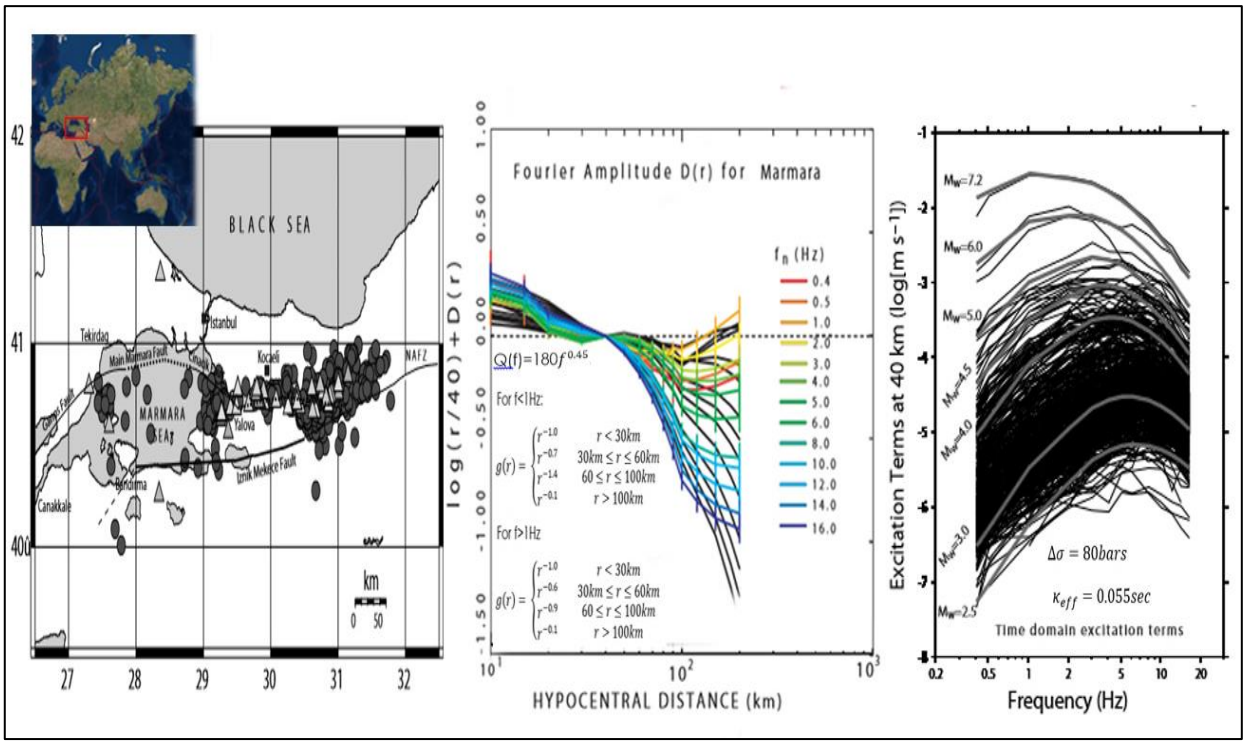

Western Anatolia

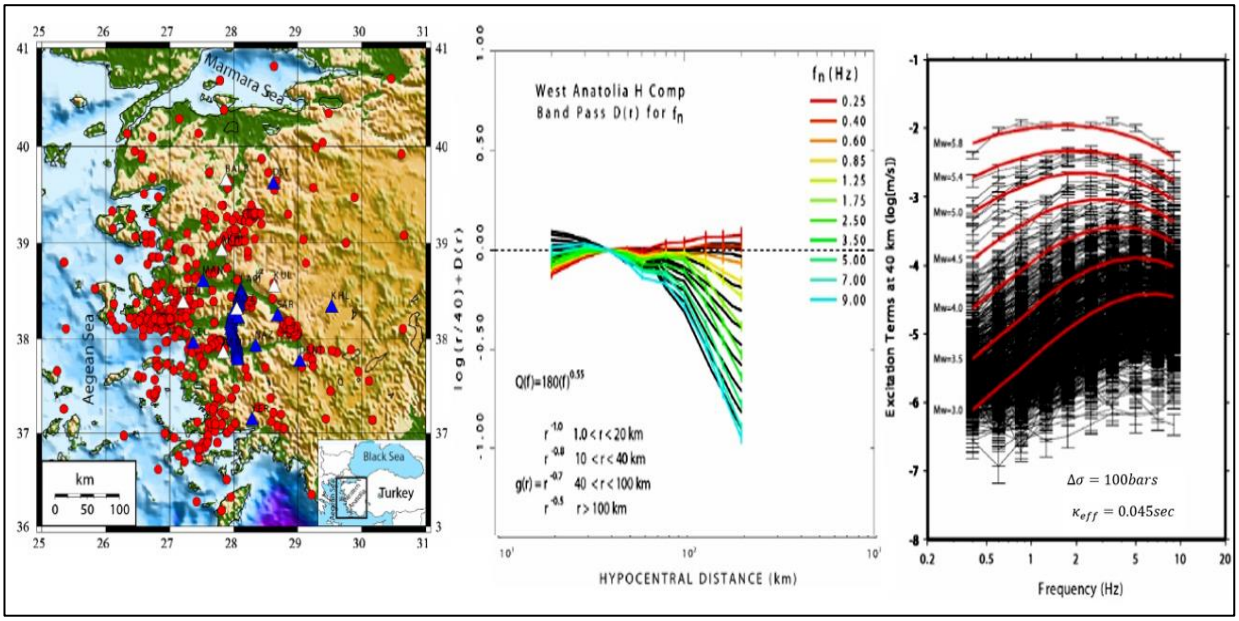

India

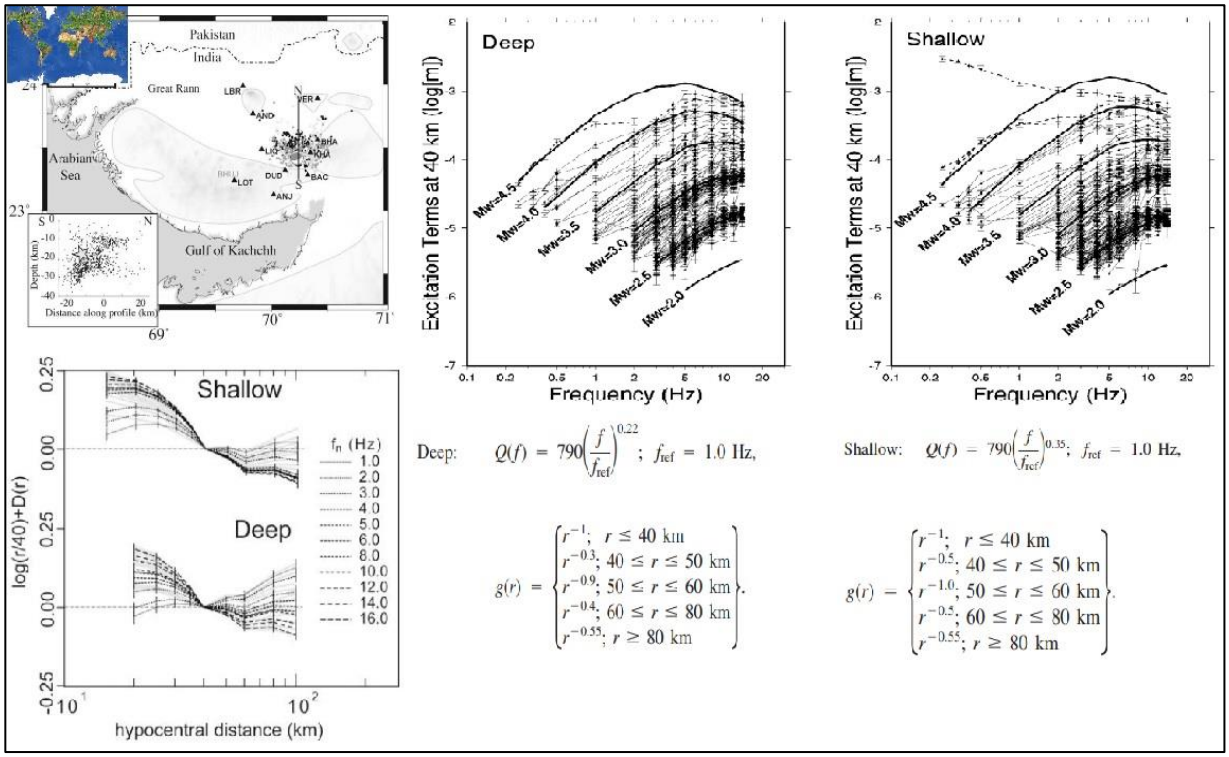

Taiwan

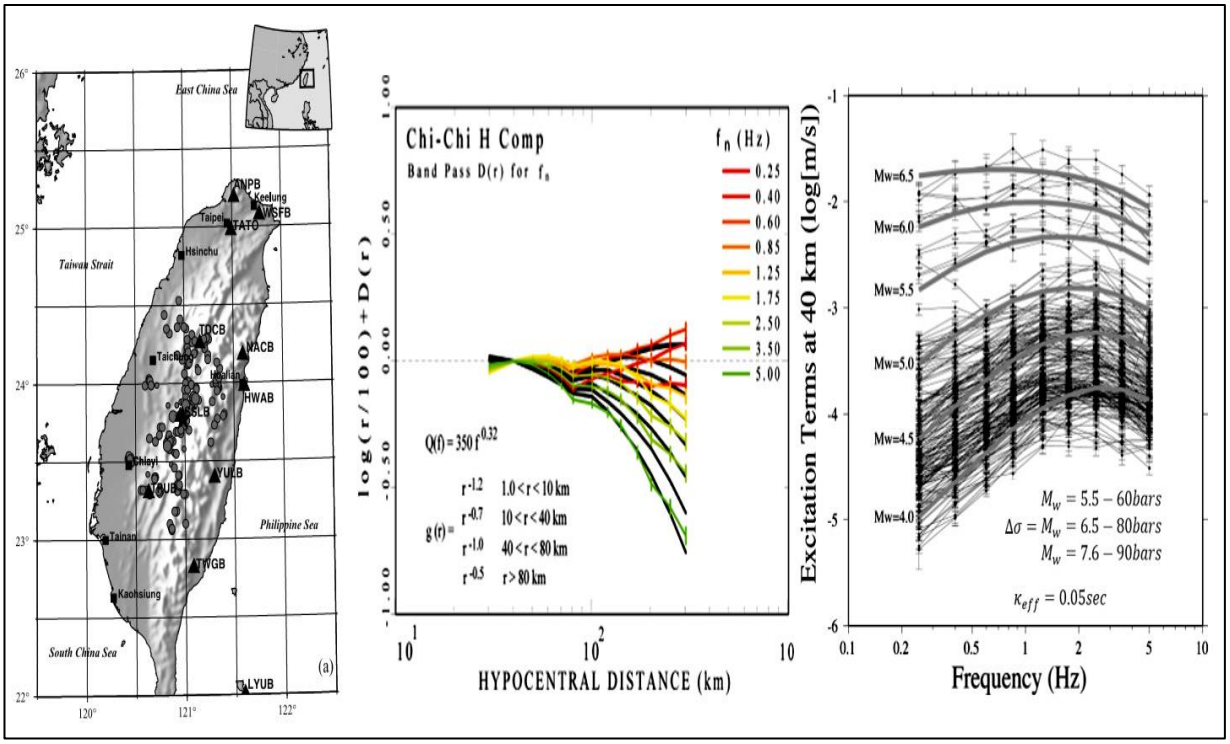

South Korea

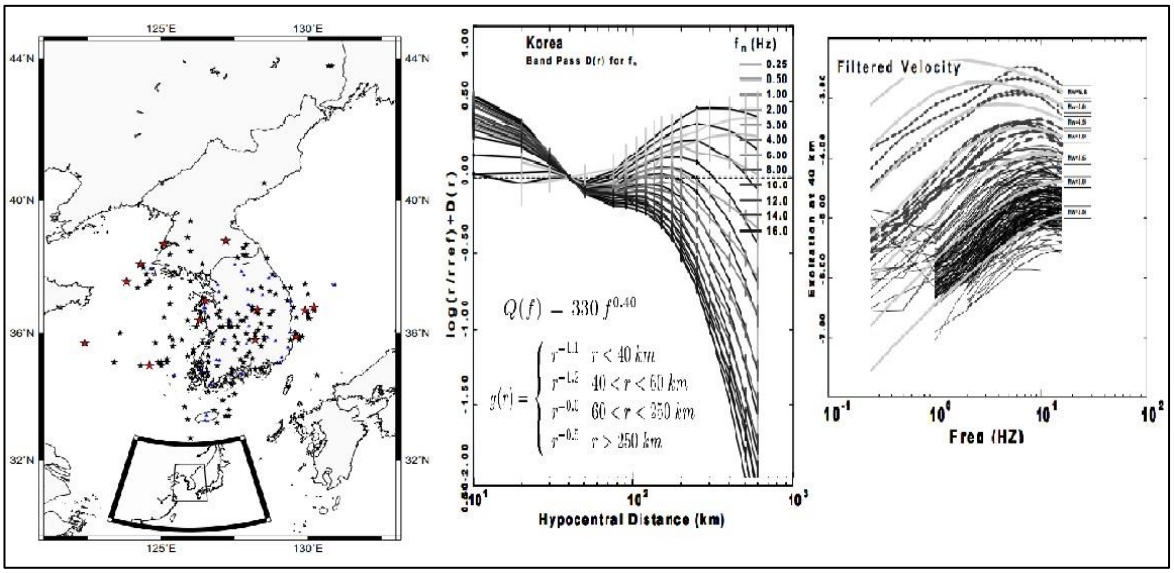

Canada

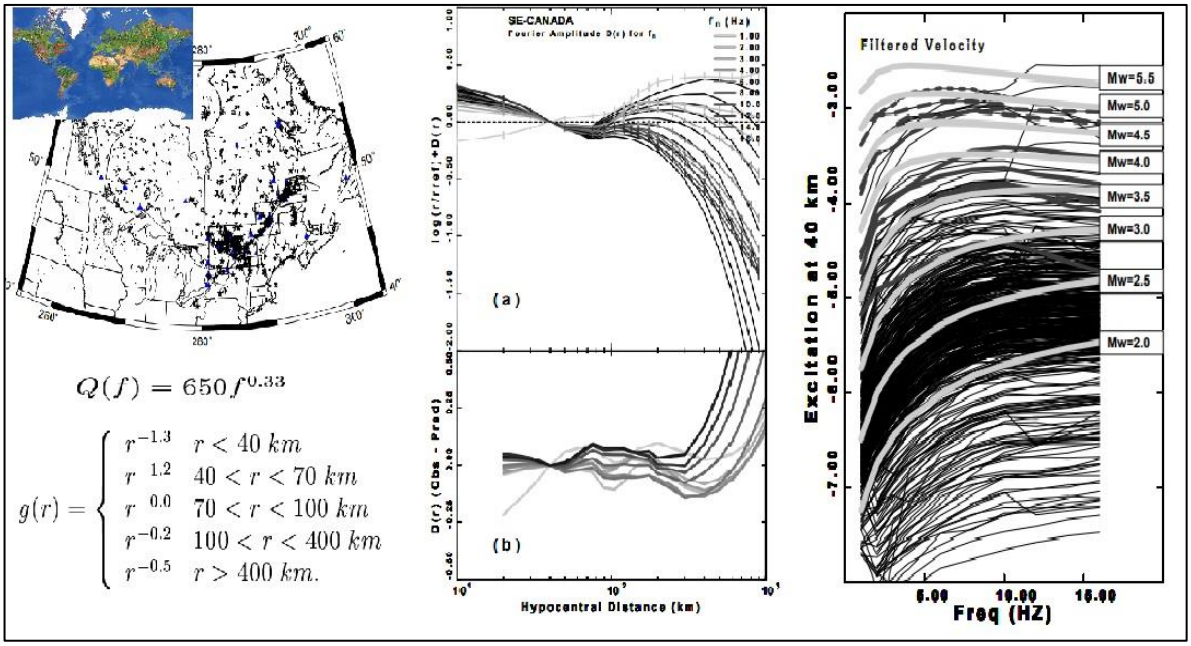
$Q(f) = 650 f^{0.33}$
$g(r) = \begin{cases} r^{-1.3} & r < 40\ km \\ r^{1.2} & 40 < r < 70\ km \\ r^{0.0} & 70 < r < 100\ km \\ r^{-0.2} & 100 < r < 400\ km \\ r^{-0.5} & r > 400\ km. \end{cases}$
SE-CANADA
Fourier Amplitude D(r) for f_n
f_n (Hz)
1.00
2.00
3.00
4.00
5.00
6.00
8.00
10.0
12.0
16.0
log(r/rref)+D(r)
(a)
D(r) (Obs - Pred)
(b)
Hypocentral Distance (km)
Filtered Velocity
Mw=5.5
Mw=5.0
Mw=4.5
Mw=4.0
Mw=3.5
Mw=3.0
Mw=2.5
Mw=2.0
Excitation at 40 km
Freq (HZ)

Appendix B

Earthquake Data used for data processing

Table 10: Small magnitude events used in study

Event I.D	Date (dd/mm/yyyy)	Time(hr:min:sec:)	Latitude	Longitude	Depth(km)	Magnitude (ML)
001	02/01/2012	08:59:38	37.8473	21.4027	25.5	2.6
002	02/01/2012	18:43:15	38.3125	22.0252	11.4	2.7
003	03/01/2012	14:11:46	38.4162	21.8297	14.3	2.5
004	04/01/2012	03:08:18	37.9413	21.6935	27.7	3.2
005	05/01/2012	20:25:49	38.9902	22.2622	21.8	3.7
006	07/01/2012	23:00:10	38.5838	21.7103	16.9	3.6
007	09/01/2012	07:21:46	38.5413	23.5965	26.2	2.5
008	10/01/2012	13:31:09	38.0328	21.9293	21.7	2.7
009	10/01/2012	16:05:55	38.1505	24.2102	24.5	2.8
010	14/01/2012	19:40:19	37.5933	21.3400	18.1	2.5
011	15/01/2012	13:10:13	38.1333	20.3408	8.2	2.6
012	16/01/2012	10:05:57	37.6120	20.9317	18.1	2.5
013	16/01/2012	10:18:24	38.1508	21.6310	22.9	3.0
014	16/01/2012	12:49:30	38.1617	21.6395	20.1	2.7
015	16/01/2012	17:47:44	38.2995	23.8927	19.1	2.6
016	18/01/2020	17:53:18	37.7172	23.0357	24.0	3.1
017	18/01/2020	19:49:23	38.9530	22.4648	23.8	3.5
018	19/01/2012	12:01:54	37.8657	22.0593	17.8	2.5
019	19/01/2012	12:50:51	38.0995	20.7653	17.4	2.5
020	20/01/2012	05:45:20	38.3828	21.8393	13.0	2.7
021	20/01/2012	07:34:07	38.3783	21.8033	7.3	2.6
022	20/01/2012	14:09:18	38.1152	21.9440	25.5	2.7
023	20/01/2012	21:21:46	38.2098	23.3798	12.0	2.6
024	21/01/2012	01:55:02	38.3763	21.8622	16.5	3.1
025	21/01/2012	12:29:38	38.1812	21.7093	23.1	2.8
026	21/01/2012	18:00:32	38.6473	23.4010	23.9	2.8
027	21/01/2012	19:24:53	38.3580	22.0873	11.1	3.1
028	22/01/2012	04:28:35	39.0708	21.9340	20.4	3.4
029	22/01/2012	12:57:36	38.1695	21.7112	17.4	2.5
030	22/01/2012	16:57:51	38.8873	23.0907	9.1	2.7
031	22/01/2012	20:01:10	38.7758	23.3272	25.4	3.0
032	24/01/2012	11:17:04	37.9710	20.1395	14.1	2.5
033	25/01/2012	07:46:54	38.1748	21.7135	22.8	2.5
034	25/01/2012	07:49:41	38.1812	21.7132	22.9	3.1
035	25/01/2012	12:05:38	38.1788	21.7015	24.6	3.0
036	25/01/2012	12:06:30	38.1753	21.7020	25.9	2.7

037	26/01/2012	15:19:46	37.8673	21.0122	14.4	2.9
038	27/01/2012	01:40:58	38.9688	21.8532	20.7	3.9
039	27/01/2012	22:40:06	37.5427	20.8707	16.3	3.0
040	28/01/2012	00:22:26	39.0262	22.3827	25.6	2.5
041	28/01/2012	14:17:12	38.7557	23.4690	24.7	2.9
042	01/02/2012	19:52:26	37.6985	21.8068	8.6	2.5
043	03/02/2012	07:45:22	39.0122	22.0938	23.6	2.6
044	03/02/2012	11:46:39	38.8785	24.1300	24.6	2.7
045	05/02/2012	08:52:00	38.4162	23.8505	25.2	2.9
046	05/02/2012	16:08:13	38.1800	21.7128	22.1	3.1
047	05/02/2012	16:11:26	38.1802	21.7260	21.9	3.1
048	06/02/2012	16:20:59	38.8787	24.1272	25.4	3.0
049	07/02/2012	10:57:49	38.4115	21.9958	11.3	2.5
050	08/02/2012	17:19:37	37.9353	21.0982	13.6	2.5
051	09/02/2012	15:20:34	38.4042	22.0137	10.4	2.5
052	10/02/2012	02:10:57	38.3447	22.0755	12.5	2.7
053	10/02/2012	20:36:55	38.0827	23.8760	19.6	3
054	11/02/2012	02:59:44	38.0698	23.8775	15.2	2.8
055	11/02/2012	04:47:07	37.7055	21.4118	13.5	3.1
056	12/02/2012	02:38:16	38.3742	22.2317	16.5	2.6
057	12/02/2012	19:25:09	39.0527	24.3327	28.0	2.7
058	12/02/2012	20:06:22	38.1350	21.8172	28.2	3
059	13/02/2012	09:40:43	38.8752	24.1357	25.5	3.6
060	13/02/2012	19:15:59	37.5515	21.8155	15.3	2.8
061	14/02/2012	10:09:20	38.0963	23.8440	13.8	2.9
062	14/02/2012	13:21:43	37.6957	20.7697	12.8	4.3
063	14/02/2012	22:47:02	38.2307	22.7513	14.9	3.1
064	17/02/2012	03:11:32	37.7693	20.2452	20.1	3.1
065	17/02/2012	08:05:04	37.8707	23.0173	17.1	4.2
066	17/02/2012	21:18:08	37.9173	21.7285	25.2	2.5
067	18/02/2012	01:57:40	37.5370	21.8892	21.4	3.5
068	18/02/2012	14:02:40	38.1020	20.7718	15.8	3.6
069	18/02/2012	15:46:14	37.7685	21.0965	7.3	2.5
070	19/02/2012	15:06:03	38.8785	21.1903	19.3	3.0
071	20/02/2012	00:51:47	38.1853	24.0952	20.9	3.1
072	20/02/2012	18:08:34	37.6408	20.8475	16.3	2.5
073	21/02/2012	08:22:12	38.0813	23.8538	17.3	2.8
074	24/02/2012	01:09:26	38.3495	21.7602	15.1	2.6
075	25/02/2012	02:39:11	38.9377	23.6055	24.4	3.0
076	27/02/2012	01:20:20	38.0753	23.8480	17.1	2.8
077	27/02/2012	18:44:32	38.1755	21.7153	21.0	3.0
078	28/02/2012	04:39:21	37.9443	20.8477	27.3	2.6
079	01/03/2012	04:56:13	37.9408	23.1607	11.1	2.5
080	03/03/2012	00:26:33	38.8543	21.6345	19.3	2.7
081	03/03/2012	07:49:42	38.5740	21.3018	27.8	2.6

082	03/03/2012	11:17:57	37.5515	22.2000	8.2	2.5
083	04/03/2012	01:15:43	38.2688	21.6223	26.9	2.8
084	04/03/2012	19:37:17	37.5302	20.4458	11.2	2.6
085	05/03/2012	03:20:33	38.2988	23.4528	22.4	2.7
086	05/03/2012	20:41:59	38.2963	23.4527	20.9	2.5
087	06/03/2012	09:55:12	38.2638	21.6313	25.8	2.5
088	06/03/2012	20:40:07	38.2688	21.6228	25.4	2.6
089	06/03/2012	22:08:20	38.6055	22.3183	23.1	2.6
090	07/03/2012	14:22:39	38.2712	21.6212	26.2	2.6
091	07/03/2012	21:51:37	38.2732	21.6302	24.1	2.5
092	07/03/2012	23:30:47	37.5740	20.8892	18.8	2.6
093	08/03/2012	03:55:51	38.1153	23.7227	17.7	2.5
094	08/03/2012	16:26:16	38.6850	21.2867	18.7	2.8
095	08/03/2012	18:25:26	38.6975	21.3015	17.8	2.7
096	08/03/2012	18:40:04	38.7008	21.2837	17.4	2.5
097	08/03/2012	18:54:24	38.7003	21.3167	16.5	3.4
098	08/03/2012	19:30:48	38.6888	21.2950	18.9	3.0
099	08/03/2012	19:39:28	38.6883	21.2647	21.2	3.2
100	09/03/2012	06:00:22	37.7733	21.4932	20.8	2.5
101	09/03/2012	20:29:52	38.6902	21.2903	17.5	3.1
102	09/03/2012	22:59:05	38.7172	21.8995	22.3	3.0
103	10/03/2012	03:39:59	38.6872	21.2945	19.0	3.3
104	11/03/2012	06:57:17	37.7747	21.5007	22.6	2.5
105	11/03/2012	07:02:22	38.6892	20.8260	27.9	2.5
106	11/03/2012	16:30:44	38.2647	21.6478	19.9	2.6
107	11/03/2012	16:33:17	38.2738	21.6348	22.7	2.5
108	12/03/2012	01:15:59	38.5998	21.7055	16.2	2.9
109	12/03/2012	01:55:12	38.0367	21.9758	17.3	2.6
110	13/03/2012	08:32:26	38.5668	24.3355	26.5	2.9
111	13/03/2012	10:04:58	38.6007	21.7098	16.3	2.9
112	13/03/2012	10:59:37	38.6033	21.7160	17.3	3.8
113	13/03/2012	19:41:24	37.7862	23.9110	17.8	2.8
114	13/03/2012	19:58:42	37.8032	23.9363	20.9	2.9
115	14/03/2012	07:40:15	38.4595	23.8030	19.8	2.8
116	14/03/2012	09:13:08	38.6153	21.7032	18.1	3.3
117	14/03/2012	10:37:06	37.8045	23.9220	24.3	2.9
118	14/03/2012	16:35:30	38.2568	21.6278	24.7	2.6
119	14/03/2012	19:45:11	38.5988	21.7095	15.3	2.8
120	14/03/2012	21:44:41	37.6725	20.0265	12.9	2.9
121	15/03/2012	05:40:58	38.6910	21.3047	15.5	4.4
122	15/03/2012	06:35:06	38.6742	21.2787	19.3	2.8
123	15/03/2012	21:14:17	37.8073	23.9263	23.1	2.5
124	15/03/2012	23:47:48	38.1358	22.6668	19.7	3.3
125	16/03/2012	17:00:16	38.6815	21.2927	18.6	2.6
126	17/03/2012	13:05:56	38.3283	22.3467	19.3	2.5

127	18/03/2012	13:52:19	38.0088	20.1160	9.3	2.9
128	18/03/2012	17:18:43	38.5970	21.7002	18.6	2.8
129	20/03/2012	16:41:50	38.1945	20.5347	19.3	2.9
130	20/03/2012	18:50:51	38.1775	20.4902	20.3	3.0
131	21/03/2012	05:50:48	38.6098	21.7133	16.5	3.8
132	21/03/2012	06:12:54	38.6262	21.7080	13.7	2.6
133	21/03/2012	06:16:09	38.6245	21.7028	18.8	2.9
134	21/03/2012	22:32:54	38.2777	20.4293	19.3	2.9
135	22/03/2012	13:03:31	38.6115	21.6900	18.2	2.7
136	25/03/2012	05:39:43	38.0697	20.1895	19.6	3.1
137	27/03/2012	05:48:40	39.0332	24.4123	19.9	2.6
138	28/03/2012	19:47:22	38.4212	21.8285	18.5	3.6
139	29/03/2012	13:15:05	37.8255	21.1345	21.6	3.0
140	29/03/2012	20:44:31	38.2680	22.1522	10.7	2.6
141	30/03/2012	12:20:32	38.2472	20.6848	19.6	2.5
142	01/04/2012	05:18:14	38.0953	23.7767	18.0	3.0
143	01/04/2012	19:23:15	38.3883	22.0058	10.9	2.7
144	03/04/2012	16:10:21	38.6008	21.6822	10.9	2.5
145	03/04/2012	19:54:30	38.1745	21.7173	25.1	2.9
146	04/04/2012	01:45:31	38.0690	21.5758	18.6	3.4
147	05/04/2012	17:24:11	38.3625	22.3007	13.5	2.5
148	07/04/2012	15:13:14	38.8830	24.1220	26.7	2.9
149	09/04/2012	18:39:18	39.0698	22.4663	14.2	2.5
150	09/04/2012	23:10:10	38.0695	21.5590	17.0	2.8
151	10/04/2012	13:33:39	37.9950	20.2698	18.8	2.5
152	10/04/2012	17:43:20	38.0053	20.0255	13.7	2.6
153	12/04/2012	07:38:10	38.7630	22.8552	17.0	2.6
154	12/04/2012	16:27:51	38.7518	22.5732	16.5	2.5
155	12/04/2012	22:55:09	37.7178	21.2637	29.0	2.7
156	12/04/2012	23:01:42	37.7868	21.3223	27.5	2.5
157	12/04/2012	23:04:31	37.7735	21.3027	27.9	2.8
158	14/04/2012	03:56:07	39.0470	23.2803	26.4	2.8
159	14/04/2012	20:19:19	38.1137	22.7142	14.7	3.3
160	16/04/2012	03:19:48	38.3033	22.1263	14.8	2.9
161	16/04/2012	08:40:22	38.3013	22.1365	17.3	3.6
162	16/04/2012	08:54:39	38.2928	22.1170	12.0	2.9
163	16/04/2012	09:41:50	38.2947	22.1225	10.5	2.6
164	16/04/2012	11:15:32	38.6013	21.6860	16.0	2.6
165	16/04/2012	12:47:58	38.3002	22.1255	10.3	3.0
166	18/04/2012	00:08:30	38.8400	21.8987	18.4	2.7
167	01/05/2012	15:33:38	38.8888	23.6582	26.7	2.6
168	03/05/2012	13:33:29	38.3738	20.3562	6.8	2.5
169	03/05/2012	15:17:04	37.7868	21.0588	21.3	3.3
170	03/05/2012	19:40:22	37.7902	21.0508	21.0	3.7
171	04/05/2012	00:09:47	38.6168	21.7092	16.8	2.9

172	04/05/2012	09:27:03	38.8148	21.6698	17.2	2.6
173	05/05/2012	16:19:39	38.3852	21.8782	15.1	2.8
174	06/05/2012	06:31:24	37.5230	20.6297	26.7	3.3
175	06/05/2012	06:38:16	38.1118	20.3958	25.1	2.8
176	07/05/2012	00:20:17	38.4247	21.8265	17.2	2.6
177	07/05/2012	06:35:49	38.1287	23.2368	16.4	2.7
178	07/05/2012	16:32:10	38.9635	21.9042	18.0	2.5
179	08/05/2012	00:31:54	38.0720	20.1305	26.5	2.5
180	08/05/2012	04:31:25	38.5260	20.5003	10.5	2.5
181	08/05/2012	17:53:05	37.6615	20.1802	10.1	2.8
182	09/05/2012	16:39:08	37.6320	20.9865	19.4	2.5
183	10/05/2012	22:56:07	38.8422	23.4475	18.1	2.8
184	11/05/2012	00:25:22	38.8572	23.4603	25.0	2.5
185	11/05/2012	16:36:28	37.8608	21.0845	28.2	2.8
186	12/05/2012	19:12:51	38.8920	20.5822	25.7	2.5
187	16/05/2012	00:00:02	37.8057	22.9142	21.6	3.1
188	17/05/2012	05:36:24	39.0607	23.4870	23.3	2.6
189	17/05/2012	19:52:01	37.8565	20.2515	17.6	2.6
190	17/05/2012	23:42:21	37.5658	21.6447	22.6	2.5
191	18/05/2012	01:32:39	38.1775	21.7277	22.6	2.5
192	18/05/2012	16:40:15	38.8110	21.8847	17.6	2.7
193	19/05/2012	04:41:41	38.2213	20.4640	16.5	2.8
194	22/05/2012	21:20:18	38.4242	21.9260	13.3	2.8
195	25/05/2012	09:30:45	37.7998	21.3840	21.2	3.2
196	25/05/2012	18:00:42	38.1173	21.6540	10.7	2.8
197	26/05/2012	00:38:13	37.8715	21.4432	24.5	3.0
198	26/05/2012	00:42:02	37.8762	21.4408	24.4	3.1
199	26/05/2012	05:48:06	38.3968	22.3412	10.6	2.6
200	27/05/2012	00:29:02	38.0140	21.6888	28.2	2.5
201	28/05/2012	15:44:13	37.9940	21.5498	19.4	4.3
202	28/05/2012	15:46:26	37.9792	21.5420	10.7	3.2
203	28/05/2012	15:57:48	37.9700	21.5192	13.2	2.6
204	28/05/2012	16:02:07	37.9890	21.5327	11.1	2.8
205	28/05/2012	16:21:45	37.9712	21.5313	16.3	2.9
206	28/05/2012	23:18:46	38.1935	21.8983	19.5	3.3
207	29/05/2012	00:54:55	38.0337	21.5873	23.3	2.5
208	29/05/2012	02:11:12	38.8653	21.9613	15.4	2.5
209	29/05/2012	04:58:02	38.2810	21.4380	11.3	3.3
210	31/05/2012	06:23:36	37.9987	21.5220	12.3	2.5
211	02/06/2012	00:11:07	39.0083	21.4608	14.6	3.2
212	02/06/2012	17:31:50	38.4000	20.4492	15.7	3.6
213	08/06/2012	03:22:37	37.5548	22.2340	19.0	2.7
214	08/06/2012	08:20:07	37.5490	22.2292	11.3	2.8
215	10/06/2012	07:23:55	38.3143	21.6283	23.4	2.9
216	11/06/2012	09:12:12	37.8513	21.0957	35.7	3.1

217	13/06/2012	19:27:31	38.0385	21.5575	23.3	3.8
218	13/06/2012	20:28:42	37.8382	21.4417	20.9	3.0
219	14/06/2012	10:59:14	38.1643	21.2120	31.2	2.6
220	15/06/2012	09:58:36	39.0405	21.0855	17.2	2.9
221	17/06/2012	12:20:11	37.6872	21.6945	18.7	2.7
222	18/06/2012	04:10:30	38.5372	21.5447	26.7	2.6
223	18/06/2012	09:11:21	37.8618	21.1260	5.4	2.9
224	18/06/2012	11:43:19	37.5327	21.8073	34.1	3.0
225	18/06/2012	12:43:06	38.0703	23.4700	18.1	2.6
226	18/06/2012	20:51:00	38.8570	20.3098	38.0	3.3
227	21/06/2012	18:03:23	38.3012	22.0982	9.1	2.7
228	23/06/2012	00:43:04	38.3392	22.2718	9.9	2.7
229	25/06/2012	06:49:00	38.3895	21.9250	15.6	3.4
230	25/06/2012	07:18:27	38.2862	22.1077	11.8	2.8
231	25/06/2012	12:43:18	38.3912	21.9222	9.7	2.8
232	26/06/2012	04:55:00	37.8058	21.2157	21.0	2.8
233	27/06/2012	18:41:08	37.9653	21.5300	18.9	2.5
234	28/06/2012	13:11:30	39.0110	23.1712	25.1	4.3
235	28/06/2012	14:42:20	38.2900	22.1688	8.6	2.5
236	29/06/2012	13:37:32	39.0065	23.1347	15.8	2.7
237	29/06/2012	19:24:35	38.2760	22.1410	14.9	2.7
238	01/07/2012	03:11:14	37.9028	20.9768	11.7	3.3
239	01/07/2012	14:54:23	38.4283	21.8625	15.9	2.7
240	02/07/2012	00:39:27	38.3557	22.8580	15.7	2.6
241	02/07/2012	15:39:38	38.8133	23.4425	24.5	2.8
242	02/07/2012	23:36:23	37.9733	20.5383	19.6	3.7
243	03/07/2012	20:39:44	37.8977	20.9258	15.3	3.0
244	03/07/2012	23:13:57	37.8893	20.9117	12.8	2.5
245	04/07/2012	15:37:19	38.9410	22.4338	20.2	2.5
246	05/07/2012	23:16:56	38.3448	22.2587	13.8	2.6
247	06/07/2012	08:21:51	37.8353	21.4700	24.1	2.9
248	06/07/2012	11:24:28	38.5068	21.5292	18.5	3.1
249	07/07/2012	01:11:29	38.2613	22.1373	10.7	2.5
250	09/07/2012	20:59:06	38.7230	22.4647	20.1	2.7
251	11/07/2012	01:05:53	39.0697	21.7113	22.8	2.7
252	11/07/2012	08:00:31	38.1487	20.7415	17.0	2.6
253	15/07/2012	13:38:24	38.2768	22.3460	12.9	2.7
254	16/07/2012	14:14:08	38.1695	22.6395	13.4	2.5
255	16/07/2012	20:26:49	38.3913	22.0215	13.1	3.0
256	17/07/2012	08:28:35	38.5868	20.0987	23.9	2.7
257	17/07/2012	13:05:17	39.0728	22.5388	19.9	3.0
258	21/07/2012	00:08:04	37.6062	21.7797	26.5	2.6
259	22/07/2012	19:47:19	38.9397	21.2663	29.4	2.7
260	23/07/2012	11:56:01	37.7482	21.3430	18.6	2.8
261	24/07/2012	12:28:48	37.6983	20.8010	13.1	3.0

262	25/07/2012	03:55:02	38.0220	20.2777	20.8	2.5
263	26/07/2012	09:16:04	38.4113	21.8798	12.7	3.2
264	26/07/2012	11:39:49	38.3538	22.0267	9.6	2.5
265	26/07/2012	17:02:30	37.9872	20.2257	15.7	2.7
266	27/07/2012	00:47:38	38.8033	23.1875	15.0	2.5
267	28/07/2012	08:58:21	37.7075	20.8900	18.5	2.6
268	31/07/2012	15:13:25	38.8107	21.2858	30.0	3.4
269	01/08/2012	12:01:48	37.9648	22.2043	5.4	3.0
270	02/08/2012	21:47:34	38.9157	21.2582	12.5	2.9
271	03/08/2012	21:12:13	37.9547	20.6115	13.7	2.8
272	04/08/2012	04:46:40	38.3870	21.9005	10.2	2.9
273	05/08/2012	12:44:32	38.1000	21.9693	25.5	3.4
274	05/08/2012	16:52:19	38.1133	21.9408	25.5	3.2
275	11/08/2012	09:51:46	38.0585	20.4720	18.5	2.7
276	11/08/2012	21:54:44	37.6823	20.8440	20.7	3.9
277	12/08/2012	02:34:10	37.7878	20.3128	17.1	2.5
278	12/08/2012	17:26:36	38.2913	22.1088	7.4	3.1
279	12/08/2012	20:22:41	38.2935	22.1135	11.2	2.9
280	16/08/2012	21:22:54	38.2777	22.5480	23.8	3.6
281	19/08/2012	04:12:00	38.0487	21.9488	13.0	2.9
282	19/08/2012	15:54:54	37.7832	22.8865	22.7	2.7
283	21/08/2012	00:58:25	37.7618	20.4505	18.9	2.8
284	21/08/2012	10:19:56	39.0055	23.2598	18.5	3.0
285	23/08/2012	06:19:12	20.2660	23.2598	15.0	2.5
286	23/08/2012	21:53:29	37.5862	21.9553	22.3	2.9
287	24/08/2012	03:12:53	38.0750	21.5353	26.2	2.7
288	24/08/2012	10:31:47	38.0213	21.2520	19.7	2.7
289	24/08/2012	10:47:02	38.0135	21.2435	22.4	2.5
290	24/08/2012	16:33:09	38.9783	21.8788	23.1	2.8
291	25/08/2012	06:17:44	38.8893	23.2202	25.5	3.8
292	25/08/2012	10:16:06	38.4468	21.0672	22.4	2.6
293	27/08/2012	14:05:13	38.1603	20.5630	20.6	3.5
294	28/08/2012	02:56:32	37.8327	21.4333	18.8	2.9
295	28/08/2012	03:57:41	37.8420	21.4260	22.1	3.2
296	28/08/2012	09:37:15	38.2565	20.2925	15.1	2.8
297	28/08/2012	15:33:40	38.4105	21.8288	14.6	2.8

Table 11: Large magnitude events used in the study (Moment tensors can be obtained from: http://bbnet.gein.noa.gr/HL/seismicity/mts/revised-moment-tensors)

Event I.D	Date (dd/mm/yyyy)	Time(hr:min:sec:)	Latitude	Longitude	Depth(km)	Magnitude (ML)
2015-06-09-01-09-03	09/06/2015	01:09:03	38.6220	23.3890	14	5.2
2015-11-17-07-10-07	17/11/2015	07:10:07	38.6662	20.5957	10	6.4
2015-11-17-08-33-40	17/11/2015	08:33:40	38.6515	20.5570	8	5
2018-02-21-23-44-56	21/02/2018	23:44:56	37.7865	20.3462	27	4.7
2018-10-25-22-22-54	25/10/2018	22:22:54	37.3482	20.5547	4	4.8
2018-10-25-22-54-52	25/10/2018	22:54:52	37.3410	20.5123	15	6.7
2018-10-26-05-48-37	26/10/2018	05:48:37	37.3597	20.5067	6	5.1
2018-10-26-12-41-12	26/10/2018	12:41:12	37.3753	20.5360	2	5.1
2018-10-30-15-12-00	30/10/2018	15:12:00	37.4692	20.4885	8	5.8
2019-03-30-10-46-19	30/03/2019	10:46:19	38.3496	22.2949	10	5.3

Appendix C

Recordings as a function of distance for each station

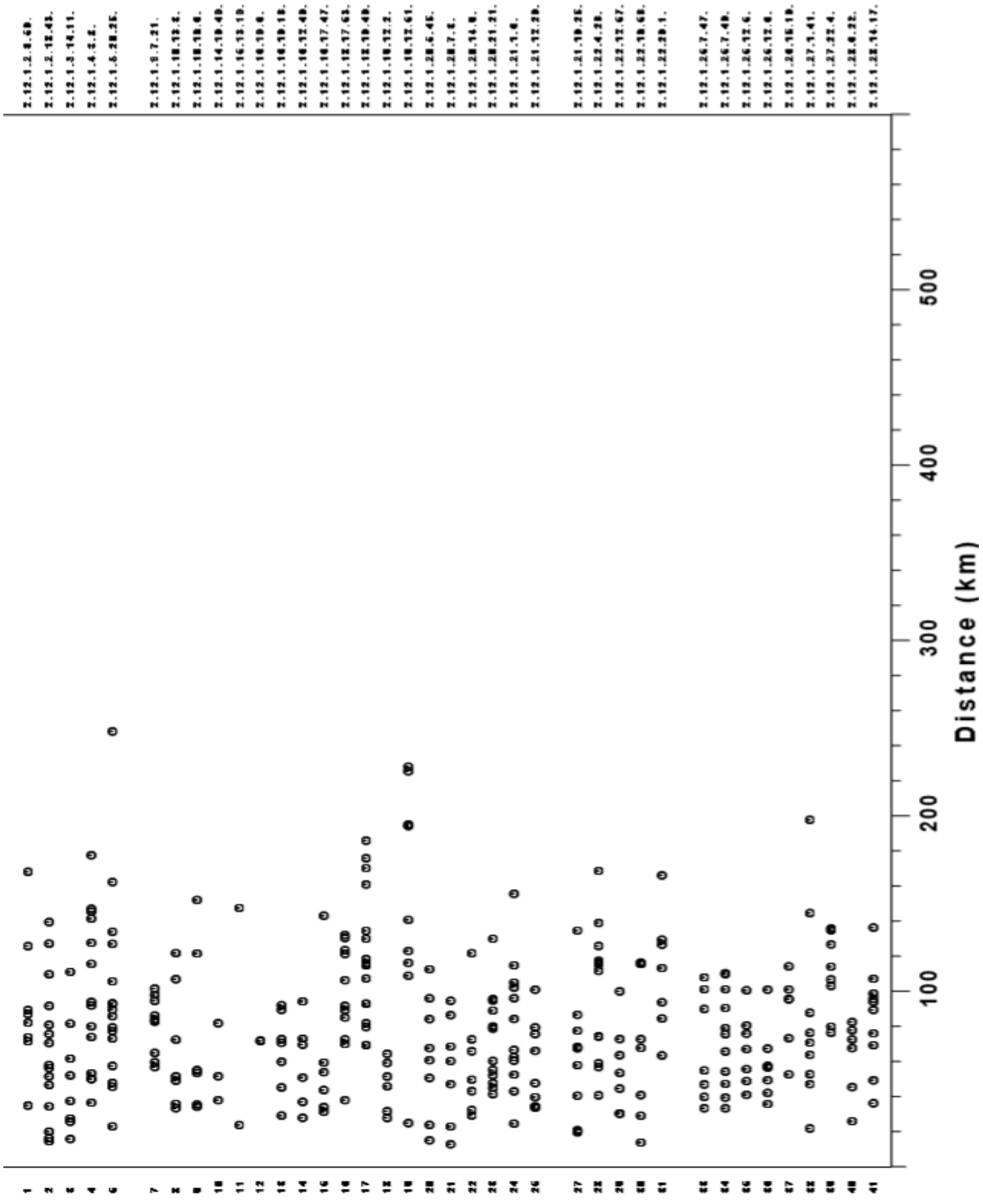

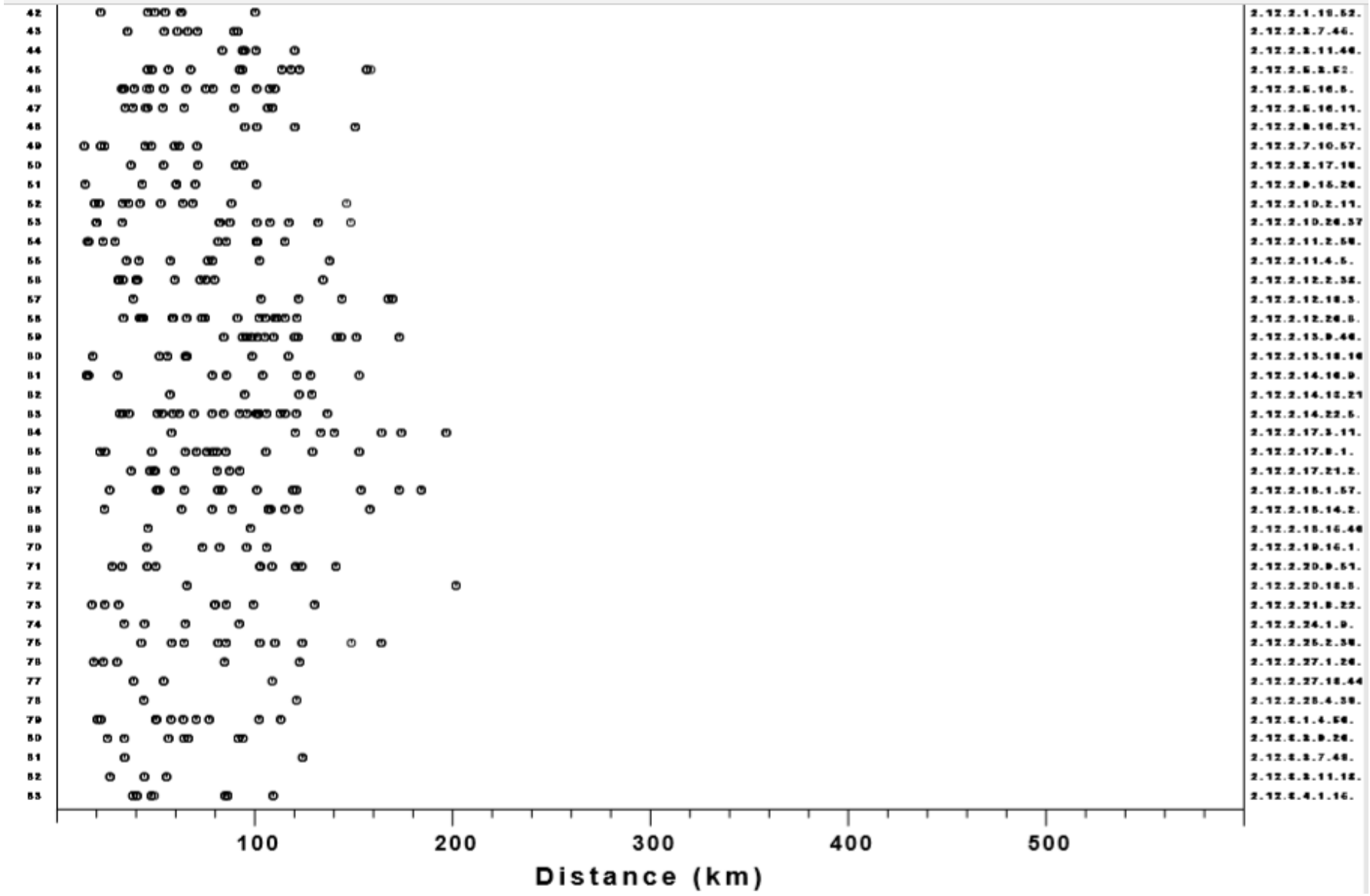
100
200
300
400
500
Distance (km)

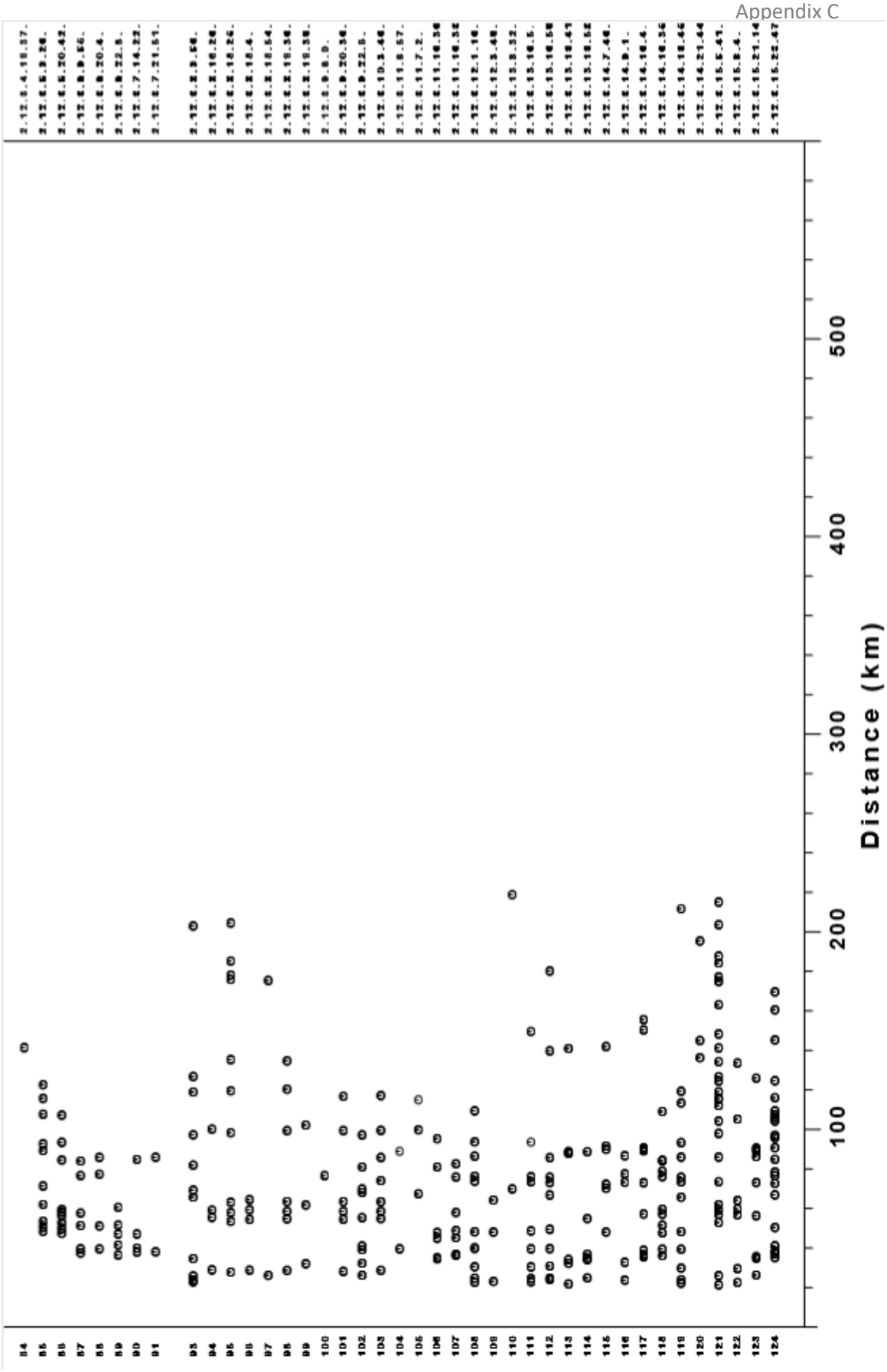
Distance (km)
100
200
300
400
500

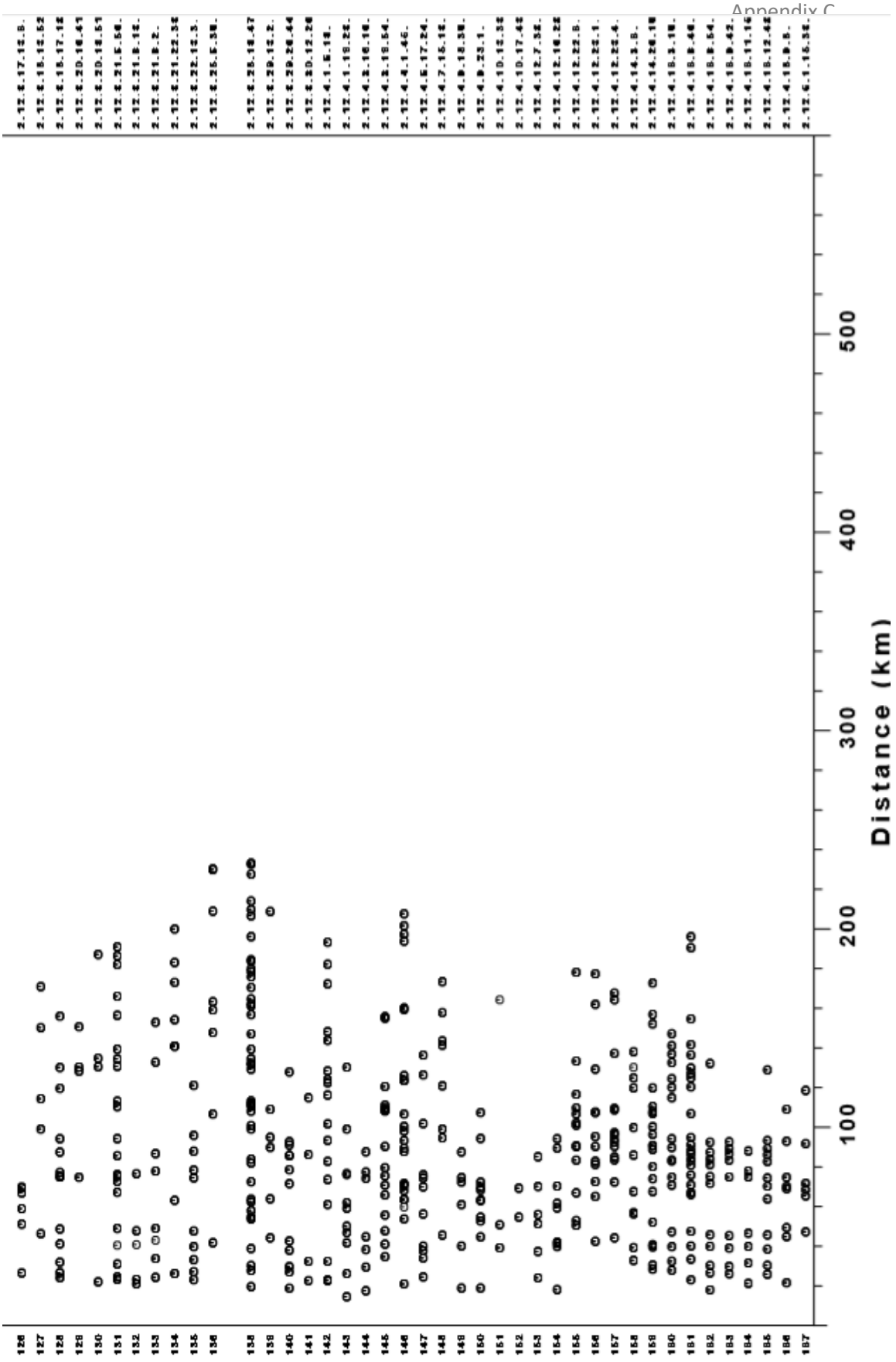
Distance (km)
100
200
300
400
500

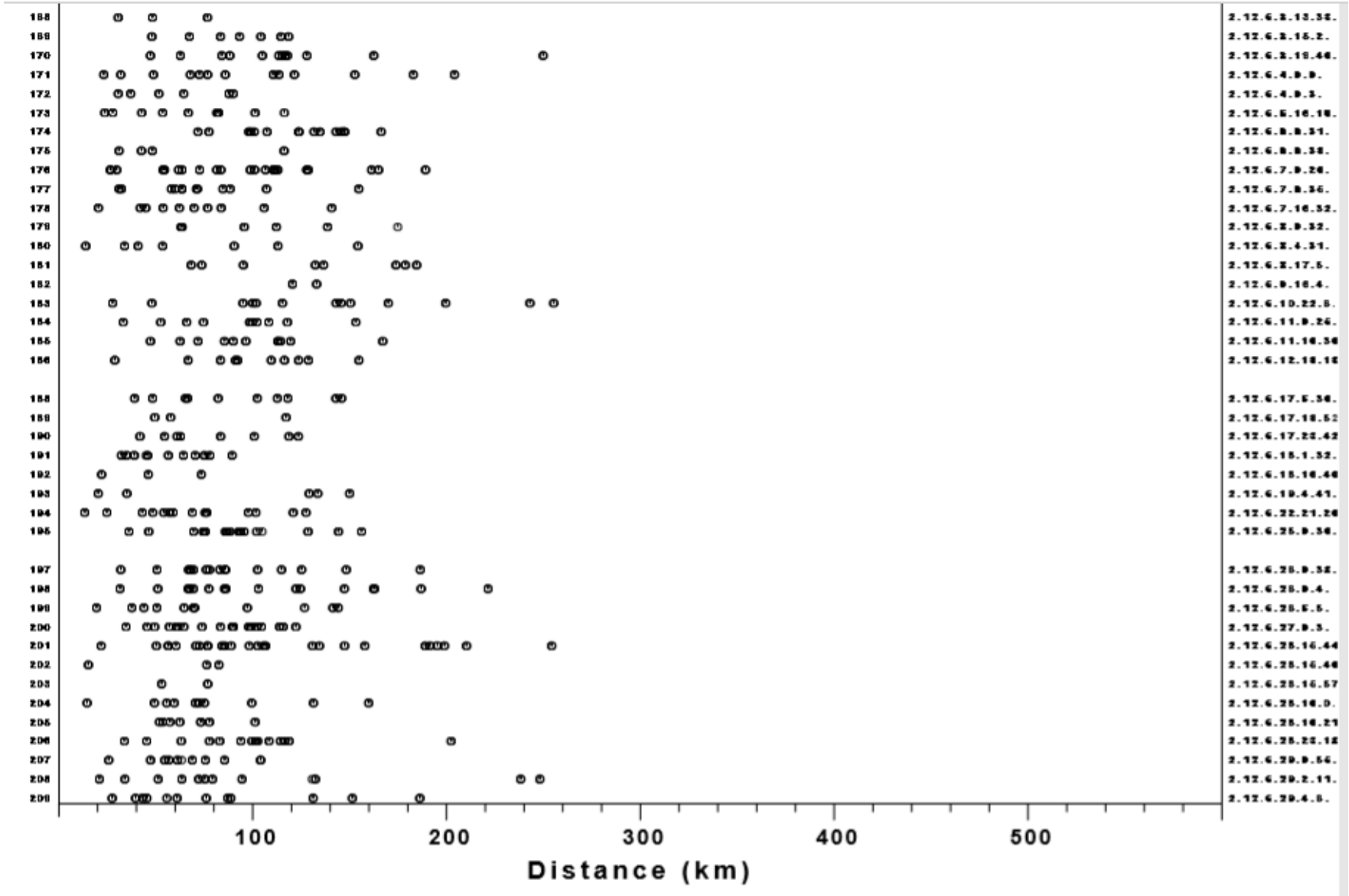
100
200
300
400
500
Distance (km)

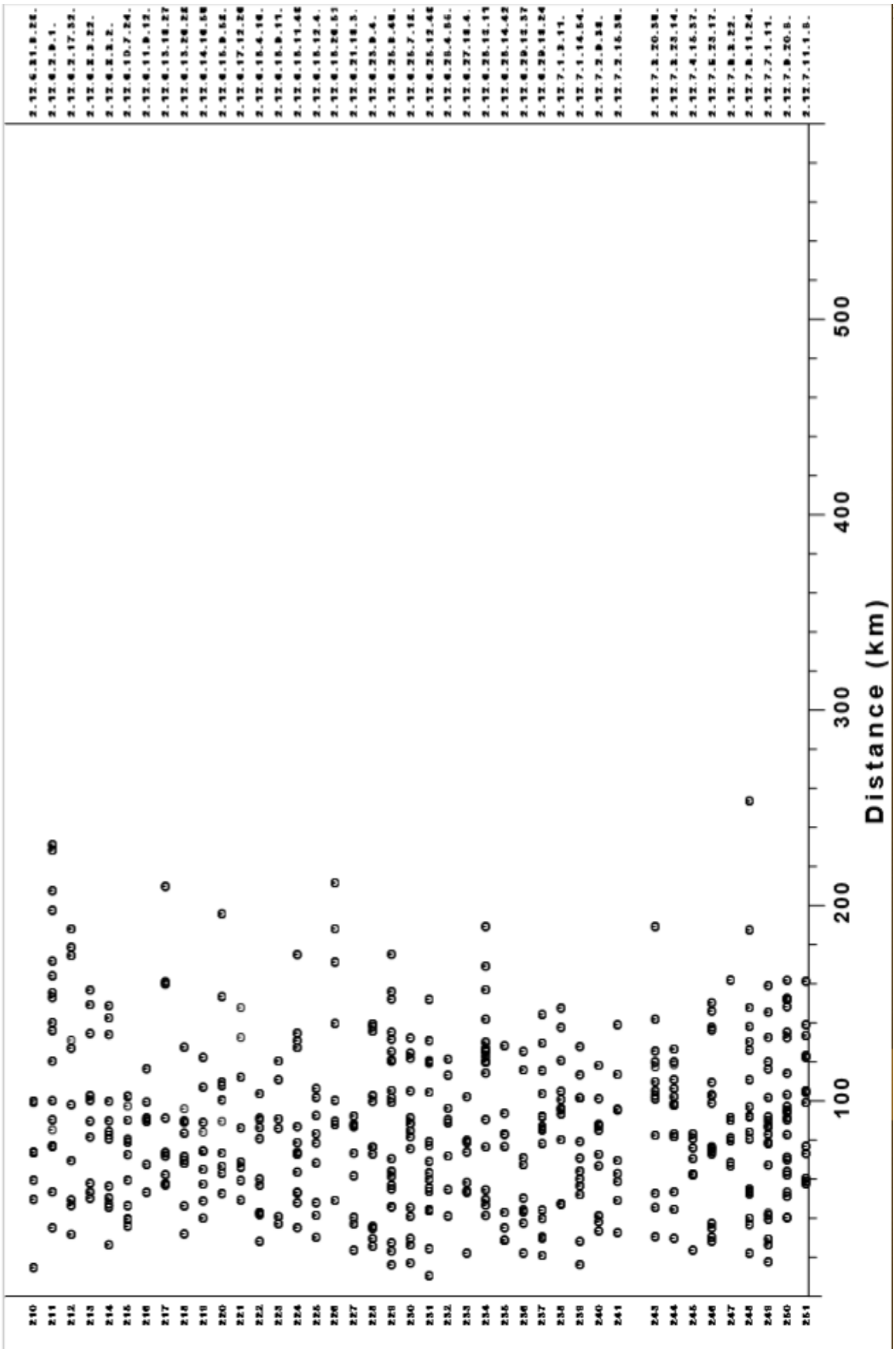
Distance (km)
100
200
300
400
500

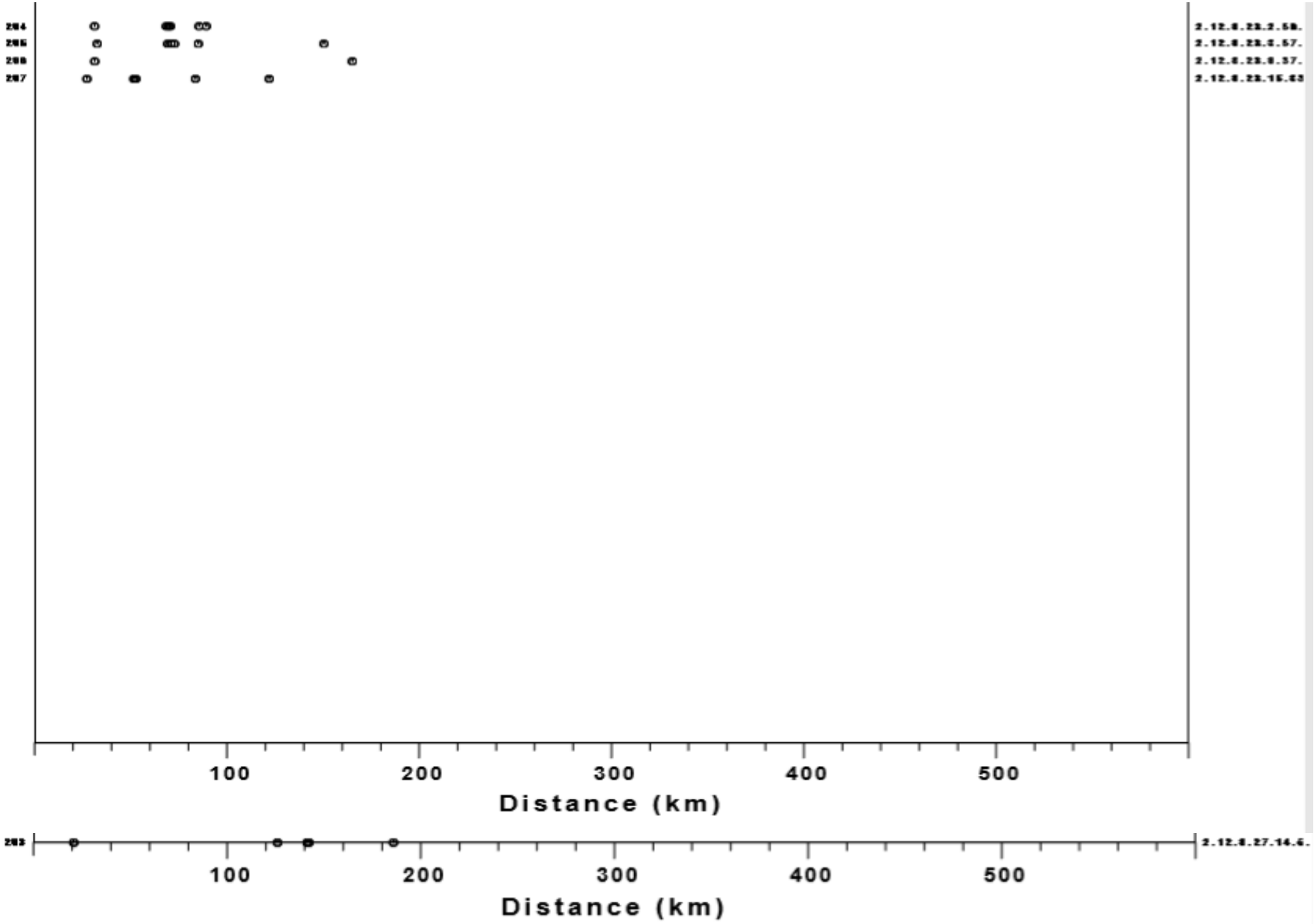
100
200
300
400
500
Distance (km)
100
200
300
400
500
Distance (km)

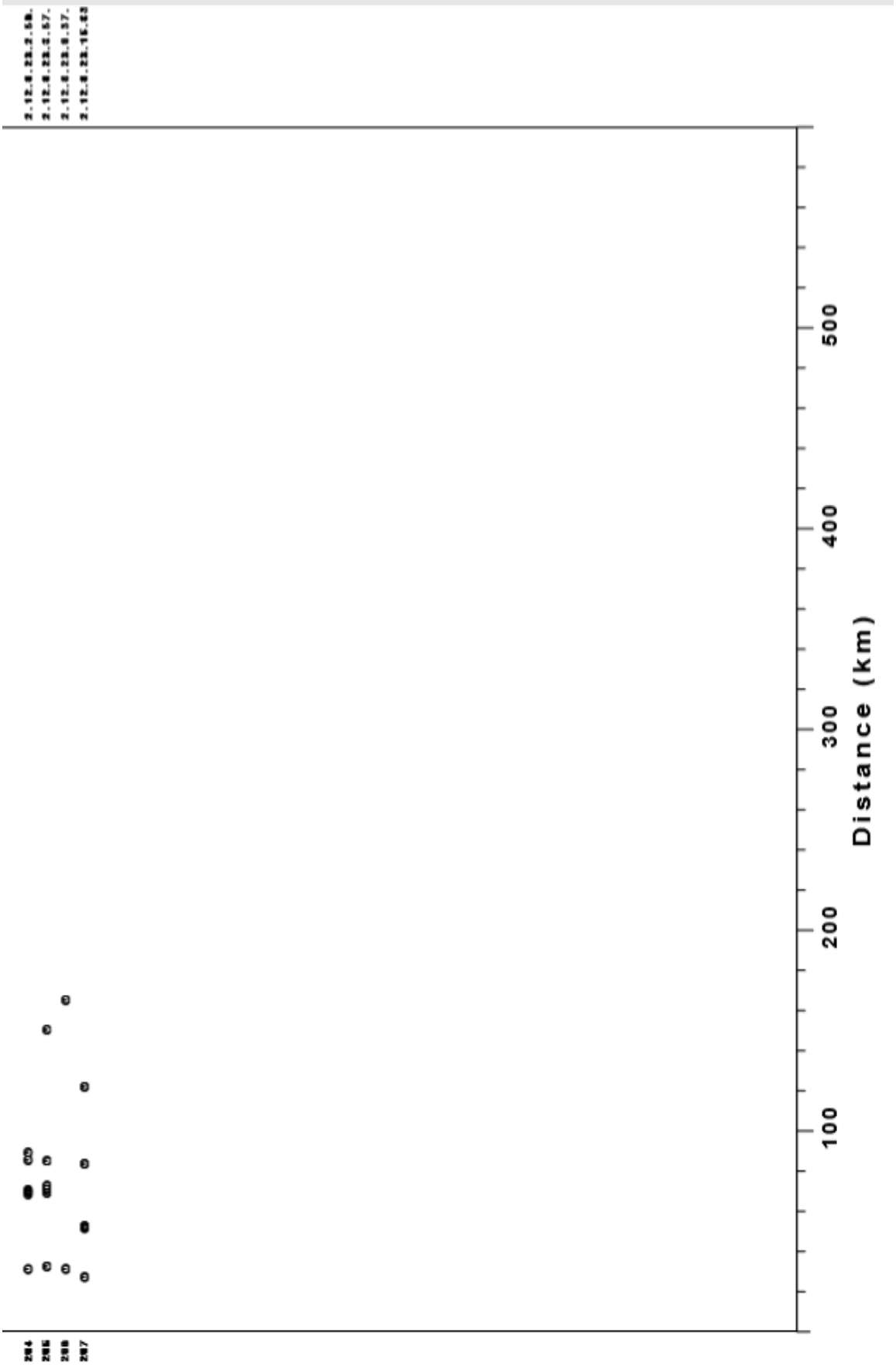
Distance (km)
100
200
300
400
500

Appendix D

Heatmaps

PGA (cm/sec^2) Heatmap for Magnitude 5 earthquake based on 1992 event

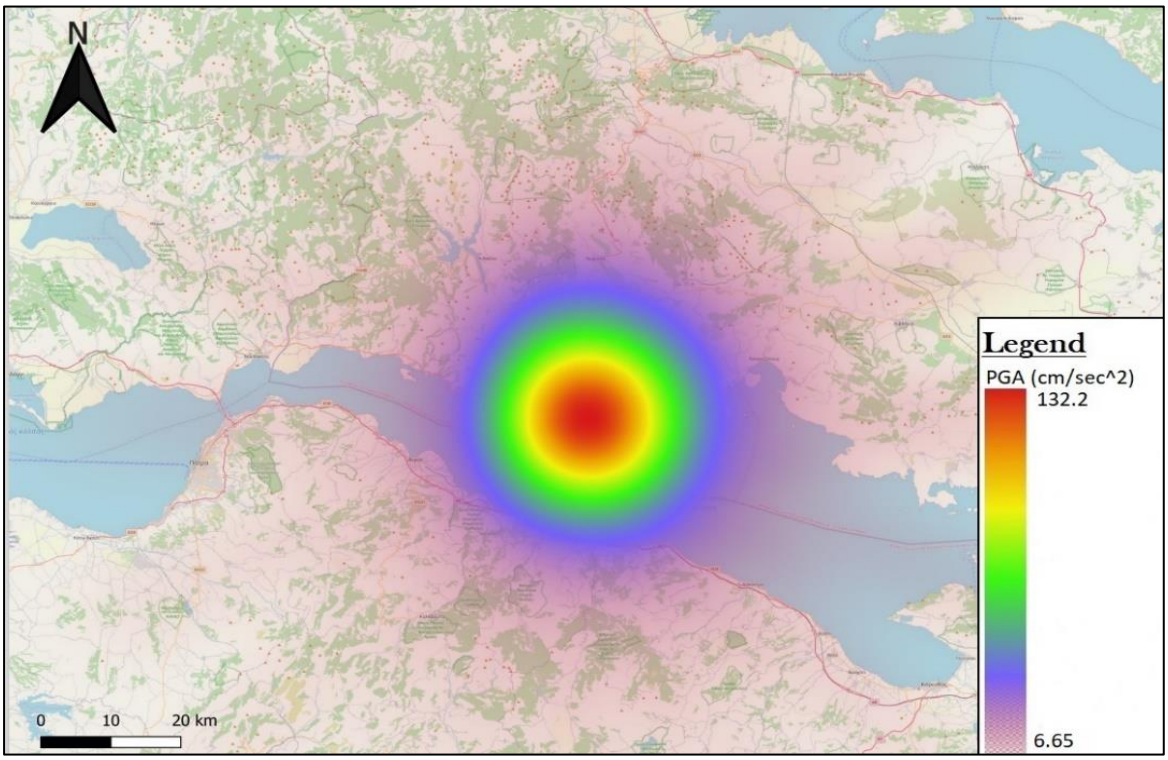

PGA (cm/sec^2) Heatmap for Magnitude 6 earthquake based on 1992 event

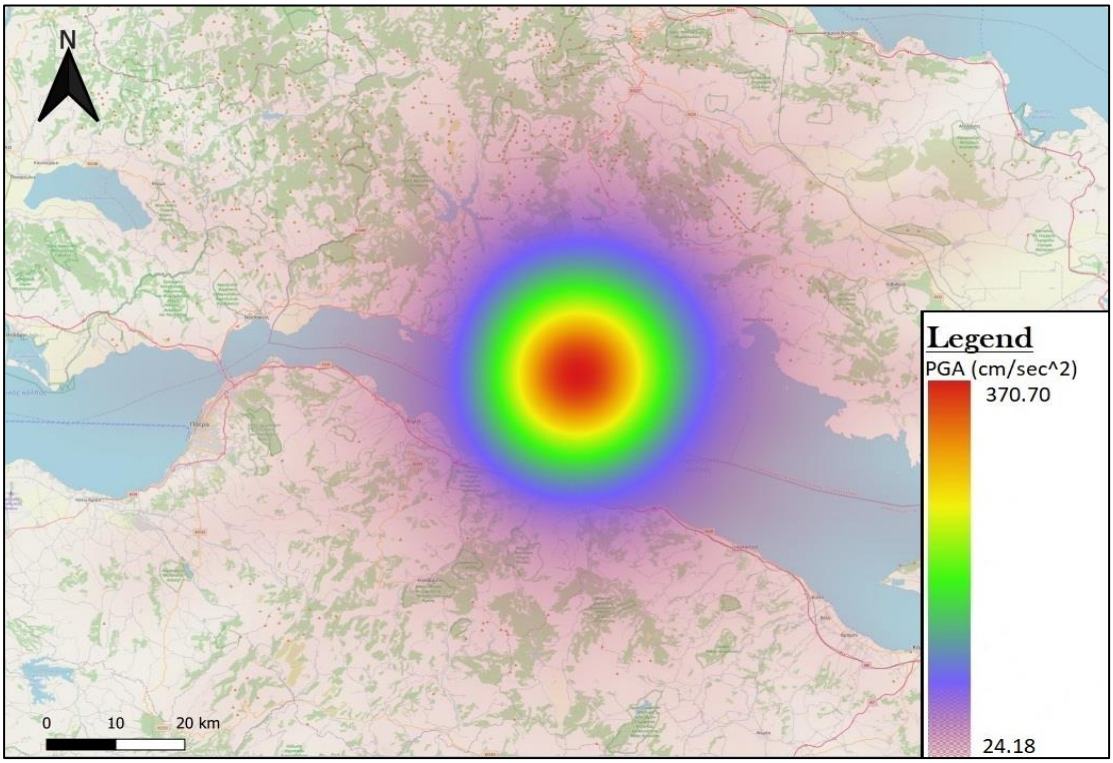

PGA (cm/sec2) Heatmap for Magnitude 7 earthquake based on 1992 event.